



Multiplatform radar-lidar synergistic retrieval for liquid and mixed-phase clouds

Clémantyne Aubry

► To cite this version:

Clémantyne Aubry. Multiplatform radar-lidar synergistic retrieval for liquid and mixed-phase clouds. Ocean, Atmosphere. Université Paris-Saclay, 2024. English. NNT : 2024UPASJ008 . tel-04594307

HAL Id: tel-04594307

<https://theses.hal.science/tel-04594307>

Submitted on 30 May 2024

HAL is a multi-disciplinary open access archive for the deposit and dissemination of scientific research documents, whether they are published or not. The documents may come from teaching and research institutions in France or abroad, or from public or private research centers.

L'archive ouverte pluridisciplinaire **HAL**, est destinée au dépôt et à la diffusion de documents scientifiques de niveau recherche, publiés ou non, émanant des établissements d'enseignement et de recherche français ou étrangers, des laboratoires publics ou privés.

Multiplatform radar-lidar synergistic retrieval for liquid and mixed-phase clouds

*Restitution synergique radar-lidar multiplateforme
pour nuages liquides et de phase mixte*

Thèse de doctorat de l'université Paris-Saclay

École doctorale n°129 Sciences de l'environnement d'Île-de-France (SEIF)

Spécialité de doctorat: Géosciences

Graduate School : Géosciences, climat, environnement et planètes

Référent : Université de Versailles-Saint-Quentin-en-Yvelines

Thèse préparée dans l'unité de recherche

LATMOS (Université Paris-Saclay, UVSQ, CNRS),

sous la direction de **Julien DELANOË**, Professeur,

la co-direction de **Silke GROß**, Privatdozentin (Équivalent Professeure)

et le co-encadrement de **Florian EWALD**, Research Scientist

Thèse soutenue à Guyancourt, le 5 avril 2024, par

Clémantyne AUBRY

Composition du jury

Membres du jury avec voix délibérative

Philippe KECKHUT

Professeur, Université de Versailles St-Quentin-en-Yvelines

Johannes QUAAS

Professeur, Universität Leipzig

Frédéric SZCZAP

Maître de conférences - HDR, Université Clermont Auvergne

Olivier JOURDAN

Maître de conférences - HDR, Université Clermont Auvergne

Martina KRÄMER

Professeure, Forschungszentrum Jülich

Président

Rapporteur

Rapporteur & Examineur

Examineur

Examinatrice

Titre: Restitution synergique radar-lidar multiplateforme pour nuages liquides et de phase mixte

Mots clés: synergie, radar, lidar, eau surfondue, nuage de phase mixte

Résumé :

Les nuages jouent un rôle important dans le cycle de l'eau et le bilan radiatif de la Terre, et tendent à significativement refroidir le climat. Cependant, de nombreuses incertitudes demeurent concernant leurs rétroactions et leur évolution dans le contexte du réchauffement climatique. Les nuages de phase mixte représentent une part non négligeable de l'effet radiatif des nuages. Ils sont constitués d'un mélange de cristaux de glace, de gouttelettes d'eau surfondues et de vapeur d'eau. Cette coexistence implique des processus complexes et la fraction de liquide et de glace affecte de manière significative leurs propriétés radiatives. Cette complexité les rend difficiles à représenter dans les modèles numériques, introduisant des biais significatifs. Il est donc crucial de mieux comprendre les processus microphysiques de ces nuages pour réduire les incertitudes des prévisions climatiques et météorologiques.

Pour observer les nuages, il existe plusieurs types d'instruments, tels que les sondes *in situ* (au contact des hydrométéores) et les instruments de télédétection (observations distantes). Les radars et les lidars nous permettent d'obtenir des informations résolues en distance et peuvent être embarqués à bord d'avions ou de satellites, offrant ainsi couvertures régionale et globale. Les radars nuages fonctionnent à des fréquences (35 et 95 GHz) pour lesquelles la réflectivité est sensible à la taille des particules, impliquant une réflectivité plus élevée pour les grosses particules nuageuses (les cristaux de glace) que pour les petites particules (les gouttelettes d'eau). Les lidars, quant à eux, fonctionnent habituellement entre 355 et 1064 nm et sont globalement plus sensibles à la concentration des particules. Ainsi, la rétrodiffusion lidar est plus élevée pour les particules très concentrées, telles que les gouttelettes d'eau. Leur synergie permet de tirer avantage des forces et des faiblesses de chacun pour restituer les propriétés des nu-

ages. Cependant, ces propriétés ne sont pas directement accessibles à partir des mesures et des algorithmes de restitution sont donc utilisés pour relier les mesures aux propriétés microphysiques.

Cette thèse propose une nouvelle méthode synergique radar-lidar dédiée à la restitution des propriétés des nuages d'eau surfondue, de glace et de phase mixte. Sur la base d'une méthode existante mais dédiée uniquement aux nuages de glace, une nouvelle approche permettant d'inclure à la fois l'eau surfondue et les situations de phase mixte a été développée. La première étape a été d'adapter et d'améliorer la classification servant à identifier la nature des particules observées. Ensuite, de nombreuses adaptations ont été apportées à l'algorithme afin de restituer séparément les propriétés des cristaux de glace et de l'eau surfondue. Cette approche est basée sur les sensibilités différentes du radar et du lidar vis-à-vis des deux types d'hydrométéores : les cristaux de glace dominant le signal radar tandis que l'eau surfondue domine le signal lidar.

Afin d'évaluer cette nouvelle méthode, les restitutions sont comparées à des mesures *in situ*, provenant d'observations colocalisées et de la littérature. La première étude compare les restitutions obtenues à partir des données satellites CloudSat-CALIPSO avec des mesures *in situ* aéroportées colocalisées. Cette étude montre que les restitutions radar-lidar suivent les mêmes tendances que les mesures *in situ* et fournissent des résultats prometteurs avec un pourcentage d'erreur moyen de 49 % pour le contenu en eau liquide et 75 % pour le contenu en glace et ce malgré des échelles de mesures différentes et une colocalisation imparfaite. La méthode développée est également appliquée aux plateformes aéroportées française et allemande RALI et HALO. Les premiers résultats sont prometteurs et les données *in situ* colocalisées obtenues lors de campagnes récentes pourront être utilisées pour évaluer davantage l'algorithme et améliorer son paramétrage.

Title: Multiplatform radar-lidar synergistic retrieval for liquid and mixed-phase clouds

Keywords: synergy, radar, lidar, supercooled water, mixed-phase clouds

Abstract: Clouds play an important role in the Earth's water cycle and radiation balance, and tend to cool the climate significantly. However, there are still many uncertainties about their feedbacks and their evolution in the context of global warming. In particular, mixed-phase clouds account for a considerable proportion of the cloud radiative effect. They are composed of a mixture of ice crystals, supercooled water droplets and water vapor. This coexistence involves complex processes and the fraction of liquid and ice significantly affects their radiative properties. This complexity makes them difficult to represent in numerical models, which introduces significant biases. For this reason, it is crucial to better understand the microphysical processes of these clouds to reduce the uncertainties in climate and weather forecasts.

To observe clouds, several instrument types exist, such as *in situ* probes (in direct contact with the hydrometeors) and remote sensing instruments (remote observations). Radar and lidar allow us to obtain distance-resolved information. They can be deployed onboard aircraft or satellites, providing regional and global coverage. Cloud radars operate at frequencies (35 and 95 GHz) at which the reflectivity is sensitive to particle size, implying higher reflectivity for large cloud particles (ice crystals) than for small particles (water droplets). Lidars, on the other hand, usually operate between 355 and 1064 nm and are generally more sensitive to particle concentration. As a result, lidar backscatter is higher for highly concentrated particles, such as water droplets. Their synergy allows us to take advantage of the strengths and weaknesses of each instrument to retrieve cloud properties. However, these properties are not directly accessible from measurements

and retrieval algorithms are therefore used to relate measurements to microphysical properties.

This thesis proposes a new radar-lidar synergistic method dedicated to retrieve supercooled water, ice and mixed-phase cloud properties. Based on an existing method dedicated solely to ice clouds, a new approach has been developed to include both supercooled water and mixed-phase situations. The first step was to adapt and improve the classification used to identify the nature of the observed particles. Next, numerous adaptations have been applied to the algorithm to retrieve separately ice crystals and supercooled water properties. This approach is based on the different sensitivities of radar and lidar to the two types of hydrometeors: ice crystals dominate the radar signal while supercooled water dominates the lidar signal.

To assess this new method, the retrievals are compared to *in situ* measurements from collocated observations and the literature. The first study compares retrievals from CloudSat-CALIPSO satellite data with collocated *in situ* airborne measurements. This comparison shows that the radar-lidar retrievals follow the same trend as the *in situ* measurements and provide promising results with mean percent error of 49 % for liquid water content and 75 % for ice water content, despite the quite different measurement scales and imperfect collocation. Additionally, this has been applied to the French and German airborne platforms RALI and HALO. These first results are promising and the collocated *in situ* data collected during recent campaigns can be used to further assess the algorithm and improve its parameterization.

Remerciements

Je souhaite, tout d'abord, remercier Julien Delanoë d'avoir fait en sorte que ce projet voit le jour ainsi que de m'avoir fait confiance. Son aide et sa bonne humeur me furent précieuses durant ces quatre années.

De même, je remercie Silke Groß et Florian Ewald de m'avoir encadrée durant ma thèse. Je souhaite, tout particulièrement, les remercier pour leur accueil et leur bienveillance.

Je tiens à remercier Frédéric Szczap et Johannes Quaas d'avoir accepté de rapporter mes travaux.

De même, je remercie Philippe Keckhut, Martina Krämer et Olivier Jourdan pour leur participation à ce jury de thèse.

Je remercie Gwendal Rivière et Olivier Jourdan d'avoir accepté d'être membre de mon comité de suivi de thèse ainsi que pour les conseils qu'ils m'ont apportés.

Je remercie Nicolas Viltard pour son aide et son soutien.

Je remercie Sophie Bounissou et Christophe Caudoux avec qui j'ai passé d'excellents moments en campagnes de mesures.

Je remercie Pragya Vishwakarma et Oscar Rojas pour l'accueil chaleureux qu'ils m'ont réservé au LATMOS.

Je tiens à remercier tout particulièrement Felipe Toledo et Susana Jorquera, mes collègues et amis, d'avoir été là pour moi durant cette période de ma vie.

Je remercie Andreas Fix pour son accueil chaleureux et les bons moments passés au DLR.

Je remercie mes collègues du DLR, Eleni Tetoni, Robert Reichert, Konstantin Krüger et Manuel Gutleben pour les bons moments que nous avons partagés ensemble.

Je tiens à remercier tout particulièrement Georgios Dekoutsidis et Christian Heske, mes collègues et amis les plus chers, pour qui je ne voulais plus quitter la Bavière !

Je souhaite également remercier toute l'équipe de SAFIRE, pour ces campagnes de mesure et ce baptême de l'air hors du commun !

Je remercie ma famille pour son soutien inconditionnel, en particulier mon frère, Arthur Aubry et mes parents, Marc et Nathalie Aubry.

Pour terminer, je souhaite remercier Paul Gautier pour son immense aide, son précieux soutien et sa patience.

Danksagungen

Zunächst möchte ich Julien Delanoë für sein Vertrauen in mich danken. Nur durch ihn wurde mir dieses Projekt möglich gemacht. Seine Hilfe sowie seine gute Laune waren in den letzten vier Jahren sehr wertvoll für mich.

Ebenso danke ich Silke Groß und Florian Ewald dafür, dass sie mich während meiner Promotion betreut haben. Insbesondere möchte ich mich bei ihnen für ihre Gastfreundschaft und ihr Wohlwollen bedanken.

Ich möchte Frédéric Szczap und Johannes Quaas dafür danken, dass sie sich bereit erklärt haben, meine Arbeit zu lesen und zu bewerten.

Ebenso danke ich Philippe Keckhut, Martina Krämer und Olivier Jourdan für ihre Bereitschaft Jury-Mitglied meiner Doktorarbeit gewesen zu sein.

Ich danke Gwendal Rivière und Olivier Jourdan für ihre Hilfe und ihre Bereitschaft Teil meines Disertationskomitees gewesen zu sein.

Ich danke Nicolas Viltard für seine Hilfe und Unterstützung.

Für die großartige, gemeinsam verbrachte Zeit auf Messkampagnen, möchte ich mich bei Sophie Bounissou und Christophe Caudoux bedanken.

Ich danke Pragya Vishwakarma und Oscar Rojas für den freundlichen Empfang, den sie mir am LATMOS bereitet haben.

Mein besonderer Dank gilt Felipe Toledo und Susana Jorquera, meinen Kollegen und Freunden, für ihre Unterstützung und Teilnahme an diesem für mich wichtigen Lebensabschnitt.

Ich danke Andreas Fix für den freundlichen Empfang und die schöne Zeit am DLR.

Ich danke meinen Kollegen vom DLR, Eleni Tetoni, Robert Reichert, Konstantin Krüger und Manuel Gutleben für die schöne Zeit, die wir gemeinsam verbracht haben.

Mein besonderer Dank gilt Georgios Dekoutsidis und Christian Heske, meinen liebsten Kollegen und Freunden, für die ich Bayern nicht mehr verlassen wollte.

Ich möchte auch dem gesamten Team von SAFIRE für die Messkampagnen und die außergewöhnliche Lufttaufe danken!

Ich danke für die bedingungslose Unterstützung meiner Familie, insbesondere meines Bruders Arthur Aubry und meiner Eltern Marc und Nathalie Aubry.

Abschließend möchte ich mich bei Paul Gautier für seine immense Hilfe, seine wertvolle Unterstützung und seine Geduld bedanken.

Contents

Introduction	11
1 Clouds and their impact on the climate	21
1.1 What is a cloud?	22
1.1.1 Clouds formation and classification	22
1.1.2 Supercooled water and mixed-phase clouds	25
1.1.3 Ice crystals and liquid droplet shape	26
1.1.4 Clouds optical and microphysical variables	29
1.2 Clouds' impact on the Earth's climate	32
1.2.1 Introduction of electromagnetic radiation	32
1.2.2 Emission, extinction and scattering	34
1.2.2.1 Emission	34
1.2.2.2 Extinction	36
1.2.2.3 Scattering	37
1.2.3 Earth water cycle and radiative budget	41
1.2.4 Cloud radiative effect and feedback	43
1.3 Conclusion	46
2 Instrumentation for cloud observation	47
2.1 <i>In situ</i> measurements	48
2.1.1 Cloud Particle Imager	48
2.1.2 Forward Scattering Spectrometer Probe	52
2.1.3 Polar Nephelometer	54
2.1.4 Two-Dimensional Stereo Probe	56
2.1.5 Cloud Droplet Probe	58
2.2 Remote sensing	60
2.2.1 Passive remote sensing	61
2.2.2 Active remote sensing	66
2.2.2.1 Radar	68
2.2.2.2 Lidar	72
2.2.3 Radar-lidar synergy	78
2.3 Spaceborne and airborne radar-lidar platforms	80
2.3.1 CloudSat and CALIPSO from A-Train	81
2.3.2 CPR and ATLID from EarthCARE	85
2.3.3 RALI: RASTA and LNG	88
2.3.4 MIRA and WALES	92
2.3.5 CRS and CPL	96
2.4 Conclusion	97

3	Method to retrieve mixed-phase clouds with radar-lidar measurements	99
3.1	Ice cloud properties retrieval	100
3.1.1	The inverse problem	100
3.1.1.1	The Bayes theorem	101
3.1.1.2	Cost function optimization	102
3.1.2	The VarPy-ice version	105
3.2	Cloud phase classifications	116
3.2.1	DARDAR-MASK v2 classification	116
3.2.2	Adaptations to mixed-phase and supercooled water	121
3.3	The VarPy-mix version	126
3.3.1	Hypothesis to retrieve supercooled water and mixed-phase	127
3.3.2	New state vector configuration	127
3.3.3	Normalized Droplet Size Distribution for liquid Look Up Table	131
3.3.4	Algorithm adaptations to the supercooled water and the mixed-phase retrieval	133
3.4	Conclusion	136
4	Application on several platforms and comparison to <i>in situ</i> measurements	139
4.1	VarPy-mix first retrievals and comparison with <i>in situ</i> measurements	140
4.1.1	Remote sensing and <i>in situ</i> measurements	141
4.1.2	VarPy-mix retrievals	144
4.1.3	Comparison between VarPy-mix retrievals and <i>in situ</i> data	148
4.2	VarPy-mix application to airborne platforms during recent campaigns	153
4.2.1	HALO-(AC) ³ case study	153
4.2.1.1	HALO-(AC) ³ campaign presentation	153
4.2.1.2	MIRA and WALES measurements	154
4.2.1.3	VarPy-mix retrievals	158
4.2.2	RALI-THINICE case study	163
4.2.2.1	RALI-THINICE campaign presentation	163
4.2.2.2	RASTA and LNG measurements	163
4.2.2.3	VarPy-mix retrievals	167
4.2.3	Comparison with <i>in situ</i> data from literature	172
4.3	Comparison between VarPy-ice, 2C-ICE and <i>in situ</i>	177
4.4	Conclusion	180
	Conclusion	181
	A Appendix	190
	References	286

Introduction

Context

Water is an omnipresent chemical compound on Earth, and is continuously in motion. Such perpetual movement, called the water cycle, is possible thanks to the transfers generated by the five elements constituting the Earth's climate system and interacting with each other: the lithosphere, the biosphere, the cryosphere, the hydrosphere and the atmosphere. We present in Figure 1 a scene showing each of these elements and we describe them in the next paragraphs.

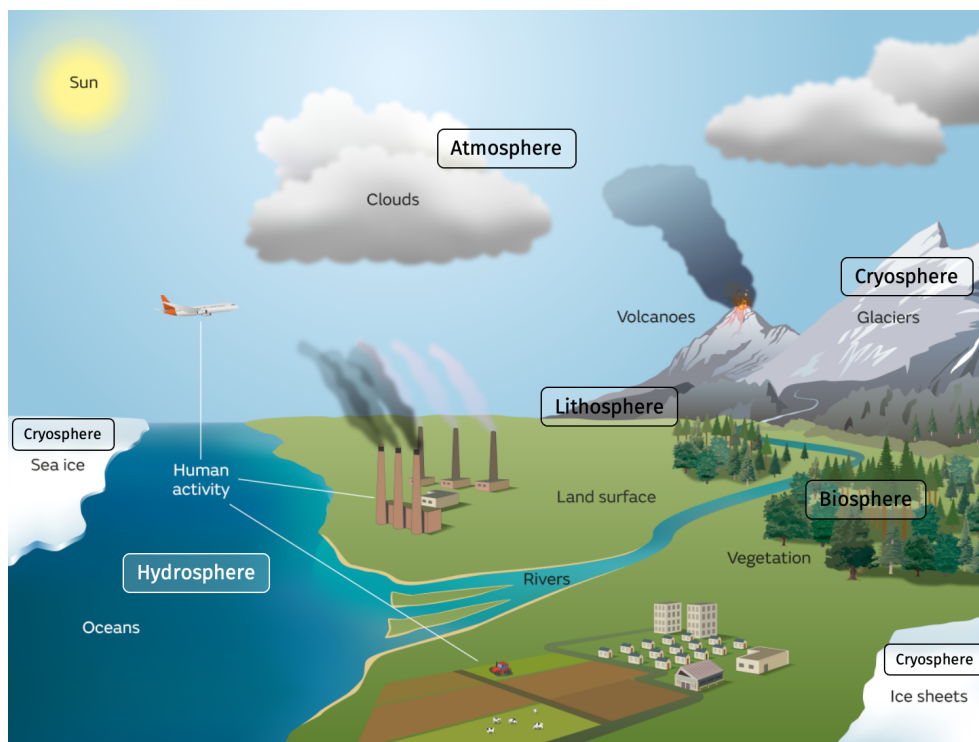


Figure 1: Earth's climate system components (from [MetOffice Website - What is Climate?](#) - with added name of the five elements)

The lithosphere, i.e. the Earth's crust (continental and oceanic) and upper mantle, plays an important role in the Earth's thermal balance. It emits heat through infrared radiation, which remains partially trapped on Earth due to the greenhouse effect. In addition, it is a major source of aerosols that will be released into the air and will interact with water vapor to form clouds. The biosphere represents all living organisms as well as their living environments.

It influences the atmosphere composition by absorbing and releasing greenhouse gases in the form of carbon dioxide and water vapor. The cryosphere, e.g. glaciers, snow surface, sea ice and permafrost, reflects solar energy due to its high albedo. When it melts, it brings water into the oceans and the albedo decreases, which modifies its radiative impact. The hydrosphere, e.g. the oceans, brings water into the air through evaporation. Ocean currents from the equator to the poles generate heat transport and have a regulating effect on the climate system. The atmosphere is the gaseous envelope surrounding the Earth and is composed, for dry air and by volume, of 78.08 % nitrogen (N₂), 20.95 % oxygen (O₂), 0.93 % argon (Ar), 420 ppmv carbon dioxide (CO₂) and other gases in small amounts. The atmosphere also contains water vapor (H₂O), whose quantity varies significantly locally and represents about 0.25 % of the atmosphere's total mass. When it condenses into a liquid or solid phase, this water forms clouds, covering about 67 % of the sky (King et al. 2013)

Consequently, each climate system element contributes to cloud formation, which partially absorb and reflect solar and terrestrial energy. The Earth's energy budget is the balance between incoming (mostly from the Sun), absorbed, reflected and outgoing energy from the climate system. Consequently, clouds play a significant role in the Earth's energy budget but also in the water cycle (Stephens 2005). The impact of clouds on the energy budget is quantified by the Net Cloud Radiative Effect (CRE) which is the difference between Earth's radiative heating for average cloud conditions and clear sky condition (Ramanathan et al. 1989). Negative CRE indicates that clouds lead to energy loss in the climate, inducing a cooling effect, and the opposite for positive CRE. The Figure 2 represents the Net CRE on Earth averaged over one year and is provided by the Clouds and the Earth's Radiant Energy Systems (CERES, Loeb et al. 2018) satellite data. We can see that the spatial distribution differs according to the region of the globe, with for example a positive CRE (warming effect) in Antarctica and North Africa and a negative CRE (cooling effect) over the oceans. The global average CRE is -19 W.m^{-2} , meaning that clouds cool significantly the Earth climate.

However, the atmospheric composition is currently changing due to human activities, affecting the radiative properties of clouds. Consequently, the cooling effect of clouds on Earth's radiation budget is also affected. This phenomenon is referred as cloud feedback and most current scientific studies indicate that clouds tend to amplify the global warming, with a positive cloud feedback of $+0.6 \text{ W.m}^{-2}.\text{°C}^{-1}$ (-0.2 to $+2.0 \text{ W.m}^{-2}.\text{°C}^{-1}$, Boucher et al. 2013).

**Net Cloud Radiative Effect
(average)**

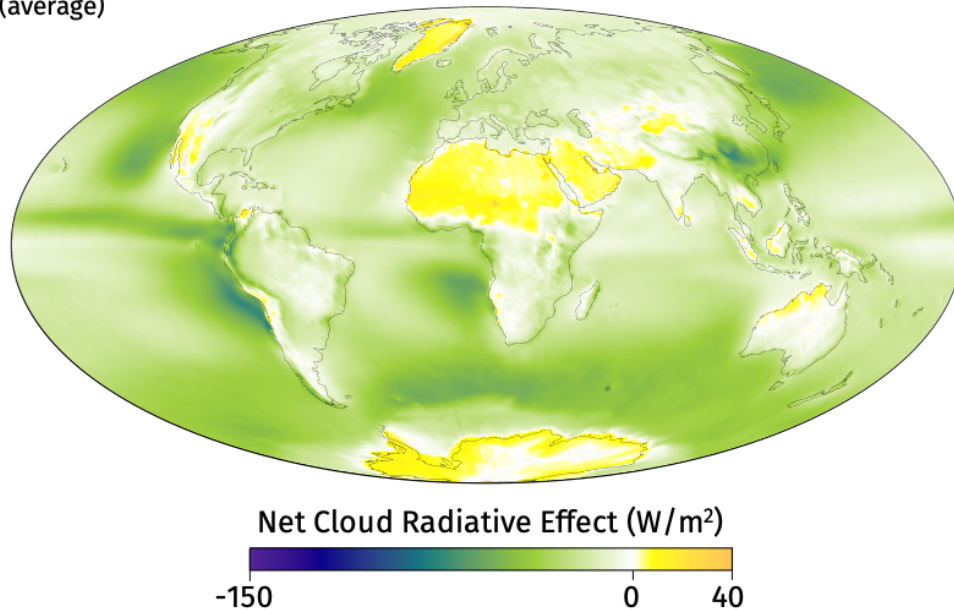


Figure 2: Net Cloud Radiative Effect from CERES. Average values between 2000 and 2015 (Credit: NASA)

The current situation concerning climate change strongly impacts our society (IPCC 2022), notably due to the increasing frequency and intensity of extreme temperatures, droughts, severe precipitation, flooding and tropical cyclones (Clarke et al. 2022). Weather and climate forecasts are therefore important to understand and predict respectively short and long term events. However, climate and weather prediction models still have lack of knowledge in some situations and scenarios where clouds remain one of the main sources of uncertainty, due to a lack of understanding of the key processes controlling their life cycle, their macrophysical and microphysical properties.

Problematic

Among all cloud types, mixed-phase clouds account for a significant proportion of the CRE (20 %, Matus and L'Ecuyer 2017). These clouds occur at all latitudes and more frequently at mid- and high-latitudes (Choi et al. 2010; Shupe 2011), reflecting efficiently solar energy back to space, and consist of a coexisting mixture of three phases of water: ice crystals, supercooled liquid droplets and water vapor at temperatures between -40°C and 0°C . This coexistence implies complex formation processes, such as primary ice nucleation (Meyers et al. 1992), secondary ice production (Field et al. 2017; Kanji et

al. 2017) and ice deposition (Meyers et al. 1992), and growing processes, such as the Wegener–Bergeron–Findeisen (WBF) process (Wegener 1911; Bergeron 1935; Findeisen 1938), water vapor deposition (Song and Lamb 1994), aggregation (Hobbs et al. 1974) and riming (Hallett and Mossop 1974). Since liquid droplets and ice crystals influence the shortwave and longwave radiation differently (Matus and L’Ecuyer 2017), the fraction of liquid and ice particles will significantly affects the radiative properties of mixed-phase clouds, altering the radiative balance of the Earth’s atmospheric system. Moreover, all these processes are difficult to represent in numerical models (Morrison et al. 2008, 2012) and mixed-phase clouds that are not well represented in models can introduce significant biases, such as a misrepresentation of the cloudy state (Pithan et al. 2014). For that reason, it is crucial to have information on mixed-phase cloud microphysics in order to reduce the uncertainties in climate and weather prediction.

Observing clouds is the key to obtaining information about them. For this, it is necessary to use instruments designed for cloud observation, i.e. sensitive to cloud properties. Two options are available: *in situ* measurements, where probes come into contact with cloud particles to sample them, and remote sensing instruments, which measure the radiation emitted or scattered by cloud particles from a distance. *In situ* measurements enable the analysis of a specific small volume, especially inside clouds, while remote sensing instruments can analyze entire range profiles of clouds. Remote sensing is generally less detailed than *in situ*, but allows a more global analysis of clouds and the processing of a larger number of cases. Remote sensors can be split into two categories: passive remote sensing, which directly measures the radiation emitted or scattered by the object, and active remote sensing, which sends energy to the target and measures the energy reflected or backscattered by the target. Active remote sensing instruments can then probe inside clouds, while passive remote sensors provide integrated information on the atmospheric column. Radar (RADio Detection And Ranging) and lidar (Light Detection And Ranging) are two instruments that use electromagnetic radiation as an energy source to observe clouds. Each instrument has its own characteristics and a specific sensitivity that depends notably on the instrument wavelength. With a wavelength between 355 nm and 1064 nm, the lidar attenuated backscatter β_a [$\text{m}^{-1}.\text{sr}^{-1}$] is more sensitive to the concentration of air molecules, hydrometeors and can detect small cloud particles and aerosols. However, this signal can be attenuated or extinguished by highly concentrated particles and cannot give information below this cloud layer. On the other hand the radar reflectivity Z [dBZ] at typical wavelength for cloud radars, at 35 GHz or 95 GHz, is more sensitive to the particle size and the signal can penetrate thick clouds (Delanoë et al. 2013; Cazenave et al. 2019).

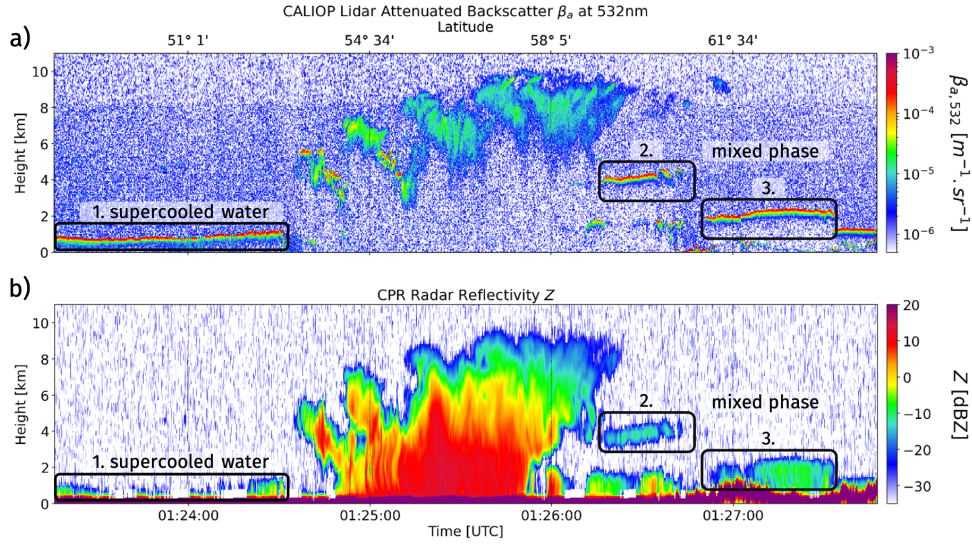


Figure 3: CALIOP lidar attenuated backscatter at 532 nm a) and CPR radar reflectivity at 95 GHz b) on 1st January 2008. Both panels share the same abscissa axes (time and latitude). The dark blue box reveal the ice cloud seen by both instrument. Data from DARDAR-MASK V2.23 products, <https://www.icare.univ-lille.fr/>, orbit ID: 2008001002019_08922

Radar and lidar can be ground-based, allowing clouds to be observed from below, or on board an aircraft or satellite, allowing large-scale cloud probing with vertical profiles seen from above. Airborne and spaceborne platforms are useful to detect the mixed-phase layer at cloud top, which is typically the case in arctic boundary layer clouds (Gayet et al. 2009; Mioche et al. 2017). On one hand, in mixed-phase clouds, the lidar is more sensitive to highly concentrated liquid droplets and gives a strong backscatter signal. On the other side, the radar reflectivity of liquid droplets is less strong than the reflectivity of ice crystals. Both instruments complement each other thanks to their different sensitivities. The Figure 3 shows an example of supercooled water layer and mixed-phase clouds detected by (panel a)) the Cloud-Aerosol Lidar with Orthogonal Polarization (CALIOP) onboard the Cloud Aerosol Lidar and Infrared Pathfinder Satellite Observations satellite (CALIPSO, Winker et al. 2003) and (panel b)) the Cloud Profiling Radar (CPR) onboard the Cloud Satellite (Cloud-Sat, Stephens et al. 2002). In the upper panel, we can see the strong backscatter signal (red color, above $10^{-4} \text{ m}^{-1} \cdot \text{sr}^{-1}$) coming from the detection of supercooled droplets and indicated by three black boxes. In the lower panel, for the box 1, the radar signal is very low revealing the lack of ice crystals over a large part of the supercooled water layer detected by the lidar. For the two other boxes, the radar signal indicates ice crystals and consequently mixed-phase. As a result, these measurements can be used to retrieve mi-

microphysical cloud properties such as the visible extinction α , the ice and liquid water contents (IWC and LWC), effective radius of the particles r_e and the total number concentration N_t . To achieve this, dedicated retrieval algorithms are required.

Lidar-radar synergistic methods were first proposed by Intrieri et al. 1993, Donovan and Lammeren 2001, Tinel et al. 2005 and Mitrescu et al. 2005 to retrieve ice clouds properties where both instrument overlap. Algorithms as 2C-ICE (Deng et al. 2010) and VarCloud (Delanoë and Hogan 2008) were later developed to retrieve ice clouds properties all along the instruments profile using CPR onboard CloudSat, CALIOP onboard CALIPSO and additionally radiometers for VarCloud. For the Earth Clouds, Aerosols and Radiation Explorer mission (EarthCARE, Illingworth et al. 2015), which is planned for launch in 2024, the unified synergistic retrieval algorithm CAPTIVATE (Mason et al. 2022) uses the ATmospheric LIDar (ATLID), the Cloud Profiling Radar (CPR) and the Multi-Spectral Imager (MSI) to retrieve clouds, precipitations and aerosols properties.

Thesis contributions

This thesis is dedicated to mixed-phase cloud observation and the development of a new synergistic radar-lidar method to retrieve cloud properties. For this, I propose to extend the variational method VarCloud to simultaneously retrieve the microphysical properties of mixed-phase clouds, ice clouds and supercooled water clouds using airborne or satellite radar and lidar synergy. As a result, it is possible to retrieve simultaneously the visible extinction for ice α_{ice} and liquid α_{liq} particles [m^{-1}], the ice and liquid water contents IWC and LWC [$g.m^{-3}$], the effective radius of ice $r_{e,ice}$ and liquid $r_{e,liq}$ particles [μm] and the ice and liquid number concentrations N_{ice} and N_{liq} [m^{-3}]. In addition, total extinction α_{tot} , total water content TWC and total number concentration N_{tot} can also be estimated. The method I propose, named VarPy-mix, relies on the following assumptions to retrieve the mixed-phase:

- The supercooled liquid droplets dominate the lidar measurements: the liquid droplets are more concentrated than ice crystals and give a stronger lidar backscatter signal since the lidar is more sensitive to highly concentrated particles;
- The ice crystals dominate the radar measurements: ice crystals are larger than liquid droplets and give a stronger radar reflectivity signal since the radar is sensitive to the particle size.

These assumptions are reasonable, but in reality, the signal from each instrument is affected by the presence of the two hydrometeors. As a result, the synergy is partial for each phase of the mixed-phase and the retrievals rely strongly on *a priori* values determined from *in situ* measurements.

VarCloud has been improved over the years with new parameterizations (Ceccaldi 2014; Cazenave et al. 2019) and is currently named VarPy-ice. Both VarPy-ice and VarPy-mix were written in Python3 during this thesis, which makes them flexible and allow them to be applied to multiple airborne and spaceborne platforms, presented in Table 1 (planned for EarthCARE). As a starting point, VarPy-mix was first developed with CloudSat and CALIPSO instruments datasets. These data have a large, robust and proven classification algorithmic statistics as well as existing cases of collocation with *in situ* measurements. With Frédéric Tridon ¹, Guillaume Mioche ² and Olivier Jourdan ², we compared VarPy-mix retrievals (CloudSat-CALIPSO data) with *in situ* data from the ASTAR campaign. This study constitutes the subject of a scientific paper submitted to the Atmospheric Measurement Techniques Journal and the results are presented in chapter 4.

Table 1: Radar-lidar airborne and satellite platforms with some instrument specifications.

Platform		RADAR			LiDAR		
		Name	Frequency	Doppler	Name	Wavelengths	HSR
✈	RALI	RASTA	95 GHz	✓	LNG	1064, 532, 355 nm	355 nm
✈	HALO	MIRA-35	35 GHz	✓	WALES	1064, 935, 532 nm	532 nm
✈	ER-2	CRS	94 GHz	✓	CPL	1064, 532, 355 nm	✗
📡	A-Train	CPR	94 GHz	✗	CALIOP	1064, 532 nm	✗
📡	EarthCARE	CPR	94 GHz	✓	ATLID	355 nm	355 nm

Additionally, I took part in four measurement campaigns during my thesis with various objectives:

- Ice-Genesis - from 18th to 30th January 2021, Dijon (France): increasing scientific knowledge about snow and improve 3D simulation of icing in aeronautics.
- CADDIWA - from 8th to 24th September 2021, Espargos (Sal, Cape Verde): observation of the interaction between cloud, atmospheric dynamics and aerosols.

¹DIATI, Politecnico di Torino, Turin, Italy

²Laboratoire de Météorologie Physique, OPGC, Aubière, France

- HALO-(AC)³ - from 6th March to 15th April 2022, Kiruna (Sweden): quasi-Lagrangian observations of air mass transformation processes during southern transports.
- RALI-THINICE - in August 2022, Longyearbyen (Svalbard, Norway): studying the dynamics of Arctic cyclones as well as their interactions with cloud microphysics (particularly mixed-phase) and sea ice.

During these campaigns, I operated several instruments (RASTA, BASTA and MIRA35 radars, the radiometers of HAMP and *in situ* probes) onboard three aircraft (the SAFIRE's ATR42, the SAFIRE's Falcon20 and the HALO). In addition, to ensure the monitoring of instruments (start-up, data saving, decision-making, problem resolution), scientific information was communicated and shared with other crew members, in particular the mission PI. After the CAD-DIWA, HALO-(AC)³ and RALI-THINICE campaigns, I processed the radar-lidar data with VarPy. Consequently, the RALI and HALO platforms were integrated into the new version of the algorithm.

As part of a collaboration with Stephen Nicholls³⁴ and Andrew Heymsfield⁵, an intercomparison study (blind test) of VarPy-ice and 2C-ICE radar-lidar inversion methods was carried out using data from the IMPACTS campaigns. This collaboration led to the submission of a paper to the JTECH journal. The data used in this study is from the Cloud Radar System (CRS) and Cloud Physics Lidar (CPL) instruments from the ER-2 platform. A new instrumental platform has therefore been integrated into the algorithm VarPy.

Document organization

In this manuscript, we present the scientific knowledge needed to understand the challenge of studying mixed-phase clouds, as well as the proposed solutions. The paper is organized into five chapters as follows:

Chapter 1 - Clouds and their impact on the climate: this first chapter contains the scientific knowledge needed to understand the importance of studying clouds, especially mixed-phase clouds. The first section of the chapter introduces the composition and the different types of clouds. I further describe the cloud particle microphysical properties that can be used to describe a given cloud volume. A second section is dedicated to the interaction between clouds and radiations, and the way clouds interact with the Earth's water cycle and the radiation balance.

³Science Systems and Applications, Inc. Greenbelt, MD

⁴NASA Goddard Space Flight Center, Greenbelt, MD

⁵National Center for Atmospheric Research, Boulder, CO

Chapter 2 - Instrumentation for cloud observation: this three-parts chapter describes the different approaches for studying clouds. The first part is dedicated to various *in situ* instruments. The second part focuses on passive and active remote sensing, particularly radar and lidar. A subsection is also devoted to explaining how radar-lidar synergy works and its benefits. The last part of the chapter describes five existing radar-lidar spaceborne or airborne platforms.

Chapter 3 - Method to retrieve mixed-phase clouds with radar-lidar measurements: this third chapter presents the variational method VarPy-mix. The first section introduces the inverse problem and the variational method principle. I detail the ice cloud property retrieval algorithm, VarPy-ice, on which our retrieval method is based. The second section is dedicated to the classifications used by retrieval algorithms to identify the hydrometeors. The last section aims to describe in detail the VarPy-mix algorithm, especially the various modifications implemented to retrieve supercooled water and mixed-phase clouds with radar and lidar measurements.

Chapter 4 - Application on several platforms and comparison to *in situ* measurements: in the last chapter the results of VarPy-mix applied to different mixed-phase cases are presented. The first part analyses a collocated case where *in situ* measurements were taken under the trajectory of CloudSat and CALIPSO satellites. A comparison is made between VarPy-mix retrieved properties and the *in situ* measurements (extinctions and water contents). Next, two other mixed-phase cases from recent field campaign are retrieved by VarPy-mix. A comparison with *in situ* data from literature is presented in a dedicated subsection. The last section summarizes a study that compares the VarPy-ice algorithm retrieving ice cloud properties with another retrieval algorithm and *in situ* measurements.

Conclusion: this document concludes by summarizing all the work achieved during this thesis and by offering an opening through work perspectives.

The List of Figures is provided on page 242 and the List of Tables on page 244. The list of used acronyms is available on page 256 and the list of scientific notations on page 252. The references can be found on page 286.

1 - Clouds and their impact on the climate

Contents

1.1 What is a cloud?	22
1.1.1 Clouds formation and classification	22
1.1.2 Supercooled water and mixed-phase clouds	25
1.1.3 Ice crystals and liquid droplet shape	26
1.1.4 Clouds optical and microphysical variables	29
1.2 Clouds' impact on the Earth's climate	32
1.2.1 Introduction of electromagnetic radiation	32
1.2.2 Emission, extinction and scattering	34
1.2.3 Earth water cycle and radiative budget	41
1.2.4 Cloud radiative effect and feedback	43
1.3 Conclusion	46

1.1 . What is a cloud?

1.1.1 . Clouds formation and classification

Most of the water vapor (99 %) of the atmosphere is located in the troposphere and constitutes 0.3 to 0.4% of the gases in this region (Reichle 2023). When the relative humidity of an air mass exceeds the saturation threshold, water vapor can condense into water droplets or be transformed into ice crystals by deposition nucleation. For these processes to occur, Cloud Condensation Nuclei (CCN) and Ice Nucleating Particle (INP) (Vali et al. 2015) are required to form droplets and crystals respectively. These condensation and nucleation products from water vapor are called hydrometeors.

The Figure 1.1 summarizes and illustrates the different processes of ice nucleation. Between 0 and -38°C , liquid droplets can form ice crystals by immersion, condensation or contact freezing (Kanji et al. 2017). These processes are categorized as heterogeneous freezing. At these temperatures and when they contain very few impurities, liquid droplets can stay in metastable state and are called supercooled water droplets. Below -38°C , these supercooled droplets freeze into ice without INP. This phenomenon, called the homogeneous freezing, is less common than heterogeneous freezing below 140 % of relative humidity with respect to ice (Kanji et al. 2017).

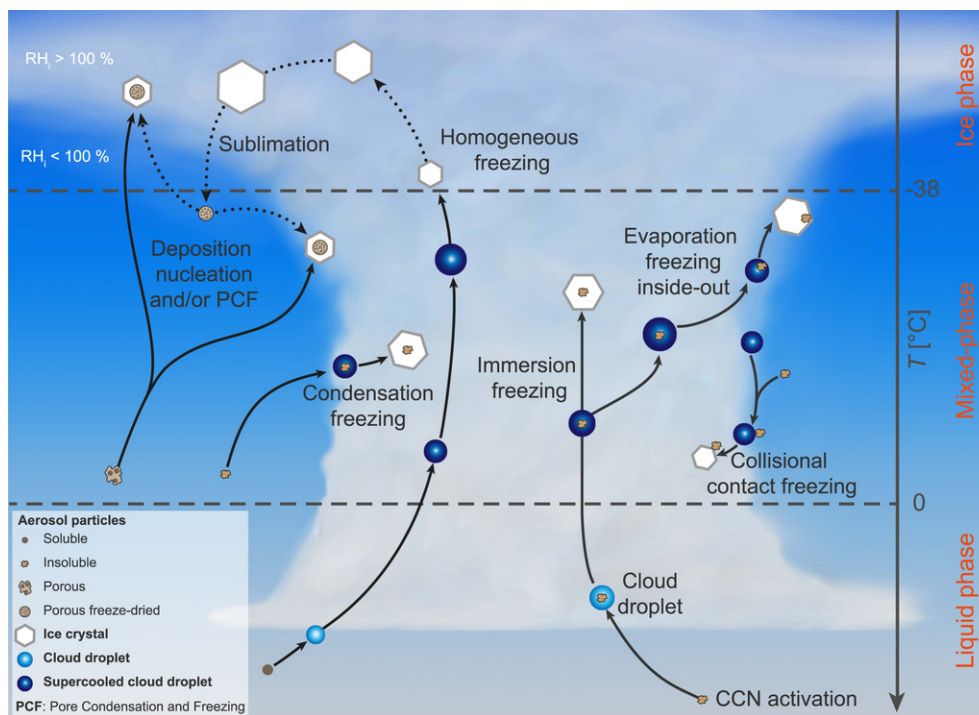


Figure 1.1: Diagram of ice nucleation processes (from Kanji et al. 2017).

The various processes involved in hydrometeors formation result in a wide variety of clouds. Howard 1803 classified clouds and splits this classification into three main parts - cirrus, stratus and cumulus - as well as intermediate cloud types such as cirrocumulus and cirrostratus. Since, the World Meteorological Organization takes this classification to recognized now ten main cloud type groups, called *genera*, illustrates by Figure 1.2 and are the following:

- Low level clouds, up to 2 km, mainly composed of liquid droplets: Stratocumulus (Sc), Stratus (St) and Cumulus (Cu)
- Mid level clouds, between 2 and 6 km, composed of both ice crystals and liquid droplets: Altocumulus (Ac), Altostratus (As) and Nimbostratus (Ns)
- High level clouds, above 6 km, mainly composed of ice crystals: Cirrus (Ci), Cirrocumulus (Cc) and Cirrostratus (Cs)
- Multi-level clouds, up to 21 km, composed of ice crystals at the top and liquid droplets at low altitude: Cumulonimbus (Cb)

In addition to these ten *genera*, two other classification levels, called species and varieties, offer the possibility to create a hundred or so combinations to classify clouds. There are fourteen species that classify clouds according to their shape and internal structure. Then, nine varieties describe the arrangement of the clouds and their transparency. The classification is constantly evolving and the new variety Volutus has recently been added. Supplementary features are also used to classify clouds and some clouds are categorised as "special clouds".

More generally, clouds are classified according to their vertical structure, which is linked to the air stability. When conditions are stable, the air mass has difficulty extending in a vertical direction and consequently spreads homogeneously horizontally. These conditions form stratiform cloud. In some cases, the cloud base is very low, even touching the ground and forming fog. On the contrary, when the conditions are unstable, with turbulence and convection, cumuliform clouds are formed. They extend more vertically than horizontally and have convective cells distinguishable by their high relief.

After their formation, clouds can dissipate by evaporation, i.e. when the water returns as vapor to the atmosphere due to a temperature rise, or by precipitation. When the particles become so heavy that upward air movements can no longer keep them suspended in the cloud, precipitation fall from the clouds. Sometimes precipitation evaporates before even touching

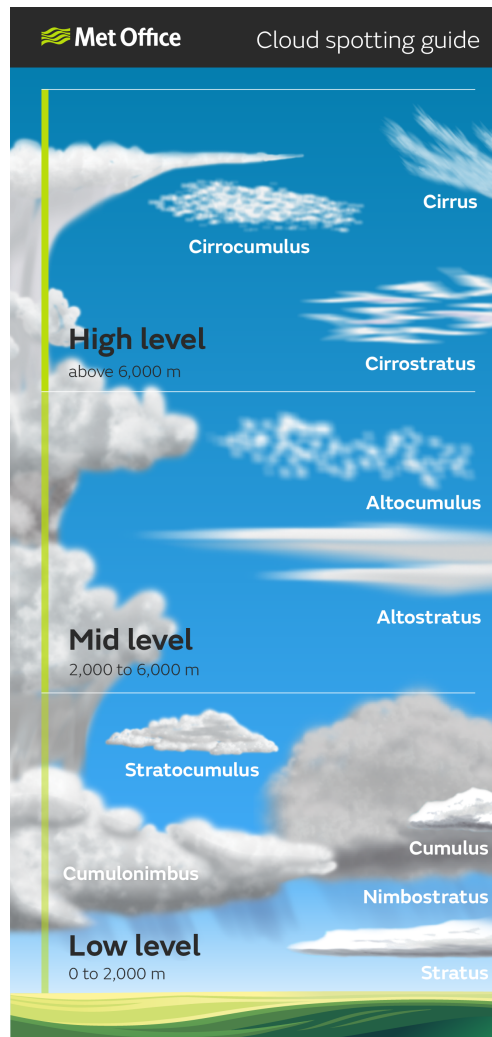


Figure 1.2: Illustration of the 10 *genera*, Cloud spotting guide (from Met Office).

the ground and the trail formed is called virga. Precipitation can be liquid (rain, drizzle), solid (snow, ice pellets, hail) or a mixture of both. Droplets become larger by coalescence, i.e. when two small droplets merge to form a larger droplet. Ice crystals can also merge to form larger crystals through the aggregation process. The Wegener–Bergeron–Findeisen (WBF) process (Wegener 1911; Bergeron 1935; Findeisen 1938) allows ice crystals to expand, at the expense of supercooled water droplets. Indeed, below 0°C the ambient vapor pressure is lower than the saturation vapor pressure over water, which implies liquid droplets evaporation. Then, the water vapor forms ice crystals through vapor deposition, as the ambient vapor pressure is higher than saturation vapor pressure over ice. This process enables precipitation, especially in supercooled clouds, and allows the formation of mixed-phase clouds.

1.1.2 . Supercooled water and mixed-phase clouds

The mixed-phase is a coexisting mixture of three water phases at temperatures between -40 and 0°C : ice crystals, supercooled liquid droplets and water vapor. This coexistence implies complex formation processes, such as primary ice nucleation (Meyers et al. 1992), secondary ice production (Field et al. 2017; Kanji et al. 2017) and deposition nucleation (Meyers et al. 1992), as well as growing processes, such as the Wegener–Bergeron–Findeisen (WBF) process (Wegener 1911; Bergeron 1935; Findeisen 1938), water vapor deposition (Song and Lamb 1994), aggregation (Hobbs et al. 1974) and riming (Hallett and Mossop 1974). Mixed-phase occurs in several type of clouds at all latitudes and more significantly at mid- and high-latitudes (Choi et al. 2010; Shupe 2011).

The Figure 1.3 (from Korolev et al. 2017) illustrates the distribution of mixed-phase within different types of clouds. In wave clouds (altocumulus, Figure 1.3 a), liquid droplets and ice crystals are formed in the upwind section of the clouds, by droplet formation with CCN, ice deposition on INP and droplet freezing (Baker and Lawson 2006; Field et al. 2012). In frontal clouds (cirrostratus and nimbostratus, Figure 1.3 b), the mixed-phase is formed inside ice cloud by the creation of water droplets caused by Kelvin-Helmholtz instability (Field et al. 2014) - when two fluids that are thermally stable are superposed and move at different speeds at their interface. In boundary layer clouds (stratus and stratocumulus, Figure 1.3 c), the WBF process plays an important role for mixed-phase formation and maintenance. The hydrometeors form, grow and evaporate by cycles. As the liquid droplets evaporate at the cloud base, the mixed-phase layer is at the top of the cloud and the ice crystals at the base. When the mixed-phase layer is inside the cloud, its lifetime does not exceed 10 to 20 minutes, since the difference of water vapor saturation over ice and liquid makes the mixed-phase condensationally unstable. However, for boundary layer mixed-phase clouds, the lifetime of the mixed-phase can persist for hours or even days (Morrison et al. 2012; Korolev et al. 2017). In deep convective clouds (cumulonimbus, Figure 1.3 d), the mixed-phase layer is inside the cloud, where the temperature is between 0 and -40°C . Vertical flows will determine the formation and lifetime of the mixed-phase layer. More information on the processes within the different cloud types can be found in Korolev et al. 2017.

The presence and proportion of supercooled water in these clouds implies interactions with solar and Earth radiation that are different from those of other cloud types (Matus and L'Ecuyer 2017). Better understanding of mixed-phase clouds is important to improve their representation in models, whose

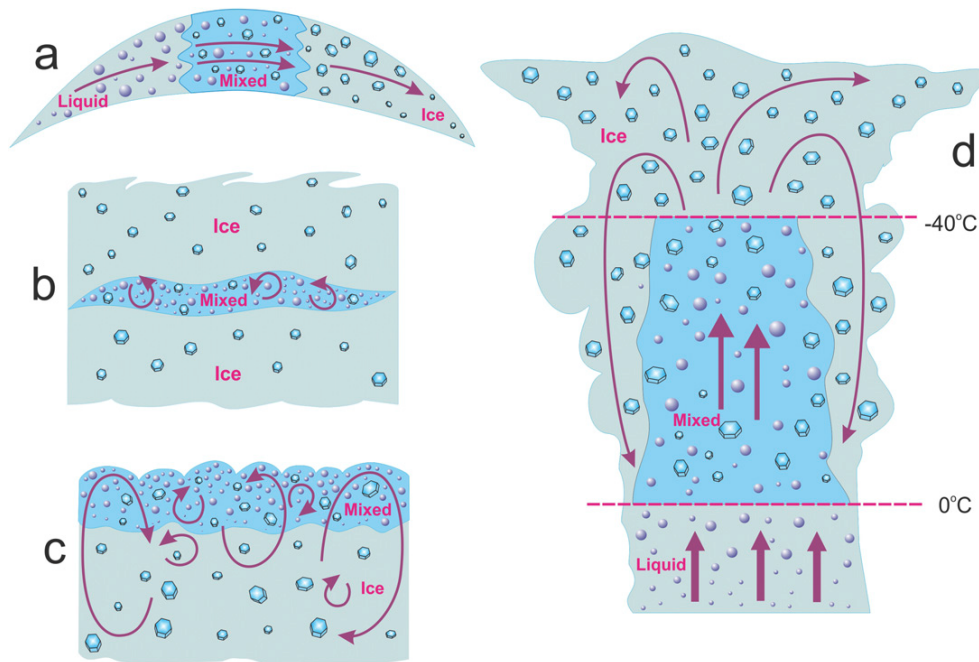


Figure 1.3: Illustration of mixed-phase (blue area) formation in a) wave clouds (Ac), b) frontal clouds (Cs, Ns), c) boundary layer clouds (St, Sc) and d) deep convective clouds (Cb) (from Korolev et al. 2017).

current uncertainty includes significant biases in climate and weather forecasts and radiation surface calculation (Ricaud et al. 2020). For this, it is necessary to characterize them, in particular through their microphysical and optical characteristics, presented in the following subsections.

1.1.3 . Ice crystals and liquid droplet shape

The average size for cloud droplets is approximately 20 μm while it is approximately 2 mm for raindrops (Pruppacher 1997). Their shape depends on the size and is spherical for cloud droplet and a slightly flattened sphere at the bottom for raindrop, that gradually flattening out as the droplet gets larger. Consequently, the shape of these drops is basic and relatively simple to represent in microphysical models. On the contrary, ice crystal shape can be very complex and can be composed of different types of simple or composite crystals. The Figures 1.4 a) to f) show image of some ice crystals. When they form, the crystals are small and often take the form of hexagonal prisms. This phenomenon is explained by the crystalline structure of water, which is hexagonal due to the angle between the hydrogen and oxygen molecules. Ice crystal then expands at the corners to form branches. This hexagonal structure is clearly observed in panels a) to c) for plate and dendrite crystals.

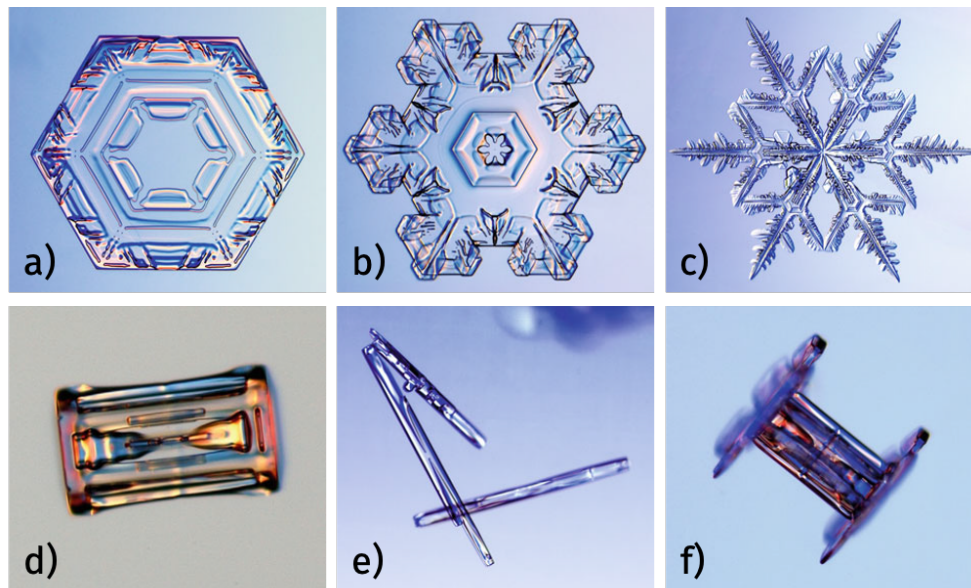


Figure 1.4: Photography of different ice crystals, from Libbrecht 2005. Panel a): Simple plate crystal, 1.4 mm from tip to tip. Panel b): More complex plate, 2.1 mm from tip to tip. Panel c): Multibranched stellar dendrite, 3.0 mm from tip to tip. Panel d): Simple hexagonal column, 0.45 mm. Panel e): Needle crystals, the largest is 1.1 mm long. Panel f): Capped column crystal, 0.6 mm long.

The variety of ice crystal shapes depends on temperature and humidity and this is shown in Figure 1.5. On one hand, temperature determines whether the crystal will be platelike or columnar. Plates and dendrites form down to around -3°C and then between -10 and -22°C . Columnar crystals like needles and hollow columns exist between -3 and -10°C . Below -22°C , plates and columns shapes coexist. On the other hand, the humidity affects the complexity of crystal structure. For example, needles are more likely to be found with a higher supersaturation relative to ice than solid prisms and the same applies to complex stellar dendrites compared to solid and thin plates. For mixed-phase clouds, Lawson et al. 2001 and Fleishauer et al. 2002 have shown that ice crystals come in a wide variety of shapes (e.g. regular sphere, columns, plates, aggregates).

However, during their formation and evolution in nature, ice crystals are affected by variations in temperature and humidity, resulting in irregular crystal shapes and, consequently, optical properties that differ from those of individual ice crystals. There are three main processes involved in the development of ice crystals:

1. Growth of ice crystal by deposition of water vapor onto the crystal surface. Atmospheric conditions (temperature and ice supersaturation) determine the growth rate and consequently the ice crystal shape.
2. Riming process involves the agglomeration of supercooled water droplets onto the ice crystals surface. These droplets nucleate and freeze during this process, increasing the mass and size of the crystal.
3. Aggregation is the process of ice crystals sticking together. At negative values close to 0°C, ice crystals have a high adhesive capability and increase the probability of cohesion between two colliding ice crystals.

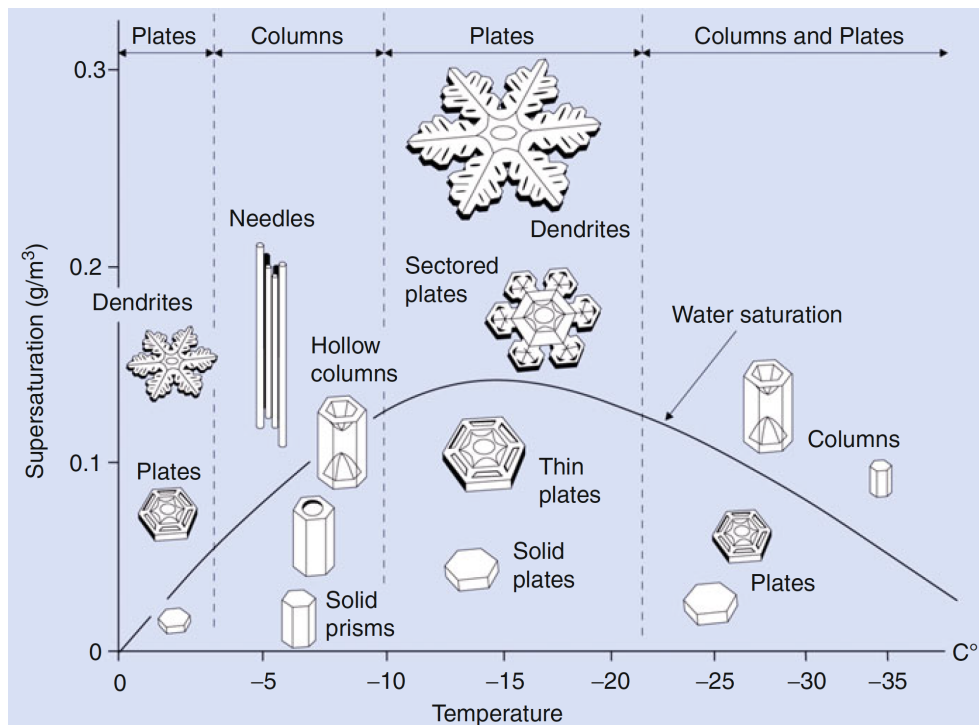


Figure 1.5: Diagram of various crystal shapes depending on water vapor supersaturation relative to ice and temperature, from Libbrecht 2005. The black line shows the supercooled water supersaturation limit, as it might be found in a dense cloud. The temperature axis is decreasing.

The hydrometeor size and shape influence other microphysical and optical properties, described in the next subsection.

1.1.4 . Clouds optical and microphysical variables

Studying cloud properties requires to consider volumes describing cloud parcels. In cloud microphysics, the use of a Particle Size Distribution (PSD) - or Droplet Size Distribution (DSD) for liquid droplets - is very popular and represents the particles number concentration N [m^{-3}] as a function of the particle maximum dimension D [m], noted $N(D)$. This allows to convert information concerning a given particle diameter into information concerning a volume and to average optical and microphysical hydrometeors properties in a volume. Consequently, ice and liquid water contents IWC and LWC [g.m^{-3}], which depend on the particle number and size, can be expressed as a function of $N(D)$ and are defined following Equations 1.1 and 1.2 respectively:

$$\text{IWC} = \int_0^{\infty} N(D)M(D) dD \quad (1.1)$$

$$\text{LWC} = \int_0^{\infty} N(D)M(D) dD \quad (1.2)$$

where $M(D)$ is the particle mass as a function of D .

In addition, the extinction coefficient α [m^{-1}] can be expressed as a function of the PSD as follows:

$$\alpha = \int_0^{\infty} \sigma_{\text{ext}}(D)N(D) dD \quad (1.3)$$

where σ_{ext} [m^2] is the extinction cross section, which describes the probability for a photon to be absorbed or scattered (explained in Section 1.2.2). At visible wavelength, the absorption by hydrometeors can be neglected. In this case, the cross section σ_{ext} is the product of the scattering efficiency $Q_{\text{sca}} = 2$ (geometric limit assumption, see Section 1.2.2.3) and the particle area as a function of its diameter $A(D)$ [m^2]. The visible extinction is consequently given by:

$$\alpha = 2 \int_0^{\infty} N(D)A(D) dD \quad (1.4)$$

The visible extinction coefficient will be referred as the extinction in this thesis.

Following this, the extinction depends on the concentration of particles in cloud and is stronger for small, highly concentrated particles than for larger, less concentrated particles. By integrating the extinction over a distance between two points l_1 and l_2 , it is then possible to define the optical depth δ . This dimensionless variable can quantify the reduction of light passing through an atmospheric layer and is given by:

$$\delta = \int_{l_1}^{l_2} \alpha(l) dl \quad (1.5)$$

Additionally, the optical depth is correlated to the transmittance of the material τ by Equation 1.6:

$$\tau = e^{-\delta} \quad (1.6)$$

Finally, the effective radius r_e [m] is also related to the PSD and is defined as the weighted average value of the cloud particle radius. It can be expressed as the ratio between the third to the second moment of the PSD and is mathematically given by Equation 1.7

$$r_e = \frac{1}{2} \frac{\int_0^\infty N(D) D^3 dD}{\int_0^\infty N(D) D^2 dD} \quad (1.7)$$

Taking into account non-spherical shapes of ice crystals, the ice effective radius $r_{e,ice}$ can be written as a function of IWC and the ice extinction α_{ice} (Equation for ice particles), given by (Foot 1988):

$$r_{e,ice} = \frac{3}{2} \frac{IWC}{\rho_i \alpha_{ice}} \quad (1.8)$$

where ρ_i is the density of ice, equals to 917 kg.m^{-3} at 0°C .

The same can be applied to water droplets to determine a relationship between liquid effective radius $r_{e,liq}$, LWC and the liquid extinction α_{liq} (Equation for water droplets) as follows:

$$r_{e,liq} = \frac{3}{2} \frac{LWC}{\rho_w \alpha_{liq}} \quad (1.9)$$

where ρ_w is the density of water, equal to 1000 kg.m^{-3} at 4°C .

Typically, the PSD is best described by a gamma function, given by Equation 1.10:

$$N(D) = N_0 D^\mu e^{-\Lambda D} \quad (1.10)$$

where N_0 is the intercept parameter, Λ is the slope parameter, μ is the shape parameter of the gamma distribution and D is the maximum dimension of the particle, found as the minimum diameter of a circle that completely covers the two dimensional particle image.

Furthermore, the “normalized PSD” formalism has been proposed by Testud 2001, Delanoë et al. 2005 and Field et al. 2005 and consists in scaling both concentration and diameter axes so that the PSD can be independent from

the water content WC and the mean volume-weighted diameter D_m . The normalization can then be expressed as follows:

$$N(D) = N_0^* F\left(\frac{D}{D_m}\right) \quad (1.11)$$

where, N_0^* [m^{-4}] is the concentration scaling parameter, also called normalized number concentration, D_m [m] acts as the diameter scaling parameter and F is the normalized shape of the particle distribution that has a modified gamma shape. As a result, the concept of the “normalized PSD” makes it possible to find a robust relationship linking α/N_0^* to any extensive and intensive variable describing clouds (Delanoë et al. 2005).

Both scaling parameters can be expressed as a function of the PSD. Indeed, D_m is expressed as the ratio between the fourth moment and the third moment of the PSD, written as follow:

$$D_m = \frac{\int_0^\infty N(D) D^4 dD}{\int_0^\infty N(D) D^3 dD} \quad (1.12)$$

and the normalized number concentration N_0^* is given by Equation 1.13:

$$N_0^* = \frac{4^4 (\int_0^\infty N(D) D^3 dD)^5}{6 (\int_0^\infty N(D) D^4 dD)^4} \quad (1.13)$$

As mentioned previously in Section 1.1.3, ice crystals can take various shapes and are not spherical. Consequently, another parameter can be used to replace D in the PSD in case of ice crystals: the mass-equivalent diameter D_{eq} [m]. It represents the diameter that a particle of mass M would have if it were a spherical liquid droplet of the same mass and is defined following Equation 1.14:

$$D_{eq} = \left(\frac{6M(D)}{\pi\rho_w} \right)^{\frac{1}{3}} \quad (1.14)$$

where ρ_w is the density of water and $M(D)$ is the particle mass as a function of D , also called mass-size relationship. $M(D)$ can be used to assess the density of these crystals, which is lower than the density of ice ρ_i . Typically, to simplify parameterizations, this relationship is expressed using a power law of the maximum dimension D (Brown and Francis 1995; Mitchell 1996; Heymsfield et al. 2010; Erfani and Mitchell 2016), given by Equation 1.15.

$$M(D) = \zeta D^\xi \quad (1.15)$$

For water droplets, that are assumed to be spherical, their mass can be obtained by multiplying their volume by the density of water ρ_w .

Finally, these properties allow us to characterize the particles composing a given cloud volume. These characteristics differ according to the hydrometeor type, and influence the interaction of clouds with the environment, especially radiation.

1.2 . Clouds' impact on the Earth's climate

Through their various microphysical and optical properties, cloud particles interact with radiation, particularly that from the Sun or the Earth surface. In this section, we describe these interactions and the impact they have on the Earth climate.

1.2.1 . Introduction of electromagnetic radiation

Any object at temperature above absolute zero (-273.15°C or 0 K) emits electromagnetic radiation, composed of electromagnetic waves. They are the result of synchronized oscillations of electric field and magnetic field propagation, perpendicular to each other and to the direction of wave propagation. The oscillation frequency ν [s^{-1} or Hz] determines the wavelength λ [m] via Equation 1.16:

$$\lambda = \frac{c}{\nu} \quad (1.16)$$

where c is the wave celerity and is equal to $299\,792\,458\text{ m.s}^{-1}$ in vacuum.

All electromagnetic waves form the electromagnetic spectrum, which is shown in Figure 1.6 regarding frequency and wavelength. It is divided in seven separated classes: the gamma rays, the X rays, the ultraviolet (UV), the visible light, the infrared (IR), the microwaves and the radio waves.

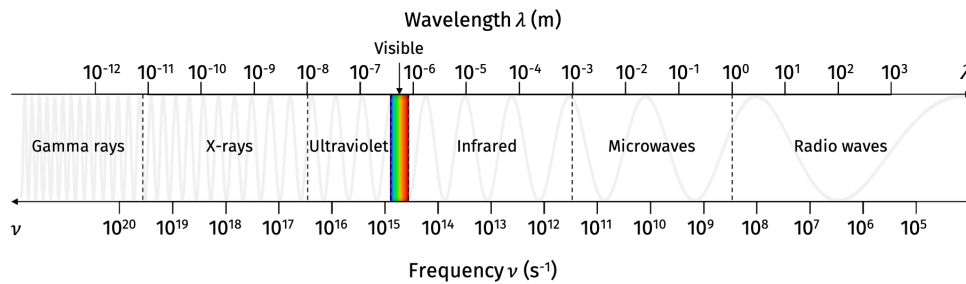


Figure 1.6: Schema of the electromagnetic spectrum.

The Wien's law states that the wavelength λ_{max} at which a black body at absolute temperature T [K] emits the most intense radiation is inversely pro-

portional to the temperature, given by Equation 1.17:

$$\lambda_{\max} = \frac{b}{T} \quad (1.17)$$

where b is the Wien's displacement constant, approximate to $2898 \mu\text{m.K}$.

The Sun's light emission is similar to the light emitted by a black body. The Sun surface temperature is approximately 5800 K, so it emits mainly in visible and ultraviolet wavelengths, also called shortwave (SW) radiations. The solar radiation spectrum - at the top of the atmosphere and at sea level - is shown in Figure 1.7, where UV, visible light and IR wavelengths region are specified. On Earth, solar radiation is absorbed and reflected by the surface and atmosphere. The Figure 1.8 presents the Earth's thermal radiance spectrum, marked by absorption bands of H_2O , CO_2 , O_3 and CH_4 present in the atmosphere. The Earth's surface (290 K) emits radiations in the infrared wavelength, called longwave (LW) radiations.

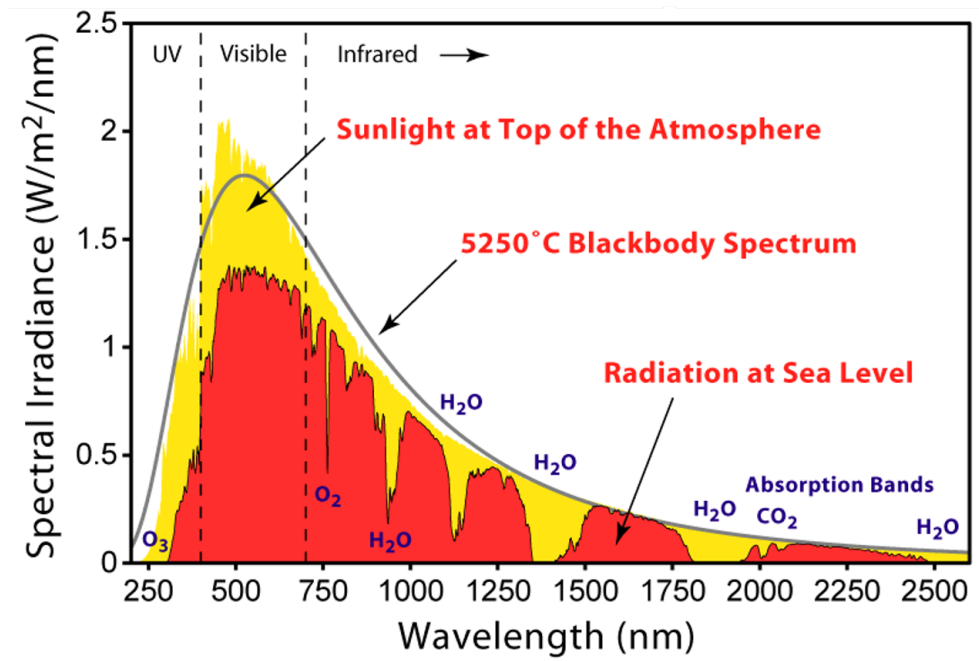


Figure 1.7: Graph of the solar radiation spectrum (from Robert A. Rohde in Wikimedia, based on NREL data). The yellow area represents the radiation at the top of the Earth's atmosphere and the red area at sea level. The black curve is the theoretical blackbody spectral irradiance at 5250°C. The H_2O , O_2 , and CO_2 absorption bands are specified in indigo and the UV, visible light and IR wavelength regions are indicated with dashed lines.

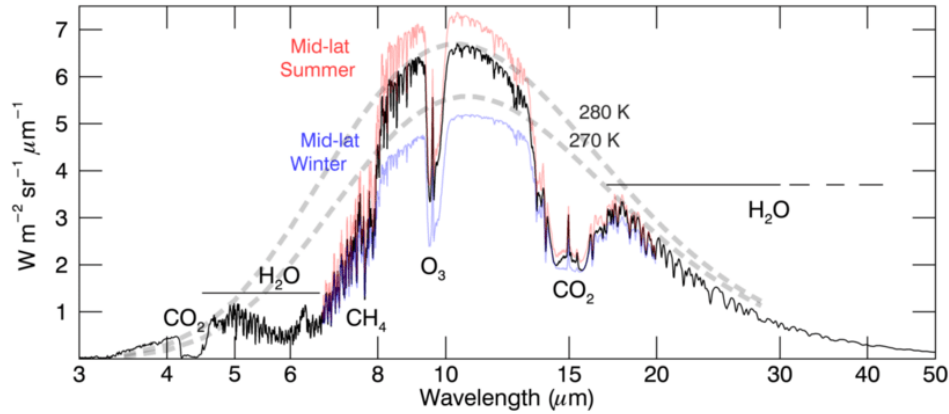


Figure 1.8: Model from the Virtual Planetary Laboratory (VPL) of the Earth's thermal radiance (from Glenar et al. 2019). The blue line represents the radiance at mid-latitude during winter and the red during summer. The black line shows the mean value of blue and red lines. The grey dashed lines display the blackbody radiances at 270 and 280 K.

Electromagnetic radiation can interact with atmospheric particles by three main different processes - emission, absorption and scattering - depending on the radiation wavelength and the particles physical properties (e.g. composition, size, emissivity). These interactions take place constantly in the atmosphere and have an impact on the Earth's radiation budget.

1.2.2 . Emission, extinction and scattering

The three main radiation-matter interaction processes are presented and detailed in this subsection. The focus will be on scattering, which is particularly important for studying clouds.

1.2.2.1 Emission

Every body emits thermal radiation depending on its temperature. At the atomic level, photon emission occurs when an atom goes from an energy level E_i to a lower level energy E_f (panel a) of Figure 1.9. The energy of the emitted photon is equal to the difference between the two energy levels ΔE , given by Equation 1.18:

$$\Delta E = h\nu \quad (1.18)$$

where ν is the frequency of the emitted photon and h the Planck constant, equal to $6.62607015 \times 10^{-34} \text{ J}\cdot\text{Hz}^{-1}$.

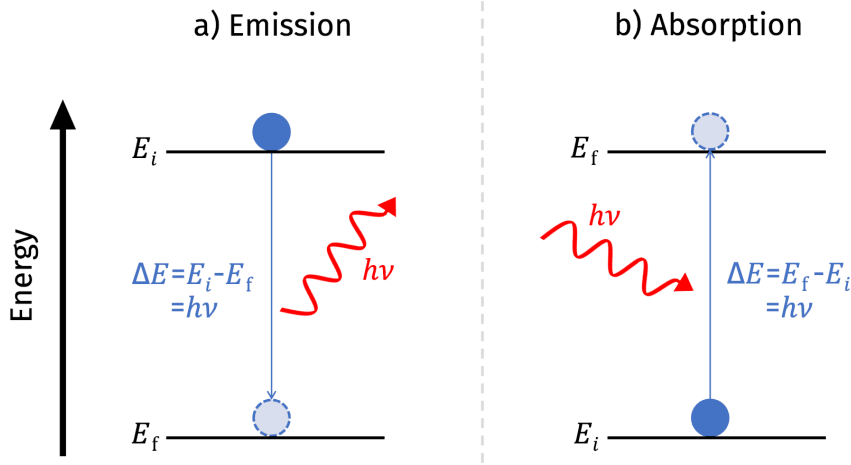


Figure 1.9: Simplified energy diagram for absorption and emission phenomena.

The emissivity ϵ_λ of a surface element corresponds to the radiative flux of thermal radiation it emits at a given temperature, relative to the flux emitted by a black body at the same temperature, which is the reference value. As the emissivity of a black body is the maximum possible value, the emissivity of a body is a value between 0 and 1, depending on the wavelength. The emitted spectral radiance of a black body B_λ [$\text{W.m}^{-3}.\text{sr}^{-1}$] at temperature T , at wavelength λ and in thermal equilibrium is given by the Planck's law:

$$B_\lambda(T) = \frac{2hc^2}{\lambda^5} \frac{1}{e^{\frac{hc}{\lambda k_b T}} - 1} \quad (1.19)$$

where k_b is the Boltzmann constant $k_B = 1.380649 \times 10^{-23} \text{ J.K}^{-1}$.

The Figure 1.10 shows the spectral radiance of black bodies at 273 K (Earth surface temperature), 1000 K, 2000 K and 5800 K (Sun surface temperature), as well as the wavelength at which the black body emits the maximum amount of radiation λ_{\max} , given by the Wien's law (Equation 1.17) and represented by dashed black lines. The emitted spectral radiance of a body $L_\lambda(T)$ [$\text{W.m}^{-3}.\text{sr}^{-1}$] can be deduced from the Planck's law and the body's emissivity ϵ_λ as following:

$$L_\lambda(T) = \epsilon_\lambda \times B_\lambda(T) \quad (1.20)$$

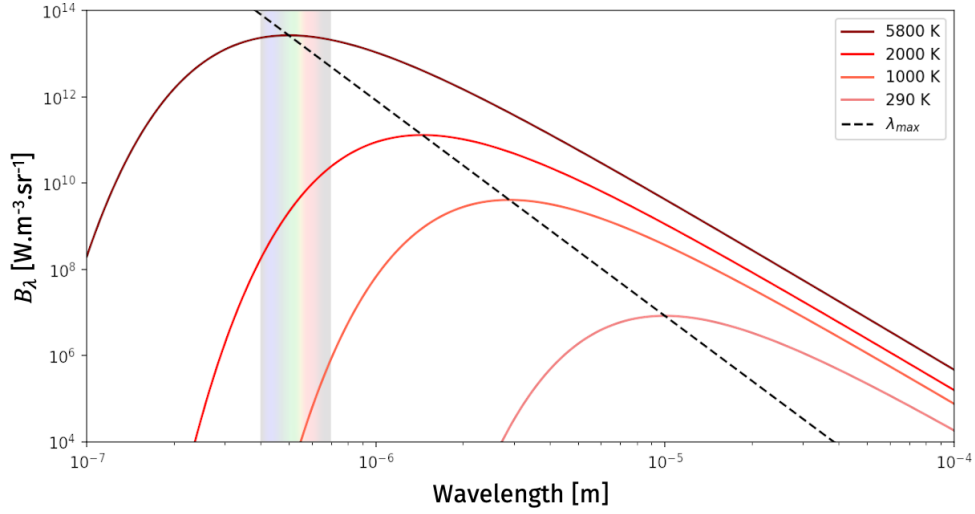


Figure 1.10: Spectral radiance distribution according to the Planck's law (Equation 1.19) and the corresponding λ_{\max} according to the Wien's law is indicated by dashed black line (Equation 1.17).

1.2.2.2 Extinction

At the atomic level, photon absorption occurs when an atom goes from an energy level E_i to a higher level energy E_f (panel a) of Figure 1.9. The energy of the absorbed photon corresponds to the difference between the two energy levels ΔE , given by Equation 1.18, where ν is the frequency of the absorbed photon. Clouds absorb the Earth's LW radiation but the extinction of visible radiation is mainly due to scattering (explained in the next subsection). Visible solar radiation is absorbed by atmospheric gases (Figure 1.7) as well as Earth's LW radiation (Figure 1.8).

The Bouguer–Lambert's law states that the intensity I of an electromagnetic wave propagating along dx length is attenuated by a factor dI , given by:

$$dI = -I_{\lambda} \times \alpha_{\lambda}^{\text{ext}} dx \quad (1.21)$$

where $\alpha_{\lambda}^{\text{ext}}$ [m^{-1}] is the extinction coefficient, that depends on the wavelength λ . As explained in Section 1.1.4 (Equation 1.3), the extinction coefficient depends on the extinction cross section $\sigma_{\lambda}^{\text{ext}}$ [m^2], which describes the probability for a photon at the wavelength λ to be absorbed or scattered:

$$\sigma_{\text{ext}} = \sigma_{\text{abs}} + \sigma_{\text{sca}} \quad (1.22)$$

Consequently, the extinction coefficient can be expressed as the sum of the absorption $\alpha_{\lambda}^{\text{abs}}$ and scattering $\alpha_{\lambda}^{\text{sca}}$ coefficients:

$$\alpha_{\lambda}^{\text{ext}} = \alpha_{\lambda}^{\text{abs}} + \alpha_{\lambda}^{\text{sca}} \quad (1.23)$$

1.2.2.3 Scattering

Electromagnetic wave can be deviated from its initial direction of propagation after interacting with matter. This phenomenon is called scattering and is considered elastic when the wave frequency remains unchanged and inelastic when the frequency changes. The inelastic scattering occurs when the energy of the incident wave is used by the atom to change its vibrational or rotational state. Sometimes scattering modifies the polarisation of the incident wave. Scattering can be uniform in all directions (isotropic) or not (anisotropic). The process is called backscattering when the direction of the scattered wave is the opposite to that of the incident wave.

The particle size is an important factor for the scattering process. Following the Mie theory (Mie 1908), the scattering efficiency Q_{sca} can be defined by the ratio of the scattering cross section σ_{sca} [m²] to the surface area of a sphere of diameter D [m], given by:

$$Q_{\text{sca}} = \frac{4\sigma_{\text{sca}}}{\pi D^2} \quad (1.24)$$

Consequently, the scattering efficiency can be linked, as for the cross sections σ_{λ} , to the absorption Q_{abs} and the extinction Q_{ext} efficiency as following:

$$Q_{\text{ext}} = Q_{\text{abs}} + Q_{\text{sca}} \quad (1.25)$$

Depending on the particle diameter D (or the radius $r = \frac{D}{2}$) and the incident wavelength λ , the efficiency and cross section scattering follow different regime. The Mie theory define, for a spherical particle, the size parameter x as the ratio of the particle perimeter $2\pi r$ to the radiation wavelength λ (Equation 1.26).

$$x = \frac{2\pi r}{\lambda} \quad (1.26)$$

The Figure 1.11 presents the different types of scattering depending on x . When $x \leq 0.002$, the scattering phenomenon become negligible. For $0.002 < x < 0.2$, D is significantly smaller than λ and the scattering follow the Rayleigh regime (Rayleigh 1899). In this case, the scattering cross section

corresponding to the Rayleigh regime $\sigma_{sca}^{Rayleigh}$ is defined by (Sauvage et al. 1999):

$$\sigma_{sca}^{Rayleigh} = \frac{\pi^5 D^6}{\lambda^4} \left| \frac{n^2 - 1}{n^2 + 2} \right|^2 \quad (1.27)$$

where n is the refractive index of the medium, whose values range from 1.0 to 1.6 for cloud particles, depending on the wavelength (Kokhanovsky 2004).

As a result, the scattering efficiency corresponding to the Rayleigh regime is defined by:

$$Q_{sca}^{Rayleigh} = \frac{4\pi^4 D^4}{\lambda^4} \left| \frac{n^2 - 1}{n^2 + 2} \right|^2 \quad (1.28)$$

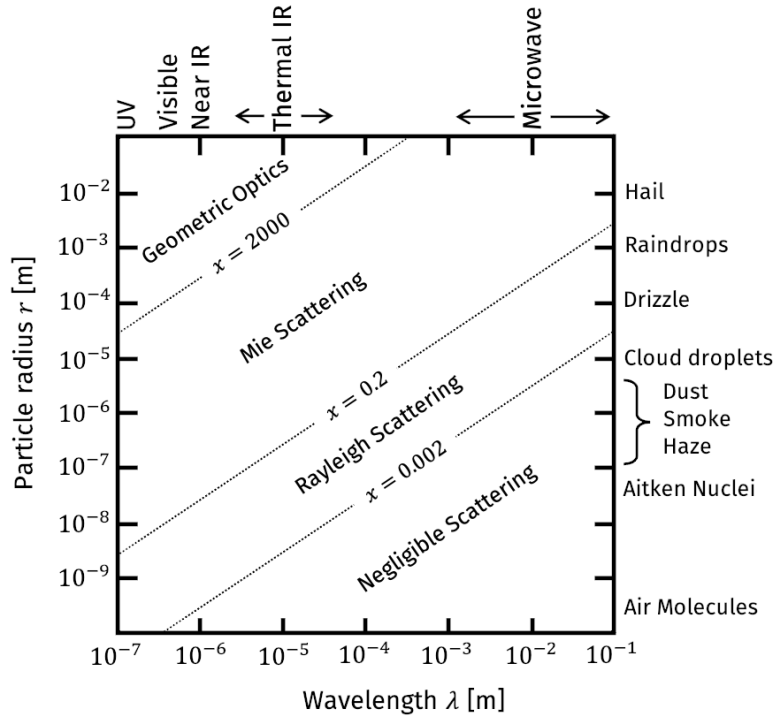


Figure 1.11: Graph of the different scattering regimes depending on the particle size (radius r), the radiation wavelength λ and the size parameter x . The particle types are shown on the right of the graph (related to the particle radius) and the wavelength band name are indicated on the top.

Consequently, the scattering effect is stronger for larger particles and shorter wavelengths. In the atmosphere, it mainly concerns air molecules interacting with solar and thermal radiations.

However, the Rayleigh regime is no longer valid when particle size and radiation wavelength have the same order of magnitude ($D \approx \lambda$). Between 0.2 and 2000 for x , the Mie scattering regime can be applied (Mie 1908). The associated cross-section σ_{sca}^{Mie} is given by (Sauvage et al. 1999):

$$\sigma_{sca}^{Mie} = \frac{\lambda^2}{4\pi} \left| \sum_{k=1}^{\infty} (-1)^k (2k+1) (|a_k| - |b_k|) \right|^2 \quad (1.29)$$

where a_k and b_k are the “Mie coefficients”, that describe respectively electric and magnetic fields multipole expansion.

This implies the scattering efficiency corresponding to the Mie regime expressed by:

$$Q_{sca}^{Mie} = \frac{\lambda^2}{\pi^2 D^2} \left| \sum_{k=1}^{\infty} (-1)^k (2k+1) (|a_k| - |b_k|) \right|^2 \quad (1.30)$$

The scattering efficiency is shown in Figure 1.12 as a function of the particle diameter and the wavelength. The relation is more complex for the Mie regime than for Rayleigh regime. Hydrometeors such as cloud droplets and drizzle are affected by Mie scattering for visible and IR wavelength. Above 2000 for x , the particle diameter is much larger than the wavelength and the scattering follow geometric optics.

The distribution of the scattered wave differs according to the scattering regime. The Figure 1.13 presents the direction and the intensity of the scattering for the Rayleigh and the Mie regimes. The scattering is symmetric in the Rayleigh case, with maxima for the forward and the backward direction. It is different for the Mie scattering, with a higher intensity in the forward direction than in the backward direction. This phenomenon becomes more intense when the particle is larger.

For the study of clouds, these two regimes only apply to water droplets and are not valid for ice crystals. Indeed, ice crystals have a wide diversity of shapes (Section 1.1.3) and cannot be described by the size parameter x . Consequently, scattering models must be adapted to the physical properties of crystals. Based on electromagnetic theory, Kahnert 2003 lists the main numerical methods for non-spherical particles. One of these methods is the Transition Matrix Method, also known as the T-matrix. This method is widely used for its high performance. It allows multiple particles to be processed with high efficiency and precision. This matrix aims to link the incident and the scattered field coefficients for a given particle, by solving the Maxwell's

equation. This operator depends on the particle optical properties but not on the incident field.

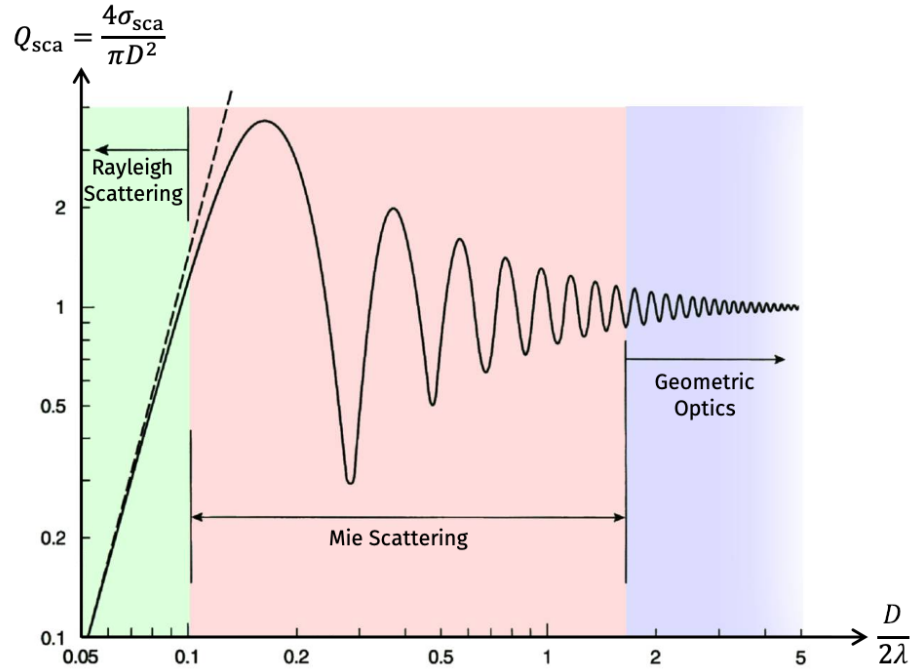


Figure 1.12: Graph of the scattering efficiency Q_{sca} as a function of $\frac{D}{2\lambda}$ according to Mie calculations (Mie 1908).

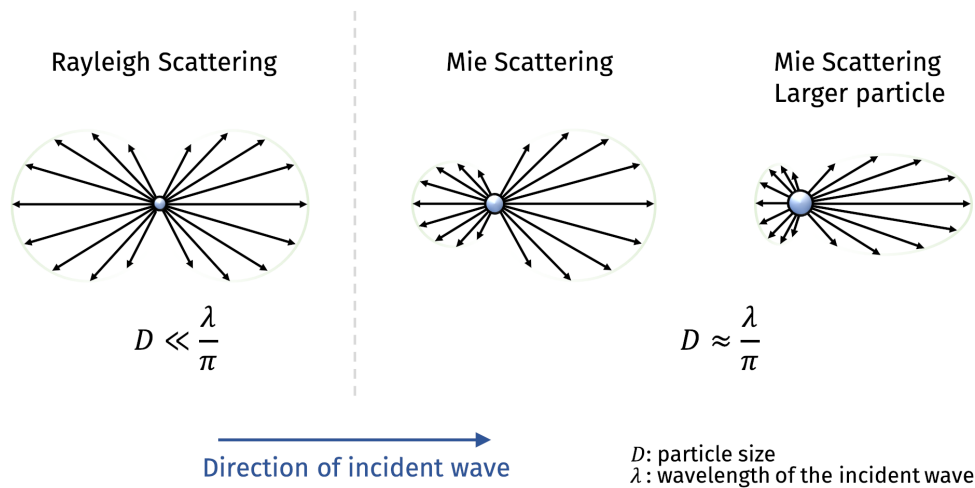


Figure 1.13: Illustration of the scattering direction and intensity for Rayleigh (left) and Mie regime, for small (center) and large (right) particle. The direction of the incident wave is indicated by the blue arrow.

However, as shown in Figure 1.11, ice crystals that are large enough follow the geometric optics for incident visible wavelengths. Due to the crystals inhomogeneity, the scattering cross section σ_{sca} in this case depends on the apparent particle area. This area can be determined by power-law function of maximum dimension, depending on temperature and crystal type (i.e. Mitchell 1996; Field et al. 2012)

As a result, the proportion of scattered radiation will depend on the microphysical properties of the particles. These interactions will have different consequences for the Earth's radiation budget.

1.2.3 . Earth water cycle and radiative budget

The Earth water cycle is a endless process of water transfer between ocean, atmosphere and land. The Figure 1.14 presents the different processes of the water cycle on Earth. These processes involve energy transfer that impacts the Earth's radiative balance and climate. For example, the evaporation of water is an endothermic process, which means that it requires energy to occur. As a result, the surface (ocean, lake, clouds) is cooling. Once produced, this water vapor condenses into cloud droplets, which releases energy in the atmosphere. Condensation is then an exothermic process and it can be noted that this energy can be used to dissipate clouds by evaporation. Clouds can also dissipate by precipitation, which releases energy in the atmosphere. As a result, the water cycle and associated processes have an impact on the global radiative balance. When one of these processes is modified, it has a global impact on the water cycle and consequently on radiative transfer (Lau et al. 2005).

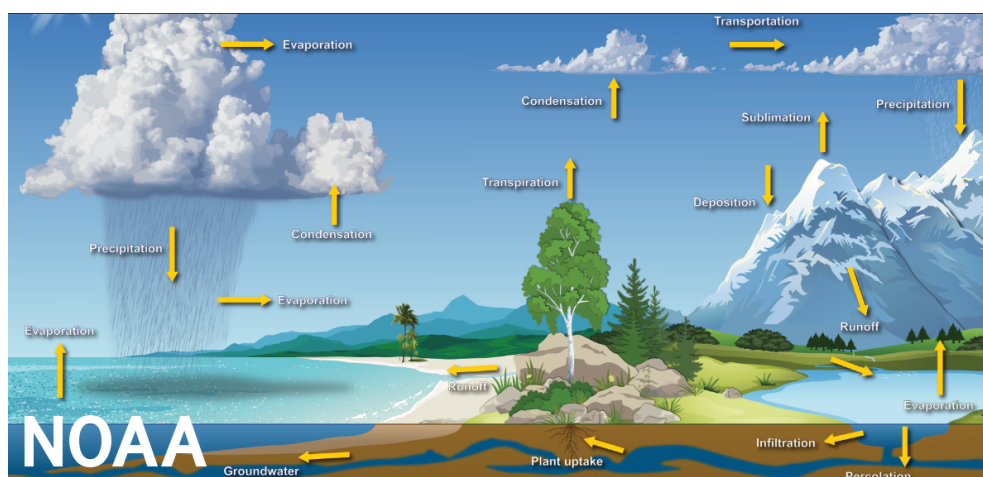


Figure 1.14: Illustration of the Earth water cycle (from NOAA website).

The Earth's energy budget is defined as the balance between the solar energy received by the Earth and the energy released by the Earth to the space. It is generally expressed at the top of the atmosphere (TOA) and over one year. The Figure 1.15 illustrates the different energy transfers included in the Earth's energy budget. The total irradiance of the Sun is $1360.8 \pm 0.5 \text{ W.m}^{-2}$ (Kopp and Lean 2011) and the average received energy of the Sun at TOA is $340.1 \pm 0.1 \text{ W.m}^{-2}$. This value represents 100 units in the Figure 1.15. Of these 100 units of SW radiation, 23 are directly reflected by clouds, going back to space. Clouds absorb 4 units and the atmosphere 19. The rest of solar energy is absorbed (47 units) or reflected (7 units) by the Earth's surface (land and ocean). The atmosphere re-emits the absorbed energy towards space and Earth's surface. The total absorbed energy by the surface is re-emitted (116 units) as LW radiation in the atmosphere and also to the space through the infrared atmospheric windows (between 8 and $13 \mu\text{m}$). Clouds and atmosphere also emit, respectively 9 and 49 units, towards space. The cloud presence and their quantity determine the amount of solar radiation (LW) reaching the Earth's surface and, consequently, the energy re-emitted by the Earth's surface (SW). As a result, clouds have a significant influence on the TOA's energy balance.

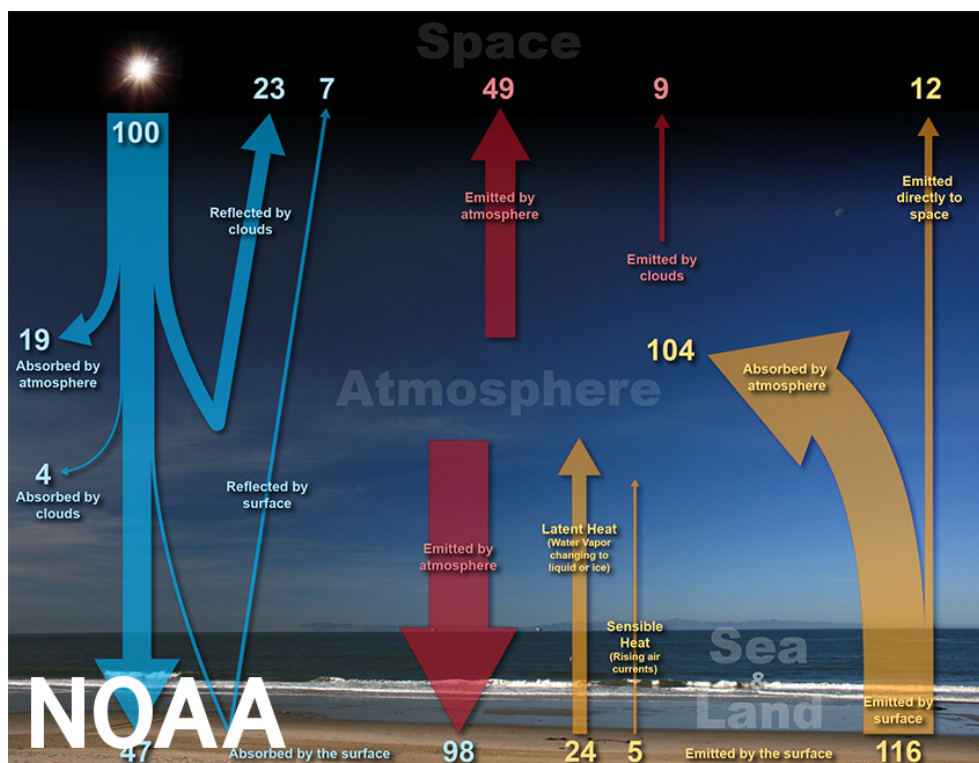


Figure 1.15: Illustration of the Earth's energy budget. The reference unit is based on 100 units of incoming solar energy. (from NOAA website)

To conclude, at TOA, the incoming solar energy is balanced by the outgoing energy from the atmosphere, the clouds and the Earth's surface. There is also an energy balance in the atmosphere and at the Earth's surface, between absorbed and released energy. Nonetheless, the Sun's radiation is not equally distributed at every latitude and is higher near the equator than in the polar regions. The outgoing energy also differs according to latitude, related in particular to the solar energy, but also to the uneven composition of the atmosphere and clouds. Consequently, there is a surplus of energy near the tropics and a deficit at the poles.

1.2.4 . Cloud radiative effect and feedback

The cloud effect on the Earth's energy budget is estimated by the Cloud Radiative Effect CRE (or forcing CRF). It is the difference in radiation between "all-sky" (with clouds) and "clear-sky" (hypothetical) conditions (Ramanathan et al. 1989):

$$CRE_{Net} = \Phi_{cloudy} - \Phi_{clear} \quad (1.31)$$

On the one hand, Φ_{cloudy} [$W.m^{-2}$] is the radiative energy of the cloudy atmosphere, given by (Ramanathan et al. 1989):

$$\Phi_{cloudy} = \Gamma(1 - \omega_{cloudy}) - F_{cloudy} \quad (1.32)$$

where:

- Γ [$W.m^{-2}$] is the solar irradiance.
- ω_{cloudy} is the clouds albedo, which describes the capacity of clouds to reflect solar radiation.
- F_{cloudy} [$W.m^{-2}$] is the LW radiative flux emitted to space in cloudy condition. This flux is given by the Stefan-Boltzmann law and is proportional to the temperature at given height z , T_z and the Stefan-Boltzmann constant σ_B as follow:

$$F_{cloudy} = \sigma_B \times T_z^4 \quad (1.33)$$

On the other hand, Φ_{clear} [$W.m^{-2}$] is the clear sky net radiative energy, given by (Ramanathan et al. 1989):

$$\Phi_{clear} = \Gamma(1 - \omega_{clear}) - F_{clear} \quad (1.34)$$

where ω_{clear} is the clear sky albedo and F_{clear} is the LW radiative flux emitted to space for clear sky condition.

Since clouds interact differently with SW and LW radiation, the net CRE can be expressed as the sum of the CRE for SW and LW radiation, CRE_{SW} and CRE_{LW} respectively (Ramanathan et al. 1989):

$$CRE_{Net} = CRE_{SW} + CRE_{LW} \quad (1.35)$$

where CRE_{SW} is defined by:

$$CRE_{SW} = \Gamma(\omega_{clear} - \omega_{cloudy}) \quad (1.36)$$

and CRE_{LW} is defined by:

$$CRE_{SW} = F_{clear} - F_{cloudy} \quad (1.37)$$

Depending on their properties, clouds can have different radiative effects. SW and LW radiations are not affected in the same way depending on cloud type:

- Low level clouds with strong albedo ω_{cloudy} and high optical depth δ , such as stratocumulus, reflect more incoming solar SW radiation into space than they absorb. As a result, the net CRE for low level clouds is negative and leads to a cooling effect of the surface.
- High level clouds with weaker albedo ω_{cloudy} and small optical depth δ , such as cirrus, act in a way similar to air since they are highly transparent to incoming solar SW radiation. These cloudstrap the Earth's LW radiation. In addition, the absorbed LW radiation is emitted out into space. Since these clouds are high and consequently cold, the emitted energy is lower than it would be without clouds. As a result, the surface is warmed (greenhouse warming), with a positive CRE.
- Thick and vertically extended clouds such as cumulonimbus have a strong albedo ω_{cloudy} and then reflect SW radiation. However, they also block LW outgoing radiation as their base is close to the Earth's surface. Consequently, both effects balance each other and the CRE of cumulonimbus is neutral, meaning that there is neither warming nor cooling.

The Clouds and Earth's Radiant Energy Systems Energy Balanced and Filled (CERES-EBAF, Loeb et al. 2018) can provide global monthly mean LW, SW and net fluxes at TOA under clear and cloudy conditions. The Figure 1.16 (from Wild et al. 2019) shows CRE_{SW} , CRE_{LW} and CRE_{Net} values at the TOA, the Earth's atmosphere and the surface. Consequently, we can note that the presence of clouds reduces the absorption of shortwave radiation by 47 W.m^{-2} , signifying

that the climate system is cooling down. The contribution of clouds regarding LW radiation is described by a positive CRE_{LW} , equal to 28 W.m^{-2} , meaning that the climate system is warming up. In conclusion, the net CRE is negative and equal to -19 W.m^{-2} , which indicates that clouds lead to a loss of energy in the climate system and cool it considerably.

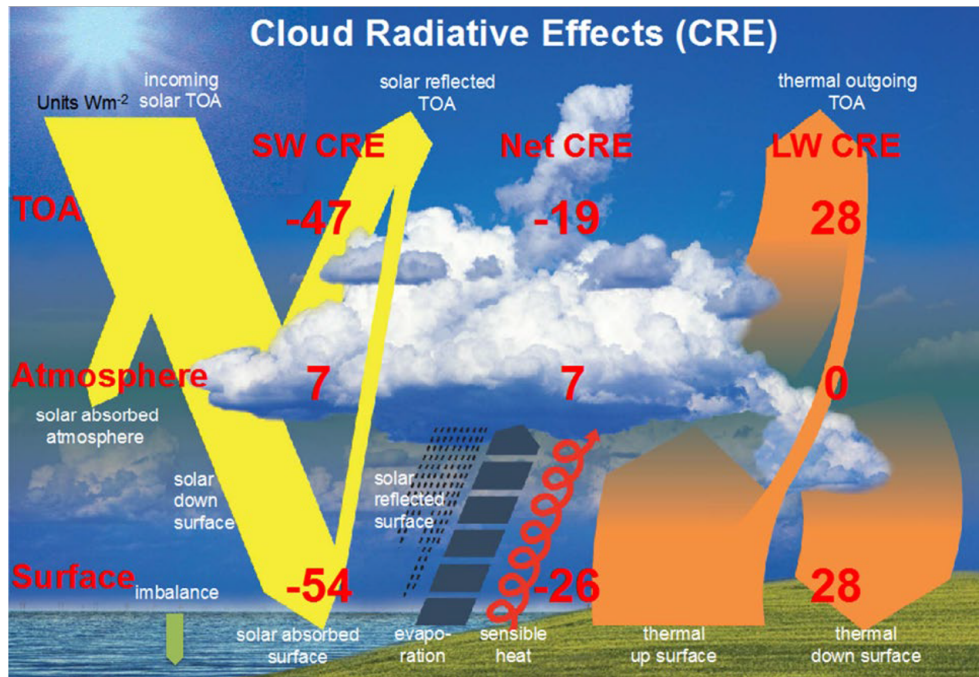


Figure 1.16: Illustration of the SW, LW and net CRE at the Earth's TOA, atmosphere and surface, from Wild et al. 2019. Unit is in W.m^{-2} .

Meanwhile, climate change related to human activities is leading to changes in atmospheric composition and surface temperature. This can affect the radiative properties of clouds and consequently the cooling effect of clouds on the Earth's radiation budget. This phenomenon is referred as cloud radiative feedback.

Quantifying this feedback is complicated because of all cloud properties (i.e. altitude, phase and albedo) and physics. For this, studies estimate cloud feedback with climate model, with a doubling of CO_2 quantity as input. In 2012, 11 models from the Cloud Feedback Model Intercomparison Project (CFMIP) has been compared by Zelinka et al. 2012b and Zelinka et al. 2012a. They show that the annual global mean of SW and LW cloud feedbacks is positive and demonstrate that various processes lead to this result, such as the increase of the cloud altitude and the increase of high latitudes cloud brightness.

Currently, scientific studies tend to show a positive cloud feedback, of $+0.6 \text{ W.m}^{-2}.\text{°C}^{-1}$ (-0.2 to $+2.0 \text{ W.m}^{-2}.\text{°C}^{-1}$, Boucher et al. 2013), which implies that clouds tend to amplify global warming.

However, misrepresentation of clouds in models can lead to biases in feedback estimation. This is notably the case for boundary layer mixed-phase clouds and the estimation of their supercooled water content (Zelinka et al. 2020). These low level clouds have significant impacts on the radiation budget and climate change (Bony and Dufresne 2005). Consequently, it is important to study them to improve their representation in models.

1.3 . Conclusion

Clouds are an important component of the Earth system, particularly within the climate system and the water cycle. Their radiative impact on the climate is significant, tending to cool it (-19 W.m^{-2}). This effect is related to the clouds interaction with radiation from the Sun and Earth, depending on the clouds microphysical and optical properties. Nevertheless, the actual context of climate change related to human activities can modify the radiative impact of clouds. Current studies tend to show that clouds amplify global warming, with a positive cloud feedback of $+0.6 \text{ W.m}^{-2}.\text{°C}^{-1}$.

Among all cloud types, mixed-phase clouds account for a significant proportion of the CRE (20 %, Matus and L'Ecuyer 2017). These clouds are composed of water vapor, supercooled water and ice crystals, all coexisting in the same volume. Our current knowledge of mixed-phase cloud properties is limited and introduces biases into weather and climate prediction models. Consequently, it is important to study these clouds, particularly their microphysical and optical properties, to improve their representation in climate models. To achieve this, we need to develop methods to observe clouds and retrieve their properties. In the next chapter, I describe various instrument types that allow us to study clouds, including mixed-phase clouds.

2 - Instrumentation for cloud observation

Contents

2.1	<i>In situ</i> measurements	48
2.1.1	Cloud Particle Imager	48
2.1.2	Forward Scattering Spectrometer Probe	52
2.1.3	Polar Nephelometer	54
2.1.4	Two-Dimensional Stereo Probe	56
2.1.5	Cloud Droplet Probe	58
2.2	Remote sensing	60
2.2.1	Passive remote sensing	61
2.2.2	Active remote sensing	66
2.2.3	Radar-lidar synergy	78
2.3	Spaceborne and airborne radar-lidar platforms . .	80
2.3.1	CloudSat and CALIPSO from A-Train	81
2.3.2	CPR and ATLID from EarthCARE	85
2.3.3	RALI: RASTA and LNG	88
2.3.4	MIRA and WALES	92
2.3.5	CRS and CPL	96
2.4	Conclusion	97

Cloud properties can be measured by instruments that directly collect cloud samples (e.g. with *in situ* probes) or by instruments that remotely measure the energy emitted or scattered by cloud particles, called remote sensing instruments. In this section, I describe these two types of cloud observations. First, I present some *in situ* probes which measure a precise volume in contact with them. The description of three of them will facilitate the understanding of the comparison made in Chapter 4. Next, I present passive and active remote sensing. A more in-depth description is given on radar and lidar active remote sensing, and a section on radar-lidar synergy and its benefits for cloud observation, especially mixed-phase clouds. The last part of the chapter is devoted to present different spaceborne and airborne radar-lidar platforms.

2.1 . *In situ* measurements

One way of observing clouds is to directly collect and analyze a sample. For this, dedicated probes are installed on aircraft or balloons to access a precise location in the cloud, or even on the ground to observe fog. These measurements are called *in situ* and rely on the interaction between light and cloud particles. As seen in the previous chapter, cloud particles interact with light and scatter it differently depending on their microphysical properties and the radiation wavelength. As a result, it is possible to access microphysical properties by measuring the properties of light scattered by a cloud sample.

There are several types of *in situ* probe dedicated to measuring the properties of crystals, water droplets or even aerosols, depending on the instrument sensitivity. In this section, I present five probes used to measure hydrometeor properties, including the first three whose data are used in this thesis. A more complete list of *in situ* probes, their principle and limitations can be found on Baumgardner et al. [2017](#).

2.1.1 . Cloud Particle Imager

The Cloud Particle Imager (CPI, Lawson et al. [2001](#)) is an *in situ* imager developed by the Stratton Park Engineering Company (SPEC) to capture high-resolution (2.3 μm) two-dimensional images of clouds particles ranging in size from 23 μm to 2300 μm . The Figure 2.1 shows the CPI fixed to the Polar 2 aircraft from the Alfred Wegener Institute for polar and marine research (AWI) during a measurement campaign in the Arctic.



Figure 2.1: The Cloud Particle Imager on the Dornier 228 Polar 2 aircraft flying over the Svalbard archipelago. (from C. Gourbeyre, <http://www.obs.univ-bpclermont.fr/atmos/fr/recherches/campagnes/astar2007.php>)

Cloud particles enter the probe to be imaged by a system composed of lasers (Light Amplification by Stimulated Emission of Radiation) and different detectors, including a Charge-Coupled Device (CCD) camera. The Figure 2.2 illustrates how the particles are detected by the CPI, the panel a) shows the various components of the instrument and panel b) is a zoom of panel a) to focus on the detection area.

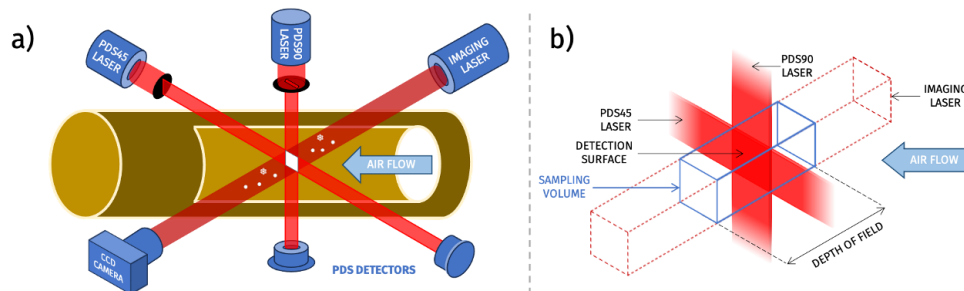


Figure 2.2: a) CPI probe detection principle (<http://www.specinc.com/cpi-operation>) and b) CPI sampling volume definition (from Mioche 2012, page 44).

Two Particle Detection System (PDS), consisting of a laser emitting at 788 nm with a power of 30 mW and a detector, are positioned at 45° (PDS45) and 90° (PDS90) to the horizontal plane. The overlap of these two lasers defines the detection surface and the sampling volume depends on this detection surface, the flight speed and the optical system's depth of field (Figure 2.2 panel b)). When both PDS simultaneously detect the presence of at least one

particle in the sampling volume, an imaging laser, with a wavelength of 850 nm and an adjustable power of up to 80 W, is activated and delivers a 25 ns pulse. The CCD camera then captures a 1024×1024 pixel image (pixel size 2.3 μm) of the particles present in the sample volume at a maximum acquisition frequency of 40 Hz. Usually, ten pixels are needed to correctly identify a cloud particle, which means that the CPI can obtain information for hydrometeors of sizes between 23 and 2300 μm . All these specifications are listed in Table 2.1.

Table 2.1: CPI specifications.

Instrument part	Properties	Values
CCD Camera	Pixel size	2.3 μm
	Colors	256 grey levels
	Resolution	1024×1024
	Particle size range	23 - 2300 μm
	Acquisition frequency	max. 40 Hz
Imaging laser	Wavelength	850 nm
	Power	up to 80 W
	Pulse duration	25 ns
PDS laser	Wavelength	788 nm
	Power	30 mW

The result is an 8 bit 256 grayscale image, enabling the shape of the particles to be identified and the observed particles to be classified. Lefèvre 2007 developed an algorithm based on Magono and Lee 1966 classification to identify ten classes of particle shapes, shown on Figure 2.3. First, the algorithm defines the contour of each particle to extract several morphological parameters such as the surface, the perimeter, the sphericity, the width, the length, the degree of symmetry and the roughness. The algorithm then uses thresholds or criteria on these parameters to determine particle shape and class. More details can be found on Lefèvre 2007. Other methods for classifying particle shape from CPI images also exist, such as those using Convolutional Neural Network (CNN; Xiao et al. 2019; Przybylo et al. 2022).

As a result, these images can be used to determine microphysical parameters of ice crystals such as the PSD, the ice concentration N_{ice} , the ice water content IWC and the extinction coefficient of ice particles α_{ice} , with uncertainties between 50 and 60 %. In addition, radar reflectivity Z (cf. Section 2.2.2.1, Equation 2.10) can be calculated from the size and shape of the particles de-

tected and the definition of a mass-diameter law for each crystal shape class, with an uncertainty of ± 4 dBZ (Mioche 2012).

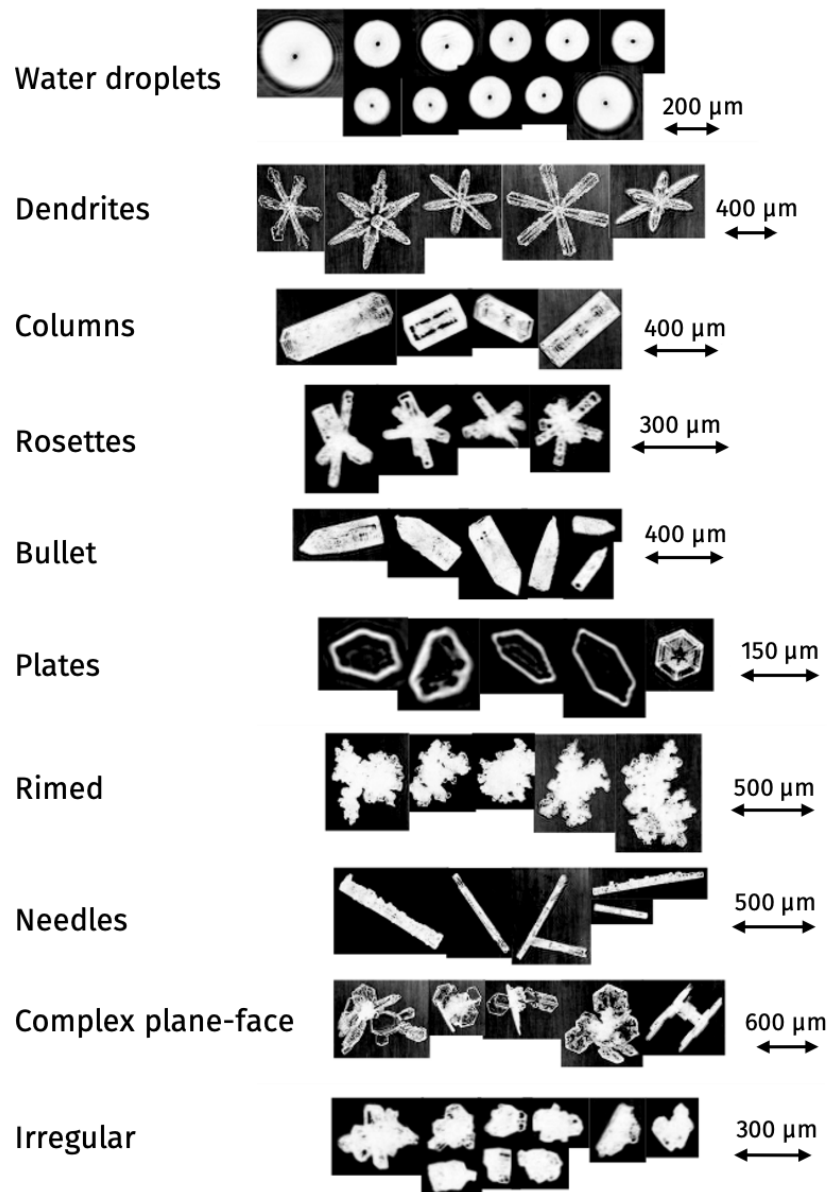


Figure 2.3: The ten classes of particle shapes recognized by the CPI image processing algorithm (Lefèvre 2007).

2.1.2 . Forward Scattering Spectrometer Probe

The Forward Scattering Spectrometer Probe (FSSP model 100, Knollenberg 1976; Baumgardner and Spowart 1990) is an Optical Particle Counter (OPC) developed by Particle Measuring Systems (PMS) to count and size water droplets with diameters ranging from 3 to 47 μm . These measurements are obtained with a resolution of 3 μm and at a frequency of 1 Hz. The Figure 2.4 presents the FSSP, which was first introduced in 1976, along with its size (1 m) and weight (16 kg). Like the CPI probe, it can be mounted under the wing of an aircraft using a pylon.



Figure 2.4: The Forward Scattering Spectrometer Probe introduced in 1976 (from Beswick et al. 2014).

The Figure 2.5 presents the FSSP operating principle, specifying the optical path of the laser beam. The laser source is a Helium Neon laser emitting at 632.8 nm, focused by an optical system to a diameter of 0.2 mm and directed perpendicular to the air flow. When particles encounter the laser beam, they scatter light in all directions, and some of the forward-scattered light is directed by a right-angle prism through a condensing lens and onto a beam splitter. A “dump spot” on the prism prevents the beam from entering the collection optics, giving a collection angle (also defined by the condensing lens aperture) between 4° and 12°. The amount of scattered energy is then collected by a photodetector.

Since the amount of scattered energy depends on the particle size, it is possible to use the collected energy by the photodetector to determine the particle diameter. Assuming that the particles are spherical and have a refractive index of 1.33, the Lorenz-Mie theory is used to obtain a calibration curve to determine the particle diameter. In practice, the calibration curve is discretized into fifteen classes. Then, the measured energy is compared with the threshold values associated with the classes and the number of particles present in each of these classes is accumulated over a pre-selected period of time. With this information, it is possible to deduce the concentration N_{liq} and the DSD

of the sampled particles, depending on the sampling volume ($50 \text{ cm}^{-3} \cdot \text{s}^{-1}$ at $200 \text{ m} \cdot \text{s}^{-1}$). All the specifications of the FSSP are summarized in Table 2.1

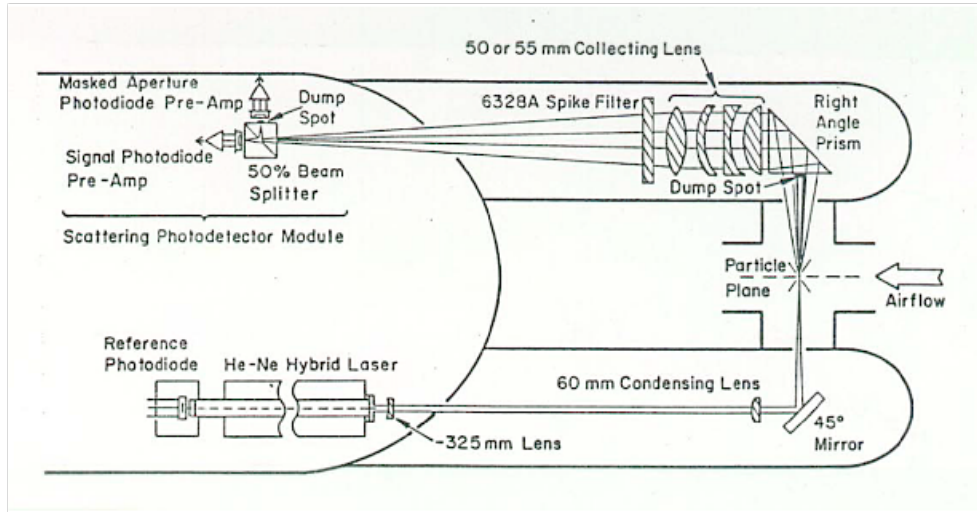


Figure 2.5: The FSSP detection principle (from Dye and Baumgardner 1984).

In addition, the extinction coefficient of liquid droplets α_{liq} and the LWC can be calculated from the DSD. The measurement errors for concentration and diameter are around 10 to 15 %, while they are at least 20 % for parameters derived from a distribution, such as liquid water content (20 to 35 %) or extinction coefficient (35 %).

Table 2.2: FSSP specifications.

Properties	Values
Laser wavelength	632.8 nm
Focus laser beam diameter	0.2 mm
Collection angle range	4 - 12°
Particle size range	3 - 47 μm
Resolution	3 μm
Acquisition frequency	1 Hz
Sampling volume at $200 \text{ m} \cdot \text{s}^{-1}$	$50 \text{ cm}^{-3} \cdot \text{s}^{-1}$

2.1.3 . Polar Nephelometer

The Polar Nephelometer (PN, Gayet et al. 1997) is an instrument developed at the Laboratoire de Météorologie Physique (LaMP) to measure the scattering phase function of cloud particles with a size range between $3\text{ }\mu\text{m}$ and about 1 mm . This describes the angular distribution of radiation scattered by a distribution of hydrometeors. The Figure 2.6 shows the PN fixed to the ATR 42 aircraft operated by the French facility for airborne research SAFIRE (Lamorthe et al. 2016) during the RALI-THINICE campaign (more details in Section 4.2.2.1) in the Arctic.



Figure 2.6: The Polar Nephelometer on the ATR 42 scientific aircraft during the RALI-THINICE campaign.

The PN uses the light scattering by particles to obtain their optical properties. The Figure 2.7 describes the measurement principle of the PN. When particles enter the probe, they are illuminated at the focus of a paraboloidal mirror by a laser beam with a wavelength of 804 nm , generated by a laser diode with a power of the order of 1 W . The laser beam is then scattered by the particles and reflected by the parabolic mirror to a circular ring composed of 56 photodiodes (the beam path is indicated by the red lines in Figure 2.7). These photodiodes cover scattering angles from $\pm 3.49^\circ$ to $\pm 172.5^\circ$. The detector position determines the energy received for each scattering angle. This characterizes the scattering phase function of the particles in the sampling volume, which depends on the microphysical characteristics of the particles - such as concentration, diameter and refractive index - and on their shape. The NP offers a large sampling volume, determined by multiplying the sampling area (i.e. 10 mm long by 5 mm in diameter) by the aircraft speed, at an acquisition frequency defined by the operator (i.e. 10 L for an aircraft speed of 200 m s^{-1} and an acquisition frequency of 1 Hz). All the specifications of

the PN are summarized in Table 2.3

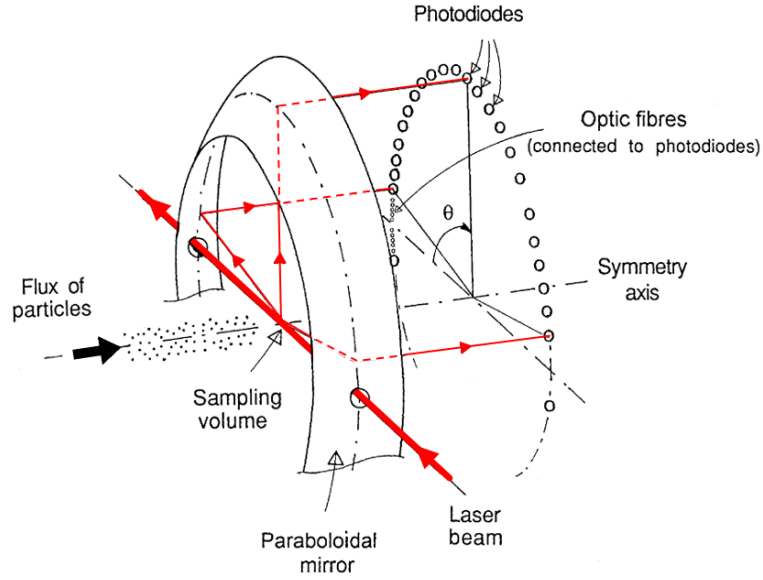


Figure 2.7: The PN measurement principle (from Gayet et al. 1997).

Table 2.3: PN specifications.

Properties	Values
Laser wavelength	804 nm
Laser power	1 W
Number of photodiodes	56
Scattering angle range	$\pm 3.49^\circ - \pm 172.5^\circ$
Particle size range	$3 \mu\text{m} - 800 \mu\text{m}$
Sampling frequency range	1-1000 Hz
Sampling volume at 200 m.s^{-1} and 1 Hz	$50 \text{ cm}^{-3}.\text{s}^{-1}$

From these measurements, it is possible to calculate the total extinction coefficient α_{tot} and the asymmetry parameter g of the sampled hydrometeor between 15° and 155° , based on the methodology proposed by Gerber et al. 2000 and Gayet et al. 2002. The asymmetry parameter is defined by:

$$g = \frac{\int_0^\pi \psi(\theta) \sin(\theta) \cos(\theta) d\theta}{\int_0^\pi \psi(\theta) \sin(\theta) d\theta} \quad (2.1)$$

where $\psi(\theta)$ is the angular scattering coefficient [$\mu\text{m}^{-1}.\text{sr}^{-1}$] measured at the scattering angle θ . The values of g range from -1 to 1 and reflect the ability of a cloud particle to scatter incident light preferentially forwards ($g > 0$) or backwards ($g < 0$), with a value of $g = 1$ indicating that all the scattered energy is concentrated in the incident direction of the light ($\theta = 0^\circ$). The value of the asymmetry factor at visible wavelengths depends on the size, the shape and therefore the type of hydrometeors. Generally, it is greater than 0.7 in clouds, and Jourdan et al. 2003b, 2010 have shown that g values measured by the PN are usually less than 0.8 in ice clouds and around $0.84 - 0.85$ in liquid-phase clouds. These measurements of extinction and asymmetry parameter make it possible to distinguish between water droplets and non-spherical ice crystals, as well as the thermodynamic phase of clouds (Jourdan et al. 2003a) and the uncertainties on these measurements are estimated at 25% and 4% respectively (Gayet et al. 2002).

2.1.4 . Two-Dimensional Stereo Probe

The Two-Dimensional Stereo Probe (2D-S, Lawson et al. 2006) is an optical imager developed by SPEC to obtain images and properties of cloud particles measuring between 10 and $1280\ \mu\text{m}$ with a resolution of $10\ \mu\text{m}$. This instrument, presented in Figure 2.8, consists of four branches, allowing two laser beams to cross each other at right angles. The detection systems are composed of 128 photodiodes each, arranged in linear arrays.



Figure 2.8: The 2D-S probe (from the Pacific Northwest National Laboratory (PNNL) et al. 2019).

Like all Optical Array Probe (OAP), the 2D-S is based on the principle that particles passing in front of a collimated laser beam create a two-dimensional shadow on linear photodiode array, enabling an image of the particles to be

reconstructed thanks to the state of the photodiodes. This principle is illustrated in Figure 2.9.

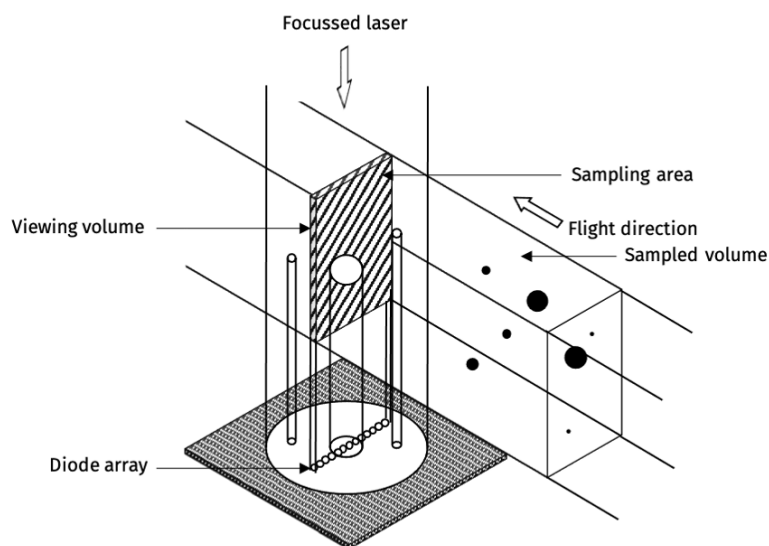


Figure 2.9: OAP principle detection (from Baumgardner et al. 2001)

The strength of the 2D-S lies in its use of two laser-photodiode detection systems, providing better detection of small particles (less than 100 μm in size) and the ability to image particles in three dimensions. In addition, this technique allows liquid water droplets to be distinguished from ice crystals. Consequently, 2D-S measurements provide information on both ice crystals and liquid water droplets, including image catalogs, the particle diameter and the particle size distribution, from which several properties listed in Table 2.4 are derived. Similarly to the CPI, the 2D-S images are in black and white, and the probed particle shape can be deduced and classified using various methods (e.g. Praz et al. 2018; Jaffeux et al. 2022). An example of images obtained with the 2D-S and the CPI is presented in Figure 2.10.

Table 2.4: Microphysical properties determined using 2D-S images.

Property	Abbreviation
Maximum diameter	D
Mean diameter	D_{mean}
Effective diameter	D_e
Droplet Size Distribution	DSD
Ice Particle Size Distribution	PSD
Liquid water content	LWC
Ice water content	IWC
Total water content	TWC
Liquid number concentration	N_{liq}
Ice number concentration	N_{ice}
Total number concentration	N_{tot}

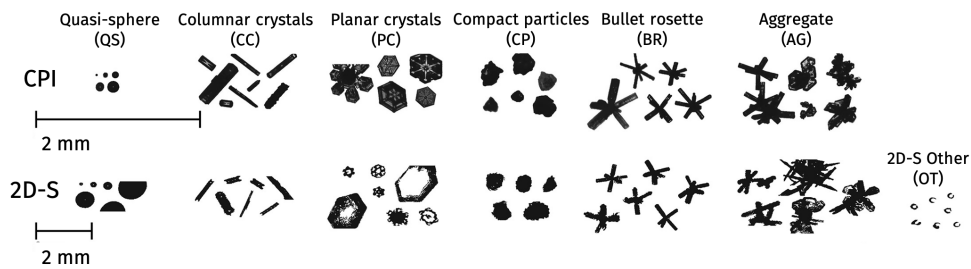


Figure 2.10: Example of particle images from the 2D-S and CPI, categorized by crystal type (from Praz et al. 2018). For each probe, a size scale is indicated.

2.1.5 . Cloud Droplet Probe

The Cloud Droplet Probe (CDP, Lance et al. 2010) is an optical scattering probe manufactured by Droplet Measurement Technologies (DMT) to measure water droplets with diameter ranging from 2 and 50 μm , with a resolution of 1 to 2 μm . Figure 2.11 presents the probe itself, while Figure 2.6 shows the probe mounted under the wing of the ATR 42 scientific aircraft of SAFIRE.

This instrument is a more recent version of the FSSP and works on a similar principle, shown in Figure 2.12. Using a 658 nm laser with a power of up to 50 mW, the instrument measures the scattering cross-section in solid angles between 4° and 12° . These measurements, performed at a frequency of 1 or 10 Hz, enable particle size to be calculated with a resolution of 1 to 2 μm .

As a result, it is possible to deduce the properties (listed in Table 2.5) of the sampled particles in the same way as for the FSSP, with better resolution. The specifications of the CDP are summed up in Table 2.5.

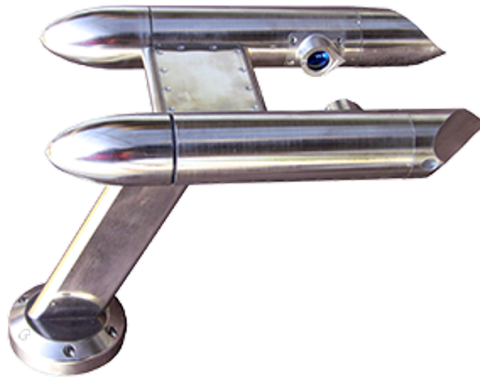


Figure 2.11: The Cloud Droplet Probe (from [DMT Website](#)).

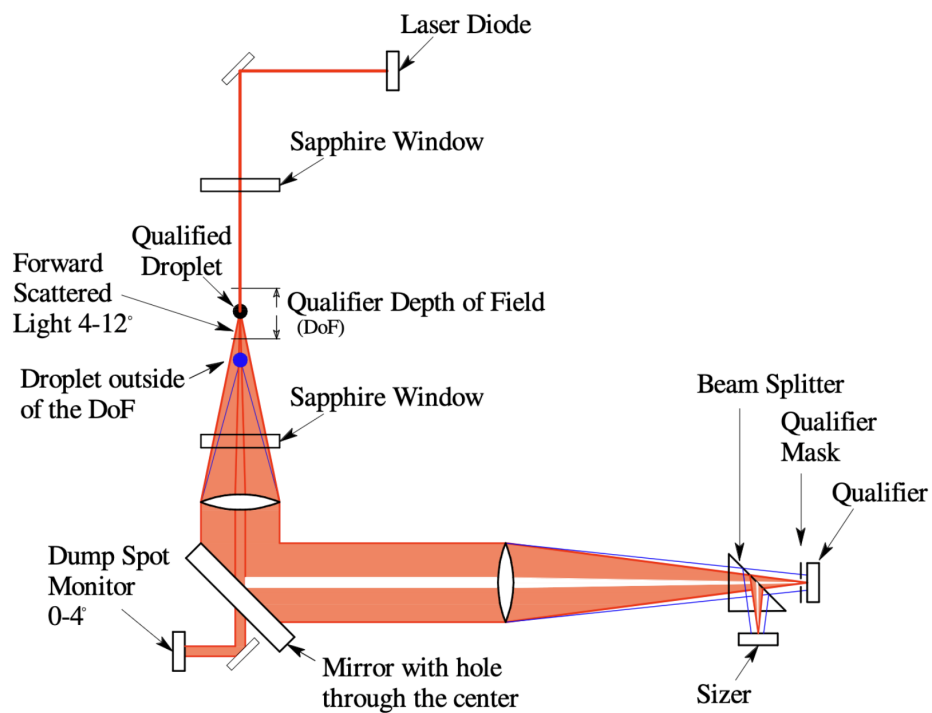


Figure 2.12: The CDP optical scheme (from Lance et al. 2010), showing in red the scattering signal for a droplet in the depth of field and in blue the scattering signal for a droplet outside the depth of field.

Table 2.5: CDP specifications.

Properties	Values
Laser wavelength	658 nm
Laser power	up to 50 mW
Scattering angle range	4° - 12°
Particle size range	2 μm - 50 μm
Resolution.	1 μm - 2 μm
Measurement frequency	1 or 10 Hz
Microphysical properties	Particle diameter D
	Droplet Size Distribution DSD
	Particle number concentration N_{liq}
	Liquid Water Content LWC
	Extinction α_{liq}
	Effective diameter D_e

2.2 . Remote sensing

The principle of remote sensing is to measure at some distance from the target the radiation emitted or scattered by cloud particles in order to obtain their location and movement, as well as their physical, optical, microphysical or even thermodynamic properties. When the instrument collects radiation initially emitted by an external source (e.g. the Sun), it is called passive remote sensing. On the other hand, when the instrument itself emits radiation in the direction of the target and collects the backscattered energy, it is referred to as an active remote sensing instrument. Thus, the two remote sensing techniques provide different information and possess their strengths and weaknesses, depending on what needs to be observed. For example, active instruments allow to vertically resolve cloud properties (range resolution) whereas passive instruments provide integrated information or from the nearest part to the instrument (e.g. cloud top information). In practice, an ice water content profile can be derived from active sensor while passive sensors are limited to ice water path. Nevertheless, the spatial cover of passive instruments is generally higher than for active instruments. Compared to *in situ*, sampled volumes are much larger, and the signal received by the instrument provides information on the average properties of the sampled volume. Furthermore, for both methods, the instrument can be ground-based or onboard a satellite, an aircraft, a stratospheric balloon or a boat. The Figure 2.13 illustrates and summarizes the difference between passive and active remote sensing. In this section, I first describe passive remote sensing in more detail, before focusing on active remote sensing.

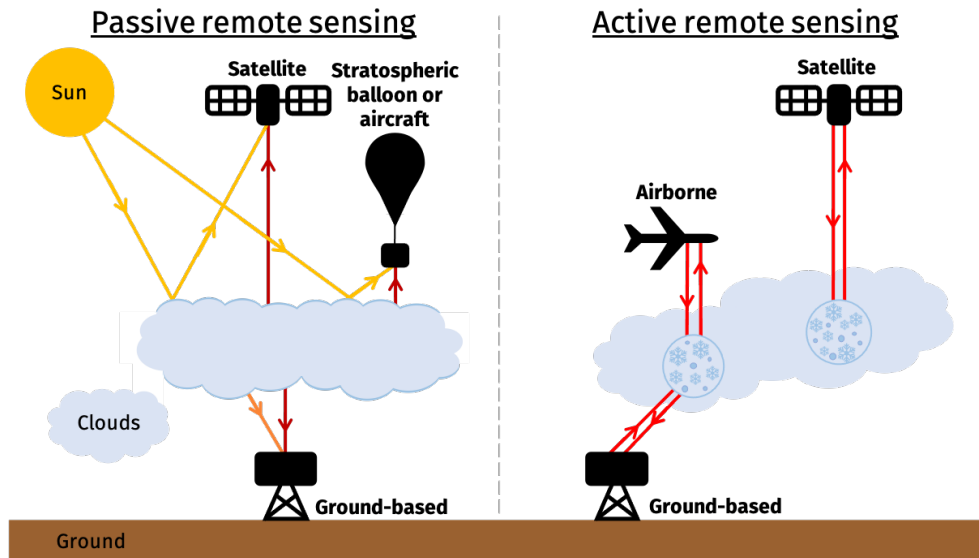


Figure 2.13: Passive and active remote sensing.

2.2.1 . Passive remote sensing

Passive remote sensing instrument collects thermal, microwave and solar radiation emitted, reflected or scattered by the Earth's surface and atmosphere. These radiations are used to determine atmospheric and cloud properties with radiative transfer models, which relate measurements to the different radiation processes. As seen in Section 1.2.2.1 with Equation 1.20, the emitted radiation of a body is given by its emissivity and the Planck's law depending on the temperature. Consequently, the wavelengths used by passive remote sensing instruments can be visible (0.4 to 0.9 μm), middle (1 to 5 μm) and thermal (8 to 15 μm) IR, and microwaves (3 mm to 30 cm). For visible wavelengths, the emissivity can be neglected, since the amount of energy studied is the energy emitted by the Sun and reflected by clouds. The inconvenience of this technique is that it can only be used during daytime. For IR, the emissivity of clouds depends on their microphysical and macrophysical properties, as well as on the wavelength. The measured radiance comes from cloud tops, and from the ground if the clouds are not sufficiently opaque at these wavelengths to block all terrestrial radiation. The radiance emitted by the Earth surface (land and ocean) often accounts for a large proportion of the radiance measured, knowing that in the thermal IR all surfaces have emissivities of over 0.7.

There are various types of passive remote sensing instrument such as the radiometers, which are instruments that measure the intensity of electromagnetic radiation flux in different wavelength ranges, and the spectrometers.

ter, which distinguishes the specific wavelengths constituting the light beam and analyzes them. Several types of radiometers exist: e.g. hyperspectral radiometer (detects hundreds of very narrow spectral bands throughout the visible, near-infrared, and mid-infrared), imaging radiometer (scans an object or a surface to produce a two-dimensional image) and spectroradiometer (measures the intensity of radiation in multiple wavelength bands).

In order to cover large areas and observe clouds frequently, these instruments are on board satellites such as the Advanced Very High Resolution Radiometer (AVHRR, Eidenshink and Faundeen 1994; Zhu and Yang 1996), the Moderate Resolution Imaging Spectroradiometer (MODIS, Platnick et al. 2003) and the Spinning Enhanced Visible Infrared Imager (SEVIRI, Schmetz et al. 2002). They have multiple wavelength channels and a resolution between 250 m (for MODIS) and 3 km (maximum for SEVIRI). Using the measurements made by these instruments, it is possible to retrieve cloud properties such as thermodynamic phase, optical thickness, effective droplet radius or even water content (e.g., Nakajima and King 1990; King et al. 2004; Roebeling et al. 2006; Bugliaro et al. 2011; Strandgren et al. 2017). Some remote sensing instruments can be on the ground or airborne, like the Spectral Modular Airborne Radiation measurement system (SMART, Wendisch et al. 2001; Ehrlich et al. 2008) and the Solar Spectral Flux Radiometer (SSFR, Pilewskie et al. 2003). The cloud properties, like the optical thickness or the particle size, are retrieved using the solar transmissivity or the reflectivity from those instruments (Kikuchi et al. 2006; McBride et al. 2011). Besides, the slope of the radiance spectrum can be used to determine the cloud phase: the slope is negative for liquid clouds and positive for ice clouds (Ehrlich et al. 2009; Jäkel et al. 2013).

More recently, the airborne and ground-based hyperspectral imager spectrometer MACS (spectrometer of the Munich Aerosol Cloud Scanner, Ewald et al. 2016) has been developed at the Meteorological Institute in Munich to measure solar radiation in the 400-2500 nm wavelength range. The instrument is presented in Figure 2.14 and is composed of two hyperspectral cameras, one is sensitive to the visible and near-IR (VNIR, 400 nm - 1000 nm) and the other to the shortwave IR (SWIR, 1000 nm - 2500 nm).



Figure 2.14: The specMACS VNIR and SWIR cameras, ground-based on the roof of the Meteorological Institute in Munich and protected from stray light by black protection visible in the front on the sensors (from Ewald et al. 2016).

An example of dataset from specMACS is presented in Figure 2.15, from Ewald et al. 2016. The instrument was ground-based and looked at the clouds from their side. The figure shows that the clouds appearance changes with wavelength, and some properties can be deduced from this. For example, clouds appear much smoother at 870 nm than at 2100 nm, revealing radiative smoothing (horizontal photon transport) (Ewald et al. 2016). The rough appearance at 2100 nm can be due to the higher absorption by cloud droplets at 2100 nm than at 870 nm. In addition, cloud tops that are darker at 2100 nm probably indicate the presence of large cloud droplets. Ewald 2016 describes how to retrieve other properties like the liquid phase and the apparent effective radius from specMACS data.

The specMACS can also be installed on board an aircraft, looking through a side window, or in nadir view, to complement measurements taken by active remote sensing instruments, which can probe inside clouds. These instruments are described in Section 2.3.4

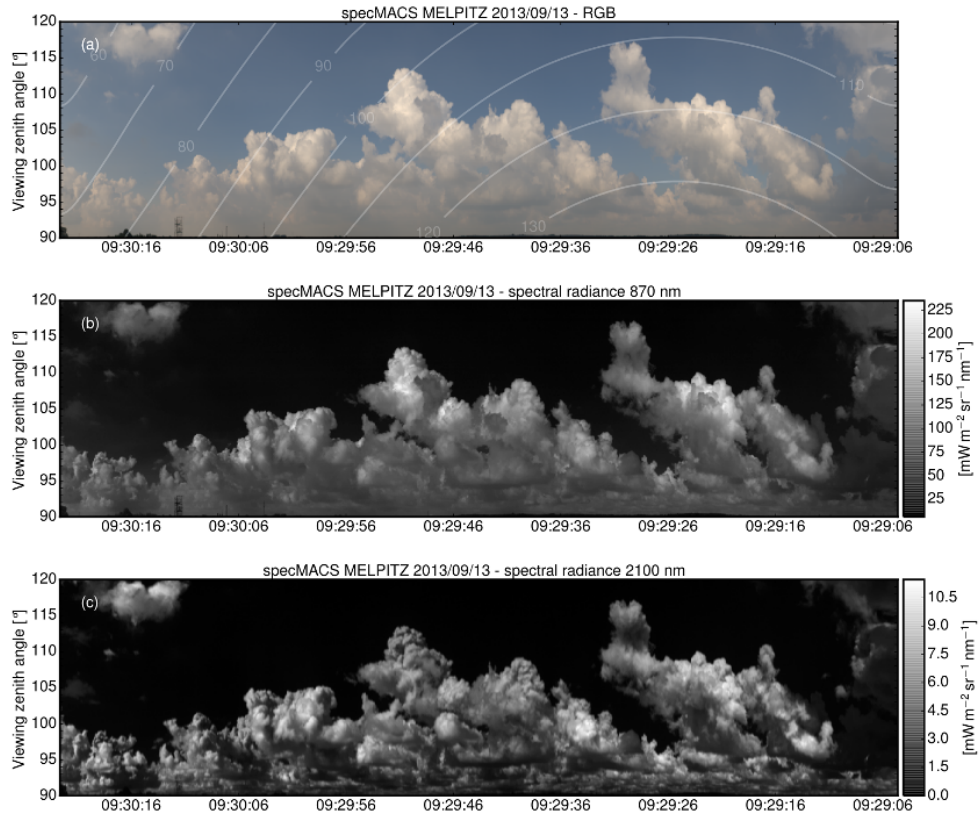


Figure 2.15: Example of specMACS measurements of cloud sides during the HOPE-Melpitz campaign in 2013: True-color image with superimposed iso-lines of the same scattering angle towards the Sun a), Calibrated spectral radiance image at 870 nm b) and at 2100 nm c) (from Ewald et al. 2016).

In addition, further passive remote sensing instruments will soon be in orbit around the Earth, onboard the EarthCARE satellite (Section 2.3.2). Four passive and active remote sensing instruments are onboard EarthCARE and their observations are collocated and complement each other. The two passive instruments are the Multi-Spectral Imager (MSI) and the Broad-Band Radiometer (BBR) and their specifications are detailed in Wehr et al. 2023. Figure 2.16 presents the viewing geometry of each instrument, showing that MSI detects over a 150 km band along the track, asymmetrical to the satellite trajectory (35 km on the right, 115 km on the left) and that BBR detects over three 100 km² zones, one at nadir, one towards the front of the satellite at an angle of 50° and one backwards with the same angle. MSI operates 7 channels in the VNIR (670 nm, 865 nm), the SWIR (1670 nm, 2210 nm) and the thermal IR (8.80 μm, 10.80 μm, 12.00 μm), providing TOA radiance and brightness temperature, which is the temperature that would be emitted by a body with the

same intensity as the one emitted by an object at wavelength λ . These measurements may be used to determine the cloud mask (which indicates if and what type of cloud is present), the cloud and aerosol microphysical parameters and the cloud top height. On the other side, BBR measures the reflected SW (0.2 – 4.0 μm) radiance at TOA with an accuracy of $2.5 \text{ W.m}^2.\text{sr}^{-1}$ and the emitted LW (4.0 - 50.0 μm) radiance with an accuracy of $1.5 \text{ W.m}^2.\text{sr}^{-1}$ at TOA. The SW and LW fluxes obtained by BBR can then be used to make a closure study by comparing them with the fluxes obtained with the other EarthCARE instruments (active and passive).

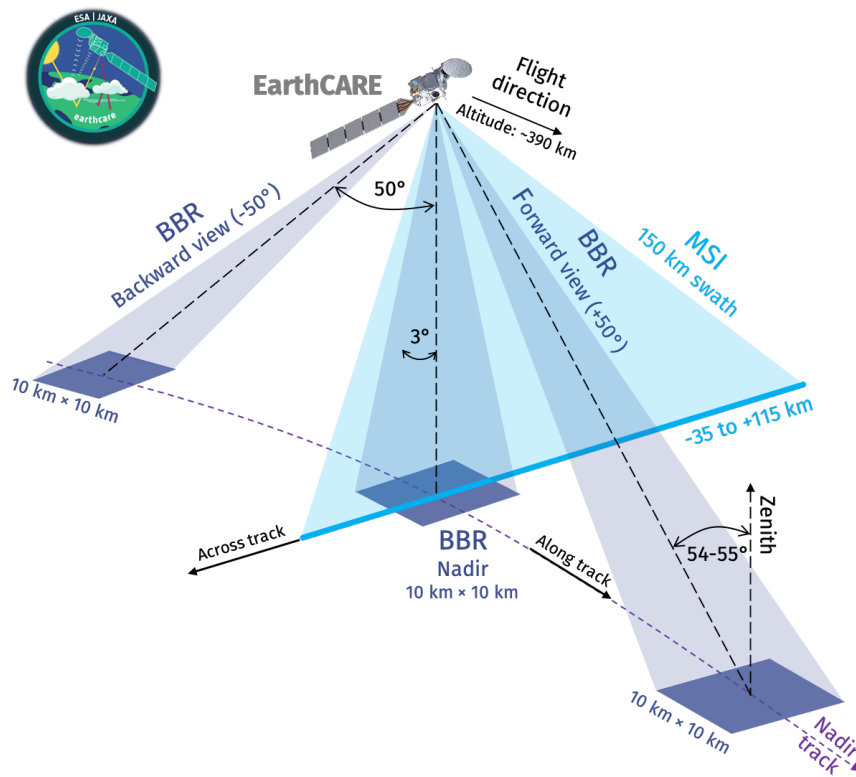


Figure 2.16: Viewing geometry of MSI and BBR onboard EarthCARE.

2.2.2 . Active remote sensing

While passive remote sensing instruments consist solely of an electromagnetic wave receiver, active remote sensing instruments emit electromagnetic waves towards the targets to be studied, and therefore combine an transmitter and a receiver. The energy emitted by the instrument at a given wavelength and power is transmitted into the atmosphere until it interacts with particles (aerosols, air molecules, ice crystals, cloud droplets etc.) or the surface (ground, mountain, ocean, sea ice, etc.). Some of the energy is then backscattered to the instrument, depending on the physical properties of the particles. Finally, the instrument receiver collects the backscattered energy, providing information on the targeted particles.

The power received by the instrument $P_r(d, \lambda)$ is given by Equation 2.2 and depends on the emitted power at wavelength λ , $P_e(\lambda)$, the instrument characteristics given by an instrumental constant C_{instr} , the distance d [m] between the target and the instrument, the target volume characteristics represented by the backscatter coefficient at distance d , $\beta(d, \lambda)$ [$\text{m}^{-1} \cdot \text{sr}^{-1}$], and the atmospheric transmission between emitting source and scattering targets $\mathcal{T}(d, \lambda)$.

$$P_r(d, \lambda) = \frac{P_e(\lambda) \cdot C_{\text{instr}} \cdot \beta(d, \lambda) \cdot \mathcal{T}^2(d, \lambda)}{d^2} \quad (2.2)$$

Since the photons in the emitted radiation travel through the medium twice (to the targeted particles and then back to the instrument), the atmospheric transmission $\mathcal{T}(d, \lambda)$ is squared in Equation 2.2 and can be expressed as follows:

$$\mathcal{T}(d, \lambda) = e^{-\varphi \cdot \delta(d, \lambda)} \quad (2.3)$$

where φ is the multiple scattering coefficient (dimensionless) and $\delta(d, \lambda)$ is the optical depth (Equation 1.5). The multiple scattering refers to the scattering of a photon by several successive scatterers before being detected by the receiving part of an instrument.

The emitted energy propagates according to the divergence of the emitted beam Θ , as shown in Figure 2.17. As a result of this geometry, the power received per unit volume decreases with distance, proportionally to $\frac{1}{d^2}$ (2.2).

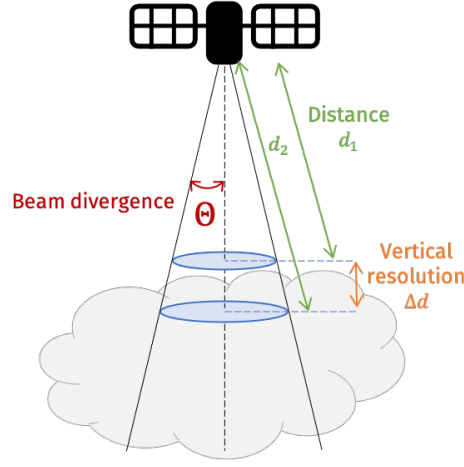


Figure 2.17: Divergence of the emitted beam Θ and range resolution Δd for active remote sensing instrument.

Remote sensing instruments emit pulsed or continuous signals, to assess the distance between the instrument and the target. On the one hand, with pulse-based instruments, the distance d to the target is given by (Skolnik 2008):

$$d = \frac{\Delta t \times c}{2} \quad (2.4)$$

where Δt is the time delay between emission and reception. All the instruments used during this thesis are pulse-based. Additionally, the temporal resolution, which also corresponds to the horizontal resolution along the instrument sight, can be determined by the pulse emission duration.

On the other hand, instruments emitting continuous signal typically rely on a frequency modulation. For example, FMCW (Frequency-Modulated Continuous Wave) instruments emit a periodic signal with a constantly decreasing or increasing frequency (chirp). To determine the distance between the instrument and the target, FMCW instruments measure the difference in frequency between the emitted and received signals $\Delta\nu$. As a result, the distance d is given by (Williams 2011; Suleymanov 2016):

$$d = \frac{\Delta\nu \times c}{2 \frac{B}{t_{\text{sweep}}}} \quad (2.5)$$

where B is the chirp bandwidth and t_{sweep} is the chirp period (also called sweep time).

Since active remote sensing instruments emit their own energy to observe clouds, measurements can be performed both day and night, unlike some passive instruments using sunlight. However, some active instruments can be affected by sunlight, resulting in signal noise.

Using energy emission and reception has the advantage of providing information inside the cloud with vertical profiles, since the energy emitted by the instrument penetrates the cloud and is backscattered towards the instrument. However, the range resolution is defined by the emitted power, the characteristics of the receiving part of the instrument and the time between two energy emission pulses. Consequently, the detected signal is from the entire sampling volume filled with several particles and not from single particle (raindrop, ice crystal, aerosol, ...). The instruments therefore measure the average characteristics of particles within a given volume.

In this thesis, two types of active remote sensing instruments are used and can be operated on the ground, onboard an aircraft or a satellite. They are described in more detail in the following subsections, and examples of existing or future platforms are presented in Section 2.3.

2.2.2.1 Radar

Generally speaking, radars (RADio Detection And Ranging) are instruments utilized to detect objects, transmitting at frequencies between 3 MHz and 220 GHz (radio waves and microwaves). They have a wide range of applications, including military, automotive and security systems. Additionally, they are useful in the scientific field, for mapping surfaces, detecting icebergs or even identifying vegetation density. For atmospheric sciences, radars are designed to study hydrometeors in clouds and precipitations, by working in the microwave domain between 1 and 220 GHz.

Several notations exist for radar frequency bands, but the most widely used is the *IEEE Standard Letter Designations for Radar-Frequency Bands 2020* established by the Institute of Electrical and Electronics Engineers, presented in Table 2.6. As explained in Section 1.2.2.3, to interact with particles, the wavelength of the instruments needs to be of the same order of magnitude (Mie regime) or greater (Rayleigh regime) than the size of the particles to be observed. For observing liquid (drizzle, rain) and solid (snow, ice pellets, hail) precipitations, radars with centimetric wavelengths (S, C and X bands) are commonly used. However, at these wavelengths, these instruments are unable to detect small cloud particles.

Table 2.6: Radar frequency bands according to *IEEE Standard Letter Designations for Radar-Frequency Bands 2020*.

IEEE Band name	Name meaning	Frequency ν	Wavelength λ
HF	High Frequency	3 - 30 MHz	10 - 100 m
VHF	Very High Frequency	30 - 300 MHz	1 - 10 m
UHF	Ultra High Frequency	300 - 1000 MHz	0.3 - 1.0 m
L	Long wave	1 - 2 GHz	15 - 30 cm
S	Short wave	2 - 4 GHz	7.5 - 15.0 cm
C	Compromise between S and X	4 - 8 GHz	3.75 - 7.50 cm
X		8 - 12 GHz	2.50 - 3.75 cm
K _u	Kurz-under	12 - 18 GHz	1.67 - 2.50 cm
K	Kurz	18 - 27 GHz	1.11 - 1.67 cm
K _a	Kurz-above	27 - 40 GHz	0.75 - 1.11 cm
V		40 - 75 GHz	4.0 - 7.5 mm
W		75 - 110 GHz	2.7 - 4.0 mm
mm	millimeter	40 - 300 GHz	1.0 - 7.5 mm
G		140 - 220 GHz	1.4 - 2.1 mm

On the other side, millimeter-wavelength radars (K_a to W) are sensitive to cloud particles, which are smaller than the hydrometeors of precipitation. Consequently, the two most widely used wavelengths for studying cloud ice crystals and cloud droplets are 35 and 95 GHz, which can penetrate thick, dense cloud layers, providing a complete scan of even the deepest clouds. Another advantage of using millimeter wavelengths is that the size of the radar antennas is smaller than for centimeter radars. This makes the instrument easier to deploy, either on the ground or on board an aircraft or satellite. Figure 2.18 shows the transmitting and receiving antennas of the BASTA (Bistatic rAdar SysTEm for Atmospheric studies, Delanoë et al. 2016) radar, described as bistatic because the receiving antenna is separate from the transmitting antenna. Some radars use the same antenna to transmit and receive the signal, in which case they are called monostatic radars.

The radar equation defines the power received by the instrument (Equation 2.6) and can be obtained by adapting Equation 2.2 to the characteristics of the instrument, and by neglecting multiple scattering. As a result, the power received by the radar is defined as follows (Sauvageot 1992):

$$P_r^{\text{radar}}(d, \lambda) = \frac{C_{\text{radar}} \cdot A \cdot Z}{d^2} \quad (2.6)$$

where C_{radar} is the radar factor, i.e. the instrument constant linked to the emission and reception parameters (e.g. antenna geometry, wavelength) of the radar. This constant can be determined by instrument calibration. A is a coefficient related to the attenuation effects that depend on atmospheric

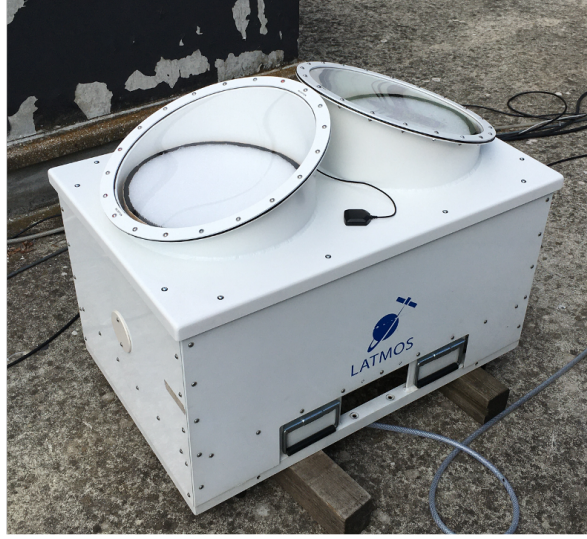


Figure 2.18: The BASTA radar (photo from Julien Delanoë) with inclined radomes (antenna protection).

composition and Z is the radar reflectivity factor, representing the average characteristics of the scattered particles in the sampled volume.

The reflectivity factor Z [$\text{mm}^6 \cdot \text{m}^{-3}$] is determined from the total radar reflectivity η [m^{-1}], which depends on the scattering cross section σ_{sca} (Section 1.2.2.3) according to the following equation (Sauvageot 1992):

$$\eta = \int N(D) \sigma_{\text{sca}}(D) dD \quad (2.7)$$

where D is the particle maximum dimension and $N(D)$ the Particle Size Distribution, defined in Section 1.1.4.

As mentioned in Section 1.2.2.3, the scattering cross section σ_{sca} differs according to Mie (Equation 1.30) or Rayleigh (1.28) scattering regime. At 35 or 95 GHz, if the cloud particles are small enough the Rayleigh scattering can be assumed and the total radar reflectivity, η^{Rayleigh} , is expressed as follows (Sauvageot 1992):

$$\eta^{\text{Rayleigh}} = \frac{\pi^5 |K|^2}{\lambda^4} \int N(D) D^6 dD \quad (2.8)$$

where:

- K is the dielectric factor given by:

$$K = \frac{n^2 - 1}{n^2 + 2} \quad (2.9)$$

- the integral represents the reflectivity factor Z , which is consequently defined by (Sauvageot 1992):

$$Z = \int N(D) D^6 dD \quad (2.10)$$

As a result, the reflectivity factor strongly depends on the particle size and most of the radar response is made by large ice crystals. Due to its large dynamic range, the reflectivity is typically expressed in decibel relative to Z , noted dBZ, obtained by:

$$Z_{\text{dBZ}} = 10 \log_{10}(Z) \quad (2.11)$$

In order to obtain accurate measurements and cloud properties retrievals, it is essential to be able to calibrate the instrument correctly, which can be a challenging task. Indeed, the internal radar calibration requires analyzing each of the radar numerous components separately to determine the total power budget (or radar factor, C_{radar} in Equation 2.6). However, this method induces biases in reflectivity of the decibel order (Anagnostou et al. 2001; Protat et al. 2009), since the connections and interactions between components are not taken into account. These biases are not negligible for cloud characterization, given that one decibel can induce uncertainties up to 15 to 20 % when retrieving ice and liquid water content (Fox and Illingworth 1997; Ewald et al. 2019). As a result, several methods propose to calibrate the instrument while it is in operation. For example, Hogan et al. 2003b calibrate a W-band radar using rainfall, assuming constant reflectivity of 19 dBZ for rainfall rates between 3 and 10 mm.h⁻¹. Li et al. 2005 developed a methodology using the ocean surface. Maneuvers over the ocean in clear-sky conditions are performed, and consist in repeating measurements at different angles by rolling the aircraft at defined angles (Li et al. 2005). The results obtained are then compared with ocean surface backscatter models as a function of incident angle and surface wind. Another way of calibrating, proposed by Ewald et al. 2019, uses measurements of the same target by multiple radars (K_a and W bands) in order to compare them. This method needs to take into account variations in signal attenuation, due to differences in gas and liquid water absorption between operating frequencies, and the scattering regime of each radar as it interacts with cloud particle. Jorquera et al. 2023 also develops a calibration method using the intercomparison of multiple radars, with or without the same frequency, when observing ice clouds. Alternatively, as proposed by Toledo et al. 2020, radar can be calibrated using a target of known reflectivity. These methods allow a calibration accuracy about 1 dBZ.

Some radars are also designed to measure a Doppler velocity spectrum, whose moments provide the mean Doppler velocity (first moment) corresponding to the velocity of the observed particles and the Doppler spectrum width (second moment) which is the standard deviation of the Doppler velocities. This measurement comes from the phase variation of the backscattered signal, which can be determined between two consecutive pulses. This additional information is particularly useful for distinguishing the cloud from its precipitation zone or vertical air motion (turbulence, Majewski et al. 2023).

It is interesting to note that a radiometric (or passive) mode can be used with some radars (e.g. CPR CloudSat, Battaglia and Panegrossi 2020), allowing for example to obtain a brightness temperature and thus a better characterization of snowfall over the ice-free ocean.

2.2.2.2 Lidar

Lidars (Light Detection And Ranging) are instruments operating globally in the same way as radars, but using a laser as an electromagnetic source. Some lidars are monostatic, meaning that they transmit and receive on the same optical chain. However, others are bistatic, implying that the transmitter (laser source) is always separate from the telescope, used to receive the signal backscattered by the targets. Consequently, as shown in Figure 2.19, the laser beam is outside the field-of-view (FOV) of the telescope over a certain distance (usually a few meters) and the telescope misses a portion of the backscattered energy. This phenomenon exists for monostatic lidars when the beam is in the shadow of the telescope mirror. To correct this, an overlap function can be used $\mathcal{O}(d)$, which depends on the instrument configuration as well as the alignment of the laser source with the telescope FOV. Nevertheless, if the laser alignment varies during the measurement, the overlap function has to be adapted, making calibration procedures complex. Consequently, it is important to avoid misalignments, and they must be corrected when necessary.

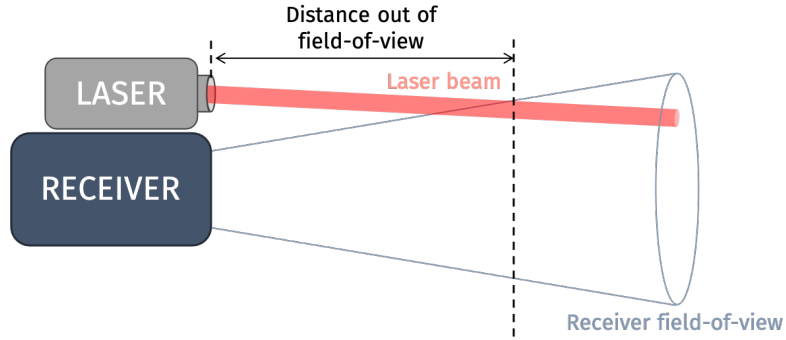


Figure 2.19: Geometry of the laser beam and the receiver FOV, showing the distance at which the receiver detects no backscattered signal.

The wavelength ranges used by lidars for cloud observation are near-UV, visible and near-IR, with three typical wavelengths: 355 nm (near-UV), 532 nm (visible, green) and 1064 nm (near-IR). At these wavelengths, which are smaller than radar wavelengths, the lidar signal can detect very thin particles such as air molecules, aerosols or small cloud particles. The lidar beam can be assumed to follow the geometry optics for large ice particles and the Mie scattering for smaller particles. In both cases, the scattering cross section is then proportional to the square of the particle diameter, i.e. its area. As a result, the lidar signal is more sensitive to concentration changes and is more affected by the scattering and absorption of particles, contributing to the attenuation of the signal. The attenuated (or apparent) backscatter [$\text{m}^{-1}.\text{sr}^{-1}$], at a distance d [m] from the instrument, measured by the lidar is given by (Weitekamp 2005):

$$\beta_a(d) = \beta(d)e^{-2 \int_0^d \alpha(z) dz} \quad (2.12)$$

where β is the backscatter coefficient [$\text{m}^{-1}.\text{sr}^{-1}$] and α is the extinction coefficient [m^{-1}] (Equation 1.1.4). The backscatter coefficient β can be dissociated into two components, since part of the backscattered energy comes from the contribution of the air molecules, β_m , and the other from the cloud particles, β_p . The same can be applied to the extinction coefficient α , giving the following equations (Weitekamp 2005):

$$\beta = \beta_m + \beta_p \quad (2.13)$$

$$\alpha = \alpha_m + \alpha_p \quad (2.14)$$

From both α and β coefficients, we can define the lidar ratio S (also known as the extinction-to-backscatter ratio) [sr], and is expressed as follows (Weitkamp 2005):

$$S = \frac{\alpha}{\beta} \quad (2.15)$$

For scatterers commonly found in the atmosphere, the lidar ratio can vary between 5 and 100 sr, depending on the nature and chemical properties of the particles. For tropospheric clouds, the lidar ratio typically ranges from 10 to 60 sr (Del Guasta 2001; Whiteman et al. 2004) with an average of 25 sr for ice clouds and 16 sr for altocumulus clouds (Yorks et al. 2011). Nevertheless, the lidar ratio of liquid cloud particles varies only slightly and can be considered constant (Pinnick et al. 1983) at a value close to 18 sr. Table 2.7 lists lidar ratio values at different wavelength and according to the particle size or type.

Table 2.7: Lidar ratio S for liquid droplet depending on cloud type, particle size and lidar wavelength.

Source	Particle or cloud type	Wavelength λ [nm]	S [sr]
Pinnick et al. 1983	Spherical water droplets	1064	18.2
		632	17.7
O'Connor et al. 2004	Median equivolumetric diameter between 8 and 20 μm	905	18.8 ± 0.8
		532	18.6 ± 1.0
		355	18.9 ± 0.4
Hogan et al. 2003a	Mie theory and distributions with median volume diameters between 5 and 50 μm	905	18.75

As the intensity of the backscattered light is highly dependent on the integration of the extinction along the light path (Equation 2.12), the lidar signal is sometimes attenuated very fast and is unable to penetrate optically thick clouds.

The power received by the lidar, P_r^{lidar} , using Equation 2.2, can be expressed as (Weitkamp 2005):

$$P_r^{\text{lidar}}(d, \lambda) = \frac{P_e(\lambda) \cdot C_{\text{lidar}} \cdot \mathcal{O}(d) \cdot \beta(d, \lambda)}{d^2} \cdot \mathcal{T}^2(d, \lambda) \quad (2.16)$$

where P_e is the emitted power, C_{lidar} the instrument constant, $\mathcal{O}(d)$ the overlap function, β the backscatter coefficient and $\mathcal{T}(d, \lambda)$ the atmospheric transmission, representing the attenuation and multiple scattering effects (Equation 2.3). The power received therefore depends on the emitted wavelength, the properties of the sampled particles, the multiple scattering effect and the attenuation along the optical path.

For air molecule detection, Rayleigh scattering is assumed for the lidar signal. Some lidars have the capability of isolating the Rayleigh signal (backscattered from air molecules, β_m) from the Mie signal (backscattered from aerosols or cloud particles, β_p), and are called High Spectral Resolution Lidars (HSRL). Figure 2.20 illustrates the backscatter signal from a mixture composed of air molecules and cloud particles. The signal can be split into two parts, with a large peak representing the Rayleigh scattering of molecules, and a higher amplitude but much narrower peak representing the Mie scattering of particles. These two peaks could be separated with an ideal filter of very fine bandwidth, as shown in gray dashed line in Figure 2.20. In practice, two types of HSRL exist for spectral filtering, using either an absorption cell (e.g. Hair et al. 2008, Esselborn et al. 2008) or interferometers (e.g. Bruneau et al. 2015).

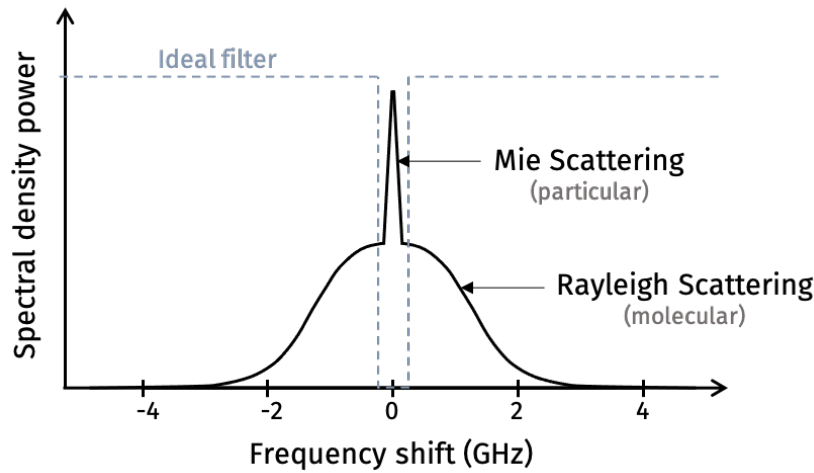


Figure 2.20: Spectral backscattered energy distribution from air molecules and cloud particles. The x axis corresponds to the frequency shift between transmitted and received signal.

There are several interferometer types, such as the Michelson (Burton et al. 2018), the Mach-Zehnder (e.g. Bruneau et al. 2015), the Fabry-Pérot (e.g. Wehr et al. 2023) and the Fizeau (e.g. Reitebuch et al. 2009), which can be used in HSRL. The principle of the interferometer is to divide the received electromagnetic beam into several beams, which then follow paths of different lengths. The beams are then recombined, forming interferences from which information can be extracted. Figure 2.21 shows the example of the Mach-Zehnder interferometer, using two mirrors, two beam splitters and two detectors.

Regardless of the filtering technique used, the High Spectral Resolution (HSR) method separates the energy backscattered by air molecules from the

total backscattered energy. Consequently, the backscatter ratio BR can be determined and is expressed as follows:

$$BR = \frac{\beta_p + \beta_m}{\beta_m} \quad (2.17)$$

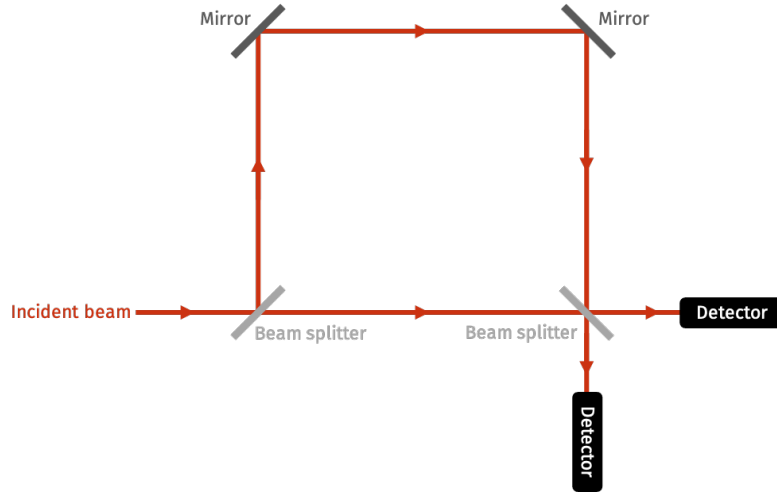


Figure 2.21: Mach-Zehnder interferometer principle.

This ratio does not take the attenuation into account. By using the attenuated molecular backscatter measurement, it is possible to retrieve the particular extinction and lidar ratio from Equations 2.18 and 2.19.

$$\beta_{a,m} = \frac{\alpha_m}{S_m} e^{-2 \int_0^R (\alpha_m(z) + \alpha_p(z)) dz} \quad (2.18)$$

$$\beta_{a,p} = \frac{\alpha_p}{S_p} e^{-2 \int_0^R (\alpha_m(z) + \alpha_p(z)) dz} \quad (2.19)$$

where S_m and S_p are the molecular and the particular lidar ratio respectively.

Another lidars capability (also found in some radars) is to use the polarization of light to deduce some properties of the observed objects. An electromagnetic wave of frequency ν consists of the coupling of an electric field \vec{E} with a magnetic field \vec{B} , oscillating at the same frequency ν . These fields define the electromagnetic wave propagation direction, as illustrated in Figure 2.22. Both fields are always perpendicular to each other and are located in a plane orthogonal to the wave propagation direction. Moreover, the electric field direction determines the light polarization:

- Linear polarization: the electric field always oscillates in the same direction it is referred as linear polarization (Figure 2.22).
- Circular polarization: the electric field oscillates equally along two components rotating at constant speed.
- Elliptic polarization: the electric field oscillates differently along two components, rotating at constant speed.

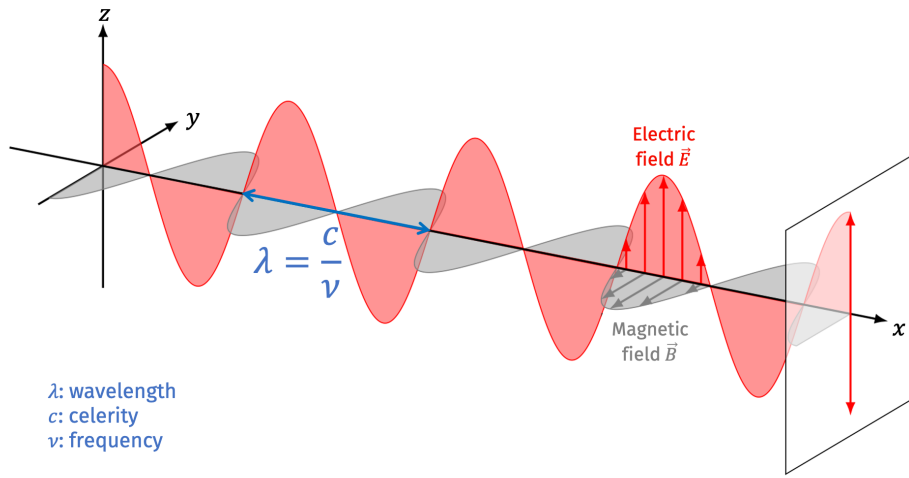


Figure 2.22: The electric field \vec{E} and the magnetic field \vec{B} of an electromagnetic wave with wavelength λ and frequency ν .

For cloud studies, the transmitted wave polarization can be imposed and compared with the polarization of the received wave using polarizers. These allow the polarization of the received wave to be determined according to two components: the polarization perpendicular to the transmitted wave \mathcal{P}_{\perp} and the polarization parallel to the transmitted wave \mathcal{P}_{\parallel} . It is therefore possible to define the depolarization ratio \mathcal{D} , describing the depolarization power of a targeted particle and given by the ratio between the perpendicular component and the parallel component of the received wave polarization:

$$\mathcal{D} = \frac{\mathcal{P}_{\perp}}{\mathcal{P}_{\parallel}} \quad (2.20)$$

This ratio become useful to distinguish the nature of some hydrometeors, since ice crystals depolarize light whereas spherical water droplets do not ($\mathcal{D} = 0$), or for determining the shape or orientation of ice crystals.

Like radar, some lidars are capable of using the Doppler signal to determine the velocity of observed hydrometeors (e.g. Grund et al. 2001; Westbrook et al. 2010; Bruneau et al. 2015) or to determine wind information. One example is the Atmospheric LAsER Doppler INstrument (ALADIN) instrument onboard the Atmospheric Dynamics Mission Aeolus (ADM-Aeolus) satellite or onboard an aircraft for its airborne version (Reitebuch et al. 2009).

Regarding lidar calibration, it is required to determine the instrument constant C_{lidar} for each wavelength channel. The most traditional method consists in using clear sky region (or “clean air”) (e.g. Sauvage et al. 1999; Beyerle et al. 2001), since it is free of any cloud particles. In this region, the lidar measurement is compared to a molecular attenuated backscatter model calculated following Bucholtz 1995, Bodhaine et al. 1999 and She 2001 atmospheric density, molecular scattering cross-section and depolarization. These models also require atmospheric information such as the temperature and the pressure (Cazenave 2019), coming from instruments collocated with the lidar to be calibrated or from weather forecasting models. Uncertainty in these atmospheric measurements can introduce calibration errors and the aerosols presence in these clear-sky regions can also lead to biases of a few percent in the calibration (Powell et al. 2009).

2.2.3 . Radar-lidar synergy

In this subsection, I focus on the radar-lidar synergy, which consists in combining the measurements of these instruments to take advantage of their complementary sensitivities. Synergy between active and passive instruments also exists, such as lidar-radiometer (Garnier et al. 2012; Sourdeval 2012; Garnier et al. 2013) and radar-radiometer (Evans et al. 2005; Vishwakarma et al. 2022) synergies used to retrieve cloud microphysical properties, with radiometric information helping for example to constrain ice water path (integration of the ice water content between two points of the atmosphere) retrieval.

As explained previously, radar and lidar do not have the same sensitivity to every hydrometeor. Figure 2.23 presents an example of the lidar attenuated backscatter at 532 nm of CALIOP (CALIPSO) in panel a) and the radar reflectivity at 95 GHz of CPR (CloudSat) in panel b). Panel c) shows which instrument signal can be used, whether it detects ice particles or liquid droplets. In this example, the lidar (panel a)) detects optically thin clouds between 8 and 11 km (box 1.), while the radar signal (panel b)) is unable to detect these small ice cloud particles. This can be explained by the sensitivity of the lidar to particle concentration, whereas the radar is more sensitive to particle size. Panel c) indicates that these high clouds are only observed by the lidar signal.

Next, between 5 and 8 km and before 21:51:45 UTC (box 2.), the lidar signal is also around $10^{-5} \text{ m}^{-1}.\text{sr}^{-1}$, while the radar signal gives a reflectivity of around -10 dBZ . Thus, this zone is one of synergy, as shown in panel c), with both radar and lidar signals detecting ice cloud particles. At 4 km (box 3.), the strong lidar backscatter signal ($> 10^{-4} \text{ m}^{-1}.\text{sr}^{-1}$) indicates the presence of liquid water droplets. The radar signal is also relatively strong in these areas, indicating the presence of ice particles. This suggests, in this case, areas of mixed-phase, and panel c) identifies an area of synergy. Below these layers of liquid water, the lidar signal is completely attenuated and is unable to detect down to the ground. In contrast, radar, which is not attenuated by these layers of liquid water, is capable of detecting cloud particles (precipitating or not) down to the ground.

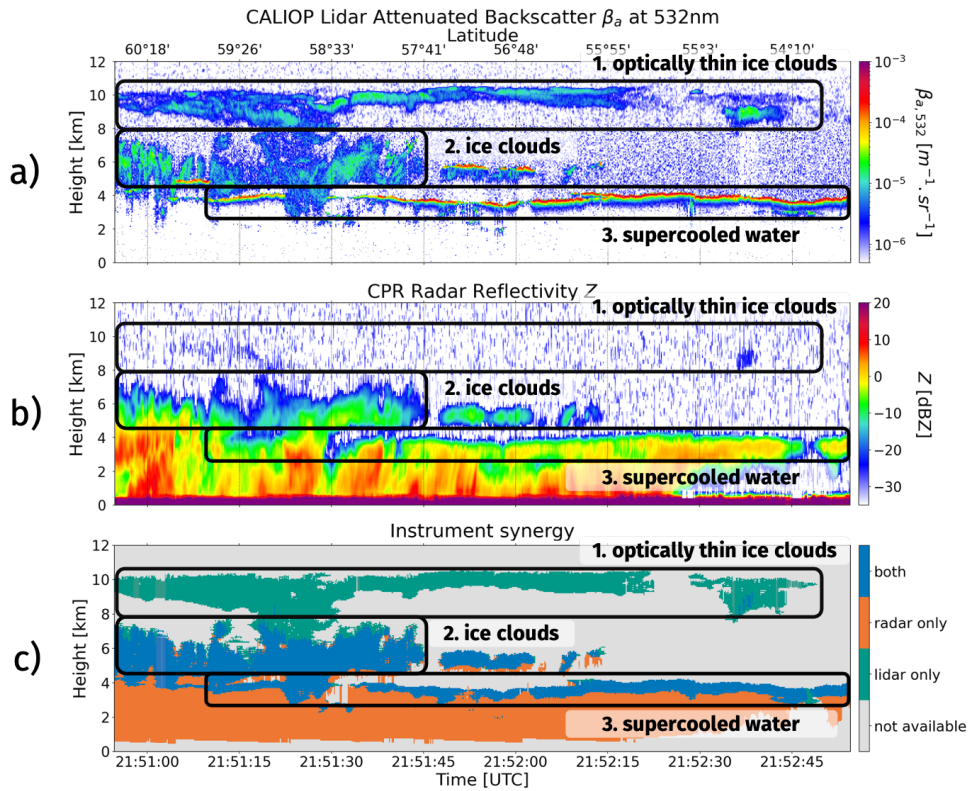


Figure 2.23: CALIOP lidar attenuated backscatter at 532 nm a), CPR radar reflectivity at 95 GHz b) and the instrument synergy (single instrument or synergy areas) c) on 21st November 2008. The three panels share the same abscissa axes (time and latitude). Data from DARDAR-MASK V2.23 products, <https://www.icare.univ-lille.fr/>, orbit ID: 2008326202854_13667

By using these two instruments in synergy, more information can be obtained than with only one. For areas where instrument synergy can be ex-

exploited, measurements from both instruments can be used to constrain the retrieval of ice or mixed-phase cloud microphysical properties. Radar-lidar synergy can also be used to build a cloud hydrometeors classification (Section 3.2), as for DARDAR-MASK (Delanoë and Hogan 2010) products designed for CPR (CloudSat) and CALIOP (CALIPSO) instrument data, or the future AC-TC products designed for the data of the lidar and radar instrument of EarthCARE (Irbah et al. 2023).

Additionally, radar-lidar synergy can be utilized in algorithms for the restitution of cloud microphysical properties. Lidar-radar synergistic methods were first proposed by Intrieri et al. 1993, Donovan and Lammeren 2001, Tinel et al. 2005 and Mitrescu et al. 2005 to retrieve ice clouds properties where both instrument overlap. Algorithms as VarCloud (Delanoë and Hogan 2008) and 2C-ICE (Deng et al. 2010) were later developed to retrieve ice clouds properties all along the instruments profile using the CPR (CloudSat), the CALIOP (CALIPSO) and additionally radiometric information for VarCloud. For the EarthCARE mission (Section 2.3.2) the unified synergistic retrieval algorithm Cloud, Aerosol, and Precipitation from multiple Instruments using a VARIational TECHnique (CAPTIVATE, Mason et al. 2022) uses the ATMospheric LIDar (ATLID), Cloud Profiling Radar (CPR), as well as MSI data to retrieve clouds, precipitations and aerosols properties.




In this thesis, I describe a new method designed to retrieve the properties of mixed-phase clouds, supercooled water and ice, using radar-lidar synergy and based on the VarCloud method. Further details are presented in Chapter 3. The VarCloud method and the one proposed in this thesis are flexible and can be applied to various radar-lidar platforms, which are introduced in the next section.

2.3 . Spaceborne and airborne radar-lidar platforms

For better collocation of synergistic measurements (in this case, radar-lidar), the instruments are often located in the same place, on the same instrument platform. Several types of radar-lidar platforms exist: onboard a satellite, an aircraft or even ground-based. Each platform has its own advantages and limitations, which are listed in Table 2.8.

During my thesis, I worked with data from both airborne and spaceborne radar-lidar platforms. In this section, I present two spaceborne platforms as well as three airborne platforms with specifications of the carrier aircraft.

Table 2.8: Advantages and drawbacks of spaceborne, airborne and ground-based radar-lidar platform.

	Platform	Advantages (+)	Drawbacks (–)
	Spaceborne	Area covered (global) Permanent / frequent observation Looking direction (from above)	Low resolution Limited number of instruments Less durable (depending on orbit altitude) Difficult to repair
	Airborne	Area covered (precise) High resolution Numerous instruments (including <i>in situ</i>) Closer to the cloud Looking direction (multiple)	Observation limited to a few hours Limited coverage
	Ground-based	High resolution Durable Easily repairable Permanent observation of the same area	Area covered Radome attenuation Observation of the same area

2.3.1 . CloudSat and CALIPSO from A-Train

The Afternoon Constellation, widely known by its nickname A-Train, consists of seven satellites (described in the following paragraphs), carrying two active remote sensing instruments and thirteen passive instruments.

- Aqua, originally called EOS PM-1 as it belongs to the National Aeronautics and Space Administration (NASA) Earth Observing System (EOS) mission, was launched on the 4th of May 2002 and is dedicated to the study of the water cycle. It possesses six passive remote sensing instruments including MODIS (swath of 2330 km across the track) and CERES (swath of 3000 km across the track). The satellite is still operational.
- Aura, originally called EOS CH-1 (also part of the NASA EOS mission), was launched on the 15th of July 2004 and is dedicated to the study of the air quality, the ozone layer and the climate. It comprises four passive remote sensing instruments operating in the UV, visible and IR. The satellite is scheduled for shutdown in 2025 or 2026.
- PARASOL (Polarization and Anisotropy of Reflectances for Atmospheric Sciences coupled with Observations from a Lidar) is a french micro-satellite from the Centre National d'Études Spatiales (CNES), the french space agency. The satellite joined the A-Train on 18th of December 2004 and exited it on 18th of December 2013. It carried the POLDER-3 radiometer (POLarization and Directionality of the Earth's Reflectances), operating nine channels in the near-UV, visible and near-IR wavelengths, to study clouds, aerosols and water vapor microphysical and radiative properties. Some of its channels were sensitive to light polarization.

- CloudSat, which is also part of the NASA EOS, was launched on the 28th of April 2006. It carries the CPR, which is a cloud radar emitting at 94.05 GHz, giving vertical profile of clouds and precipitation. The radar specifications are given in Table 2.9. CloudSat and its components are illustrated in Figure 2.24. After seventeen years of operation, the radar was turned off on the 20th of December 2023.

Table 2.9: CPR (CloudSat) specifications (from <https://cloudsat.atmos.colostate.edu/instrument>).

Parameter	Value
Frequency	94.05 GHz
Pulse repetition frequency	4300 Hz
Range resolution	500 m
Across-track resolution	1.4 km
Along-track resolution	1.7 km
Pulse width	3.3 μ s
Nadir angle	0.16°
(since 15 th of August 2006)	
Minimum detectable Z (atmospheric attenuated not included)	< -29 dBZ
Data window	0 to 25 km
Antenna diameter	1.85 m
Dynamic range	70 dB
Data rate	20 kbit.s ⁻¹

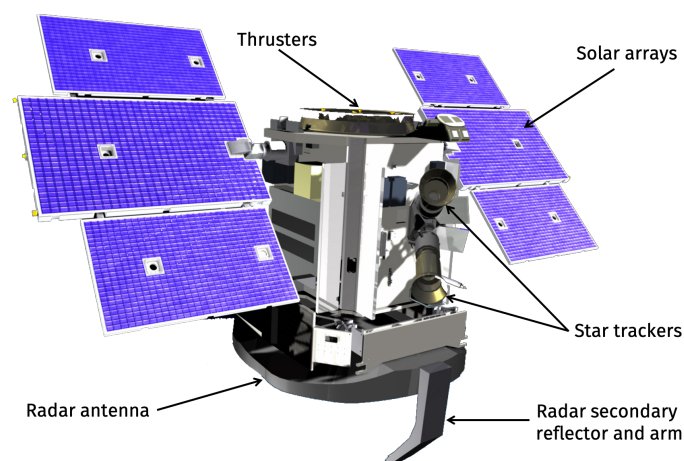


Figure 2.24: The CloudSat satellite and its components.

- CALIPSO, operated by both CNES and NASA, was launched at the same time as CloudSat and its operation ended on the 1st of August 2023. It is also part of the EOS mission and carries the lidar CALIOP, emitting at 532 and 1064 nm, with the 532 nm channel sensitive to polarization, and providing high-resolution vertical profiles of clouds and aerosols. In 2007, the instrument pointing was adjusted to 3° from nadir to avoid specular reflection from ice crystals. The lidar specifications are given in Table 2.10. Figures 2.25 shows the lidar (panel a)) and satellite (panel b)) with their respective components. Two passive instruments are also onboard CALIPSO: the Wide Field of View Camera (WFC) and the Infrared Imager Radiometer (IIR), providing context for day and night lidar measurements respectively.

Table 2.10: CALIOP (CALIPSO) specifications (from <https://calipso.cnes.fr/en/CALIPSO/lidar.htm> and Feofilov et al. 2023).

Parameter	Value
Lidar type	Nd:YAG, diode-pumped Q-switched, frequency doubled
Wavelength	532 and 1064 nm
Pulse repetition frequency	20 Hz
Range resolution* (troposphere)	30 m
Horizontal resolution*	333 m
Nadir angle (since 28 th of November 2007)	3°
Telescope aperture	1 m
Telescope FOV	130 μrad
Laser beam divergence	100 μrad
Footprint (diameter)	90 m
Data rate	316 kbit.s ⁻¹

* The range and horizontal resolution of CALIPSO data varies with altitude and the wavelength channel, see Winker et al. 2009 for further details.

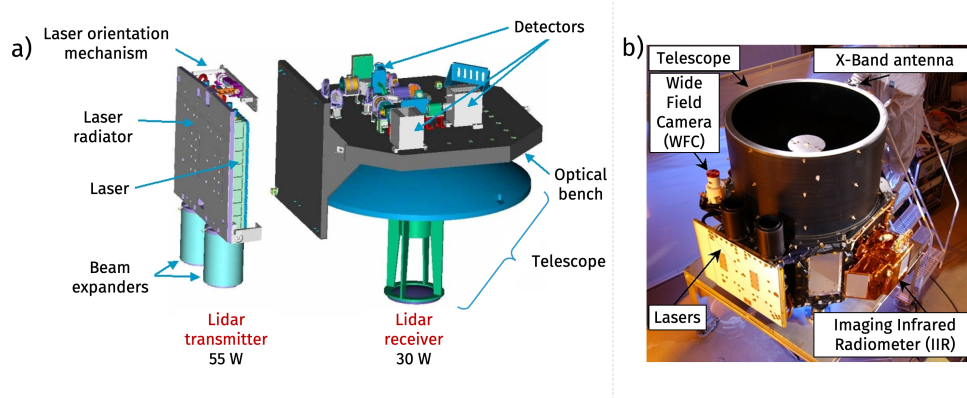


Figure 2.25: a) CALIOP transmitter and receiver, and b) the CALIPSO satellite components (CALIOP, WFC and IIR). Images from <https://calipso.cnes.fr/en/CALIPSO/lidar.htm>.

- GCOM-W1, for Global Change Observation Mission - Water 1 (also named Shizuku), is a satellite from the Japan Aerospace eXploration Agency (JAXA) launched on the 17th of May 2012. It transports the Advanced Microwave Scanning Radiometer 2, that scans a 1450 km cone-shaped swath between 6.925 and 89 GHz (6 channels). It was designed to be the follow-up to AMSR-E (Advanced Microwave Scanning Radiometer for EOS), onboard Aqua, and is dedicated to the water cycle study.
- OCO-2, for Orbiting Carbon Observatory-2, was launched on the 2nd of July 2014 and is operated by NASA. Thanks to three channels in the near-IR, it is used for high-resolution observation of CO₂ from space.

Figure 2.26 shows the composition of A-train in 2018. Until 2018, the all A-Train satellites orbit at 705 km altitude, in a circular near-polar (inclination 98.2°) sun-synchronous orbit (crossing the equator at 1:30 pm local time). In February 2018, CloudSat moved its orbit down to 16.5 km below the other satellites, due to technical issues that could affect the maneuverability of the satellite. To ensure that the two active remote sensing instrument CPR and CALIOP remain side by side, CALIPSO performed a series of maneuvers in September 2018 to join the orbit of CloudSat, resulting in the creation of the C-Train constellation. Consequently, since 2018, the Afternoon Constellation consists in the A-Train satellites Aura, Aqua, GCOM-W1 and OCO-2 and the C-Train satellites CloudSat and CALIPSO, whose tracks cross approximately every 20 days, making it possible to continue collocated observations.

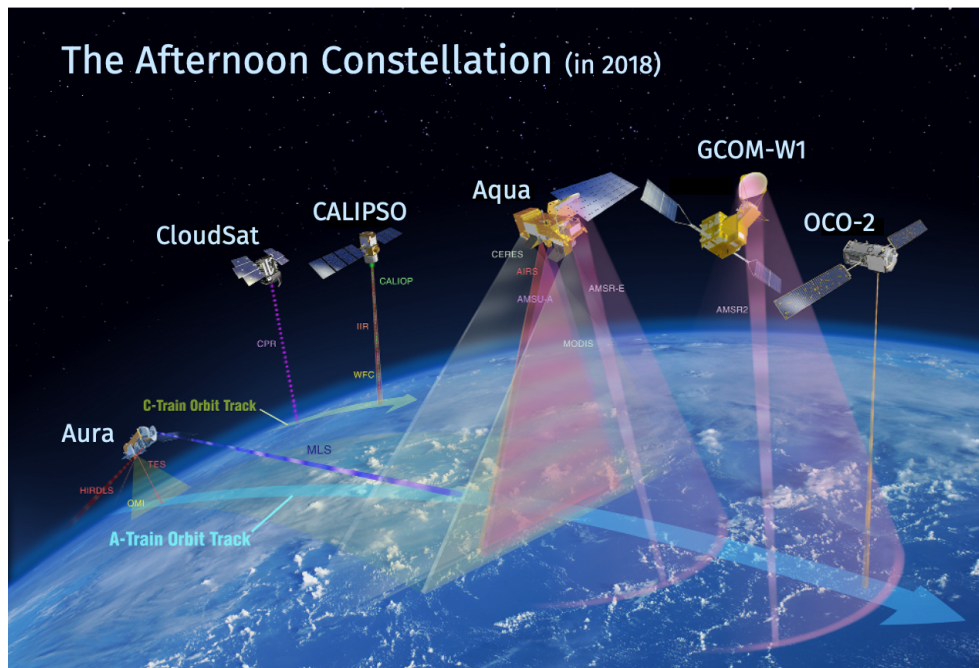


Figure 2.26: The Afternoon Constellation (A-Train and C-Train) in 2018 (from <https://atrain.nasa.gov/>). PARASOL exited the constellation in 2013 and the orbit of CloudSat and CALIPSO has been changed in 2018, creating the C-Train. Active remote sensing instruments are indicated with dashed lines (CPR of CloudSat et CALIOP of CALIPSO). Passive remote sensing instruments are color coded as follows: microwaves (AMSR-E, AMSR-2, AMSU-A, CPR, MLS) are represented with colors ranging from red-purple to deep purple, solar wavelengths (OMI, OCO-2) with yellow, solar and infrared wavelengths (MODIS, CERES) with gray and other infrared wavelengths (IIR, AIRS, TES, HIRDLS) with red.

2.3.2 . CPR and ATLID from EarthCARE

The Earth Clouds, Aerosols and Radiation Explorer (EarthCARE, Illingworth et al. 2015) is a joint satellite of the European Space Agency (ESA) and the JAXA, scheduled for launch in May 2024. It is composed of four instruments, shown in Figure 2.27, including two active remote sensing instruments, the CPR radar and the ATLID lidar, and two passive remote sensing instruments, MSI and BBR (described in Section 2.2.1). The satellite is expected to operate at an altitude of 393 km, in a polar Sun-synchronous regime with an inclination of 97.1° . The altitude is much lower than for CloudSat-CALIPSO, in order to improve the spatial resolution and the sensitivity. The collocation of these four instruments is expected to improve our understanding of the Earth radiation balance and its effects on the climate.

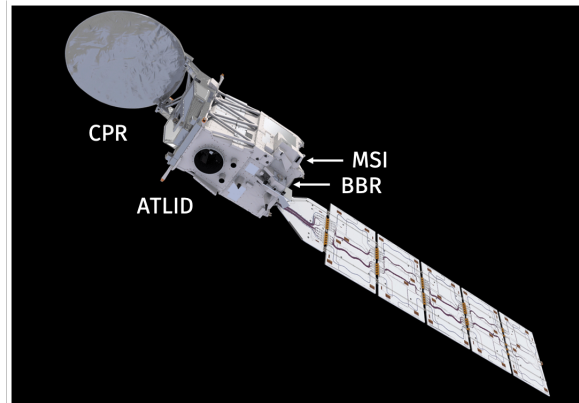


Figure 2.27: Artistic view of the EarthCARE satellite (from Wehr et al. 2023).

Complementing Figure 2.16 in Section 2.2.1, Figure 2.28 shows the pointing and footprints of each EarthCARE instrument, including CPR and ATLID.

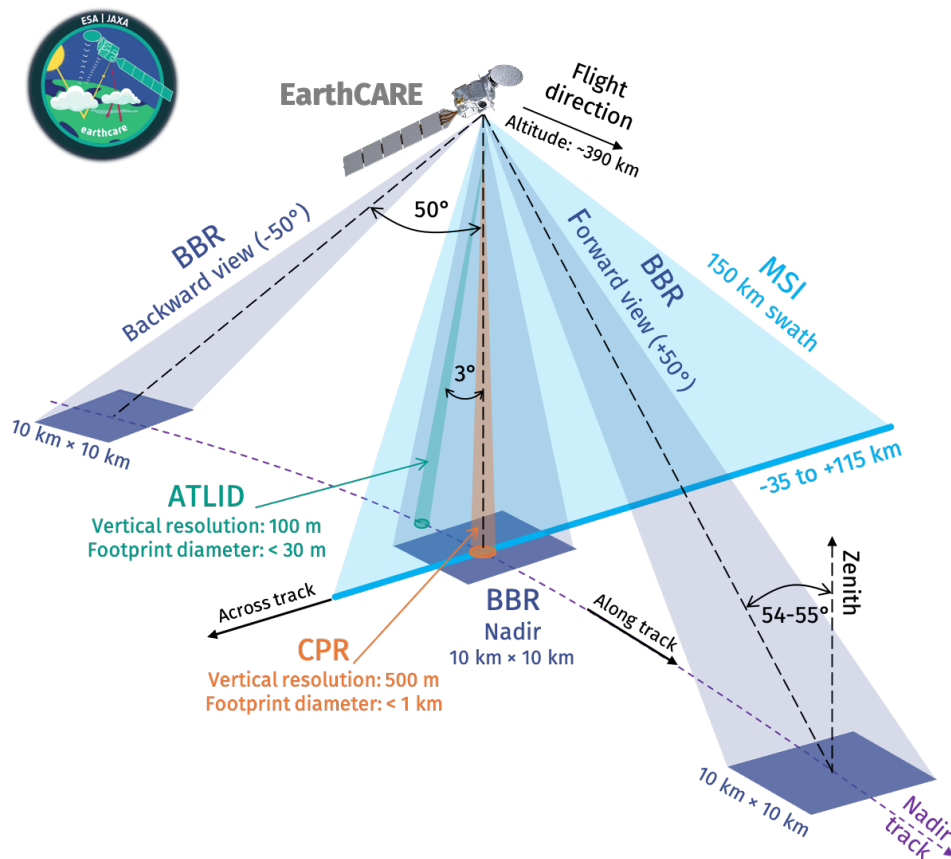


Figure 2.28: Viewing geometry of CPR (in orange), ATLID (in green), MSI (in cyan) and BBR (in blue) onboard EarthCARE.

The CPR of EarthCARE uses an extended interaction klystron at the same frequency as the CPR of CloudSat, 94.05 GHz, and with Doppler capability, which will make it the first spaceborne Doppler cloud radar. It operates at nadir with a beam width of 0.095° (3 dB), its horizontal and range resolution are 500 m, but the range resolution can be oversampled at 100 m. CPR-EarthCARE is expected to have a better sensitivity than CPR-CloudSat, of −35 dBZ, thanks to its lower orbit and larger antenna. The instrument will provide radar echo product, target classification (Irbah et al. 2023), reflectivity profiles used to retrieve clouds and precipitation properties and vertical motion of hydrometeors. The CPR specifications are listed in Table 2.11 and more details can be found in Illingworth et al. 2015 and Wehr et al. 2023.

Table 2.11: CPR (EarthCARE) specifications.

Parameter	Value
Frequency	94.05 GHz
Pulse repetition frequency	6100 to 7500 Hz
Range resolution	500 m (oversampled at 100 m)
Across-track resolution	~ 500 m
Along-track resolution	~ 1 km
Pulse width	3.3 μ s
Antenna diameter	2.5 m
Reflectivity sensibility	−35 dBZ
Data rate	270 kbit.s ^{−1}

ATLID will operate at 355 nm including polarization sensitivity and HSR thanks to a Fabry-Pérot interferometer. As with CALIOP, the pointing of ATLID is 3° from nadir direction to avoid specular reflection from oriented ice crystals. Consequently, CPR and ATLID measurements will not be perfectly collocated. The telescope FOV is 64 μ rad and the laser beam divergence is 45 μ rad, which are thinner than those of CALIOP, helping to reduce the solar radiation contamination and multiple scattering effects. The instrument will provide target classification (combined with CPR target classification, Irbah et al. 2023) as well as backscatter and depolarization vertical profiles, used to retrieve aerosols and clouds properties. The ATLID specifications are listed in Table 2.12 and more details can be found in Illingworth et al. 2015, Wehr et al. 2023 and Feofilov et al. 2023.

Table 2.12: ATLID specifications.

Parameter	Value
Laser type	Nd:YAG tripled frequency
Wavelength	355 nm
Pulse repetition frequency	51 Hz
Range resolution (between 0 and 20 km)	100 m
Horizontal resolution	285 m
Nadir angle	3°
Telescope aperture	0.6 m
Telescope FOV	64 μ rad
Laser beam divergence	45 μ rad
Footprint (diameter)	29 m
Data rate	642 kbit.s ⁻¹

Thanks to the unification of passive and active instruments in a single satellite, it will be convenient to develop synergies with these instruments, as shown for example by Mason et al. 2022 with the CAPTIVATE algorithm. The algorithm developed in this thesis can also be adapted to EarthCARE data to retrieve the microphysical properties of mixed-phase, supercooled water and ice clouds with CPR and ATLID measurements.

2.3.3 . RALI: RASTA and LNG

The radar RASTA (RAdar SysTem Airborne, Delanoë et al. 2013) and the lidar LNG (LÉANDRE New Generation - Lidars aéroportés pour l'Étude des Aérosols, des Nuages, de la Dynamique, du Rayonnement et du cycle de l'Eau, Bruneau et al. 2015), together with the radar BASTA, form the airborne measurement platform called RALI (for RAdar-Lidar). These instruments were developed at LATMOS (Laboratoire Atmosphères et Observations spatiales) and DT-INSU (Division Technique de l'Institut National des Sciences de l'Univers) and can be integrated onboard the SAFIRE ATR 42 aircraft (Figure 2.32) for measurement campaigns. The previous version of the platform was installed onboard the SAFIRE Falcon 20 (without BASTA), which stopped operating in 2021.

The position and pointing of each instrument onboard the ATR 42 are represented in Figure 2.29. LNG is positioned at the front of the aircraft with two observation positions at nadir and zenith (alternately), while RASTA is positioned further back with three antennas pointing above the aircraft (zenith, 28° backward, 20° transverse) and three below (nadir, 28° backward, 20° trans-

verse). Any RASTA antenna can be switched on or off in real time to suit the mission objectives. Meanwhile, BASTA is installed next to RASTA, at a window on the starboard side of the aircraft to get a horizontal side view. This configuration offers the possibility to obtain profiles in several directions around the aircraft. In addition, the synergy between the various instruments provides microphysical and dynamical properties of clouds, aerosols and precipitation.

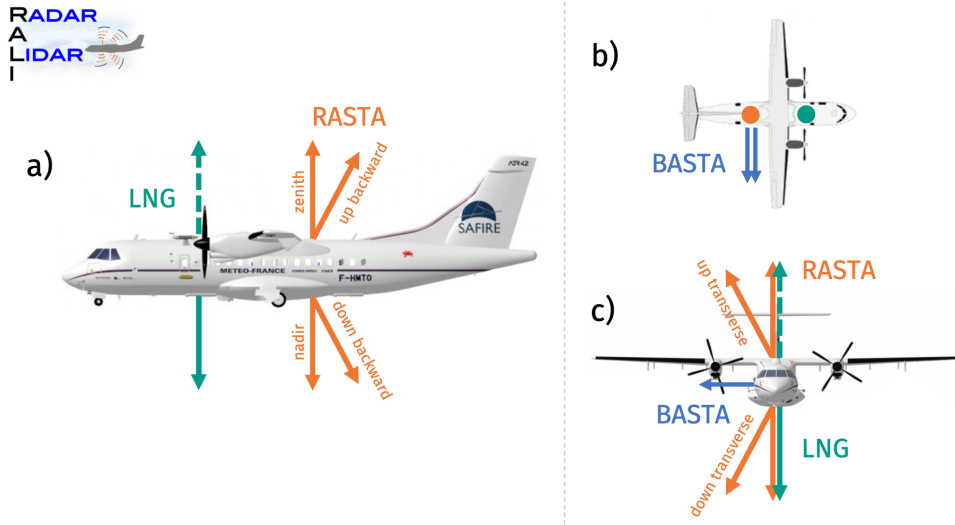


Figure 2.29: Configuration of RALI onboard the ATR 42 (since 2022). Panel a): Side view, panel b): Top view, panel c): Front view. In panel c), the nadir and zenith pointing of RASTA and LNG are not superimposed for better visual readability.

In this thesis, I focus on the synergy between RASTA and LNG, which are describe in the next paragraphs. The BASTA specifications, which provides Doppler velocity and reflectivity along the horizontal direction on the right-hand side of the aircraft, are not described here and can be found in Delanoë et al. 2016 and <https://rali.aeris-data.fr/airborne-basta/>.

RASTA emits 1.5 kW pulses at 95 GHz, almost the same wavelength as CPR radars, allowing for example validation and calibration campaigns for these satellite instruments using RALI. In addition to being equipped with six antennas, the spatial resolution of RASTA can be adapted as required, with values ranging from 15 m to 120 m in resolution and 6 to 15 km in distance. For each operation mode, this distance depends on the time delay between two pulses. The same applies to the ambiguous velocity (V_a), meaning that the Doppler velocities measured by RASTA are in the Nyquist interval (Bringi and Chandrasekar 2001) and need to be corrected from “folding” when they are out-

side the interval $[-V_a, +V_a]$ (Brown and Wood 2007). The different possible resolution configurations are listed in Table 2.13, which also gives the number of values per profile for each configuration (when available). The Doppler capability of RASTA, combined with its six antennas, enables the retrieval of 3D wind fields, as well as the microphysical and dynamic properties of hydrometeors. Other RASTA specifications are listed in Table 2.14, such as its dimensions, the size of its antennas and its beam width and panel b) of Figure 2.30 shows the radar installed onboard the ATR 42.

Table 2.13: Number of values per profile depending on RASTA range resolution and distance (since 2022, from <https://rali.aeris-data.fr/rasta/>).

Distance	Ambiguous velocity	Resolution			
		Pulse length			
		15 m 100 ns	30 m 200 ns	60 m 400 ns	120 m 800 ns
6 km	19.71 m.s ⁻¹	400	200	100	-
7.5 km	15.76 m.s ⁻¹	500	250	125	-
9 km	13.14 m.s ⁻¹	600	300	150	-
12 km	9.85 m.s ⁻¹	800	400	200	-
15 km	7.88 m.s ⁻¹	-	500	250	125
18 km	6.57 m.s ⁻¹	-	-	300	150

Table 2.14: Specifications of RASTA (since 2022, from <https://rali.aeris-data.fr/rasta/>).

Parameter	Value
Frequency	95 GHz
Energy	1.5 kW (Klystron)
Integration time	250 to 1000 ms
Antenna size	30 cm
Beam width	0.8°
Sensitivity at 1 km (depends on configuration)	Nadir: -35 dBZ Zenith: -28 dBZ Others: -32 dBZ
Weight	110 kg
Dimensions	82 × 102 × 150 cm

LNG is operating three wavelength channels at 355 (linear polarization, UV), 532 (visible, green) and 1064 nm (NIR) for the transmission and four wavelength channels for the reception, at 355 nm parallel polarization, 355 nm perpendicular polarization, 532 nm and 1064 nm. Emitted energies and beam divergence for each wavelength are specified in Table 2.15. Additionally, a Mach-Zehnder interferometer (Section 2.2.2.2, page 75) provides HSR capability for the UV channel. LNG specifications such as the range resolution and the laser type are listed in Table 2.15 and the panel a) of Figure 2.30 shows LNG onboard the ATR 42 aircraft. The instrument provides optical parameters of aerosols and clouds, as well as along-sight wind.

Table 2.15: Specifications of LNG transmitter and receiver (before 2024, from <https://rali.aeris-data.fr/high-spectral-resolution-lidar/>).

Parameter	Value		
Wavelength	355 nm	532 nm	1064 nm
Transmitter energy	~ 40 mJ	~ 9 mJ	~ 45 mJ
Transmitter energy	0.15 mrad	4 mrad	5.6 mrad
Receiver FOV	0.5 mrad	5 mrad	7 mrad
Receiver spectral bandwidth	9 nm	0.2 nm	1 nm
Receiver detector	PM	PM	APD
Laser type	flashlamp-pumped Nd:YAG Q-switched oscillator		
Transmitter frequency	20 Hz		
Range resolution	37 m		
Range	15 km		

PM: PhotoMultiplier, APD: Avalanche PhotoDiode.
Information provided in this table is subject to change in 2024,
as LNG is currently being refurbished.

During measurement campaigns, the ATR 42 flies at an average speed of 100 m.s^{-1} , for a period of between four and six hours, and at an average altitude of 5 km. All onboard instruments are operated during the entire flight by a person physically present in the aircraft. LNG requires careful attention, since laser calibration and alignment procedures must be performed regularly and because LNG pointing must be set to nadir or zenith manually, depending on scientific requirements.

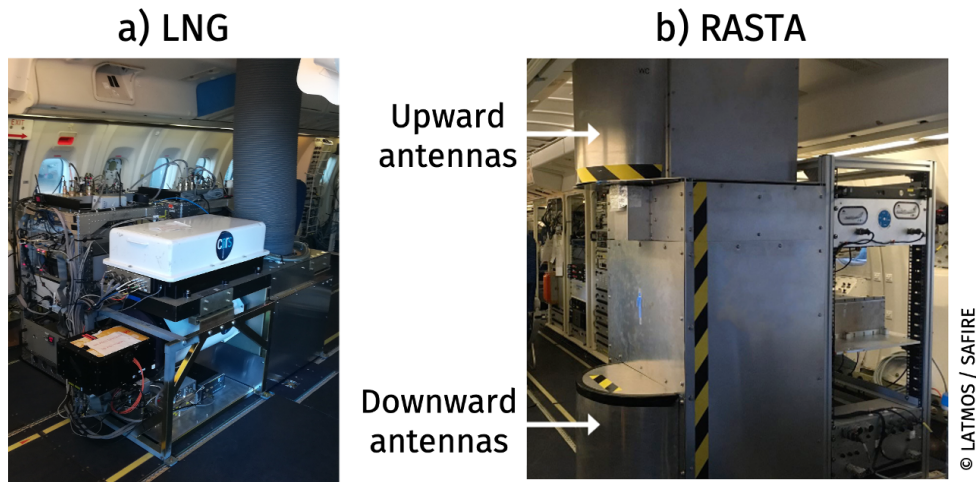


Figure 2.30: a) LNG and b) RASTA instrument onboard the ATR 42 aircraft.

2.3.4 . MIRA and WALES

The cloud radar MIRA (Melchionna et al. 2008; Mech et al. 2014) and the lidar WALES (WATER vapor Lidar Experiment in Space, Wirth et al. 2009) can be installed onboard the German research aircraft HALO (High Altitude and Long Range Research Aircraft, Figure 2.32). Both instruments transmit and receive downwards through the belly pod windows of HALO, as indicated in Figure 2.31. To avoid specular reflection for WALES, the aircraft has an angle attack during flight of 2.5 to 3°. This Gulfstream G550 modified for scientific measurement campaigns (like the SAFIRE ATR 42) can fly at speeds up to 300 m.s⁻¹ at a typical altitude of 9 to 10 km, and is capable of flying for more than ten hours. Besides the two active remote sensing instruments, HALO can also carry several passive instruments such as specMACS or the radiometers from HAMP (HALO Microwave Package, Mech et al. 2014), which includes MIRA.

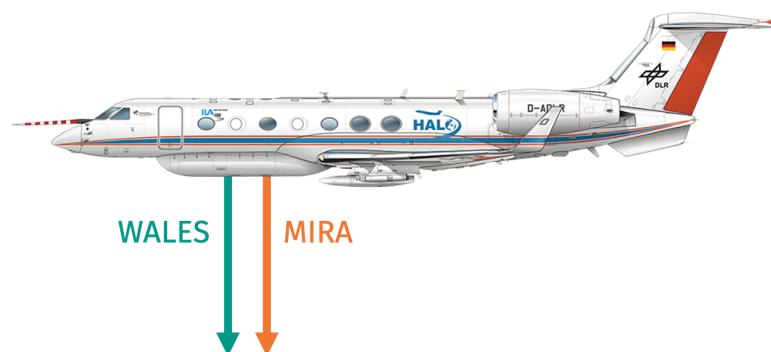


Figure 2.31: WALES and MIRA positioning and pointing onboard HALO.



Figure 2.32: The SAFIRE ATR 42 and HALO aircraft in Kiruna (Sweden) in 2022 during Arctic measurement campaigns.

MIRA is an instrument commercialized by METEK (Meteorologische Messtechnik) that operates at 35.2 GHz (K_a -band) with Doppler capability and polarization sensitivity. It provides reflectivity and velocity vertical profiles, used to retrieve clouds and precipitation microphysical and dynamical properties. Panels a) and b) of Figure 2.33 present the instrument onboard the HALO. The transmitter and emitter electronics accessible in the aircraft cabin and the antennas are in the belly pod. MIRA possesses a different sensitivity to hydrometeors than CPR radars and RASTA, with a reflectivity sensitivity of -38 dBZ at 5 km. In addition, it has a range resolution of 30 m with a footprint at 13 km of 130 m. Other specifications are listed in Table 2.16.

Table 2.16: MIRA specifications (from Mech et al. 2014).

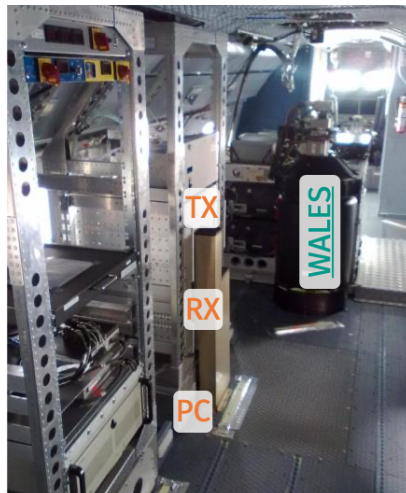
Parameter	Value
Frequency	35.563 GHz
Peak power	30 kW
Pulse length	200 ns
Pulse repetition rate	5 kHz
Antenna diameter	1 m
Beam width	0.6°
Minimum detection signal at 5 km	-38 dBZ
Footprint at 13 km	130 m
Range resolution	30 m

WALES has been developed at the Deutsches Zentrum für Luft- und Raumfahrt (DLR, the German Aerospace Center) and operates at 532 nm with HSR using iodine filter (Esselborn et al. 2008) and at 1064 nm. Additionally, the visible channel is sensible to polarization. Both channels produce vertical profiles of backscatter and extinction, making it possible to characterize aerosols and cloud particles. Additionally, WALES has four channels (three absorption line and one off line) around 935 nm for water vapor Differential Absorption Lidar (DIAL) capabilities, providing the water vapor mixing ratio used to obtain for example the cloud relative humidity using temperature models (e.g. Dekoutsidis et al. 2023). More information on the DIAL function can be found in Wirth et al. 2009. The characteristics of each channel are listed in Table 2.17, as well as the other instrument specifications. Figure 2.33 shows WALES onboard HALO, with a two-angle view with panels a) and d). Panel c) shows the belly pod as seen from the cabin and the window through which the lidar transmits and receives, and panel d) also presents the control station of WALES.

Table 2.17: WALES specifications (from Wirth et al. 2009).

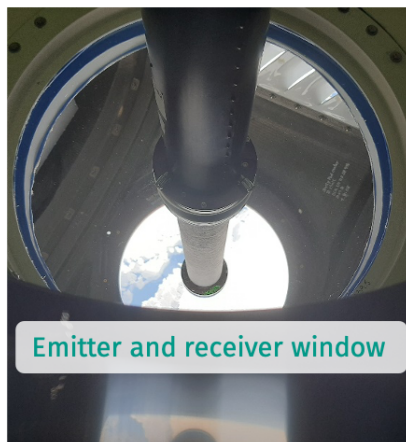
Parameter	Value		
Wavelength	532 nm (HSR)	935 nm (H ₂ O DIAL)	1064 nm
Pump laser			
pulse energy	220 mJ	-	400 mJ
System output	75 mJ	45 mJ	120 mJ
Pulse length	7.5 ns	5.5 ns	8 ns
Detector type	PM	APD	APD
Beam divergence		1 mrad	
Laser type		Nd:YAG laser pumped Two Q-switched monolithic, OPO	
Telescope diameter		480 mm	
Telescope FOV		1.6 mrad	
Nadir angle	2.5 to 3°		
Pulse response		100 ns	
Sampling rate		10 MHz	
Resolution		30 m	
Footprint at 10 km		16 m	
Total weight		450 kg	
Dimension		1.7 × 1.1 × 1.2 m	
Length × Width × Height			

PM: PhotoMultiplier, APD: Avalanche PhotoDiode, OPO: Optical Parametric Oscillator.



MIRA

TX: transmitter
RX: receiver
PC: computer



Emitter and receiver window



WALES

Figure 2.33: MIRA and WALES onboard HALO. The transmitter and receiver system of MIRA is indicated in panels a) and b). Panels a), c) and d) presents the different parts of WALES.

2.3.5 . CRS and CPL

The Cloud Radar System (CRS, Li et al. 2004) and the Cloud Physics Lidar (CPL, McGill et al. 2004) from NASA can be installed onboard the Earth Resources 2 (ER-2) NASA research aircraft, with nadir pointing for both instruments, as indicated in Figure 2.34. The ER-2 typically flies for eight to ten hours, at a speed of 210 m.s^{-1} and at a maximum altitude around 20 km. At these altitudes, the instruments aboard ER-2 operate above 94 % of the atmosphere, and can therefore be used as spaceborne instrument simulators. In addition to the CRS radar, the platform can also include the High-altitude Imaging Wind and Rain Airborne Profiler (HIWRAP) and the ER-2 X-band Doppler Radar (EXRAD), which work at 13.5 GHz (K_u -band), 35 GHz (K_a -band) and 9.6 GHz (X-band) respectively.

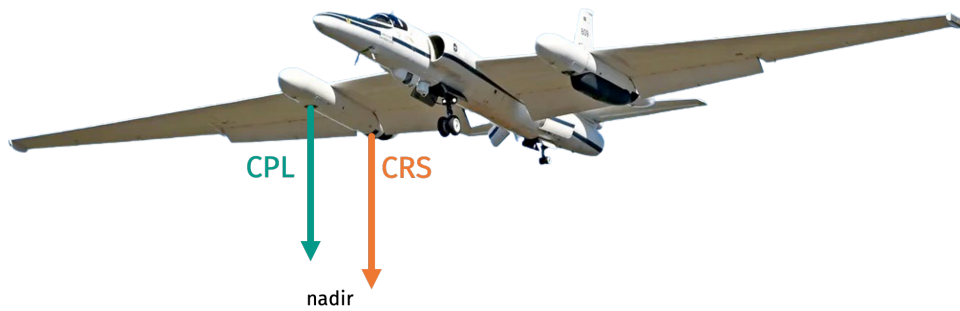


Figure 2.34: CRS and CPL positioning and pointing on ER-2 aircraft.

CRS operates at 94 GHz and provide radar reflectivity and Doppler velocity. These measurements characterize clouds and precipitation, and can be used in synergy with CPL lidar data to retrieve cloud microphysical properties. On the other hand, the CPL works with three wavelengths at 355, 532 and 1064 nm, giving vertical backscatter profiles with a resolution of 30m, making it possible to obtain information on aerosols, dust, ice clouds and liquid water. CRS and CPL specifications are presented in Tables 2.18 and 2.19 respectively.

Table 2.18: CRS specifications.

Parameter	Value
Frequency	94.155 GHz
Peak power	1.7 W
Sensitivity at 10 km range	−29 dBZ
Pulse repetition frequency	0.5 to 20 kHz
Range resolution	115 m
Antenna beamwidth	0.46°

Table 2.19: CPL specifications.

Parameter	Value
Laser type	Solid state Nd:YVO4
Wavelength	355, 532 and 1064 nm
Laser output energy at 355 and 1064 nm	50 µJ
Laser output energy at 532 nm	25 µJ
Laser repetition rate	5 kHz
Telescope diameter	20 cm
Telescope FOV	100 µrad
Range resolution	30 m
Horizontal resolution	200 m (1 s)

2.4 . Conclusion

Observing clouds and determining their optical, dynamic and microphysical properties can be achieved in a variety of ways. *In situ* instruments can be used to obtain detailed information about a cloud specific area, down to crystal images. Meanwhile, remote sensing instruments provide average characteristics of a sampled volume or surface without physical contact.

By using all these tools, clouds can be described on several scales, helping to improve weather and climate models. The observations obtained can be compared with the predictions, enabling possible model biases to be identified.

Radar-lidar synergy combines two active remote sensing instruments, offering cloud vertical profiles. These two instruments can be deployed on airborne and spaceborne platforms, providing wide cloud coverage. Additionally, they observe clouds from above, allowing straightforward detection of the mixed-phase layers present at cloud tops.

Nevertheless, the microphysical properties of clouds are not directly available from these measurements. For this, it is necessary to rely on retrieval algorithms, which use scattering models to relate radar-lidar measurements to the microphysical properties. Furthermore, *in situ* measurements can be used to improve the parameterization of these algorithms, as well as for their validation.

In the following chapter, I explain the inverse problem method used to retrieve the microphysical properties of clouds. In particular, 3.3 describes in detail the method proposed in this thesis to retrieve the properties of clouds composed by ice and/or supercooled water.

3 - Method to retrieve mixed-phase clouds with radar-lidar measurements

Contents

3.1 Ice cloud properties retrieval	100
3.1.1 The inverse problem	100
3.1.2 The VarPy-ice version	105
3.2 Cloud phase classifications	116
3.2.1 DARDAR-MASK v2 classification	116
3.2.2 Adaptations to mixed-phase and supercooled water	121
3.3 The VarPy-mix version	126
3.3.1 Hypothesis to retrieve supercooled water and mixed-phase	127
3.3.2 New state vector configuration	127
3.3.3 Normalized Droplet Size Distribution for liquid Look Up Table	131
3.3.4 Algorithm adaptations to the supercooled water and the mixed-phase retrieval	133
3.4 Conclusion	136

Thanks to radar-lidar synergy, methods to retrieve ice cloud particle microphysical properties have been developed, providing clouds characterization and information for forecast and climate models. Nevertheless, mixed-phase clouds are not well represented in climate and weather forecasting models, due to a lack of the key processes controlling their life cycle, as explained in Chapter 1. Since these clouds play a significant role in the climate, developing methods to study them becomes crucial, despite the complexity of mixed-phase cloud processes and the difficulty of observing two cloud phases simultaneously. In this thesis, we propose a method to retrieve mixed-phase, ice and supercooled water cloud properties from airborne or satellite radar and lidar measurements. In this chapter, I explain this approach based on the VarCloud algorithm initially developed by Delanoë and Hogan 2008, which characterizes clouds consisting solely of ice crystals from radar, lidar and radiometric data. VarCloud principle is presented in the first section. Notably, I detail the latest version I have designed, called VarPy-ice. Since ice and liquid water have distinct physical properties, a classification is required to process them. The second section is devoted to explaining these classifications involved in retrieval algorithms. Finally, the last section focuses on the extension of VarPy-ice to liquid water and the mixed-phase, carried out during this thesis and named VarPy-mix.

3.1 . Ice cloud properties retrieval

Radar-lidar measurements cannot directly provide the cloud microphysical properties. To overcome this limitation, we can formulate it as an inverse problem that can be solved by a Bayesian variational method, as proposed by VarCloud. In this section, I present the inverse problem applied to the ice cloud properties retrieval. The VarPy-ice algorithm is detailed as an example in the second part of this section.

3.1.1 . The inverse problem

An inverse problem is a situation where the causes of a phenomenon are determined from experimental observations of its effects. This can be applied in many scientific fields, notably in atmospheric science. In the case of radar and lidar measurements, the radar reflectivity Z [$\text{mm}^6.\text{m}^{-3}$] and the lidar backscatter β [$\text{m}^{-1}.\text{sr}^{-1}$] are linked to the clouds microphysical vertical structure. For example the water content is strongly correlated with the reflectivity (Atlas 1954) and the lidar backscatter is related to the extinction coefficient α (Section 2.2.2.2, Equation 2.12). Nevertheless, the relationship between the measurement and the microphysical and optical property is not direct. This situation can be associated with an inverse problem expressed by the following equation :

$$Y = f(X) + \varepsilon \quad (3.1)$$

where:

- Y is the observation vector composed of the measured radar reflectivity Z_{obs} and lidar apparent backscatter β_{obs} .
- X is the state vector composed of the variables that describe the system, in our case clouds microphysical properties.
- f is the forward function (Rodgers 2000, p. 14). It corresponds to the radar and lidar forward models, which link the observation vector Y to the state vector X . The radar forward model estimates Z_{fwd} values from the state vector while the lidar estimates β_{fwd} values. This function is usually very complex and non-invertible. This means that X cannot be directly calculated from Y and the inverse forward function f^{-1} via the equation $X = f^{-1}(Y - \varepsilon)$.
- ε is the error vector, representing the models and measurements uncertainties.

For cloud studies, the solution to the inverse problem can be derived from empirical relationships between measurements and cloud properties (e.g. Hogan et al. 2006b), from a statistical approach using neural networks (e.g. Wang et al. 2022) or from a probabilistic method based on the Bayes theorem (e.g. Delanoë and Hogan 2008). The latter is a variational method used in our algorithm and is detailed in the next subsection.

3.1.1.1 The Bayes theorem

The Bayes theorem is defined by the following equation:

$$P(X | Y) = \frac{P(Y | X)P(X)}{P(Y)} \quad (3.2)$$

where:

- $P(X)$ and $P(Y)$ are the Probability Density Functions (PDF) of X and Y , respectively. They are independent and can be considered as defining a probable state volume in a multidimensional space. $P(X)$ expresses the volume in the state space containing the *a priori* (i.e. before the measurement) probable states set centered on X . As a result, $P(X) dX$ expresses the probability of having the state between X and dX . This represents the *a priori* state space.

- $P(Y | X)$ is the conditional probability of Y given X .
- $P(X | Y)$ is the conditional probability of X given Y . This represents the PDF of a state after a measurement is made at $P(X)$ and $P(Y | X)$. $P(X | Y)$ describes the *a posteriori* probable states volume, i.e. after knowing the information provided by the measurement.

If the measurement provides information on the state vector, the *a posteriori* probable state volume is reduced compared to the *a priori* one. The information contained in the measurement space can be used to minimize the *a priori* probable state number contained in the state space. Consequently, the variational method consists in finding the value of X that maximizes $P(X | Y)$, taking into account any *a priori* information we have on the state vector as well as model and observations errors. One approach, detailed in the next subsection, is to calculate a cost function and to minimize its result.

3.1.1.2 Cost function optimization

If we assume that the previous PDF can be represented by a Gaussian distribution, $P(X)$ can be expressed as follows:

$$P(X) = \frac{1}{(2\pi)^{\frac{u}{2}} |B|^{\frac{1}{2}}} e^{-\frac{1}{2}(X-X_a)^T B^{-1}(X-X_a)} \quad (3.3)$$

where:

- u is the state vector dimension.
- X_a is the *a priori* state vector. It defines our knowledge of X before measurement. It has the same dimension as X .
- B is the error covariance matrix of the *a priori*. It represents the uncertainties associated with X_a (explained in 3.1.2). It is a square matrix of the same dimension as X_a .

In the same way, the conditional probabilities $P(Y | X)$ is given by:

$$P(Y | X) = \frac{1}{(2\pi)^{\frac{v}{2}} |R|^{\frac{1}{2}}} e^{-\frac{1}{2}(Y-f(X))^T R^{-1}(Y-f(X))} \quad (3.4)$$

where:

- v is the observation vector dimension.
- $f(X)$ represents the forward model values when applied to X (i.e. Z_{fwd} and β_{fwd}).
- R is the measurement error covariance matrix. It represents the uncertainties associated with Y (explained in 3.1.2). It is a square matrix of the same dimension as Y .

Since $P(Y)$ is an irrelevant physical quantity for inversion problems, it is considered as a scaling factor which is not presented here. Finally, the conditional probability $P(X | Y)$ can be calculated by replacing the terms from Equation 3.2 with Equations 3.3 and 3.4:

$$P(X | Y) = \frac{1}{(2\pi)^{\frac{u+v}{2}} |R|^{\frac{1}{2}} |B|^{\frac{1}{2}}} e^{-\frac{1}{2}((Y-f(X))^T R^{-1} (Y-f(X)) + (X-X_a)^T B^{-1} (X-X_a))} \quad (3.5)$$

In addition, Equation 3.5 can be written according to the covariance matrix of the vector \hat{X} , $S_{\hat{X}}$, which represents the state vector after knowledge of the measurement and corresponds to the state vector best estimate. This is generally referred to as the retrieved state vector. As a result, $P(X)$ can be expressed as follows:

$$P(X | Y) = \frac{1}{(2\pi)^{\frac{u}{2}} |S_{\hat{X}}|^{\frac{1}{2}}} e^{-\frac{1}{2}(X-\hat{X})^T S_{\hat{X}}^{-1} (X-\hat{X})} \quad (3.6)$$

Furthermore, \hat{X} can be determined by minimizing the cost function J defined as follows (Rodgers 2000):

$$2J = (Y - f(X))^T R^{-1} (Y - f(X)) + (X - X_a)^T B^{-1} (X - X_a) \quad (3.7)$$

The cost function can be assimilated to a random variable following a chi-squared (χ^2) distribution and can be minimized under two conditions:

1. The difference $Y - f(X)$ (between the measurement and the forward model value) is small, taking into account a weighting by the measurement error covariance matrix R . This condition means that the state vector enables $f(X)$ to be close enough to the measurement.

2. The difference $X - X_a$ (between the state vector and its *a priori*) is small, weighted by the matrix B . This condition imposes that the retrieved state vector parameters must be part of the *a priori* probable state volume.

Non-linear models require to use an iterative method to minimize the cost function and determine \hat{X} . For example, the Newton method consists in decomposing the cost function J to the second order around the state vector value at iteration i , X_i :

$$2J_X = 2J_{X_i} + \frac{\partial 2J_{X_i}}{\partial X}(X - X_i) + \frac{1}{2} \frac{\partial^2 2J_{X_i}}{\partial^2 X}(X - X_i)^2 \quad (3.8)$$

where:

- J_X is the cost function for the state vector X .
- J_{X_i} is the cost function for the state vector at iteration i , X_i
- $\frac{\partial 2J_{X_i}}{\partial X}$ and $\frac{\partial^2 2J_{X_i}}{\partial^2 X}$ are respectively the first and the second partial derivatives of $2J_{X_i}$ with respect to X .

As a result, the state vector at iteration $i + 1$, X_{i+1} , can be obtained by:

$$X_{i+1} = X_i - \frac{\partial 2J_{X_i}}{\partial X} \frac{\partial^2 2J_{X_i}}{\partial^2 X}^{-1} \quad (3.9)$$

The first and second derivatives of the cost function are given by Equations 3.10 and 3.11, respectively:

$$\frac{\partial 2J_{X_i}}{\partial X} = -K^T R^{-1}(Y - f(X_i)) + B^{-1}(X_i - X_a) \quad (3.10)$$

where K is the matrix containing the partial derivatives of the observations with respect to the state vector parameters. This matrix plays a crucial role in this optimization method, because it represents the sensitivity of each state vector parameter to each observation vector component. It is often called the Jacobian matrix or Kernel.

Furthermore, the second derivative is often called the Hessian matrix, noted H :

$$H = \frac{\partial^2 2J_{X_i}}{\partial^2 X} = K^T R^{-1} K - \frac{\partial K^T}{\partial X} R^{-1}(Y - f(X_i)) + B^{-1} \quad (3.11)$$

where $\frac{\partial K}{\partial X}$ represents the forward model second derivative. It is neglected in the Gauss-Newton method (Rodgers 2000), allowing the cost function second derivative to be described by the following equation:

$$H = K^T R^{-1} K + B^{-1} \quad (3.12)$$

Finally, by replacing Equation 3.9 terms with Equations 3.10 and 3.12, the state vector at iteration $i + 1$ can be defined by:

$$X_{i+1} = X_i + H^{-1}(K^T R^{-1}(Y - f(X_i)) - B^{-1}(X_i - X_a)) \quad (3.13)$$

The computation of X_{i+1} is iterated until convergence is reached, i.e. when J minimum value is found, taking into account the uncertainties associated with the forward models, the measurements and X *a priori*. In this last step, $S_{\hat{X}}$ can be calculated according to the following equation:

$$S_{\hat{X}} = (K^T R^{-1} K + B^{-1})^{-1} \quad (3.14)$$

which corresponds to the inverse of the Hessian matrix, H^{-1} . In this equation, K value is the one corresponding to the iteration chosen as minimizing the cost function.

This optimization method is used by the VarCloud algorithm proposed by Delanoë and Hogan 2008. The next subsection describes the main parameters involved in this algorithm, notably the state vector parameters.

3.1.2 . The VarPy-ice version

The variational method VarCloud aims to retrieve ice clouds properties using radar, lidar and radiometers data. First written in C++, this algorithm has been improved with new parameterization for ice clouds retrievals (Ceccaldi 2014; Cazenave et al. 2019). During this thesis, I improved the algorithm on certain points, notably by writing its latest version in Python 3, offering more flexible parameterization and the ability to be applied to multiple airborne and spaceborne platforms. This version is called VarPy-ice, to distinguish it from the VarPy-mix version (described in 3.3), which additionally retrieves the properties of the mixed-phase and supercooled water clouds.

In this subsection, I describe the main VarPy-ice components. The diagram of Figure 3.1 summarizes the whole structure of the variational scheme.

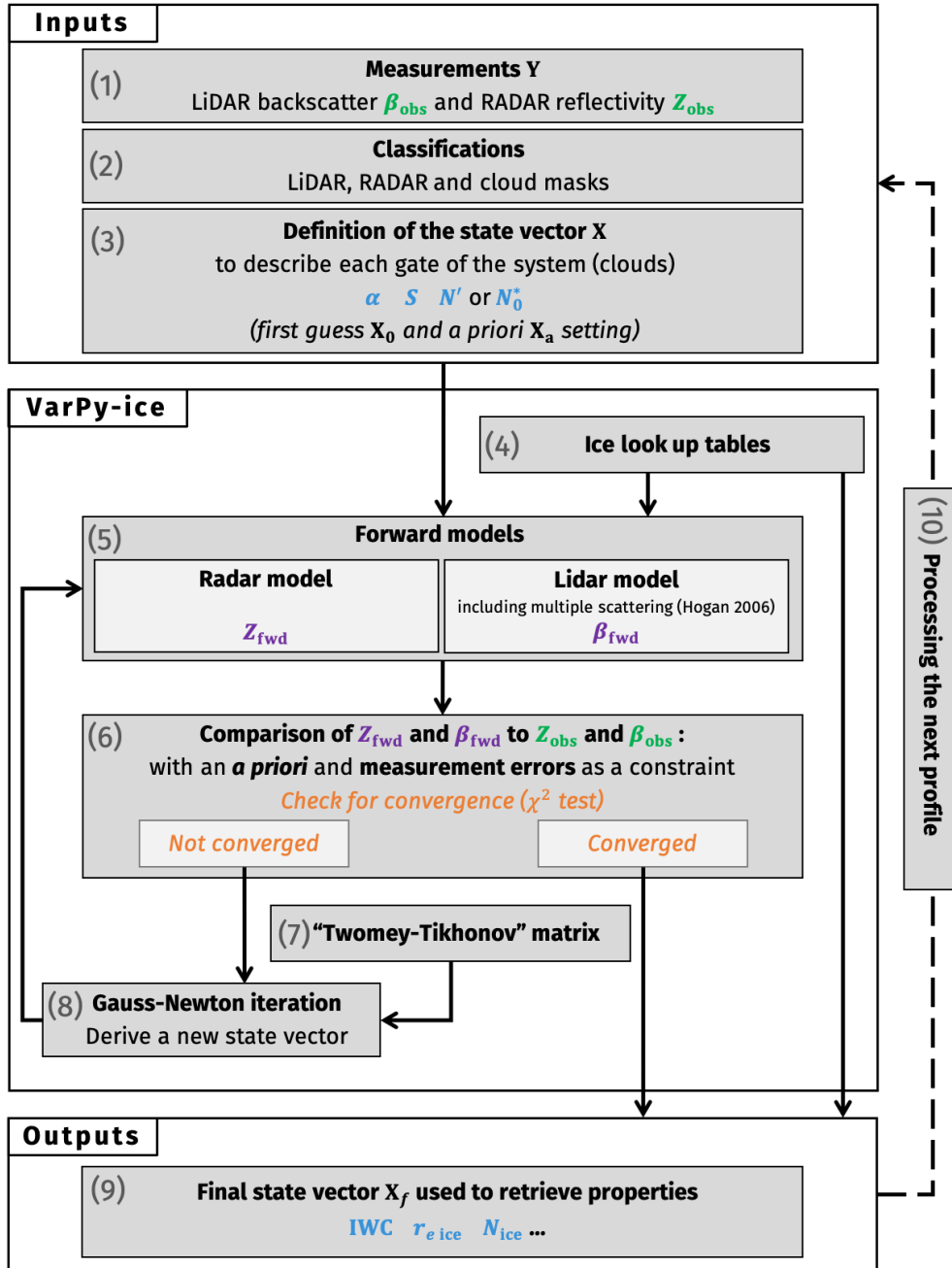


Figure 3.1: VarPy-ice retrieval method scheme.

First, one of VarPy-ice main inputs is the observation vector Y (box 1 of Figure 3.1) composed of the measured radar reflectivity Z_{obs} and the measured lidar backscatter β_{obs} . The natural logarithm is applied to Y variables to avoid the unphysical possibility to retrieve negative values. The vector is defined for one measurement profile and as a function of the distance from the instrument. In addition, radar and lidar do not have the same amount of values per profile (also called hereafter gate): there are q values of $\ln(Z_{\text{obs}})$ for a profile and p values for $\ln(\beta_{\text{obs}})$. As a result, the observation vector Y is defined for a single profile as follows:

$$Y = \begin{pmatrix} \ln(Z_{\text{obs},0}) \\ \vdots \\ \ln(Z_{\text{obs},q}) \\ \ln(\beta_{\text{obs},0}) \\ \vdots \\ \ln(\beta_{\text{obs},p}) \end{pmatrix} \quad (3.15)$$

Secondly, the radar, lidar and cloud phase classifications identified from the measurements are used as input to the algorithm (box 2 of Figure 3.1) to determine the gates to be retrieved. More information on these classifications can be found in 3.2. For VarPy-ice, only gates containing ice (pure or mixed-phase) are retrieved. Nevertheless, two conditions must be considered:

- The lidar signal is more sensitive to water droplets than to ice crystals. Consequently, for mixed-phase clouds, the lidar signal cannot be exploited to retrieve the ice crystal properties.
- The lidar signal is strongly attenuated after a supercooled water layer (pure or mixed-phase), meaning that it cannot retrieve ice clouds below this layer.

Consequently, mixed-phase and ice cloud below supercooled water are not retrieved via radar-lidar synergy but only with the radar signal. For these cases, the retrieval strongly relies on the state vector *a priori* values.

Next, the state vector is initialized with the first guess values, giving X_0 (box 3 of Figure 3.1). Additionally, the *a priori* state vector, X_a , is defined during the same step. Similarly to Y , the natural logarithm is applied to X_0 and X_a variables to avoid negative values and the vectors are defined for one measurement profile and as a function of the distance from the instrument. The state vector is composed of three variables:

- The extinction coefficient α [m^{-1}] (also simply referred to as the extinction). For n measurements gates, the state vector is composed of n values of $\ln(\alpha)$
- The extinction-to-backscatter ratio S [sr], which is the inverse of the normalized phase function value at 180° . It is assumed to be a function of temperature T [$^\circ\text{C}$], adapted from Platt et al. 2002 and derived using radar-lidar data from previous version of DARDAR-CLOUD (Cazenave et al. 2019). Consequently, the lidar ratio S is not represented in the state vector for each gate but by the two coefficients $a_{\ln(S)}$ and $b_{\ln(S)}$ that are the slope and the intercept coefficient from the temperature dependence relationship, given by:

$$\ln(S) = a_{\ln(S)} + b_{\ln(S)} \cdot T \quad (3.16)$$

As a result, the dimension of the lidar ratio S is given by $k = 2$. For VarPy-ice, the lidar ratio values can range from approximately 15 to 60 sr, with an average value of 35 sr, for a temperature range from -60°C to -20°C (Cazenave et al. 2019). The lidar ratio can be determined using HSRL, but this technique is not used in VarPy-ice.

- The number concentration parameter N' , related to the extinction and the normalized number concentration parameter N_0^* [m^{-4}] (cf. Section 1.1.4 Equations 1.11 and 1.13):

$$N' = \frac{N_0^*}{\alpha^\gamma} \quad (3.17)$$

where γ is an empirically determined coefficient normalizing N' (Delanoë and Hogan 2010; Delanoë et al. 2014). Values for this coefficient are shown in Table 3.1. Contrary to α , N' is not retrieved for each gate. A cubic-spline basis function (Hogan 2007) interpolates the N' profile with a number concentration parameter spacing factor κ_N set to 4 to decreases the number of N' values to m . Consequently, the retrieved N' is continuous in itself and until its second derivatives. This approach smooths N' profile and improves computing efficiency by reducing calculation time (Hogan 2007; Delanoë and Hogan 2008). As a result, like α , N' is represented as a function of the distance in the state vector, but with a number of values m less than the number of gates n .

As a result, for VarPy-ice the state vector, X_{ice} , to retrieve a n -gate profile is given by:

$$X_{ice} = \begin{pmatrix} \ln(N'_0) \\ \vdots \\ \ln(N'_m) \\ a_{\ln(S)} \\ b_{\ln(S)} \\ \ln(\alpha_0) \\ \vdots \\ \ln(\alpha_n) \end{pmatrix} \quad (3.18)$$

Once defined, the X and Y vectors are used as input to the radar and lidar forward models. Nevertheless, an intermediate step is required, since the forward models calculate the partial derivatives with respect to each variable entire profile. For this, a conversion matrix C multiplies the state vector to obtain n values for each variable α , S and N' . This matrix is $(m + k + n) \times (3 \times n)$ dimension and is as follows:

$$C = \begin{pmatrix} Y_{(0,0)} & \dots & Y_{(0,m)} & 0 & 0 & 0 & \dots & 0 \\ \vdots & \ddots & \vdots & \vdots & \vdots & \vdots & \ddots & \vdots \\ Y_{(n,0)} & \dots & Y_{(n,m)} & 0 & 0 & 0 & \dots & 0 \\ 0 & \dots & 0 & 1 & T_0 & 0 & \dots & 0 \\ \vdots & \ddots & \vdots & \vdots & \vdots & \vdots & \ddots & \vdots \\ 0 & \dots & 0 & 1 & T_p & 0 & \dots & 0 \\ 0 & \dots & 0 & 0 & 0 & 1 & \dots & 0 \\ \vdots & \ddots & \vdots & \vdots & \vdots & \vdots & \ddots & \vdots \\ 0 & \dots & 0 & 0 & 0 & 0 & \dots & 1 \end{pmatrix} \quad (3.19)$$

where:

- $Y_{(i,j)}$ are the values derived from the cubic-spline basis function. These $(n \times m)$ elements (highlighted in blue) correspond to N' . This provides a value of N' for each gate.
- The two columns at $m + 1$ and $m + 2$ (highlighted in green) consist of ones and temperature values T , corresponding to the lidar ratio S . The first column is multiplied by $a_{\ln(S)}$ and the second by $b_{\ln(S)}$, resulting in the lidar ratio according to Equation 3.16.
- The terms highlighted in yellow represent an n -dimensional identity matrix corresponding to the extinction. This means that the matrix C has no effect on the α elements of the state vector.

Once the C matrix is applied to the state vector, the forward models (box 5 of Figure 3.1) are finally utilized to compute $\ln(Z_{\text{fwd}})$ and $\ln(\beta_{\text{fwd}})$ values, as well as the Jacobian K defined by:

$$K = \begin{pmatrix} \frac{\partial \beta_0}{\partial N'_0} & \dots & \frac{\partial \beta_0}{\partial N'_m} & \frac{\partial \beta_0}{\partial a_{\ln(S)}} & \frac{\partial \beta_0}{\partial b_{\ln(S)}} & \frac{\partial \beta_0}{\partial \alpha_0} & \dots & \frac{\partial \beta_0}{\partial \alpha_n} \\ \vdots & \ddots & \vdots & \vdots & \vdots & \vdots & \ddots & \vdots \\ \frac{\partial \beta_p}{\partial N'_0} & \dots & \frac{\partial \beta_p}{\partial N'_m} & \frac{\partial \beta_p}{\partial a_{\ln(S)}} & \frac{\partial \beta_p}{\partial b_{\ln(S)}} & \frac{\partial \beta_p}{\partial \alpha_0} & \dots & \frac{\partial \beta_p}{\partial \alpha_n} \\ \frac{\partial Z_0}{\partial N'_0} & \dots & \frac{\partial Z_0}{\partial N'_m} & \frac{\partial Z_0}{\partial a_{\ln(S)}} & \frac{\partial Z_0}{\partial b_{\ln(S)}} & \frac{\partial Z_0}{\partial \alpha_0} & \dots & \frac{\partial Z_0}{\partial \alpha_n} \\ \vdots & \ddots & \vdots & \vdots & \vdots & \vdots & \ddots & \vdots \\ \frac{\partial Z_q}{\partial N'_0} & \dots & \frac{\partial Z_q}{\partial N'_m} & \frac{\partial Z_q}{\partial a_{\ln(S)}} & \frac{\partial Z_q}{\partial b_{\ln(S)}} & \frac{\partial Z_q}{\partial \alpha_0} & \dots & \frac{\partial Z_q}{\partial \alpha_n} \end{pmatrix} \quad (3.20)$$

For better readability, the indices $_{\text{fwd}}$ of Z and β are not displayed and the natural logarithm of Z , β , N_0^* and α are not written. The Jacobian is $(p + q) \times (m + k + n)$ -dimensional and consists of:

- The β Jacobian, K_β , given by the lidar forward model (p first lines in K , highlighted in teal).
- The Z Jacobian, K_Z , given by the radar forward model (q last lines in K , highlighted in orange).

To obtain $\ln(\beta_{\text{fwd}})$, K_β , $\ln(Z_{\text{fwd}})$ and K_Z , the forward models use the ratio $\frac{\alpha}{N_0^*}$ derived from the state vector. This ratio is linked via an one-dimensional Look Up Table (LUT, box 4 of Figure 3.1) to the reflectivity Z for the radar forward model and the equivalent area radius r_a [m] for the lidar forward model. r_a corresponds to the radius of a sphere with the same cross-sectional area as the entire size distribution mean area and is an input to Multiscatter code from Hogan 2006 (box 5 of Figure 3.1) to compute $\ln(\beta_{\text{fwd}})$ and K_β . Two LUTs can be used to retrieve the ice cloud properties:

- The “Heymsfield Composite” (HC) LUT uses the Transition Matrix Method (T-matrix) and the mass-size relationship from Heymsfield et al. 2010.
- The “Brown and Francis modified” (BF) LUT is based on a combination of Brown and Francis 1995 and Mitchell 1996 mass-size relationships.

Delanoë et al. 2014 and Cazenave 2019 provide further information on these LUTs, which are used to retrieve DARDAR v3.00 (BF, Delanoë 2023a) and v3.10 (HC, Delanoë 2023b) products.

In addition, the LUT setting involves defining the state vector *a priori* and first guess values. The *a priori* values are important for regions where only one instrument is available and this constrains the scheme towards temperature dependent empirical relationships. In VarPy-ice, *a priori* and first guess values are equal. We have postulated previously that the lidar ratio is given by a temperature-dependent relationship (Equation 3.16). $a_{\ln(S)}$ and $b_{\ln(S)}$ *a priori* and first guess values are listed in Table 3.1. For the number concentration parameter $\ln(N')$, the *a priori* and first guess values are given as a function of the temperature T [°C] (Delanoë and Hogan 2008):

$$\ln(N') = a_{\ln(N')} + b_{\ln(N')} \cdot T \quad (3.21)$$

Table 3.1 lists the values of $a_{\ln(N')}$ and $b_{\ln(N')}$ used for each mass-size relationship (BF and HC). The coefficient γ linking N_0^* to α and N' differs according to the mass-size relationship and the values are also given in Table 3.1. For the extinction, the *a priori* and first guess are constant values.

Table 3.1: *A priori* and first guess values for each variable of the state vector in VarPy-ice. (BF: Brown and Francis modified LUT, HC: Heymsfield Composite LUT).

Variable	Values	
	BF	HC
$a_{\ln(N')}$	22.234435	21.94
$b_{\ln(N')}$	-0.090736	-0.095
γ	0.61	0.67
$a_{\ln(S)}$	3.18	3.18
$b_{\ln(S)}$	-0.0086	-0.0086
$\ln(\alpha)$	-7	-7

Regarding the Multiscatter code implied in the lidar forward model, it involves numerous calculations and considerably slows down profile retrieval times. This is mainly due to the interface between the Multiscatter code written in C and VarPy written in Python. At the beginning of this thesis, I modified the data transfer between Multiscatter and VarPy. Instead of retrieving values one by one, we now retrieve whole vectors, as indicated in Figure 3.2. This approach considerably speeds up profile processing (execution time is reduced by a factor 2).

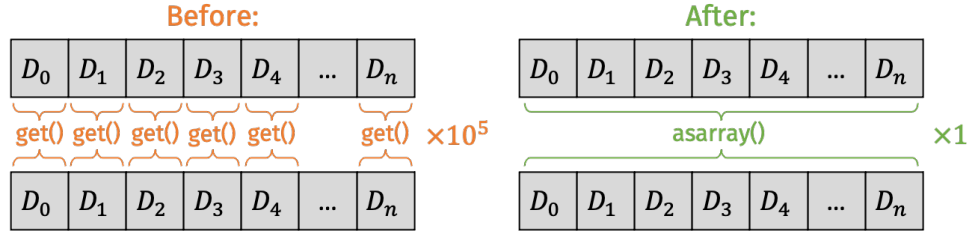


Figure 3.2: Correction implemented in the interface with the Multiscatter code. The figure on the left (orange) shows the way to get the data from the Multiscatter code before the correction, and the figure on the right (green) indicates the new procedure.

Next, calculating the cost function requires to compute the measurement error covariance matrix R . This matrix represents instrumental and forward model errors. It is an v -dimensional diagonal square matrix, meaning that the errors are not spatially correlated and is composed of the standard deviation σ_Y^2 associated with each instrument, giving:

$$R = \begin{pmatrix} \sigma_{Z,0}^2 & 0 & \dots & \dots & \dots & 0 \\ 0 & \ddots & \ddots & \ddots & \ddots & \vdots \\ \vdots & \ddots & \sigma_{Z,q}^2 & 0 & \ddots & \vdots \\ \vdots & \ddots & 0 & \sigma_{\beta,0}^2 & \ddots & \vdots \\ \vdots & \ddots & \ddots & \ddots & \ddots & 0 \\ 0 & \dots & \dots & \dots & 0 & \sigma_{\beta,p}^2 \end{pmatrix} \quad (3.22)$$

For the lidar backscatter, the variance σ_β is given by:

$$\sigma_\beta = \sqrt{\left(\frac{\sigma_{\text{lidar}}}{\beta_{\text{obs}}}\right)^2 + \sigma_{\beta,\text{fwd}}^2} \quad (3.23)$$

where:

- σ_{lidar} is the lidar instrumental error, generally provided with the measurements and varies along the profile. During this thesis, I introduced an option to add a default value, constant along the profile, particularly relevant when the dataset does not provide information regarding σ_{lidar} . In addition, the code has been improved, as it was noticed that with some datasets, the σ_β vector could contain default values that could affect the retrieval (e.g. -999). In these particular cases, an interpolation function has been implemented to smooth the σ_β profile and thus avoid using these values for retrieval.
- $\sigma_{\beta,\text{fwd}}$ is the lidar forward model error, set to 0.5 (Delanoë and Hogan 2008).

For the radar reflectivity, the variance σ_Z is expressed as follows:

$$\sigma_Z = \sqrt{\ln(10^{0,1 \times \sigma_{\text{radar}}})^2 + \ln(10^{0,1 \times \sigma_{Z_{\text{fwd}}}})^2} \quad (3.24)$$

where:

- σ_{radar} is the radar instrumental error, generally provided with the measurements and varies along the profile. If the errors are not available, the default and constant value for the entire profile is 1 dBZ.
- $\sigma_{Z_{\text{fwd}}}$ is the radar forward model error, set to 1 dBZ (Delanoë and Hogan 2008).

Additionally, the cost function computation required the *a priori* error covariance matrix B . Generally, radar and lidar signals do not both cover simultaneously the entire vertical cloud profile. In many ice clouds cases, lidar in downward direction first detects the cloud top, while radar only detects thicker cloud regions down to the ground. The lidar signal does not detect the cloud lower layers if it gets strongly attenuated or extinguished. To ensure that the results tend towards physical values in regions where a single instrument is available, state vector *a priori* parameterization and errors are used. The *a priori* errors are defined by the *a priori* error covariance matrix B and express how strong is the constrain of the *a priori*. This matrix is composed of the state vector *a priori* error variances σ_X^2 and is diagonal in the simplest case where no information propagates between gates.

To overcome the limitation of single instrument retrieval, the matrix B can be used to spread information in range. Additional off-diagonal elements can be added to propagate information from synergistic regions to single instrument ones. In VarPy-ice, the B off-diagonal terms corresponding to N' are given by Equation 3.25 (Hogan 2007; Delanoë and Hogan 2008):

$$B_{i,j} = B_{i,i} \times e^{-\frac{|z_j - z_i|}{z_0}} \quad (3.25)$$

where:

- z_i and z_j are the centered heights at which the two functions whose correlations are calculated.
- z_0 is the decorrelation distance, a parameter set to 600 m for VarPy-ice (initially set to 1 km for VarCloud first version). This value is set for CloudSat-CALIPSO and can be adapted to the resolution of the data used.

As a result, the matrix B is composed of diagonal terms for each state vector variable and additional non-diagonal terms for N' , resulting in:

$$B = \begin{pmatrix} \sigma_{\ln(N'),(0,0)}^2 & \dots & \sigma_{\ln(N'),(0,m)}^2 & 0 & 0 & 0 & \dots & 0 \\ \vdots & \ddots & \vdots & \vdots & \vdots & \vdots & \ddots & \vdots \\ \sigma_{\ln(N'),(m,0)}^2 & \dots & \sigma_{\ln(N'),(m,m)}^2 & 0 & 0 & 0 & \dots & 0 \\ 0 & \dots & 0 & \sigma_{a_{\ln(S)}}^2 & 0 & 0 & \dots & 0 \\ 0 & \dots & 0 & 0 & \sigma_{b_{\ln(S)}}^2 & 0 & \dots & 0 \\ 0 & \dots & 0 & 0 & 0 & \sigma_{\ln(\alpha),0}^2 & \dots & 0 \\ \vdots & \ddots & \vdots & \vdots & \vdots & \vdots & \ddots & \vdots \\ 0 & \dots & 0 & 0 & 0 & 0 & \dots & \sigma_{\ln(\alpha),n}^2 \end{pmatrix} \quad (3.26)$$

The *a priori* error variances values are listed in Table 3.2 and are assumed to be constant with height.

Table 3.2: *A priori* error variances used in VarPy-ice for the *a priori* error covariance matrix B

Variable	Value
$\sigma_{\ln(N')}$	1
$\sigma_{a_{\ln(S)}}$	0.1
$\sigma_{b_{\ln(S)}}$	0.0001
$\sigma_{\ln(\alpha)}$	5

The last step before cost function calculation is to smooth the extinction profile. In fact, each measurement is limited by the instrument performance and the signal-to-noise ratio. This is notably the case for the lidar and this can affect the extinction retrieval (Hogan et al. 2006a). To limit the impact of measurement noise, a “Twomey-Tikhonov” matrix T (box 7 of Figure 3.1) is used to penalize the extinction profile second derivative. Since we only want to smooth the extinction profile, the T values corresponding to the lidar ratio S and the number concentration parameter N' are set to 0. As a result, T is a $(m + k + n)$ dimension square matrix composed of a “Twomey-Tikhonov” matrix at indices $m + k + 1$ to $m + k + n$ corresponding to the extinction α and noted T_α . For $n = 6$, T_α is defined by:

$$T_\alpha = \kappa \times \begin{pmatrix} 1 & -2 & 1 & 0 & 0 & 0 \\ -2 & 5 & -4 & 1 & 0 & 0 \\ 1 & -4 & 6 & -4 & 1 & 0 \\ 0 & 1 & -4 & 6 & -4 & 1 \\ 0 & 0 & 1 & -4 & 5 & -2 \\ 0 & 0 & 0 & 1 & -2 & 1 \end{pmatrix} \quad (3.27)$$

where κ is a coefficient setting the smoothness degree of T . Its value was arbitrarily set to 100.

At each iteration, the matrix T is applied to the state vector in the cost function calculation (box 6 of Figure 3.1) to smooth α profile. Consequently, the cost function expressed by Equation 3.7 is modified and becomes:

$$2J = (Y - f(X))^T R^{-1} (Y - f(X)) + (X - X_a)^T B^{-1} (X - X_a) + X^T T X \quad (3.28)$$

As a result, the state vector update at the next iteration $i + 1$ (box 8 of Figure 3.1) is given by:

$$X_{i+1} = X_i + H^{-1} (K^T R^{-1} (Y - f(X_i)) - B^{-1} (X_i - X_a) - T X_i) \quad (3.29)$$

The state vector is updated at iteration $i + 1$ until convergence is achieved. A chi-square (χ^2) test is performed to determine the convergence status. It estimates, at each iteration i , whether the forward model outputs are close to the observations by the following expression:

$$\chi_i^2 = \sum_j^v \frac{(Y_j - f(X_i)_j)^2}{R_{j,j}} \quad (3.30)$$

where:

- \sum_j^v sums the matrix elements.
- $R_{j,j}$ are the diagonal elements of R , i.e. σ_β^2 and σ_Z^2 .

Consequently, convergence is achieved when the following condition is reached (Cazenave 2019):

$$\exists i_{\text{test}} \in \mathbb{I}, \forall i \in [i_{\text{test}}, i_{\text{test}} + 6], \chi_{i_{\text{test}}}^2 - \chi_{i_{\text{test}}+1}^2 < 0.01 \quad (3.31)$$

where \mathbb{I} is the possible iteration set, i.e. integers from 0 to 20. This means that χ_i^2 reaches a plateau.

Finally, the state vector X_f selected to retrieve the microphysical properties (box 9 of Figure 3.1) is determined by the χ^2 test with the lowest value, χ_{\min}^2 . The ratio $\frac{\alpha_f}{N_{0,f}^*}$ calculated with the X_f values are related to the $\frac{IWC}{N_0^*}$, $\frac{N_{\text{ice}}}{N_0^*}$ and r_e values in the chosen LUT. These ratios finally determine the values of IWC , N_{ice} and r_e .

3.2 . Cloud phase classifications

As explained in the previous chapter, radar and lidar detect cloud particles, as well as aerosols (for lidar) and precipitation (for radar). Consequently, the particles detected by the instruments must be identified to ensure that only those to be retrieved by the algorithm are processed (i.e. ice crystals for VarPy-ice). For this, a hydrometeor classification is established for each instrument according to the sensitivity of each instrument. Typically, the lidar classification distinguishes aerosols and cloud phases, while the radar classification identifies precipitations and clouds. Additionally, combining the lidar and the radar classifications results in a more detailed merged classification, called hereafter the radar-lidar classification, which is an important input to the algorithm (box 2 of Figure 3.1) and more significantly regarding the mixed-phase in VarPy-mix.

Each radar-lidar platform has its own classifications, based on the instruments intrinsic characteristics. In this section, I focus solely on DARDAR-MASK v2 (Delanoë and Hogan 2010; Ceccaldi et al. 2013), the classification developed for CloudSat and CALIPSO, to present the three classifications (radar, lidar and radar-lidar) required for the algorithm. Nevertheless, in some cases, supercooled water and especially the mixed-phase can be incorrectly identified by DARDAR-MASK, leading to misclassifications. In this thesis, I have improved the algorithm input classifications to enable better identification of the hydrometeors to be retrieved and to better adapt the classifications to the algorithm. The second subsection describes the modifications that have been applied to improve the mixed-phase and supercooled water cloud property retrieval.

3.2.1 . DARDAR-MASK v2 classification

DARDAR (raDAR/liDAR) project originates from the collaboration between LATMOS and the Cloud Group of the Meteorology Department at the University of Reading. It aims to retrieve ice cloud microphysical properties from CloudSat and CALIPSO measurements. The three DARDAR components are:

- CS-TRACK (CloudSat-Track) product: CloudSat and CALIPSO collocated measurements. Horizontal (along track) and range resolution are 1.7 km and 60 m respectively. Additionally, MODIS, IIR and ECMWF (European Centre for Medium-Range Weather Forecasts) data are include in this product.
- DARDAR-MASK product: CloudSat and CALIPSO classifications and the radar-lidar classification realized by combining the 2B-GEOPROF CloudSat radar mask, the CALIPSO vertical lidar feature mask CAL-LID-L2-VFM

and CALIPSO L1 measurements with a multi-threshold decision tree (Ceccaldi et al. 2013).

- DARDAR-CLOUD: ice cloud retrieval from CloudSat and CALIPSO measurements and classifications (Delanoë et al. 2014; Cazenave et al. 2019). Two versions are currently available, v3.00 (Delanoë 2023a) and v3.10 (Delanoë 2023b), respectively applying BF and HC LUT.

In addition, the DARDAR-Nice product (Sourdeval et al. 2018) can be included as a supplement to DARDAR-CLOUD. It retrieves the ice concentration of clouds with an IWC higher than 10^{-8} kg.m⁻³. All these products are publicly available to any ICARE website user at <https://www.icare.univ-lille.fr/>.

In this section, I present a general overview on the three DARDAR-MASK classifications (CloudSat, CALIPSO and radar-lidar) applied in VarPy. More information on the identification of target particles can be found in Delanoë and Hogan 2010 and Ceccaldi et al. 2013.

First, the two main steps required to obtain the radar and the lidar classifications are:

1. Identification and separation between pixels (or gates) corresponding to noise, clear sky and particles (e.g. aerosols, cloud particles and precipitation).
2. Particle nature identification: the radar classification detects and distinguishes cloud particles from precipitation, while the lidar detects and discriminates cloud particles and aerosols.

Once the radar and the lidar classifications have been obtained, they can be combined to produce a more complete and detailed radar-lidar classification. Figure 3.3 presents an example with a precipitating cloud and an aerosol layer. First, we focus on box 1 on panels a) and b), which present lidar backscatter and radar reflectivity measurements, respectively. On the one hand, in this area, radar reflectivity is very high, extending right down to the ground. In addition, we can discern the bright band (indicated by the blue dotted box), which indicates the melting layer formed by ice particles becoming precipitation. However, at 95 GHz, the bright band can be difficult to distinguish. In this case (e.g. for DARDAR-MASK), the melting zone is identified by the wet bulb temperature provided by the ECMWF model (1 K uncertainty), which is the lowest temperature that can be reached by the evaporation of the water contained in the air at constant pressure. Under the melting layer, the gates

are consequently classified as rain. This is termed “cold rain” (panel d)) since the radar reflectivity is higher than -17 dBZ, the temperature is above 0°C and the rain originates from an ice cloud (Ceccaldi et al. 2013). Similarly, “warm” rain follows the same conditions, but does not originate from an ice cloud. On the other hand, there is no lidar backscatter signal in this area, since the lidar signal is fully attenuated by the ice cloud above the rain zone. In any case, the lidar wavelength is not appropriate to detect raindrops.

Nevertheless, lidar is able to detect small particles, such as aerosols. Box 2 on panels a) and b) indicates that there is no radar signal in this area, meaning that the radar detects no particles, while the lidar signal distinguishes small particles. These are aerosols, as represented by panel c). By combining the two classifications, the two zones (box 1 and 2) are indexed in a single classification.

Next, when we analyze the measurements (panels a) and b)), we observe the behavior described in Section 2.2.3 regarding instrument sensitivity to ice cloud particles:

- Optically thin clouds (box A): the lidar detects these clouds while the radar is unable to detect these small particles.
- Deeper inside clouds (box B): the lidar signal is attenuated or extinguished when the cloud is optically too thick, while the radar signal is strong for these particles.

For each radar and lidar classification, the “cloud” class indicates cloud particle detection by the instrument (panels c) and d)). These two classifications are then combined to produce the DARDAR-MASK radar-lidar classification (panel e). In the example presented in Figure 3.3, clouds A and B are merged to form a single ice cloud represented by box C. In other cases, the cloud phase (warm liquid, supercooled water or ice) can be determined by combining radar and lidar classifications, measurements and additional information like the wet bulb temperature. An example is presented in Figure 3.4 and described in the next paragraph.

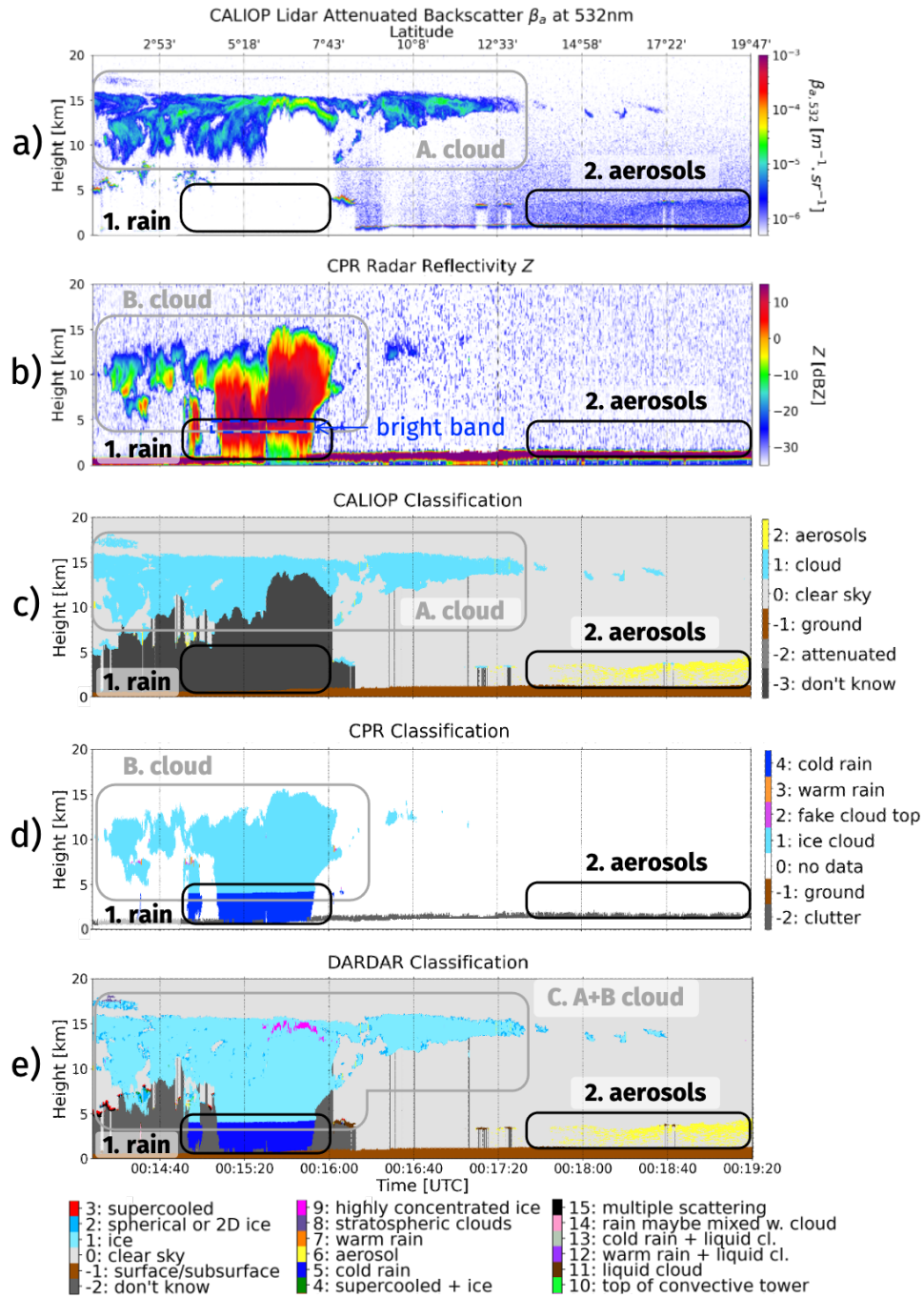


Figure 3.3: CALIOP lidar attenuated backscatter at 532 nm a), CPR radar reflectivity at 95 GHz b), CALIOP classification c), CPR classification d) and DARDAR-MASK classification e) on 11th April 2009. Black boxes indicate rain or aerosol areas. The radar bright band is indicated by the blue dotted box. All panels share the same abscissa axes (time and latitude). Data from DARDAR-MASK V2.23 products, <https://www.icare.univ-lille.fr/>, orbit ID: 2009101001352_15708

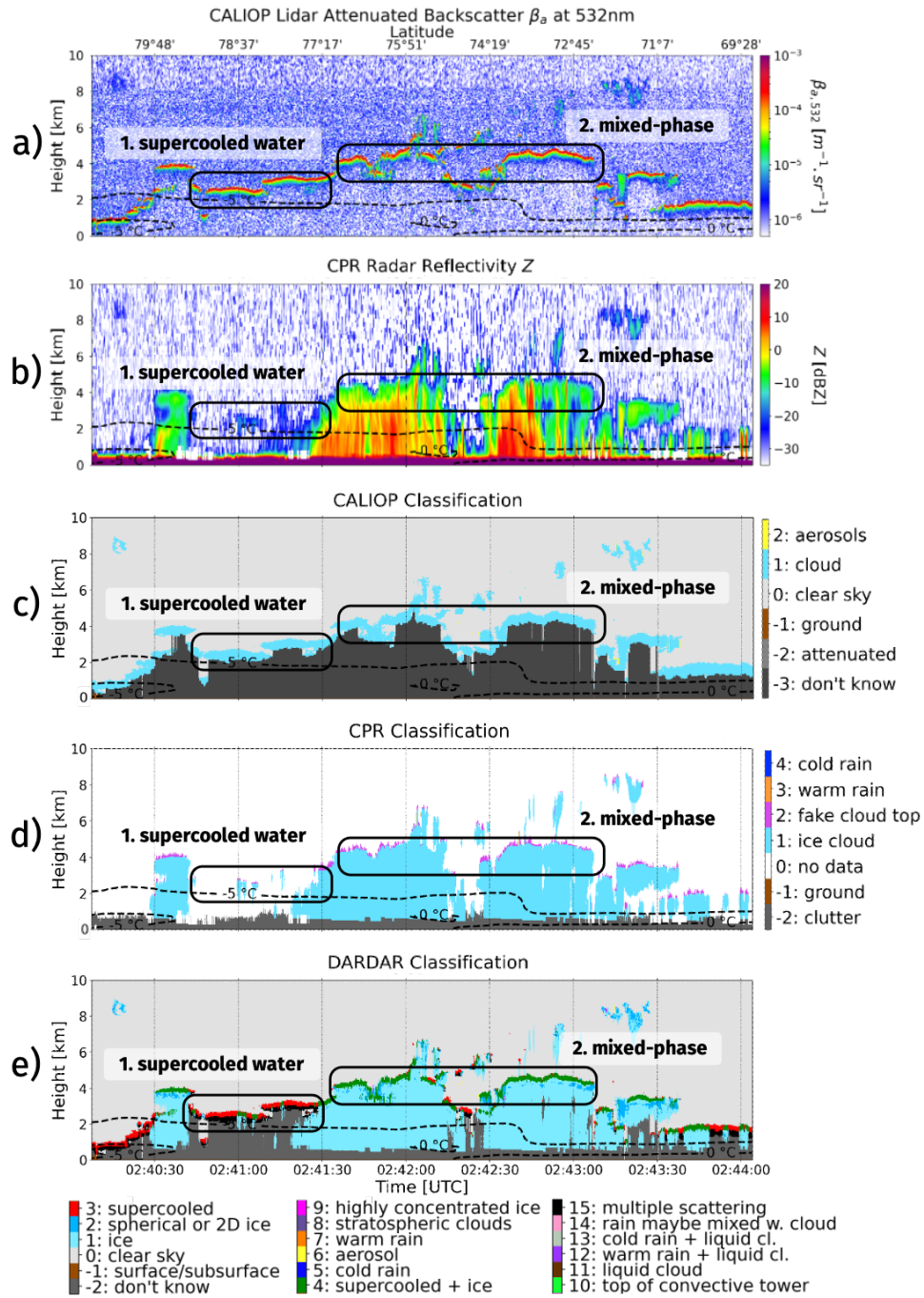


Figure 3.4: CALIOP lidar attenuated backscatter at 532 nm a), CPR radar reflectivity at 95 GHz b), CALIOP classification c), CPR classification d) and DARDAR-MASK classification e) on 14th May 2019. Black boxes indicate supercooled or mixed-phase area examples. Isotherms at 0 and -5°C are displayed in black dotted lines. All panels share the same abscissa axes (time and latitude). Data from DARDAR-MASK V2.23 products, <https://www.icare.univ-lille.fr/>, orbit ID: 2019134012452_69470

First, we notice that the lidar backscatter measurements (panel a)) in Figure 3.4 are very different from those in Figure 3.3. Backscatter values are higher ($> 2 \times 10^{-5} \text{ m}^{-1}.\text{sr}^{-1}$) and then decrease significantly with height, revealing narrow cloud layers (panel c)) in Figure 3.4). Regarding the radar measurements (panel b)), the reflectivity indicates several ice clouds between 1 and 8 km (panel d)). Focusing on the area indicated by box 1, we observe that the cloud detected by the lidar is not detected by the radar. By combining radar and lidar classifications with the backscatter ($> 2 \times 10^{-5} \text{ m}^{-1}.\text{sr}^{-1}$) and the wet bulb temperature ($> 0 \text{ }^{\circ}\text{C}$) values, this area (box 1) can be identified as supercooled water, since particles are too small to be detected by the radar.

Second, in the box 2 area, both instruments detect cloud particles (panels c) and d)). Nevertheless, the backscatter values ($> 2 \times 10^{-5} \text{ m}^{-1}.\text{sr}^{-1}$) indicate supercooled water (negative temperatures) and the radar signal reveals ice crystals. Consequently, this area consists of supercooled water and ice crystals (mixed-phase). In conclusion, radar-lidar classification (panel e)) identifies supercooled water and mixed-phase clouds for boxes 1 and 2 respectively.

Finally, eighteen classes are identified with DARDAR-MASK v2.23, which are listed in Table 3.3. Nevertheless, only classes corresponding to ice crystals are processed by VarPy-ice, which are currently: the “ice cloud”, the “spherical or 2D ice”, the “supercooled water and ice”, the “highly concentrated ice crystals” and the “top of the convective tower” classes. These classes form a single group to be processed. However, the classification must be adapted and improved to handle supercooled water and mixed-phase, as described in the following subsection.

3.2.2 . Adaptations to mixed-phase and supercooled water

To include supercooled water microphysical property retrieval (pure or in mixed-phase), we need to identify supercooled water with the radar-lidar classification. In DARDAR-MASK, two classes correspond to the identification of supercooled water: the “supercooled water” and the “multiple scattering due to supercooled water” classes. Consequently, I have appended these two classes as input to the VarPy-mix algorithm. However, since supercooled water microphysical properties differ from those of ice and require specific processing, I have introduced the “liquid” group composed of the “supercooled water”, the “multiple scattering due to supercooled water” and the “supercooled water and ice” classes. As a result, “supercooled water and ice” (mixed-phase) now belongs to both groups, since it represents the coexistence of supercooled water droplets and ice crystals. Table 3.4 lists the “ice” and “liquid” group composition.

Table 3.3: DARDAR-MASK v2.23 classes.

Number	Class
-2	Presence of liquid unknown
-1	Surface and subsurface
0	Clear sky
1	Ice clouds
2	Spherical or 2D ice
3	Supercooled water
4	Supercooled water and ice
5	Cold rain
6	Aerosol
7	Warm rain
8	Stratospheric clouds
9	Highly concentrated ice crystals
10	Top of convective towers
11	Liquid clouds
12	Warm rain and liquid clouds
13	Cold rain and liquid clouds
14	Rain maybe mixed with liquid
15	Multiple scattering due to supercooled water (lidar)

In the current versions of VarPy-ice and VarPy-mix, an intermediate classification is created based on these groups and consists of four classes:

- 0: “unprocessed”: it indicates the gates that are not processed by the algorithm.
- 1: “ice”: it corresponds to the “ice” group.
- 2: “supercooled water”: it corresponds to the “liquid” group.
- 3: “mixed-phase”: it corresponds to the “supercooled water and ice” class.

This intermediate classification is flexible and easily adapts to classifications other than DARDAR-MASK.

Nonetheless, before producing this intermediate classification, it is important to correct misclassifications in order to improve the microphysical properties retrieval. The first step is to avoid isolated nonphysical gates that can lead to artifacts in the retrieval. A method has been implemented to erode isolated supercooled water and mixed-phase gates. For supercooled water and multiple scattering classes, the gates are replaced by clear sky in the radar-lidar classification and the same correction is made for the lidar classification. On the other hand, for the mixed-phase, only the radar-lidar classification is modified and the gates are replaced by ice gates.

Table 3.4: Cloud phases processed by VarPy-ice and VarPy-mix. Single group for VarPy-ice and two groups (ice and liquid) for VarPy-mix.

Number	Class	VarPy-ice	VarPy-mix	
			Group "ice"	Group "liquid"
1	Ice clouds	✓	✓	
2	Spherical or 2D ice	✓	✓	
3	Supercooled water			✓
4	Supercooled water and ice	✓	✓	✓
9	Highly concentrated ice crystals	✓	✓	
10	Top of convective towers	✓	✓	
15	Multiple scattering due to supercooled water			✓

Afterwards, the next step is to correct some mixed-phase misclassifications. Indeed, a strong lidar backscatter signal ($\beta_{532} > 2 \times 10^{-5} \text{ m}^{-1}.\text{sr}^{-1}$; Delanoë and Hogan 2010) can be a detection of warm water, top of convective tower, highly concentrated ice crystals or supercooled water. For DARDAR-MASK, a decision tree is used to classify mixed-phase and to differentiate it from highly concentrated crystals, based on the wet bulb temperature (Ceccaldi et al. 2013). This decision tree is detailed in Figure 3.5. We note that a cloud layer thickness higher than 300 m and/or a temperature below -40°C indicates highly concentrated ice crystals. However, if the temperature is higher than -40°C with a layer thickness < 300 m, the lidar signal reveals the presence of supercooled water and if the radar detects ice, this corresponds to mixed-phase. In some cases, highly concentrated crystals areas are incorrectly classified as mixed-phase and need to be corrected for VarPy-ice and VarPy-mix. Consequently, these gates are replaced by highly concentrated ice crystals in the radar-lidar classification.

In addition, a final modification has been added to the DARDAR-MASK classification. Regarding supercooled water layers, we noticed that the thickness of these layers in the classification do not match the layer thickness on the backscatter measurements. To correct this, I have extended the mixed-phase layer by replacing gates classified as "ice" by "mixed-phase" gates in the radar-lidar classification (and by extension the intermediate classification). In comparison with pure supercooled water clouds, this corresponds to the "multiple backscatter due to supercooled water" class. In the current version, the added gates number is fixed at 4.

To illustrate these various modifications to the radar-lidar classification, I present an example in Figure 3.6. Panels a) and b) show lidar backscatter

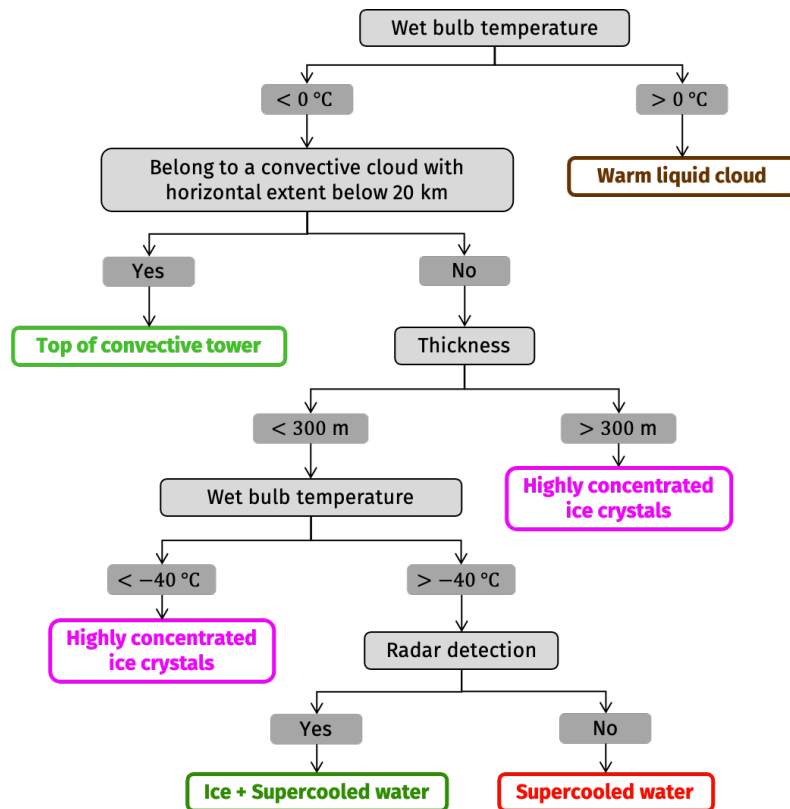


Figure 3.5: DARDAR-MASK decision tree to classify layers with a strong lidar backscatter signal (from Ceccaldi et al. 2013).

and radar reflectivity measurements, which indicate several layers of supercooled water or mixed-phase, as well as precipitating ice clouds. Next, panel c) presents the radar-lidar classification provided by DARDAR-MASK. Red boxes indicate areas where isolated supercooled water pixels are present and need to be corrected. Panel d) shows the intermediate classification when no correction is applied, and panel e) when the isolated supercooled water pixels are replaced by clear sky. Meanwhile, the same is applied to the green boxes on panels c) to e), which identify areas of mixed-phase that have been replaced by (highly concentrated) ice crystals. Furthermore, the mixed-phase layers are thicker in panel e) than in panel d).

The extended and corrected radar-lidar classification is one of the VarPy-mix inputs. This new version of the algorithm improves, corrects and, above all, extends the retrieval to supercooled water (pure or mixed-phase). I describe these improvements in the next section.

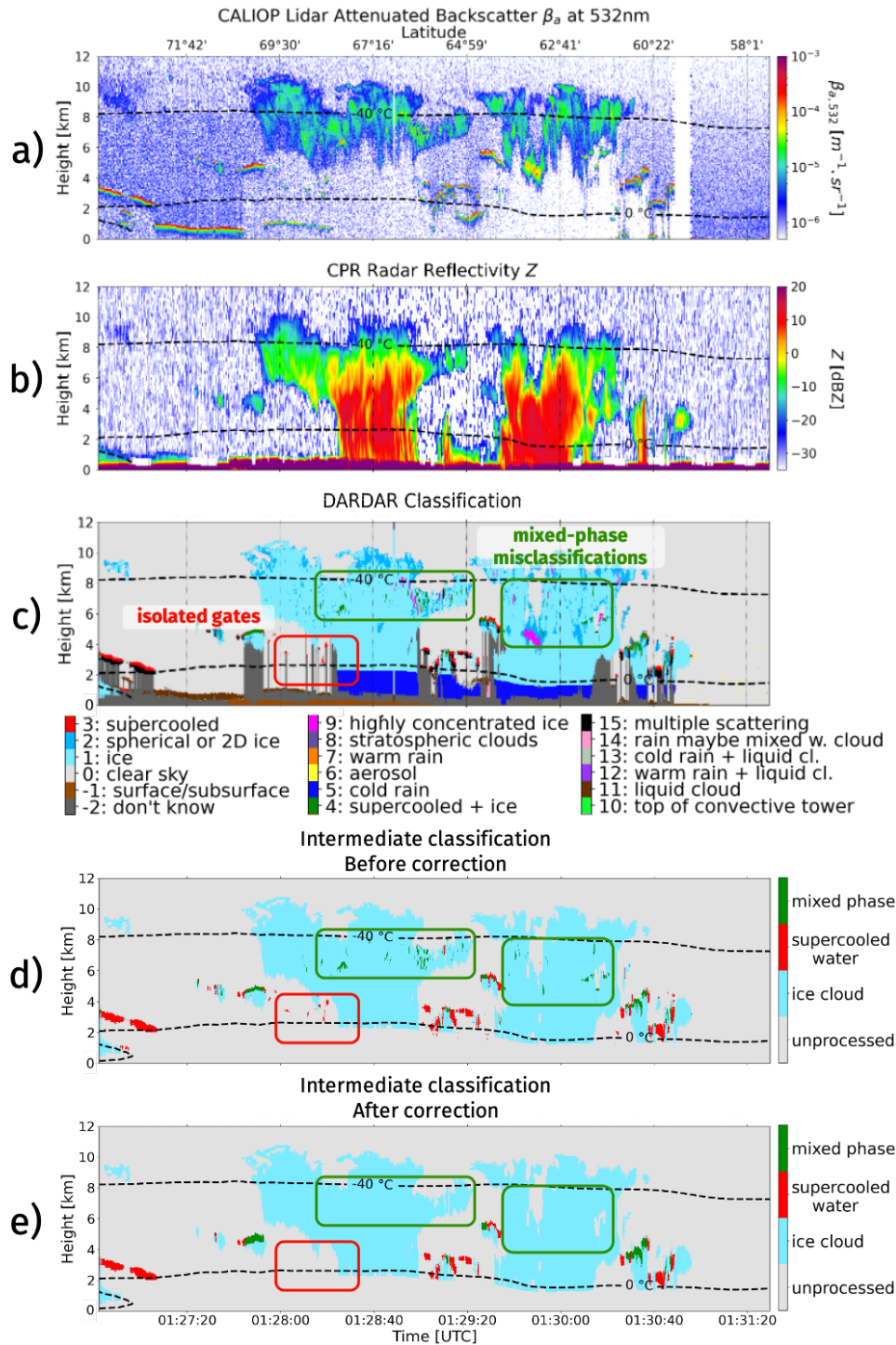


Figure 3.6: CALIOP lidar attenuated backscatter at 532 nm a), CPR radar reflectivity at 95 GHz b), DARDAR-MASK classification c), and the intermediate classification before d) and after e) corrections on 12th May 2019. Red boxes indicate supercooled water isolated gates and green boxes mixed-phase misclassifications. Isotherms at 0 and -40 °C are displayed in black dotted lines. All panels share the same abscissa axes (time and latitude). Orbit ID: 2019132000852_69440 125

3.3 . The VarPy-mix version

In this section, I explain the various improvements implemented to build up VarPy-mix. For this, I rely on its diagram presented in Figure 3.7 and based on the VarPy-ice diagram explained in Section 3.1.2.

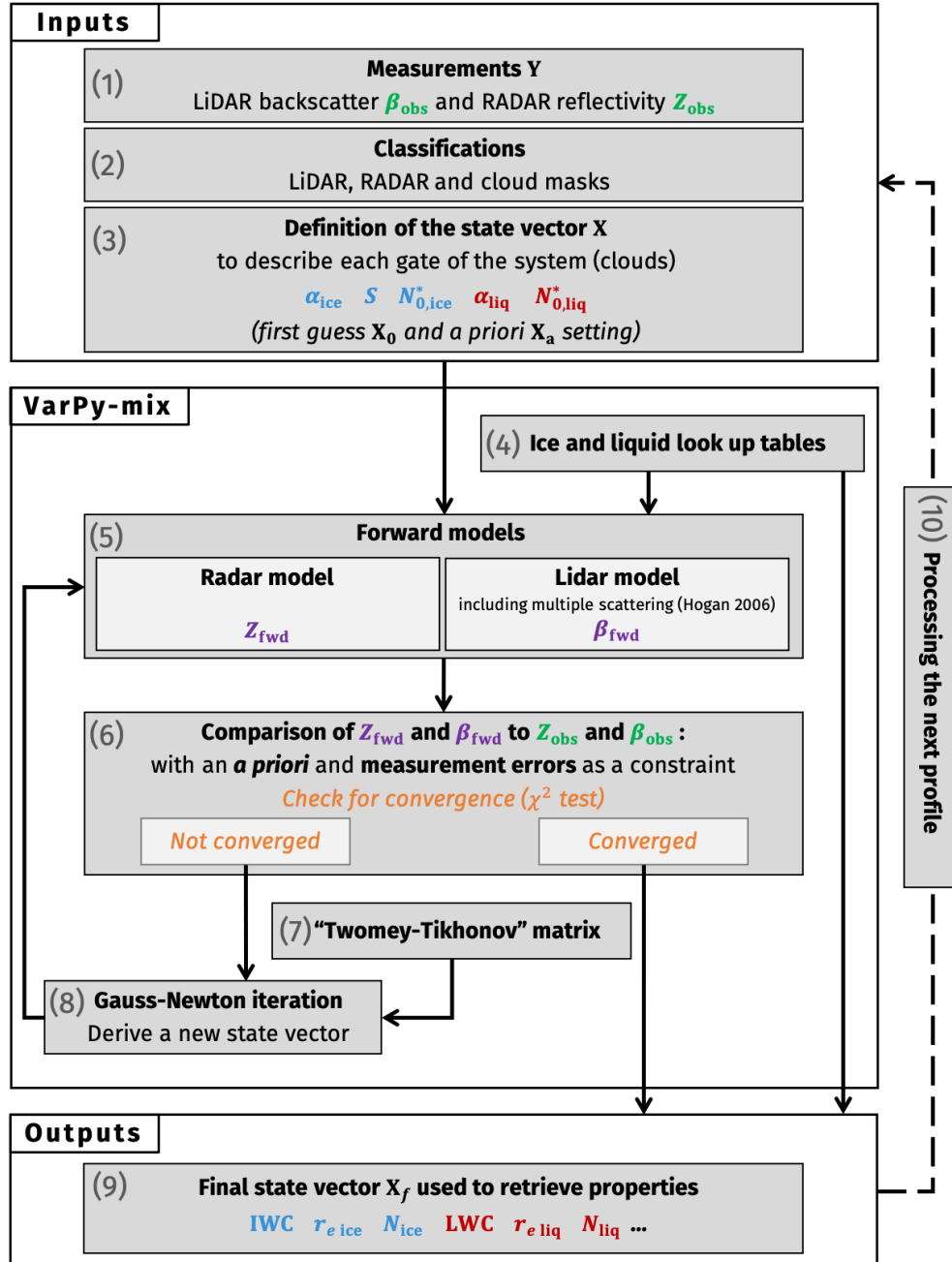


Figure 3.7: VarPy-mix retrieval method scheme.

First, I present our hypotheses to retrieve both ice and supercooled water, particularly in the mixed-phase, with a unique algorithm. In the second subsection, I focus on the new state vector which plays a major role in the algorithm adaptation. The next subsection describes the method I chose to produce a liquid LUT to retrieve supercooled water properties. Finally, modifying the state vector implies adapting the other matrices involved in the structure of the algorithm. I describe these changes in the last section.

3.3.1 . Hypothesis to retrieve supercooled water and mixed-phase

As previously stated, lidar and radar have different sensitivities to the mixed-phase and it is essential to consider the liquid and ice parts of the mixed-phase separately. The ideal situation would be to retrieve the mixed-phase with both instruments simultaneously, but this is highly complicated since we do not have access to the exact fraction of each phase with the radar reflectivity and the lidar backscatter only. For example, additional information such as radar Doppler spectrum or lidar depolarization would be required to estimate this phase fraction. Consequently, we propose to simplify the situation by considering only the main response of each instrument to ice or liquid. Indeed, as the lidar signal is more sensitive to small and highly concentrated particles such as supercooled water droplets, it is used in VarPy-mix to retrieve the liquid part of the mixed-phase. Radar signal, on the other hand, is sensitive to large particles and is designed to retrieve the ice part of the mixed-phase.

VarPy-mix aims to retrieve several cloud phases using the same variational method with a improved structure and parameterization adapted to supercooled water and mixed-phase. Although an important part of VarPy-ice has been preserved to maintain the method strengths and the results consistency, significant changes have been introduced, notably to the state vector, which is a key element in the variational method.

3.3.2 . New state vector configuration

For the method we propose, the state vector (box 1 of Figure 3.7) needs to be adapted to include supercooled water properties. In addition, the specific case of the mixed-phase must be taken into account. As stated in the previous subsection, the supercooled water and the ice particles properties are retrieved separately for the mixed-phase. Consequently, the state vector is divided in two parts: one part of the variables retrieves ice properties and the other part retrieves liquid properties. Mixed-phase ice crystals are included in the ice part and the supercooled droplets are in the liquid part. The state vector composition differs from the VarPy-ice version and is described in the next paragraphs.

Since liquid droplet concentration does not depend on the air temperature like for ice crystals, the temperature-dependent concentration parameter N' is not required to retrieve liquid cloud properties. Instead of N' , I decided to use N_0^* in the state vector. I include this variable for each state vector part: $N_{0,\text{ice}}^*$ for the ice part and $N_{0,\text{liq}}^*$ for the liquid part. Choosing N_0^* allows us to keep the *a priori* and first guess values for the ice with the following temperature dependent relationship, based on Equation 3.21 used for N' *a priori* and first guess values:

$$\ln(N_{0,\text{ice}}^*) = (a_{\ln(N')} + b_{\ln(N')} \cdot T) + \gamma \cdot \ln \alpha_{\text{ice}} \quad (3.32)$$

based on Equation 3.21 used for N' *a priori* and first guess values where γ is empirically determined and links N' to N_0^* and α (Equation 3.17). To keep the old scheme benefits, the cubic-spline basis function interpolates the $N_{0,\text{ice}}^*$ values with a spacing factor κ_N set to 4. This is unusable for the liquid group since the detected supercooled layers are thin and corresponds to insufficient gate numbers. In addition, I have implemented in the VarPy-ice algorithm the ability to retrieve ice properties using the normalized number concentration parameter N_0^* . This enables the ice retrieval of VarPy-mix to be compared with VarPy-ice retrieval to avoid any inconsistencies.

Next, regarding the lidar ratio S , we keep the same configuration in the state vector with the two coefficients $a_{\ln(S)}$ and $b_{\ln(S)}$. As previously explained in Section 2.2.2.2, the lidar ratio for liquid droplets can be assumed to be constant (Pinnick et al. 1983). Based on the values listed in Table 2.7, I fixed the lidar ratio value at 18.6 sr for supercooled water (pure or in mixed-phase) at 532 nm. In the state vector, $a_{\ln(S)}$ and $b_{\ln(S)}$ represent only the lidar ratio values for ice crystals (pure or in mixed-phase).

Finally, the extinction α is still part of the state vector. Like for $N_{0,\text{ice}}^*$ and $N_{0,\text{liq}}^*$, the extinction is divided into two variable: α_{ice} for the ice properties and α_{liq} for the liquid ones.

As a result, we end up with the state vector, X_{mix} , given by Equation 3.33:

$$X_{\text{mix}} = \begin{pmatrix} \ln(N_{0,\text{ice},0}^*) \\ \vdots \\ \ln(N_{0,\text{ice},m_i}^*) \\ \\ a_{\ln(S)} \\ b_{\ln(S)} \\ \\ \ln(\alpha_{\text{ice},0}) \\ \vdots \\ \ln(\alpha_{\text{ice},n_i}) \\ \\ \ln(N_{0,\text{liq},0}^*) \\ \vdots \\ \ln(N_{0,\text{liq},n_l}^*) \\ \\ \ln(\alpha_{\text{liq},0}) \\ \vdots \\ \ln(\alpha_{\text{liq},n_l}) \end{pmatrix} \quad (3.33)$$

where:

- n_i is the number of ice gates in the profile.
- n_l is the number of liquid gates in the profile.
- m_i is derived from n_i in the same way as m (Section 3.1.2) depending on the spacing factor κ_N .

These state vector modifications imply adjustments in the conversion matrix C_{mix} , which becomes:

$$C_{\text{mix}} = \begin{pmatrix} Y_{(0,0)} & \dots & Y_{(0,m_i)} & 0 & 0 & 0 & \dots & 0 & 0 & \dots & 0 & 0 & \dots & 0 \\ \vdots & \ddots & \vdots & \vdots & \vdots & \vdots & \ddots & \vdots & \vdots & \ddots & \vdots & \vdots & \ddots & \vdots \\ Y_{(n_i,0)} & \dots & Y_{(n_i,m_i)} & 0 & 0 & 0 & \dots & 0 & 0 & \dots & 0 & 0 & \dots & 0 \\ 0 & \dots & 0 & 1 & T_0 & 0 & \dots & 0 & 0 & \dots & 0 & 0 & \dots & 0 \\ \vdots & \ddots & \vdots & \vdots & \vdots & \vdots & \ddots & \vdots & \vdots & \ddots & \vdots & \vdots & \ddots & \vdots \\ 0 & \dots & 0 & 1 & T_{s_i} & 0 & \dots & 0 & 0 & \dots & 0 & 0 & \dots & 0 \\ 0 & \dots & 0 & 0 & 0 & 1 & \dots & 0 & 0 & \dots & 0 & 0 & \dots & 0 \\ \vdots & \ddots & \vdots & \vdots & \vdots & \vdots & \ddots & \vdots & \vdots & \ddots & \vdots & \vdots & \ddots & \vdots \\ 0 & \dots & 0 & 0 & 0 & 0 & \dots & 1 & 0 & \dots & 0 & 0 & \dots & 0 \\ \vdots & \ddots & \vdots & \vdots & \vdots & \vdots & \ddots & \vdots & \vdots & \ddots & \vdots & \vdots & \ddots & \vdots \\ 0 & \dots & 0 & 0 & 0 & 0 & \dots & 0 & 1 & \dots & 0 & 0 & \dots & 0 \\ \vdots & \ddots & \vdots & \vdots & \vdots & \vdots & \ddots & \vdots & \vdots & \ddots & \vdots & \vdots & \ddots & \vdots \\ 0 & \dots & 0 & 0 & 0 & 0 & \dots & 0 & 0 & \dots & 1 & \dots & 0 \\ \vdots & \ddots & \vdots & \vdots & \vdots & \vdots & \ddots & \vdots & \vdots & \ddots & \vdots & \vdots & \ddots & \vdots \\ 0 & \dots & 0 & 0 & 0 & 0 & \dots & 0 & 0 & \dots & 0 & \dots & 1 \end{pmatrix} \quad (3.34)$$

where:

- $Y_{(i,j)}$ are the values derived from the cubic-spline basis function. These $(n_i \times m_i)$ elements (highlight in blue) corresponds to $\ln(N_{0,ice}^*)$.
- The two columns at $m_i + 1$ and $m_i + 2$ (highlighted in green) consist of ones and temperature values T , corresponding to the ice lidar ratio S . As for VarPy-ice, the first column is multiplied by $a_{\ln(S)}$ and the second by $b_{\ln(S)}$, resulting in the lidar ratio according to Equation 3.16. In VarPy-mix, since the lidar ratio is fixed at 18.6 sr for the mixed-phase, there are s_i values of temperature and ones, corresponding to the s_i ice gates detected by the lidar.
- The terms highlighted in yellow represent an n_i -dimensional identity matrix corresponding to the ice extinction $\ln(\alpha_{ice})$. As for VarPy-ice, this means that the matrix C_{mix} has no effect on the $\ln(\alpha_{ice})$ elements of the state vector.
- The terms highlighted in red represent an n_i -dimensional identity matrix corresponding to $\ln(N_{0,liq}^*)$. The cubic-spline basis function is not applied to $\ln(N_{0,liq}^*)$, consequently the matrix C_{mix} does not modify these state vector elements.
- As with the ice extinction, the matrix C_{mix} elements corresponding to the liquid extinction $\ln(\alpha_{liq})$ (highlight in purple) are an n_l -dimensional identity matrix.

These matrix multiplies the state vector X_{mix} to obtain a version of the state vector where each N_0^* , S and α variable has a value for each gate. This “converted” state vector is thus of dimension $(2n_i + s_i + 2n_l)$ and provide a complete profile for each variable:

- N_0^* profile is obtained by combining $N_{0,ice}^*$ (converted with C) and $N_{0,liq}^*$ profiles.
- Lidar ratio S profile is produced by converting $a_{\ln(S)}$ and $b_{\ln(S)}$ with C for pure ice gates and adding constant values (18.6 sr) for supercooled water (pure or mixed-phase).
- α is obtained by combining α_{ice} and α_{liq} profiles.

Next, the “converted” state vector is given as input to the forward models to calculate $\ln(\beta_{fwd})$, $\ln(Z_{fwd})$ and the Jacobian. For this, forward models require a LUT. However, supercooled water has different microphysical properties compared to ice, meaning that LUTs describing ice properties cannot be used

for supercooled water. For this reason, I decided to create a LUT dedicated to supercooled water.

3.3.3 . Normalized Droplet Size Distribution for liquid Look Up Table

For VarPy-mix, I decided to keep some of the VarPy-ice configuration, in particular the two LUTs used to relate the ice crystals microphysical properties to each other, for a given PSD. However, the PSD differs between ice crystals and liquid droplets. Consequently, I decided to define a DSD for liquid droplets to create a LUT dedicated to retrieve liquid properties. The literature proposes two types of distribution: the gamma distribution (Miles et al. 2000) and the log-normal distribution (Frisch et al. 1995; Fielding et al. 2015). For this study we use the following log-normal relationship define by Frisch et al. 1995:

$$N(r) = \frac{N_{\text{liq}}}{\sigma_{N(r)} \sqrt{2\pi}} e^{-\frac{(\ln(r) - \ln(r_0))^2}{2\sigma_{N(r)}^2}} \quad (3.35)$$

where:

- $N(r)$ [m^{-3}] is the DSD, the number concentration at a given cloud droplet radius r [μm].
- N_{liq} [m^{-3}] is the total number of liquid droplets per unit volume.
- r_0 [μm] is the modal radius.
- $\sigma_{N(r)}$ is the geometric standard deviation. Fielding et al. 2014 and Fielding et al. 2015 set this value to $\sigma = 0.3 \pm 0.1$ and Frisch et al. 1995 at $\sigma = 0.35$. We have chosen to set this value at $\sigma_{N(r)} = 0.3$.

The k^{th} moment $\langle r^k \rangle$ of this distribution can be expressed as follows:

$$\langle r^k \rangle = \frac{1}{N_{\text{liq}}} \int_0^\infty N(r) r^k dr \quad (3.36)$$

It permits to relate the following variables to the mean volume-weighted diameter D_m [m], which is proportional to the ratio between the fourth moment and the the third moment (presented in Section 1.1.4 by Equation 1.12):

- The reflectivity Z [$\text{mm}^6 \cdot \text{m}^{-3}$]: proportional to the sixth moment of the DSD, as we are looking at small droplets, presented in Section 2.2.2.1 by Equation 2.10

- The liquid water extinction α_{liq} [m^{-1}]: proportional to the second moment, presented in Section 1.1.4 by Equation 1.1.4.
- The liquid water content LWC [$\text{kg} \cdot \text{m}^{-3}$]: proportional to the third moment, presented in Section 1.1.4 by Equation 1.2.
- The liquid water effective radius $r_{e,\text{liq}}$ [m]: proportional to the ratio between the third moment and the the second moment, presented in Section 1.1.4 by Equation 1.7.
- The equivalent area radius r_a [m], equivalent to the effective radius for droplets. It corresponds to the radius of a sphere with the same cross-sectional area as the entire size distribution mean area.
- The total number of water droplets per unit volume N_{liq} .

Those variables are then normalized by $N_{0,\text{liq}}^*$ [m^{-4}], which is proportional to the ratio between the third moment to the fifth power and the fourth moment to the fourth power (presented in Section 1.1.4 by Equation 1.13). As a result, the LUT ends up with the following composition: $\frac{Z}{N_{0,\text{liq}}^*}, \frac{\alpha_{\text{liq}}}{N_{0,\text{liq}}^*}, \frac{\text{LWC}}{N_{0,\text{liq}}^*}, \frac{N_{\text{liq}}}{N_{0,\text{liq}}^*}, r_a$ and $r_{e,\text{liq}}$ as a function of D_m and the standard deviation $\sigma_{N(r)}$.

Defining the LUT involves to determine the state vector *a priori* and first guess values. In VarPy-mix, the $\ln(N_{0,\text{ice}}^*)$ *a priori* is calculated with $a_{\ln(N')}$, $b_{\ln(N')}$ and $\ln(\alpha_{\text{ice}})$ *a priori* values via Equation 3.32. These values are the same as for VarPy-ice and are summarized in Table 3.5, depending on the LUT. For the lidar ratio S , the *a priori* values of $a_{\ln(S)}$ and $b_{\ln(S)}$ are the same as for VarPy-ice (see Table 3.5) and corresponds to pure ice. Regarding $\ln(\alpha_{\text{ice}})$, we kept the *a priori* values of VarPy-ice extinction, set to -7 (Table 3.5). For the liquid part of the *a priori* state vector, we have set constant values for $\ln(N_{0,\text{liq}}^*)$ and $\ln(\alpha_{\text{liq}})$, to 30 and -5 respectively. We assume that $\ln(N_{0,\text{liq}}^*)$ does not depend on temperature. $\ln(N_{0,\text{liq}}^*)$ and $\ln(\alpha_{\text{liq}})$ values were chosen based on the DSD, with $D_m = 20 \mu\text{m}$.

Table 3.5: *A priori* and first guess values for each variable of the state vector in VarPy-mix. (BF: Brown and Francis modified LUT, HC: Heymsfield Composite LUT).

Variable	Values	
	BF	HC
$a_{\ln(N')}$	22.234435	21.94
$b_{\ln(N')}$	-0.090736	-0.095
γ	0.61	0.67
$a_{\ln(S)}$	3.18	3.18
$b_{\ln(S)}$	-0.0086	-0.0086
$\ln(\alpha_{\text{ice}})$	-7	-7
$\ln(N_{0,\text{liq}}^*)$	30	30
$\ln(\alpha_{\text{liq}})$	-5	-5

As with ice LUT, the liquid one is involved in two algorithm steps (as illustrated in Figure 3.7, boxes 4, 5 and 9) with the ratio $\frac{\ln(\alpha_{\text{liq}})}{\ln(N_{0,\text{liq}}^*)}$ from the state vector values. This ratio retrieves the corresponding value in the LUT, by interpolation. First, at each iteration to predict $\ln(Z_{\text{fwd}})$, $\ln(\beta_{\text{fwd}})$ (via $\ln(r_a)$ and the fast multiple-scattering model of Hogan 2006, Multiscatter) and the Jacobian terms (box 5). At the end, with the final state vector, the ratio $\frac{\ln(\alpha_{\text{liq}})}{\ln(N_{0,\text{liq}}^*)}$ permits to obtain LWC, $r_{e,\text{liq}}$ and N_{liq} (box 9). These two steps are explained in further detail in the next subsection.

3.3.4 . Algorithm adaptations to the supercooled water and the mixed-phase retrieval

After initializing the state vector and determining the ice and liquid LUTs, we need to compute the Jacobian K_{mix} as well as $\ln(Z_{\text{fwd}})$ and $\ln(\beta_{\text{fwd}})$ thanks to the radar and lidar forward models (box 5 of Figure 3.7). For clarity, I have split the Jacobian into two parts: the Jacobian of the state vector “ice” part $K_{\text{mix, ice}}$ (Equation 3.37) and the one of the “liquid” part $K_{\text{mix, liq}}$ (Equation 3.38).

$$K_{\text{mix, ice}} = \begin{pmatrix} \frac{\partial \beta_0}{\partial N_{0,i,0}^*} & \dots & \frac{\partial \beta_0}{\partial N_{0,i,m_i}^*} & \frac{\partial \beta_0}{\partial a_{\ln(S)}} & \frac{\partial \beta_0}{\partial b_{\ln(S)}} & \frac{\partial \beta_0}{\partial \alpha_{i,0}} & \dots & \frac{\partial \beta_0}{\partial \alpha_{i,n_i}} \\ \vdots & \ddots & \vdots & \vdots & \vdots & \vdots & \ddots & \vdots \\ \frac{\partial \beta_p}{\partial N_{0,i,0}^*} & \dots & \frac{\partial \beta_p}{\partial N_{0,i,m_i}^*} & \frac{\partial \beta_p}{\partial a_{\ln(S)}} & \frac{\partial \beta_p}{\partial b_{\ln(S)}} & \frac{\partial \beta_p}{\partial \alpha_{i,0}} & \dots & \frac{\partial \beta_p}{\partial \alpha_{i,n_i}} \\ \frac{\partial Z_0}{\partial N_{0,i,0}^*} & \dots & \frac{\partial Z_0}{\partial N_{0,i,m_i}^*} & \frac{\partial Z_0}{\partial a_{\ln(S)}} & \frac{\partial Z_0}{\partial b_{\ln(S)}} & \frac{\partial Z_0}{\partial \alpha_{i,0}} & \dots & \frac{\partial Z_0}{\partial \alpha_{i,n_i}} \\ \vdots & \ddots & \vdots & \vdots & \vdots & \vdots & \ddots & \vdots \\ \frac{\partial Z_q}{\partial N_{0,i,0}^*} & \dots & \frac{\partial Z_q}{\partial N_{0,i,m_i}^*} & \frac{\partial Z_q}{\partial a_{\ln(S)}} & \frac{\partial Z_q}{\partial b_{\ln(S)}} & \frac{\partial Z_q}{\partial \alpha_{i,0}} & \dots & \frac{\partial Z_q}{\partial \alpha_{i,n_i}} \end{pmatrix} \quad (3.37)$$

$$K_{\text{mix, liq}} = \begin{pmatrix} \frac{\partial \beta_0}{\partial N_{0,l,0}^*} & \dots & \frac{\partial \beta_0}{\partial N_{0,l,n_l}^*} & \frac{\partial \beta_0}{\partial \alpha_{l,0}} & \dots & \frac{\partial \beta_0}{\partial \alpha_{l,n_l}} \\ \vdots & \ddots & \vdots & \vdots & \ddots & \vdots \\ \frac{\partial \beta_p}{\partial N_{0,l,0}^*} & \dots & \frac{\partial \beta_p}{\partial N_{0,l,n_l}^*} & \frac{\partial \beta_p}{\partial \alpha_{l,0}} & \dots & \frac{\partial \beta_p}{\partial \alpha_{l,n_l}} \\ \frac{\partial Z_0}{\partial N_{0,l,0}^*} & \dots & \frac{\partial Z_0}{\partial N_{0,l,n_l}^*} & \frac{\partial Z_0}{\partial \alpha_{l,0}} & \dots & \frac{\partial Z_0}{\partial \alpha_{l,n_l}} \\ \vdots & \ddots & \vdots & \vdots & \ddots & \vdots \\ \frac{\partial Z_q}{\partial N_{0,l,0}^*} & \dots & \frac{\partial Z_q}{\partial N_{0,l,n_l}^*} & \frac{\partial Z_q}{\partial \alpha_{l,0}} & \dots & \frac{\partial Z_q}{\partial \alpha_{l,n_l}} \end{pmatrix} \quad (3.38)$$

The matrix K_{mix} is consequently obtained by concatenating the two matrices $K_{\text{mix, ice}}$ and $K_{\text{mix, liq}}$, as follows:

$$K_{\text{mix}} = K_{\text{mix, ice}} \mid K_{\text{mix, liq}} \quad (3.39)$$

For better readability of Equations 3.37 and 3.38, the indices $_{\text{fwd}}$ of Z and β are not displayed, the $_{\text{ice}}$ and $_{\text{liq}}$ indices of N_0^* and α are replaced respectively by $_i$ and $_l$ indices and the natural logarithm of Z , β , N_0^* and α are omitted. The dimension of K_{mix} is $(p+q) \times (m_i + 2 + n_i + 2n_l)$. As for the state vector, we can divide the Jacobian in two parts: the derivatives of $\ln Z$ and $\ln \beta$ with respect to $\ln N_{0,\text{ice}}^*$, $a_{\ln(S)}$, $b_{\ln(S)}$ and $\ln \alpha_{\text{ice}}$ for the ice part ($K_{\text{mix, ice}}$, Equation 3.37) and the derivatives of $\ln Z$ and $\ln \beta$ with respect to $\ln N_{0,\text{liq}}^*$ and $\ln \alpha_{\text{liq}}$ for the liquid part ($K_{\text{mix, liq}}$, Equation 3.37). For the mixed-phase, both liquid and ice parts are used, but each part is retrieved with only one instrument. Indeed, the radar is not used to retrieve the supercooled water neither in pure liquid clouds nor in mixed-phase clouds, consequently:

$$\frac{\partial \ln(Z_j)}{\partial \ln(N_{0,\text{liq},k}^*)} = 0 \quad \forall j, k \quad (3.40)$$

$$\frac{\partial \ln(Z_j)}{\partial \ln(\alpha_{\text{liq},k})} = 0 \quad \forall j, k \quad (3.41)$$

On the other hand, the lidar signal retrieves ice clouds properties but not the ice part of the mixed-phase. As a result, for any j and k corresponding to mixed-phase gates, we have:

$$\frac{\partial \ln(\beta_j)}{\partial \ln(N_{0,\text{ice},k}^*)} = 0 \quad (3.42)$$

$$\frac{\partial \ln(\beta_j)}{\partial \ln(\alpha_{\text{ice},k})} = 0 \quad (3.43)$$

To derive $K_{\text{mix, ice}}$ matrix values, the forwards models apply one or other LUT used by VarPy-ice (HC or BF).

Next, since the observation vector Y remains unchanged with $\ln(Z_{\text{obs}})$ and $\ln(\beta_{\text{obs}})$ values (Equation 3.15), the measurement error covariance matrix R remains the same as for VarPy-ice (Equation 3.22).

Regarding the *a priori* error covariance matrix B_{mix} , its structure has been adapted to the new state vector composition. In order to keep the same configuration as VarPy-ice, the off-diagonal terms are calculated for the pure ice part of $N_{0,\text{ice}}^*$ (not for the mixed-phase gates). B_{mix} remains diagonal regarding the other variables and the *a priori* error variances values are listed in Table 3.6. These values are assumed to be constant with height.

Table 3.6: *A priori* error variances used in VarPy-mix for the *a priori* error covariance matrix B_{mix}

Variables	Values
$\sigma_{\ln(N_{0,\text{ice}}^*)}$	1
$\sigma_{a_{\ln(S)}}$	0.1
$\sigma_{b_{\ln(S)}}$	0.0001
$\sigma_{\ln(\alpha_{\text{ice}})}$	5
$\sigma_{\ln(N_{0,\text{liq}}^*)}$	1
$\sigma_{\ln(\alpha_{\text{liq}})}$	5

The next step is to configure the T_{mix} matrix (box 7 of Figure 3.7). We keep the same approach as for VarPy-ice, which is to smooth only the extinction profile. Consequently, the T_{mix} elements corresponding to $\ln(N_{0,\text{ice}}^*)$, $a_{\ln(S)}$,

$b_{\ln(S)}$ and $\ln(N_{0,\text{liq}}^*)$ are set to zero. Contrary to VarPy-ice, we cannot use a single matrix to smooth the entire extinction profile, since we have separated the liquid ($\ln(\alpha_{\text{liq}})$) and ice ($\ln(\alpha_{\text{ice}})$) parts of the extinction. In addition, liquid droplets extinction values are different from ice crystals extinction. Nevertheless, both extinction parts require to be smoothed with a “Twomey-Tikhonov” matrix. Consequently, for VarPy-mix, a function has been developed to separate different profile section according to the smoothing to be applied: the separation is established between ice, liquid and where there is clear sky. As a result, one « Twomey-Tikhonov » matrix is applied to each section and the dimension of the final matrix is $(m_i + k + n_i + 2n_l) \times (m_i + k + n_i + 2n_l)$. The smoothness coefficient κ is set to 100 for $\ln(\alpha_{\text{ice}})$, to keep the VarPy-ice parameterization. Since the detected liquid layers are thinner than ice cloud, the coefficient applied to the $\ln(\alpha_{\text{liq}})$ is lower and set to 10.

For the next steps, the cost function J calculation and the convergence determination by χ^2 test remain the same as for VarPy-ice and are explained in Section 3.1.2. Finally, the final state vector $X_{\text{mix},f}$ determined by the minimization of the cost function J allows us to compute $\frac{\alpha_{\text{ice},f}}{N_{0,\text{ice},f}^*}$ and $\frac{\alpha_{\text{liq},f}}{N_{0,\text{liq},f}^*}$ ratios.

On the one hand, the first ratio is combined to the chosen ice LUT to retrieve the ice water content (IWC), the ice particle number concentration N_{ice} and the ice particle effective radius $r_{e,\text{ice}}$. On the other hand, the second ratio is combined with the liquid LUT created during this thesis to retrieve the liquid water content (LWC), the liquid droplets number concentration N_{liq} and the liquid droplets effective radius $r_{e,\text{liq}}$. In addition, liquid and ice microphysical properties can be summed up to produce profiles of:

- total extinction α_{tot} [m^{-1}], defined by:

$$\alpha_{\text{tot}} = \alpha_{\text{ice}} + \alpha_{\text{liq}} \quad (3.44)$$

- total water content TWC [$\text{kg} \cdot \text{m}^{-3}$] defined by:

$$\text{TWC} = \text{IWC} + \text{LWC} \quad (3.45)$$

- total number concentration N_{tot} [m^{-3}] defined by:

$$N_{\text{tot}} = N_{\text{ice}} + N_{\text{liq}} \quad (3.46)$$

3.4 . Conclusion

This thesis aims to retrieve the microphysical properties of supercooled water, ice and mixed-phase clouds from radar-lidar synergy in a single algorithm. To this end, I have extended and adapted the VarPy-ice algorithm to

include the retrieval of supercooled water, either pure or mixed with ice crystals. This variational method enables the radar and lidar measurements to be converted into cloud microphysical properties. It is based on an approach that consists to solve an inverse problem using the Bayes theorem and the Gauss-Newton method.

First, I have improved and adapted the classification used to identify the observed particles to include supercooled water and the mixed-phase to hydrometeors to be retrieved. Next, numerous adaptations have been introduced to the algorithm, notably to the state vector, which describes ice crystals and water droplets separately. This approach is based on the different sensitivities of radar and lidar to these two types of hydrometeors: the ice crystals are retrieved with the radar signal and the supercooled water with the lidar signal. Consequently, the ice clouds are retrieved with both instruments in synergy areas while each phase of the mixed-phase and pure supercooled water clouds are retrieved only with single instrument. In the latter case, the retrievals relies strongly on empirically determined *a priori* values, that depend on temperature, and error values. Finally, the last main improvement is the inclusion of a LUT for liquid water, created from a log-normal DSD. It links the state vector variables to microphysical properties such as liquid water content LWC, effective radius r_e and liquid number concentration N_{liq} . Besides, the LUTs defined for VarPy-ice are included in VarPy-mix to retrieve ice crystal properties. At the end, VarPy-mix provides:

- Ice and liquid extinction profiles, α_{ice} and α_{liq} [m^{-1}], which can be summed to produce total extinction α_{tot} profile.
- Ice and liquid water content profiles, IWC and LWC [$kg.m^{-3}$], which can be summed to produce total water content TWC profile.
- Ice and liquid number concentration profiles, N_{ice} and N_{liq} [m^{-3}], which can be summed to produce total number concentration N_{tot} profile.
- Ice and liquid effective radius profile, $r_{e,ice}$ and $r_{e,liq}$ [m].

This method was mainly developed with data from CloudSat-CALIPSO. Nevertheless, our method strength is its flexibility, allowing it to be adapted to several radar-lidar platforms, which are described in Chapter 2. In the following chapter, I present the application of the VarPy-mix algorithm on different platforms. Furthermore, this methodology relies on strong assumptions concerning the mixed-phase, where each phase (liquid, ice) is retrieved by a single instrument (lidar, radar, respectively). To evaluate this approach, VarPy-mix retrievals with *in situ* data collocated with the CloudSat-CALIPSO platform are described and compared at the beginning of the next chapter.

4 - Application on several platforms and comparison to *in situ* measurements

Contents

4.1 VarPy-mix first retrievals and comparison with <i>in situ</i> measurements	140
4.1.1 Remote sensing and <i>in situ</i> measurements . . .	141
4.1.2 VarPy-mix retrievals	144
4.1.3 Comparison between VarPy-mix retrievals and <i>in situ</i> data	148
4.2 VarPy-mix application to airborne platforms during recent campaigns	153
4.2.1 HALO-(AC) ³ case study	153
4.2.2 RALI-THINICE case study	163
4.2.3 Comparison with <i>in situ</i> data from literature . .	172
4.3 Comparison between VarPy-ice, 2C-ICE and <i>in situ</i> .	177
4.4 Conclusion	180

Space missions and airborne measurement campaigns provide precious data for our understanding of clouds. Radar-lidar data collected during these missions are converted into cloud microphysical properties by retrieval algorithms. During this thesis, I mainly processed data from the CloudSat and CALIPSO satellites to develop VarPy-mix. To assess the algorithm, I decided to compare VarPy-mix retrieval with *in situ* data. For this, the microphysical properties of an Arctic mixed-phase cloud observed with CloudSat-CALIPSO are retrieved by VarPy-mix and compared with *in situ* measurements. The results are presented in the first section of this chapter.

Furthermore, recent airborne measurement campaigns provide numerous mixed-phase cloud data. In the second section, I present two cases of mixed-phase clouds in the Arctic collected by the RALI and HALO airborne platforms and retrieved by VarPy-mix. The possibility to adapt our algorithm to data collected from different measurement platforms attests to its great flexibility.

In the last section, I summarize a comparison study between VarPy-ice and 2C-ICE accepted in the Journal of Atmospheric and Oceanic Technology added in Appendix A.

4.1 . VarPy-mix first retrievals and comparison with *in situ* measurements

In this section, I present an Arctic case study combining satellite and collocated airborne *in situ* measurements. The satellite measurements are provided by CloudSat and CALIPSO and the VarPy-mix results are compared to collocated *in situ* data collected during the Arctic Study of Tropospheric Aerosol, Cloud and Radiation (ASTAR 2007, Ehrlich et al. 2009; Gayet et al. 2009) field campaign that took place from 25th of March to 19th of April 2007. The ASTAR project aims to characterize the microphysical and optical properties of mixed-phase clouds in the Arctic using *in situ* measurements. The three *in situ* probes onboard the Polar-2 aircraft (Dornier 228-101) operated by AWI are the CPI, FSSP and PN, described in Section 2.1.

First, I present the context of this study and the satellite measurements as well as the three *in situ* probes onboard the aircraft. Second, the microphysical properties retrieved by VarPy-mix are analyzed and compared with *in situ* data, notably extinctions and water contents. The results presented in this section have been accepted in the Atmospheric Measurement Techniques journal (Aubry et al. 2024).

4.1.1 . Remote sensing and *in situ* measurements

During this campaign, four legs coming from the same flight were performed on the 7th of April 2007 over the ocean near Svalbard archipelago. For this study, the radar and lidar measurements as well as the classifications come from the DARDAR-MASK v2.23 product (see Section 3.2.1). The case presented in this section is one of the rare CloudSat-CALIPSO transect with collocated airborne *in situ* measurements of mixed-phase clouds. The comparison between *in situ* data and VarPy-mix retrievals is possible because cloud detection as well as phase identification between DARDAR-MASK and *in situ* observations are in overall good agreement. Indeed, Mioche and Jourdan 2018 shows that 91 % of clear sky events and 86 % of DARDAR-MASK cloudy gates match with the Polar Nephelometer *in situ* probe from samples collected during the ASTAR 2007 and POLARCAT 2008 (see the Special Issue on POLARCAT in *Atmos. Chem. Phys.*) campaigns. In addition, the Polar Nephelometer is used to estimate the cloud phase observed (ice, liquid water and mixed-phase) thanks to thresholds on the asymmetry parameter g (Jourdan et al. 2010), defined by Equation 2.1. Using the Polar Nephelometer as a reference, Mioche and Jourdan 2018 shows that 61 % of DARDAR-MASK classification corresponding to ice phase match with Polar Nephelometer data, 67 % for liquid phase while 24 % for mixed-phase. This identification difference may be due to the temporal and spatial difference between satellite and *in situ* observations or to the detection limit of supercooled water by lidar due to attenuation.

The selected latitude range is shown in Figure 4.1, which present the profiles of the lidar backscatter measurements on panel a), the radar reflectivity on panel b), the intermediate classification on panel c) and the instrument flag to know which instrument is used for the retrieval on panel d). The strong lidar backscatter signal at the top of the cloud means that there is a large amount of small particles such as supercooled water droplets. Since the radar also detects particles in this part of the cloud this means that ice particle are present. Consequently, the intermediate classification indicates the presence of an ice cloud with mixed-phase layer at the top. As presented in Figure 4.1 panel d), the mixed-phase is retrieved with both radar and lidar. However, since the lidar is strongly attenuated and extinguished due to the supercooled water of the mixed-phase, the ice cloud below is mainly retrieved by radar only. As a result, the base of the supercooled liquid layer within the mixed-phased cloud cannot be determined unequivocally.

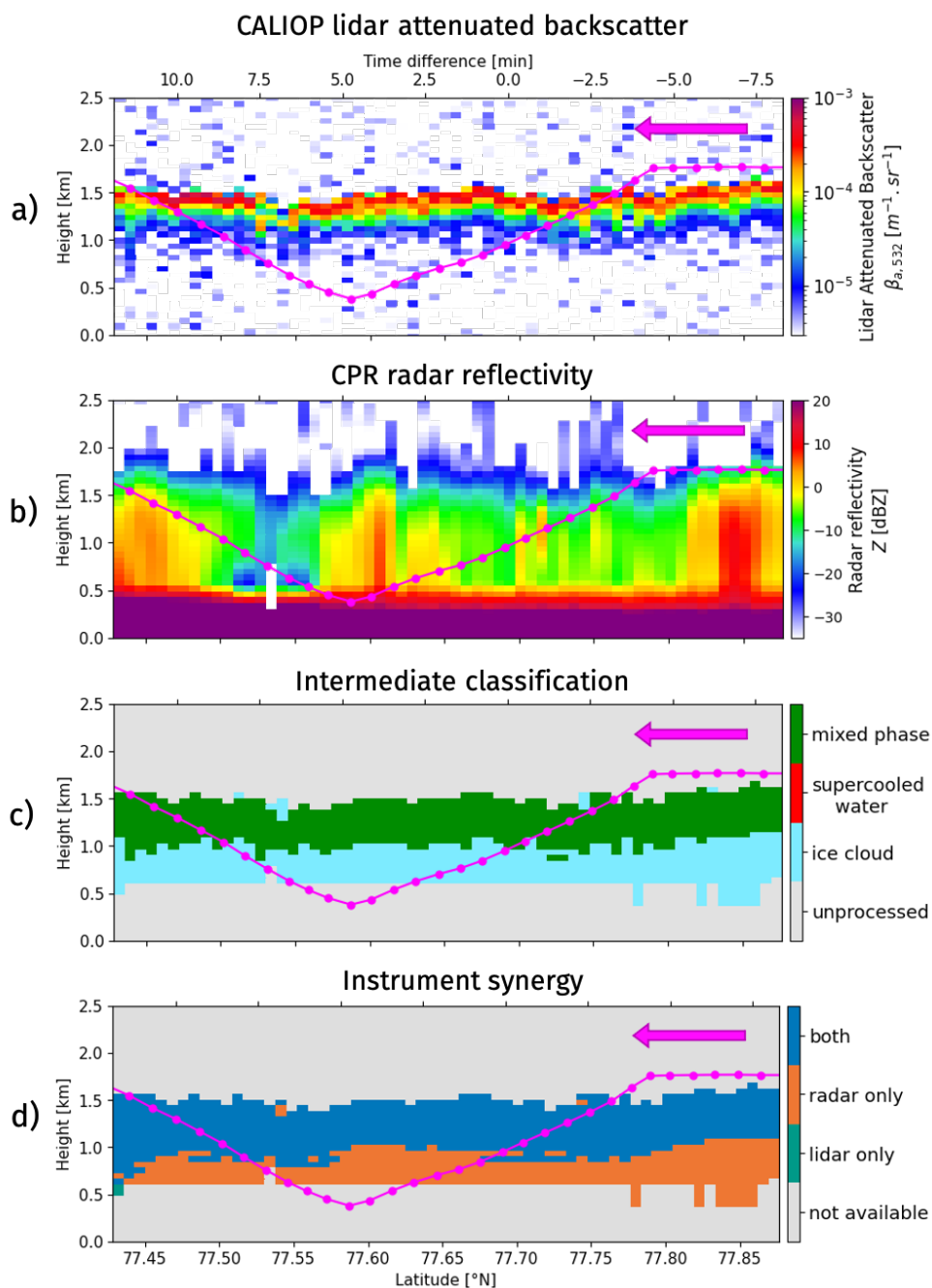


Figure 4.1: Selected profiles of CALIPSO attenuated backscatter a), CloudSat reflectivity b), intermediate classification c) and instrument synergy d) on 7th April 2007. The trajectory and direction of Polar-2 are shown by respectively magenta line and arrow. All panels share the same abscissa axes (time and latitude). Data from DARDAR-MASK V2.23 products, <https://www.icare.univ-lille.fr/>, orbit ID: 2007097090635_05010

Besides, the three *in situ* instruments onboard the Polar-2 aircraft were the CPI, the FSSP-100 and the PN, presented in Section 2.1. Since the aircraft was not flying exactly along the satellites trajectory, nor at the same time, the collocation is quite challenging. Among the four legs, the third one is temporarily the closest to the satellites overpass with less than a ten minutes delay, as shown on the top x axis of Figure 4.1. We focus this study on this leg to compare VarPy-mix retrievals to the *in situ* measurements. The altitude of the aircraft is shown by the magenta line in Figure 4.1, where each point corresponds to a thirty second averaged probe measurements and the magenta arrow indicates the flight direction. Since the aircraft flew above the cloud before going inside the cloud and passing through the mixed-phase layer twice, we have a vertical description of the cloud and the comparison with VarPy-mix retrieval is more complete.

The size range sensitivity of each probe is summarized in Figure 4.2. As explained in Section 2.1, the CPI gives information about the ice particles and the FSSP about liquid droplets. For this study, we take the ice cloud extinction α_{CPI} and ice water content IWC_{CPI} from the CPI, the liquid cloud extinction α_{FSSP} and liquid water content LWC_{FSSP} from the FSSP. By summing extinctions and water contents from both instruments, the total water content $\text{TW}_{\text{CPI+FSSP}}$ and the total extinction $\alpha_{\text{CPI+FSSP}}$ can be obtained. The PN also provides the total extinction α_{PN} . These *in situ* measurements are presented in the next subsection in Figure 4.3 and 4.4 besides VarPy-mix retrieval results and are detailed in the comparison in Section 4.1.3. All measurements uncertainties are listed in Table 4.1.

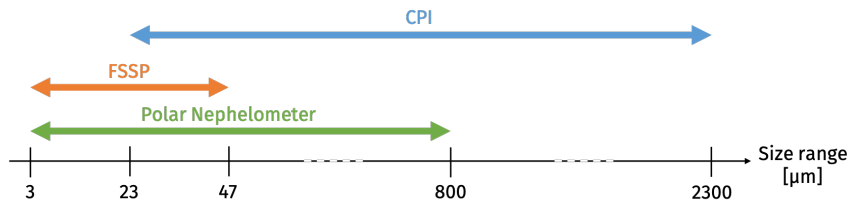


Figure 4.2: CPI, FSSP and PN range sensitivities.

Table 4.1: Uncertainties of extinction and water contents from CPI, FSSP and PN probes from Mioche et al. 2017.

Properties	CPI	FSSP	PN
Extinction α	55 %	35 %	25 %
Water Content(IWC or LWC)	60 %	20 %	-

4.1.2 . VarPy-mix retrievals

First, to retrieve cloud properties with VarPy-mix, some parameters need to be defined. For this case, the classification has been adapted by eroding few isolated supercooled gates and by adding four gates below the mixed-phase layer, as explained in Section 3.2.2 (page 123). The other parameter to choose is the ice LUT used to retrieve ice properties. We have selected the HC LUT, implying the application of the corresponding *a priori* values (see Section 3.3.3, Table 3.5). The choice here is arbitrary, but also because the LUT was developed more recently.

Consequently, the ice and liquid extinctions retrieved by VarPy-mix are presented by the curtain in Figure 4.3 a) and b) and are used to retrieve other ice and liquid properties via the ice and liquid LUTs. Figures 4.4 a) and b) show the IWC and LWC and Figure 4.5 a) to d) show N_{ice} , N_{liq} , $r_{e,ice}$ and $r_{e,liq}$ retrievals. For each microphysical properties, the ice and liquid parts are retrieved, according to the classification. As a result, for the ice cloud between 0.5 and 1 km, only the ice properties are available. Nevertheless, ice and liquid properties are both retrieved for the mixed-phase gates.

Table 4.2 presents the mean values in all selected pixels for all retrieved properties. These values combined to a global view in Figures 4.3, 4.4 and 4.5 curtains allow us to observe trends for each variable. The extinction of liquid droplets is stronger than ice crystals by a factor of 7. The same trends is observed between LWC and IWC with average values 30 % larger for LWC. The ice crystals are larger than liquid droplets by a factor of 5 for the mean values of effective radius. The liquid number concentration is much higher than ice number concentration by a factor 10^3 .

Finally, both extinctions and water contents can be compared with *in situ* measurements. For extinction, water content and concentration, we can sum the ice and liquid variables to obtain the total extinction α_{tot} (curtain in Figure 4.3 c)), the total water content TWC (curtain in Figure 4.4 c)) and the total number concentration N_{tot} (panel e) of Figure 4.5).

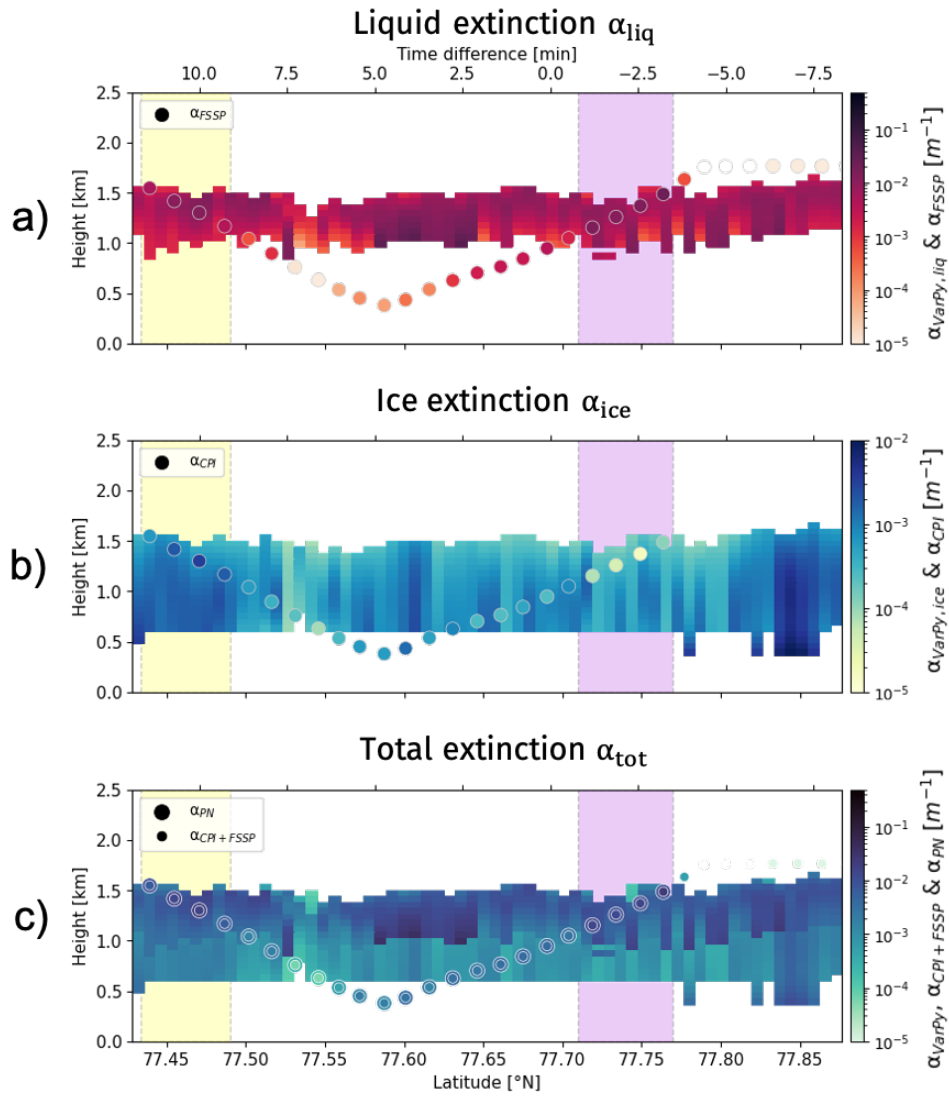


Figure 4.3: Liquid a), ice b) and total c) extinctions from VarPy-mix retrievals (curtain) and *in situ* probes (dots) regarding the latitude and the height. The yellow and purple shading represents the latitude range where mixed-phase retrievals are compared with *in situ*. All panels share the same abscissa axes (time difference and latitude).

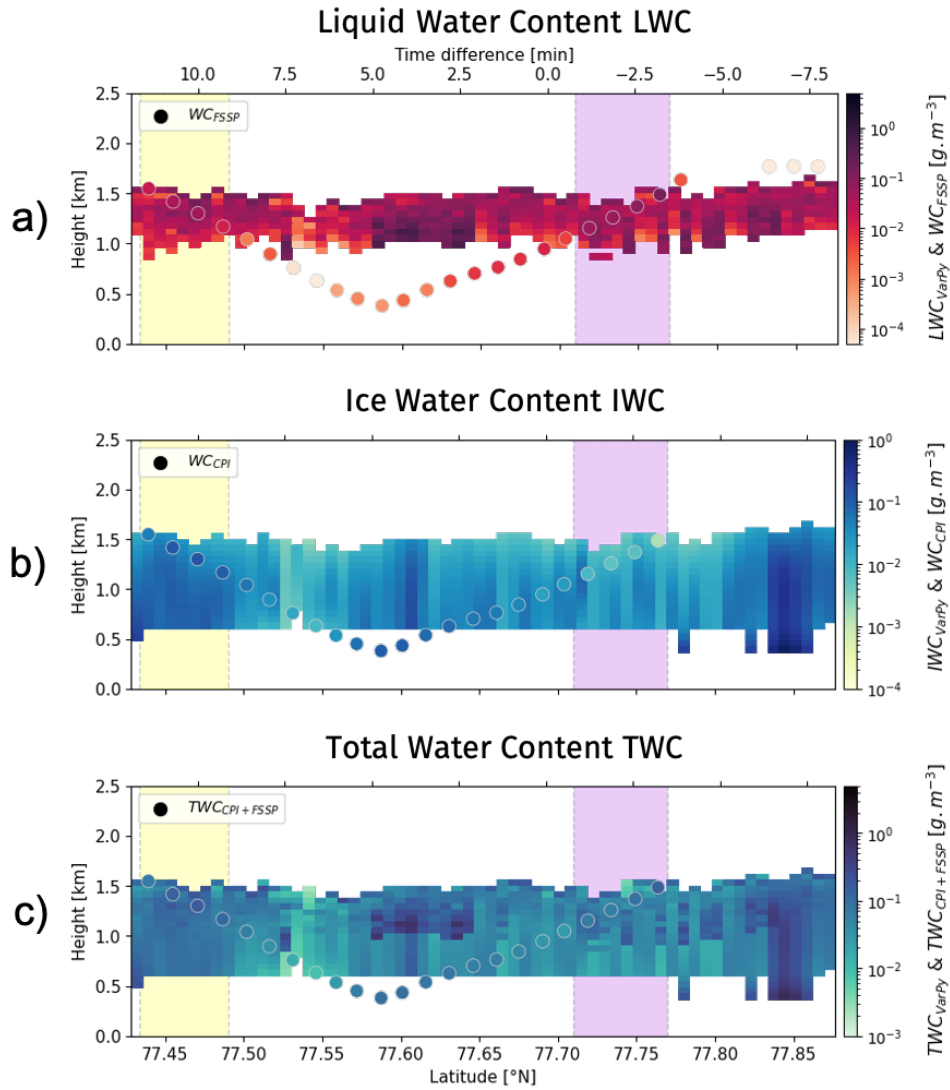


Figure 4.4: Liquid a), ice b) and total c) water content from VarPy-mix retrievals (curtain) and *in situ* probes (dots) regarding the latitude and the height. The yellow and purple shading represents the latitude range where mixed-phase retrievals are compared with *in situ*. All panels share the same abscissa axes (time difference and latitude).

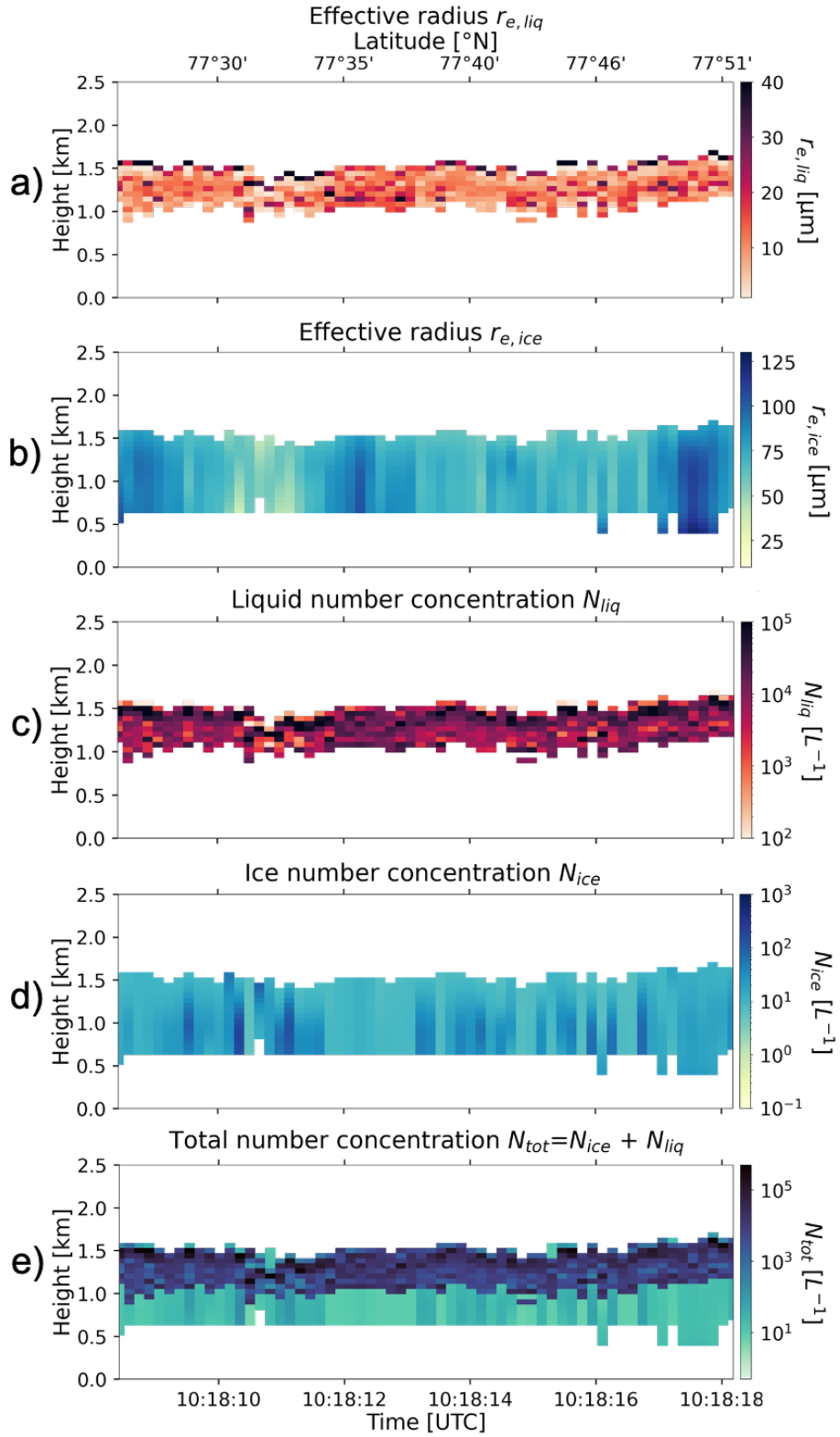


Figure 4.5: Liquid a) and ice b) number concentration and liquid c) and ice d) effective radius retrieved by VarPy-mix. All panels share the same abscissa axes (time and latitude).

Table 4.2: Mean values of retrieved properties.

Properties	Mean
α_{ice}	$1.03 \times 10^{-3} \text{ m}^{-1}$
α_{liq}	$7.28 \times 10^{-3} \text{ m}^{-1}$
α_{tot}	$4.91 \times 10^{-3} \text{ m}^{-1}$
IWC	$5.32 \times 10^{-2} \text{ g.m}^{-3}$
LWC	$6.89 \times 10^{-2} \text{ g.m}^{-3}$
TWC	$8.99 \times 10^{-2} \text{ g.m}^{-3}$
$r_{e,ice}$	75.2 μm
$r_{e,liq}$	13.5 μm
N_{ice}	$2.01 \times 10^{-2} \text{ cm}^{-3}$
N_{liq}	$3.73 \times 10^1 \text{ cm}^{-3}$

4.1.3 . Comparison between VarPy-mix retrievals and *in situ* data

For VarPy-mix, the retrieved total extinction of the mixed-phase layer is higher than the ice layer due to the presence of supercooled liquid droplets (panel c) of Figure 4.3). The extinctions from the CPI and FSSP have been summed in order to compare it to the total extinction of VarPy-mix and the one from the PN. These results are presented in Figure 4.3 c) by the dots and share the same colorscale as VarPy-mix curtain. Above the cloud, where it is clear sky for VarPy-mix (coming from radar and lidar measurements and classifications), the PN detects no particle and CPI+FSSP total extinction is very low (10^{-8} m^{-1} for the FSSP). This demonstrates the consistency between remote sensing and *in situ* measurements. Inside the cloud, we can observe the same trend between VarPy-mix retrieval and probe results, which is mainly different between ice only area and the mixed-phase layer.

In order to provide a more detailed comparison, we keep only the gates from VarPy-mix that are closest to the *in situ* measurements. Figure 4.6 c) displays by dots and lines the total extinction from the probes and from VarPy-mix. The points corresponding to the mixed-phase layer are highlighted on all figures by yellow and purple vertical shading and the others correspond to the ice cloud. Between 77.52 and 77.64° N in Figure 4.6 c), there is no data for VarPy-mix because these points corresponds to ground clutter (ocean) area for the radar. The extinction for mixed-phase is higher than for the ice cloud and this trend is observed for all results. In general, VarPy-mix total extinction is lower than total extinction from probes, especially in regions where cloud phase classification is defined as ice. In these regions the FSSP detects liquid droplets while CALIOP signal cannot be used because of the attenuation

(extinguished). This can explain why α_{VarPy} is lower than $\alpha_{\text{CPI+FSSP}}$.

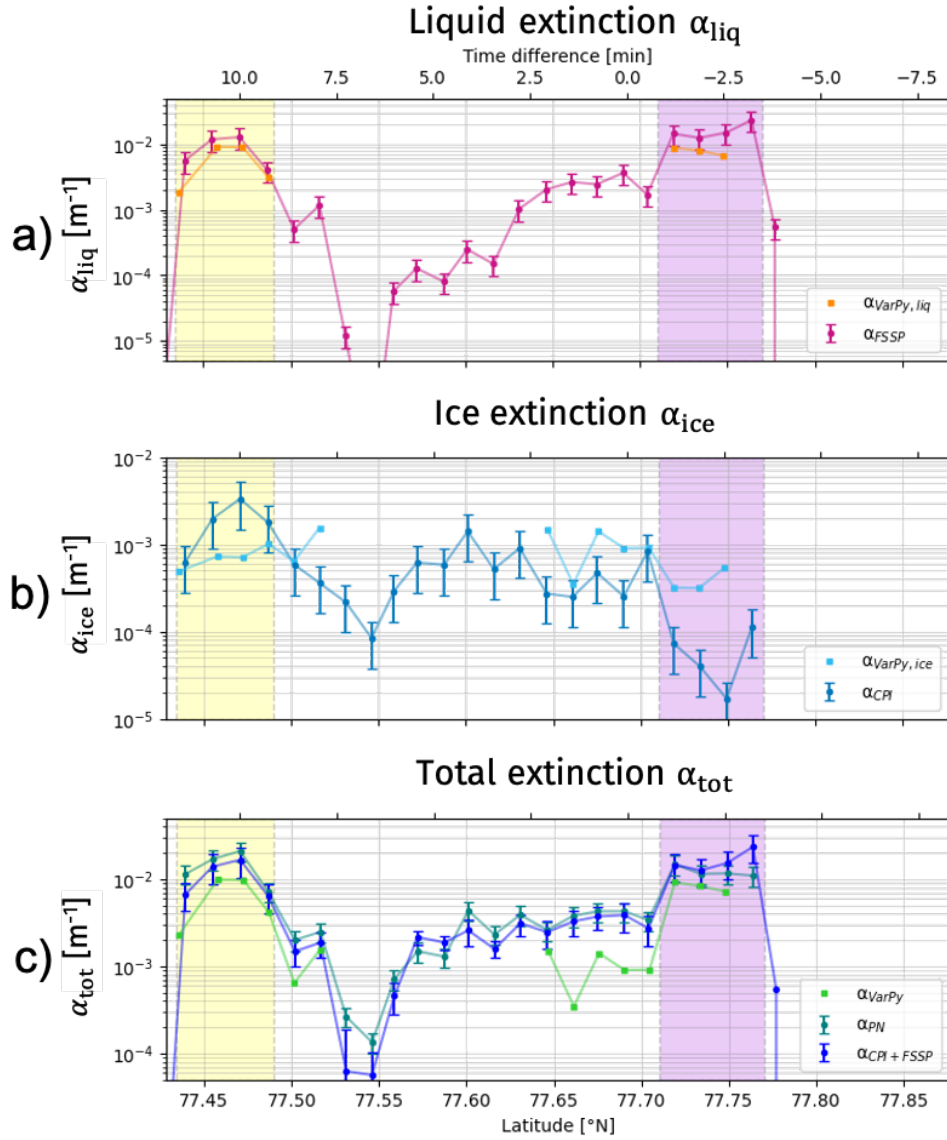


Figure 4.6: Liquid a), ice b) and total c) extinctions from VarPy-mix retrievals (curtain) and *in situ* probes (dots) regarding the latitude. The error bars of *in situ* measurements (uncertainties from Table 4.1) are displayed in each panel. The yellow and purple shading represents the latitude range where mixed-phase retrievals are compared with *in situ*. All panels share the same abscissa axes (time difference and latitude).

Next, in mixed-phase layer, IWC and LWC are both retrieved by VarPy-mix and can be compared to *in situ* data, respectively from the CPI and the FSSP. The TWC is also used in this comparison. The results are shown in all panels of Figures 4.4 and 4.7. In both regions of mixed-phase measurements, the LWC retrieved by VarPy-mix is between 2×10^{-2} and $2 \times 10^{-1} \text{ g.m}^{-3}$ and agree well with the FSSP. Regarding the IWC, both CPI and VarPy-mix retrieve similar trends in these regions. In the region below, due to the extinction of the lidar signal, only ice properties are retrieved by VarPy, but the FSSP detects also liquid in this region which impacts the TWC comparison. For that reason, in this region we only compare the IWC retrieved by VarPy-mix to the IWC from CPI, which are close to each other (40 % mean percent error). For the same reason as for the extinction, the region between 77.52 and 77.64° N cannot be compared.

Finally, for all variables, the mean absolute error (the mean of the absolute difference between each value of VarPy-mix and *in situ*) and the mean percent error regarding *in situ* (the mean of the absolute difference between each value of VarPy-mix and *in situ* divided by *in situ* value and expressed as a percentage) are calculated and are presented in Table 4.3. The liquid extinction retrieved by VarPy-mix differs from *in situ* by 39 %, which is similar to *in situ* uncertainties (35 %), and is the closest to the *in situ* measurements. On the contrary, the mean percent error of ice extinction is 398 %. This can be explained by the large difference around 77.75° N , shown by the purple shading. In addition, the uncertainties of *in situ* probes (Table 4.1) need to be taken into account.

Table 4.3: Mean absolute error and mean percent error for each property regarding *in situ*.

Properties	Mean absolute error	Mean percent error
α_{ice}	$7.2 \times 10^{-4} \text{ m}^{-1}$	398 %
α_{liq}	$4.3 \times 10^{-3} \text{ m}^{-1}$	39 %
α_{tot} (CPI+FSSP)	$3.4 \times 10^{-3} \text{ m}^{-1}$	50 %
α_{tot} (PN)	$4.2 \times 10^{-3} \text{ m}^{-1}$	56 %
IWC	$2.9 \times 10^{-2} \text{ g.m}^{-3}$	75 %
LWC	$2.6 \times 10^{-2} \text{ g.m}^{-3}$	49 %
TWC	$3.0 \times 10^{-2} \text{ g.m}^{-3}$	39 %

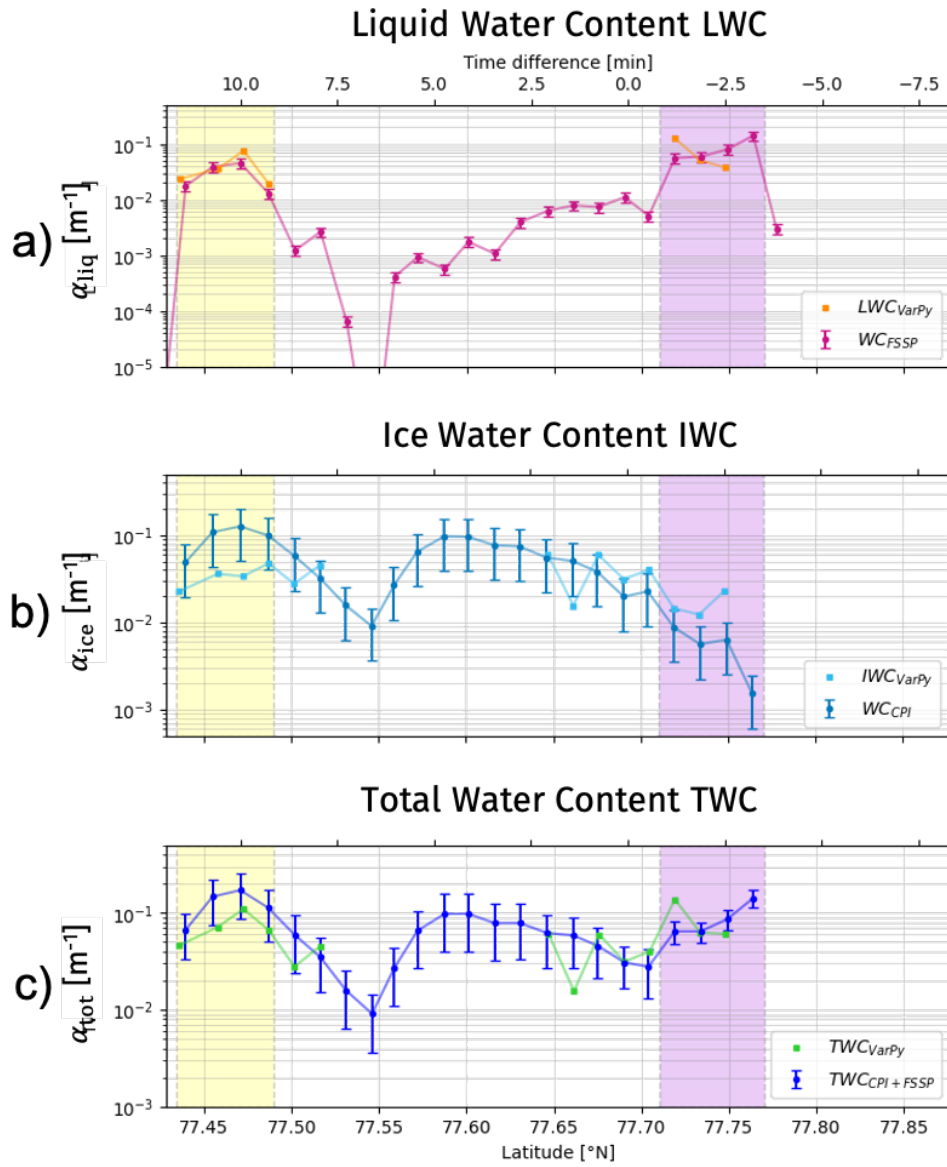


Figure 4.7: Liquid a), ice b) and total c) water content from VarPy-mix retrievals (curtain) and *in situ* probes (dots) regarding the latitude. The error bars of *in situ* measurements (uncertainties from Table 4.1) are displayed in each panel. The yellow and purple shading represents the latitude range where mixed-phase retrievals are compared with *in situ*. All panels share the same abscissa axes (time difference and latitude).

The comparison between VarPy-mix retrieval and the *in situ* measurements is limited by two main considerations:

1. The collocation in space is not perfect which can lead to biases and restrain this study to one case. The Polar-2 aircraft flew almost exactly under CloudSat and CALIPSO trajectory during the third leg by crossing it around 77.6° N. If we do not consider the measurement points above the clouds, the maximum spatial shifts are 1.68 km around 77.44° N and 1.34 km around 77.78° N. In addition, the temporal shift is the best for the third leg with less than ten minutes between the two platforms.
2. The probe sampling volumes are much smaller than those of the remote sensing instruments. Additionally, the vertical (500 m) and horizontal (1.7 km) resolutions of VarPy-mix products are larger than the probe sampling volume.

Another bias source comes from the partial synergy of the VarPy-mix version in the mixed-phase. Indeed, the retrieval relies more strongly on the *a priori* values than when both instruments are used to retrieve ice clouds properties (Delanoë et al. 2013). In addition, the ice cloud is mainly retrieved with radar only. Consequently, in this case the retrieval relies strongly on *a priori* values (which are assumed temperature dependent) and the look up tables, which includes some bias in the comparison with *in situ*. A fully synergistic retrieval would be much more reliable, with both instruments retrieving each part of the mixed-phase. Another possible improvement would be to optimize the LUT, the *a priori* and first guess values for liquid with *in situ* statistics. Additionally, this study focuses on only one case of mixed-phase at high latitude, above the ocean, which does not allow to know how the algorithm would retrieve globally the mixed-phase and the supercooled water.

Finally, VarPy-mix retrieves simultaneously ice and liquid properties of mixed-phase and ice clouds. The comparison with *in situ* measurements validates the retrieval method.

As already stated the method is not limited to satellite measurements. In the next section, I describe two other cases of mixed-phase observed in the Arctic over the ocean, sampled by airborne radar-lidar platforms.

4.2 . VarPy-mix application to airborne platforms during recent campaigns

The two cases presented in this section are mixed-phase layers inside or at the top of Arctic ice clouds. They differ in being observed by two different airborne platforms during two recent campaigns conducted in 2022. For each case, I briefly present the measurement campaign during which the data were collected. Next, I describe the measurements and classifications for each platform, before presenting the results retrieved with VarPy-mix. Finally, as the campaigns are recent, comparison with *in situ* measurements has not yet been done. Consequently I present a comparison with *in situ* data from literature.

4.2.1 . HALO-(AC)³ case study

4.2.1.1 HALO-(AC)³ campaign presentation

The (AC)³ project (Arctic Amplification: Climate relevant Atmospheric and surface processes and feedback mechanisms) aims to perform airborne observations of air-mass transformation processes during meridional transports, especially warm air intrusions and marine cold air outbreaks in the Arctic region. During the HALO-(AC)³ measurement campaign, which was carried out from the 5th March to the 15th April 2022, three aircraft were involved in the measurements: the Polar-5 and Polar-6 aircraft operated by AWI and based in Longyearbyen (Svalbard), and HALO based in Kiruna (Sweden). Numerous *in situ* (Polar 6) and remote sensing (Polar 5 and HALO) instruments have provided huge amounts of data and various collocated situations to characterize clouds in the Arctic region. For this case study, I am interested in the radar MIRA and lidar WALES measurements onboard HALO, whose configurations are presented in Section 2.3.4.

During this campaign, HALO performed seventeen flights illustrated in Figure 4.8. The selected case is part of the scientific flight RF06 operated on the 16th March 2022. This flight is highlighted in blue in Figure 4.8 and the case study in red. The measurements are described in the next subsection.

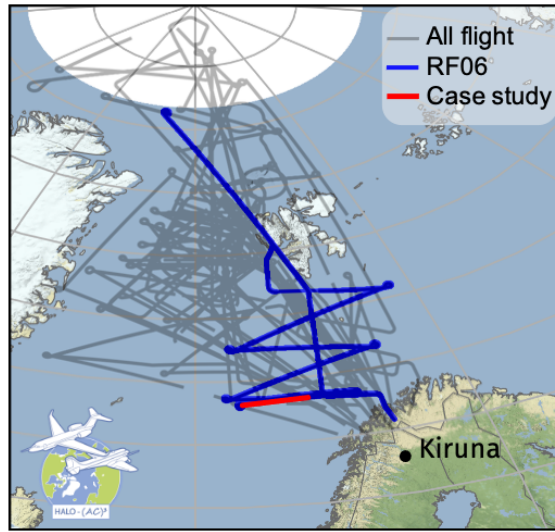


Figure 4.8: Flight tracks during HALO-(AC)³. The flight RF06 is indicated in blue line and the selected case for our study is marked by the red line.

4.2.1.2 MIRA and WALES measurements

The WALES lidar backscatter at 532 nm and the MIRA radar reflectivity at 35 GHz are presented in Figure 4.9 by panels a) and b) respectively. Both instrument signals detect the presence of an ice cloud culminating at an altitude of 8 km. In addition, the high lidar backscatter values ($> 2 \times 10^{-5} \text{ m}^{-1} \cdot \text{sr}^{-1}$) indicates supercooled water droplets layers, which are highlighted by two black boxes. In the same regions, the radar detects ice crystals, revealing mixed-phase layers.

Consequently, the classification for each instrument and the merged radar-lidar classification are determined and are presented in panels c) to e) in Figure 4.9. These classifications are similar to those of DARDAR (see Section 3.2.1) and distinguish between aerosols, rain and cloud phase. Thanks to MIRA sensitivity, the bright band is clearly visible in this case, indicating precipitation from the ice cloud. Finally, radar-lidar classification shows a precipitating ice cloud extending up to 8 km in altitude. This cloud contains mixed-phase layers at two locations, indicated by the black boxes on each panel of Figure 4.9.

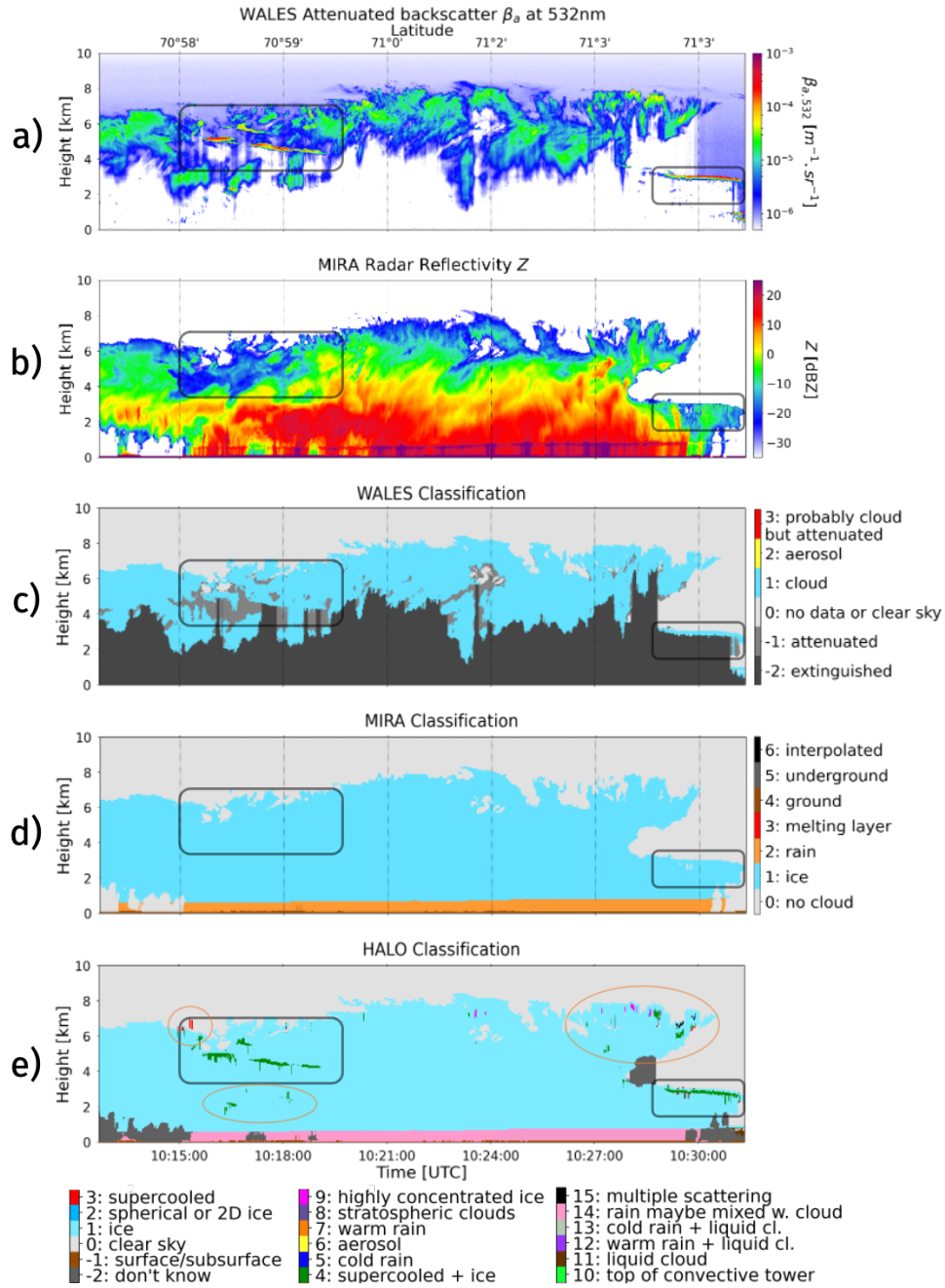


Figure 4.9: WALES lidar attenuated backscatter at 532 nm a), MIRA radar reflectivity at 35 GHz b), WALES classification c), MIRA classification d) and merged classification e) on 16th March 2022 (HALO-(AC)³ RF06). All panels share the same abscissa axes (time and latitude). The black boxes indicate mixed-phase layers. The orange circles identify mixed-phase misclassifications and the red dashed circles indicate supercooled water misclassifications.

For HALO, classifications are not included in the input file and need to be determined by an algorithm external to VarPy-mix (or VarPy-ice) before each processing. To test the algorithm, this step became time-consuming, since the mask required recalculation for each new processing. To overcome this limitation, I developed during this thesis a saving classifications (lidar, radar and radar-lidar) mechanism. The collected data is serialized into binary form using the Python Pickle module allowing lightweight saves and fast loads. This process significantly accelerates the data processing speed of the HALO platform.

Before being used as input to the VarPy-mix algorithm, the radar-lidar classification requires the following corrections:

- The isolated mixed-phase and supercooled water pixels are eroded, as explained in Section 3.2.2.
- Numerous gates have been incorrectly classified as “mixed-phase”, as indicated by the orange boxes in panel e) of Figure 4.9. They have been replaced by ice gates, as shown in the corrected intermediate classification in panel a) of Figure 4.10. This correction type is explained in Section 3.2.2.
- Some gates are incorrectly classified as “supercooled water” or “multiple scattering due to supercooled water”, indicated by red dashed line circles in Figure 4.9. They have been replaced by clear sky in the intermediate classification. Unfortunately, these corrections are never perfect and some gates are still classified as supercooled water.
- The mixed-phase layer thickness must correspond to the layer thickness detected by lidar. Contrary to DARDAR, the gates must be added above the layer to match the measurements. For this case, I added two gates to the valid mixed-phase layers indicated by the black boxes in Figure 4.9.

As a result, I present the corrected intermediate classification in Figure 4.10 as well as the instrument synergy, which is the flag indicating which instrument signal is used to retrieve properties. Nevertheless, all these corrections have to be applied manually, and require a significant amount of time. For example, for the case presented here, there are 1120 profiles composed of 249 gates each, representing 278880 gates to check. As a result, it is impossible to check every single gate and global rules have to be used, implying that some gates may be incorrectly classified.

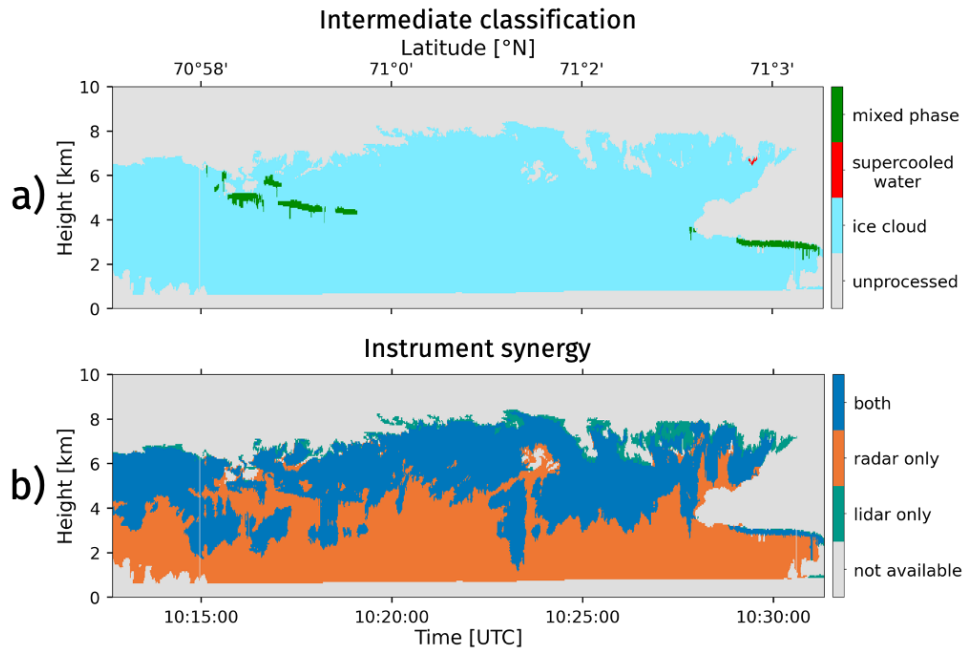


Figure 4.10: Corrected intermediate classification a) and instrument synergy b) for the study case on 16th March 2022 (HALO-(AC)³ RF06). All panels share the same abscissa axes (time difference and latitude).

Finally, all this data is used as input to VarPy-mix to retrieve the ice crystal and supercooled water droplet properties of the observed cloud.

4.2.1.3 VarPy-mix retrievals

VarPy-mix simultaneously retrieves the supercooled water properties with the liquid LUT and the ice crystal properties with the HC LUT selected to process this case. Consequently, liquid and ice microphysical properties retrieved by VarPy-mix are presented in Figures 4.11 (extinctions, α_{ice} and α_{liq}), 4.12 (effective radii, $r_{e,\text{ice}}$ and $r_{e,\text{liq}}$), 4.13 (water contents, IWC and LWC) and 4.14 (particles number concentrations, N_{ice} and N_{liq}). Additionally, the total extinction α_{tot} (Equation 3.44), the total water content TWC (Equation 3.45) and the total concentration N_{tot} (Equation 3.46) are calculated and presented in panel c) of Figures 4.11, 4.13 and 4.14 respectively. In all figures, we observe that the supercooled water properties are retrieved for the mixed-phase layers and that the ice properties are retrieved for both the mixed-phase and the rest of the ice cloud.

Additionally, to analyze the properties of each phase of the mixed-phase, Table 4.4 lists the mean, minimum and maximum values for each variable for the mixed-phase layers.

Table 4.4: Mean, minimum and maximum values for each variables in the mixed-phase (HALO-(AC)³ case study).

Variable	Unit	Mean	Minimum	Maximum
α_{ice}	m^{-1}	2.23×10^{-4}	2.51×10^{-5}	1.97×10^{-3}
α_{liq}	m^{-1}	8.60×10^{-3}	1.13×10^{-7}	3.66×10^{-1}
α_{tot}	m^{-1}	8.98×10^{-3}	5.44×10^{-5}	3.66×10^{-1}
IWC	g.m^{-3}	8.76×10^{-3}	6.63×10^{-4}	8.40×10^{-2}
LWC	g.m^{-3}	9.29×10^{-2}	5.82×10^{-8}	9.75
TWC	g.m^{-3}	1.03×10^{-1}	1.01×10^{-3}	9.76
$r_{e,\text{ice}}$	μm	63.9	31.6	98.0
$r_{e,\text{liq}}$	μm	10.0	0.5	40.0
N_{ice}	cm^{-3}	1.38×10^{-2}	6.06×10^{-4}	2.98×10^{-1}
N_{liq}	cm^{-3}	9.42	1.91×10^{-1}	4.77×10^1
N_{tot}	cm^{-3}	9.58	1.94×10^{-1}	4.77×10^1

Consequently, we can analyze each variable regarding each cloud phase:

- On average, the liquid extinction ($8.60 \times 10^{-3} \text{ m}^{-1}$) is higher than ice extinction ($2.23 \times 10^{-4} \text{ m}^{-1}$) for the mixed-phase. Panel c) of Figure 4.11 highlights this result by revealing high total extinction values for the mixed-phase. Due to the presence of supercooled water droplets in the mixed-phase, the mixed-phase total extinction is higher than the rest of the ice cloud.

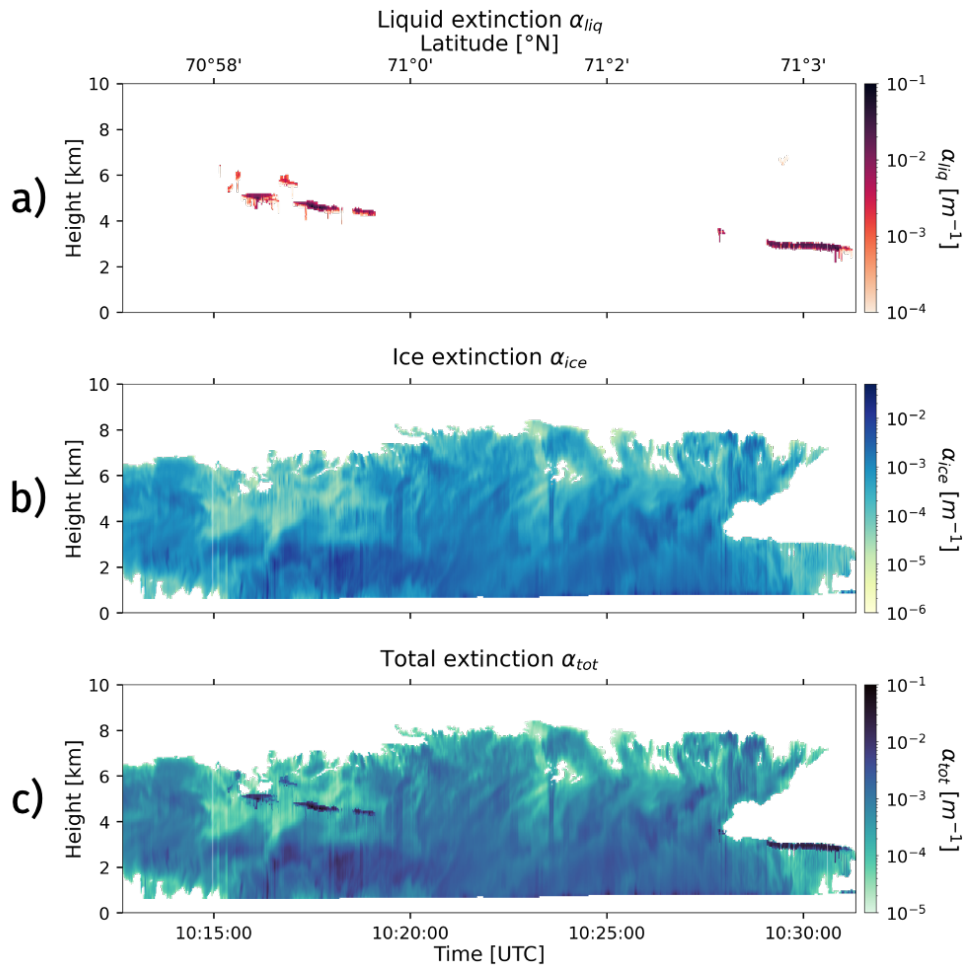


Figure 4.11: Liquid a), ice b) and total c) extinction retrieved by VarPy-mix (HALO-(AC)³ case, RF06). All panels share the same abscissa axes (time difference and latitude).

- As shown in Figure 4.12, the supercooled water droplets effective radius is smaller than the effective radius of the mixed-phase ice crystals, on average by a factor 6. The ice crystals in the mixed phase have an effective radius close to the surrounding ice crystals and larger than the supercooled water in the mixed phase. In addition, we can observe in Figure 4.12 panel b) that the ice crystals are smaller at the top of the cloud and larger at the base.

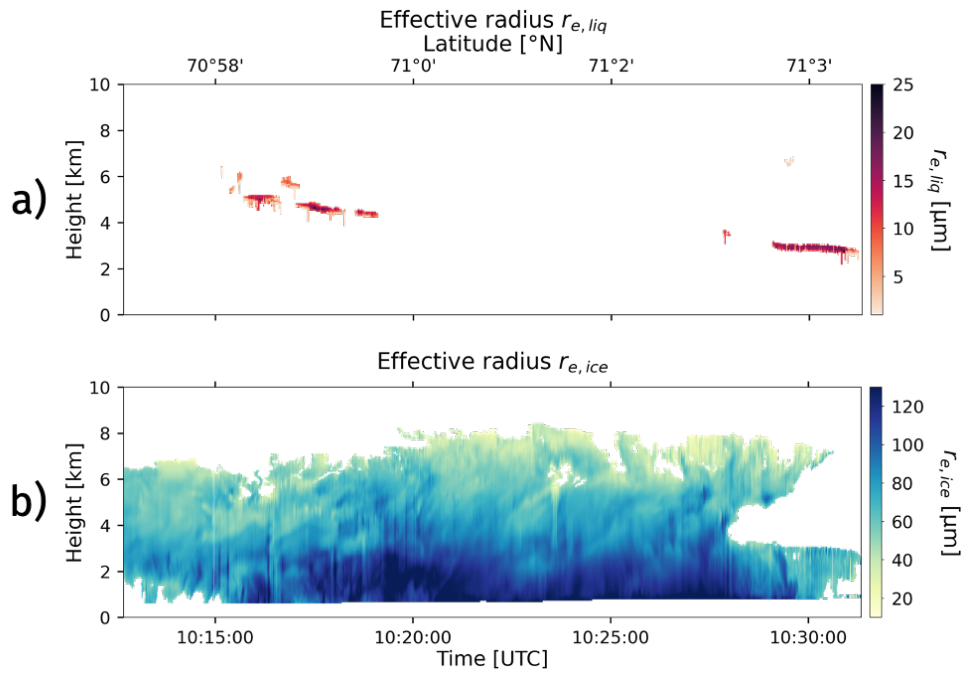


Figure 4.12: Liquid a) and ice b) effective radius retrieved by VarPy-mix (HALO-(AC)³ case, RF06). Both panels share the same abscissa axes (time difference and latitude).

- Regarding water content (Figure 4.13), the observation is the same as for extinction, with lower water content for ice crystals than for supercooled water droplets on average by a factor 10. Additionally, panel c) of Figure 4.13 indicates higher total water content in the mixed-phase than in the rest of the cloud, due to the presence of supercooled water.

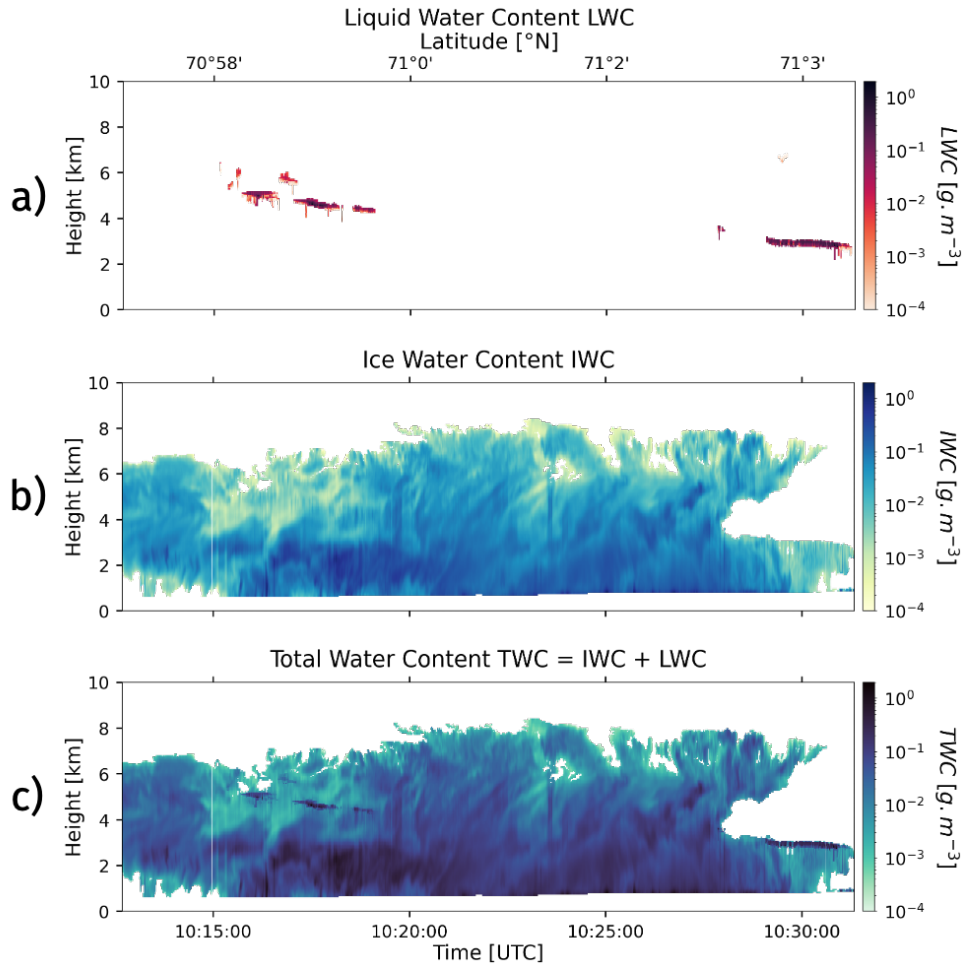


Figure 4.13: Liquid a), ice b) and total c) water content retrieved by VarPy-mix (HALO-(AC)³ case, RF06). All panels share the same abscissa axes (time difference and latitude).

- Figure 4.14 highlights very high concentrations of supercooled water droplets (close to 10^1 cm^{-3}), which are much higher than the ice crystal concentration on average by a factor close to 700.

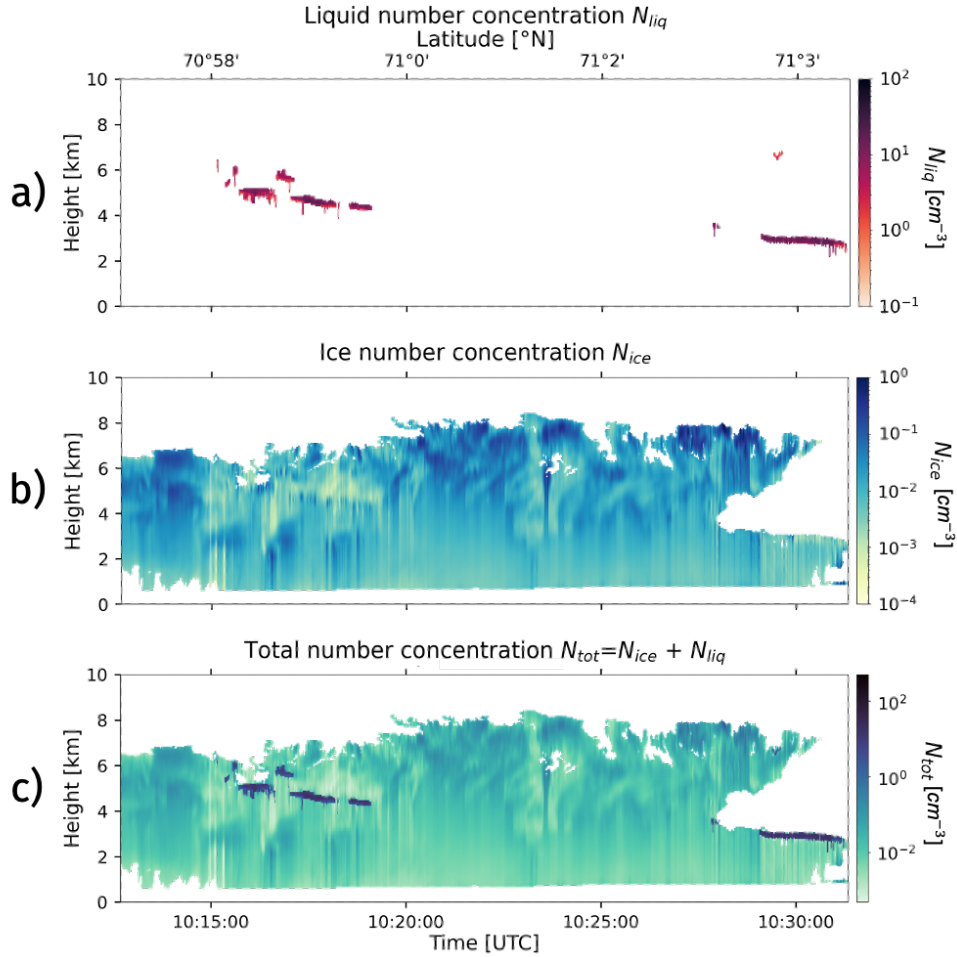


Figure 4.14: Liquid a), ice b) and total c) number concentration retrieved by VarPy-mix (HALO-(AC)³ case, RF06). All panels share the same abscissa axes (time difference and latitude).

In conclusion, the microphysical properties of both the mixed phase and the ice cloud are retrieved by VarPy-mix. The supercooled water properties of the mixed phase differ from those of ice, as in the ASTAR case. Adaptation to an airborne platform requires modifications of the algorithm input data, especially the classification.

4.2.2 . RALI-THINICE case study

4.2.2.1 RALI-THINICE campaign presentation

The THINICE campaign (Rivière et al. 2024) aims to understand Arctic cyclones development and their interaction with tropopause polar vortices, summer sea ice and clouds, in particular mixed-phase clouds. The campaign took place in August 2022 and brings together three measurement platforms:

1. The ATR 42 aircraft operated by SAFIRE. It was based in Longyearbyen (Svalbard) during the period of the RALI-THINICE campaign, the French branch of the THINICE. The aircraft carried the RALI remote sensing platform (described in Section 2.3.3) as well as six *in situ* probes, including the CDP, the PN and the 2D-S (described in Section 2.1).
2. The Twin Otter aircraft operated by the British Antarctic Survey was flying at low altitude to measure turbulent fluxes in the atmospheric boundary layer and characterize the sea-ice and its interaction with the lower troposphere.
3. Instrumented balloons operated by Windborne Systems sample Arctic cyclone and tropopause polar vortices over long periods.

During RALI-THINICE, the ATR 42 performed sixteen flights, illustrated in Figure 4.15. The studied case is the scientific flight F53, indicated by the thickened orange line in Figure 4.15. The measurements are described in the next subsection.

4.2.2.2 RASTA and LNG measurements

The LNG lidar backscatter at 532 nm and the RASTA radar reflectivity at 95 GHz are presented in Figure 4.16 by panels a) and b) respectively. The ATR 42 altitude is indicated on both panels by the magenta line revealing that the aircraft first flew above the clouds before lowering its altitude and flying inside the clouds on three different levels. On the one hand, the lidar backscatter signal indicates several supercooled water layers and the presence of ice crystals in some areas. Below supercooled water layers, the lidar signal is extinguished and consequently detects nothing below these layers. On the other hand, the radar reflectivity shows ice clouds extending from 6 km to the ground (ocean and sea ice). Where the lidar detects supercooled water, the radar signal indicates the presence of ice crystals, revealing mixed-phase layers at the top and inside the ice clouds. Furthermore, for the mixed-phase layers at the cloud top, the radar does not detect ice crystals on top of these layers, revealing a pure supercooled water layer above these mixed-phase layers.

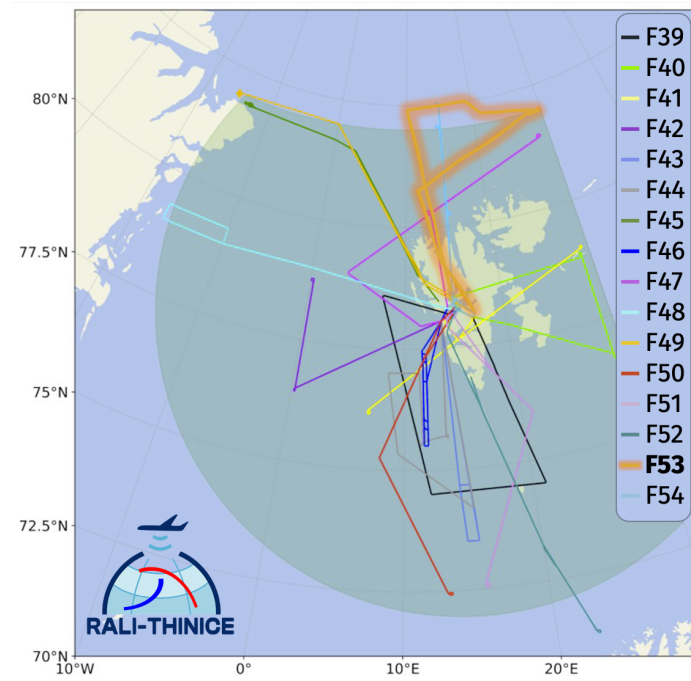


Figure 4.15: Flight tracks during RALI-THINICE. The selected case for our study is the flight F53, indicated by the thickened orange line.

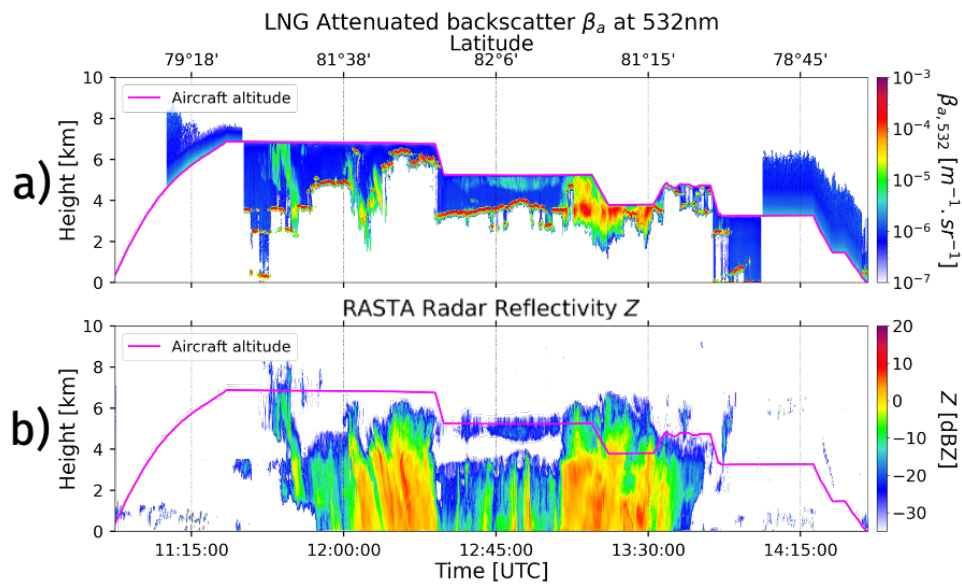


Figure 4.16: LNG lidar attenuated backscatter at 532 nm a) and RASTA radar reflectivity at 95 GHz b) on 25th August 2022 (RALI-THINICE, F53). Both panels share the same abscissa axes (time and latitude). The magenta line indicates the ATR 42 altitude.

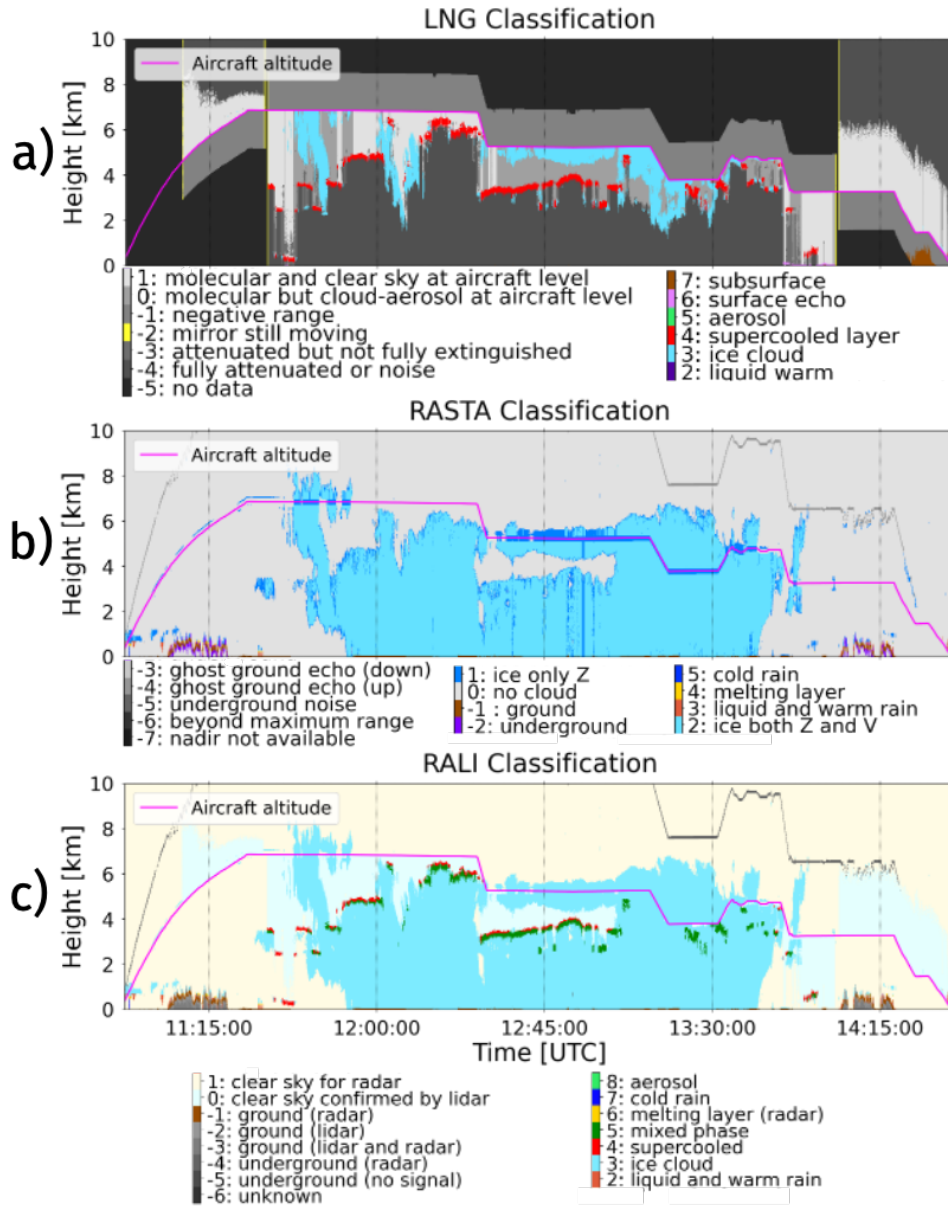


Figure 4.17: LNG lidar classification a), RASTA radar classification b) and RALI radar-lidar classification on 25th August 2022 (RALI-THINICE, F53). All panels share the same abscissa axes (time and latitude). The magenta line indicates the ATR 42 altitude.

The radar, lidar and merged radar-lidar classifications are presented in Figure 4.17 and displays the various mixed-phase layers identified as well as the ice cloud. RALI platform classifications are obtained by a complete processing chain external to VarPy (like DARDAR-MASK) and are supplied in the same file as the measurements. The RALI processing chain has recently been re-

refurbished and the supercooled water detection is slightly more sophisticated than for the HALO and DARDAR-MASK platforms. In the analyzed case, no mask correction has been performed.

As a result, I present the intermediate classification and the synergy instrument used by VarPy-mix to process the data in Figure 4.18. We can observe that some profiles are missing, meaning that VarPy-mix has encountered a convergence problem for these profiles. In this case, the instrument synergy indicates that the properties of the majority of the ice cloud are retrieved by only the radar, while the mixed-phase layers are retrieved by both instruments. Consequently, few ice areas are retrieved by the radar-lidar synergy for this case.

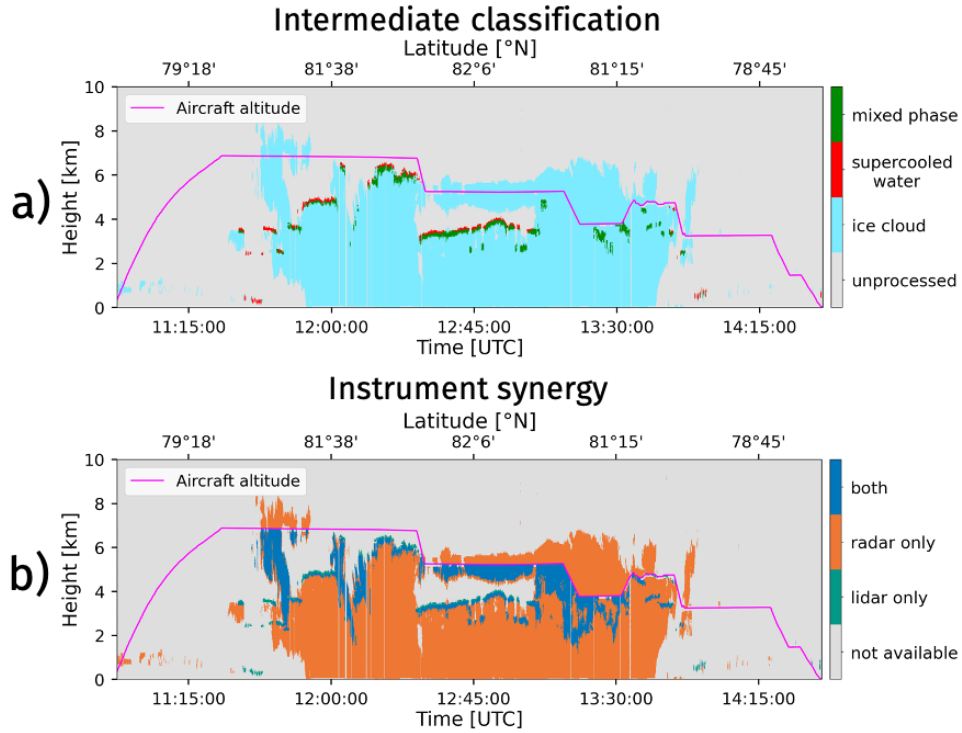


Figure 4.18: Intermediate classification a) and instrument synergy b) for the study case on 25th August 2022 (RALI-THINICE, F53). The magenta line indicates the ATR 42 altitude.

Finally, all this data is used as input to VarPy-mix to retrieve the ice crystals and supercooled water droplet properties of this case. The results are presented in the next subsection.

4.2.2.3 VarPy-mix retrievals

As for the HALO-(AC)³ case, the supercooled water properties are retrieved with the liquid LUT and the ice crystals properties with the HC LUT. Consequently, liquid and ice microphysical properties retrieved by VarPy-mix are presented in Figures 4.19 (extinctions, α_{ice} and α_{liq}), 4.20 (effective radii, $r_{e,\text{ice}}$ and $r_{e,\text{liq}}$), 4.21 (water contents, IWC and LWC) and 4.22 (particles number concentrations, N_{ice} and N_{liq}). In addition, the total extinction α_{tot} (Equation 3.44), the total water content TWC (Equation 3.45) and the total concentration N_{tot} (Equation 3.46) are calculated and presented in panel c) of Figures 4.19, 4.21 and 4.22 respectively. In all figures, we observe that the supercooled water properties are retrieved for the mixed-phase layers and that the ice properties are retrieved for both the mixed-phase and the rest of the ice cloud. Contrary to the HALO-(AC)³ case, the mixed-phase layers detected by RALI are more numerous, which allows us to establish more general trends regarding retrieval behavior.

Table 4.5 lists the mean, minimum and maximum values for each variable for the mixed-phase layers.

Table 4.5: Mean, minimum and maximum values for each variables in the mixed-phase (RALI-THINICE case study).

Variable	Unit	Mean	Minimum	Maximum
α_{ice}	m^{-1}	1.54×10^{-4}	1.51×10^{-6}	3.80×10^{-3}
α_{liq}	m^{-1}	1.29×10^{-2}	1.33×10^{-6}	5.38
α_{tot}	m^{-1}	1.34×10^{-2}	9.68×10^{-6}	5.38
IWC	g.m^{-3}	6.58×10^{-3}	3.26×10^{-5}	1.48×10^{-1}
LWC	g.m^{-3}	1.94×10^{-1}	6.98×10^{-7}	3.33×10^2
TWC	g.m^{-3}	2.30×10^{-1}	7.17×10^{-5}	3.33×10^2
$r_{e,\text{ice}}$	μm	56.3	5.1	134.4
$r_{e,\text{liq}}$	μm	12.1	0.8	92.9
N_{ice}	cm^{-3}	2.05×10^{-2}	1.31×10^{-4}	3.53×10^1
N_{liq}	cm^{-3}	1.17×10^1	4.46×10^{-1}	1.30×10^2
N_{tot}	cm^{-3}	1.16×10^1	4.49×10^{-1}	1.30×10^2

As for the HALO-(AC)³ case, we compare each variable regarding each cloud phase:

- The liquid extinction is on average higher than the ice extinction by a factor close to 10^2 . In addition, the total extinction reveals higher values in the mixed-phase layer than for the ice clouds. This is explained by the high supercooled water extinction.

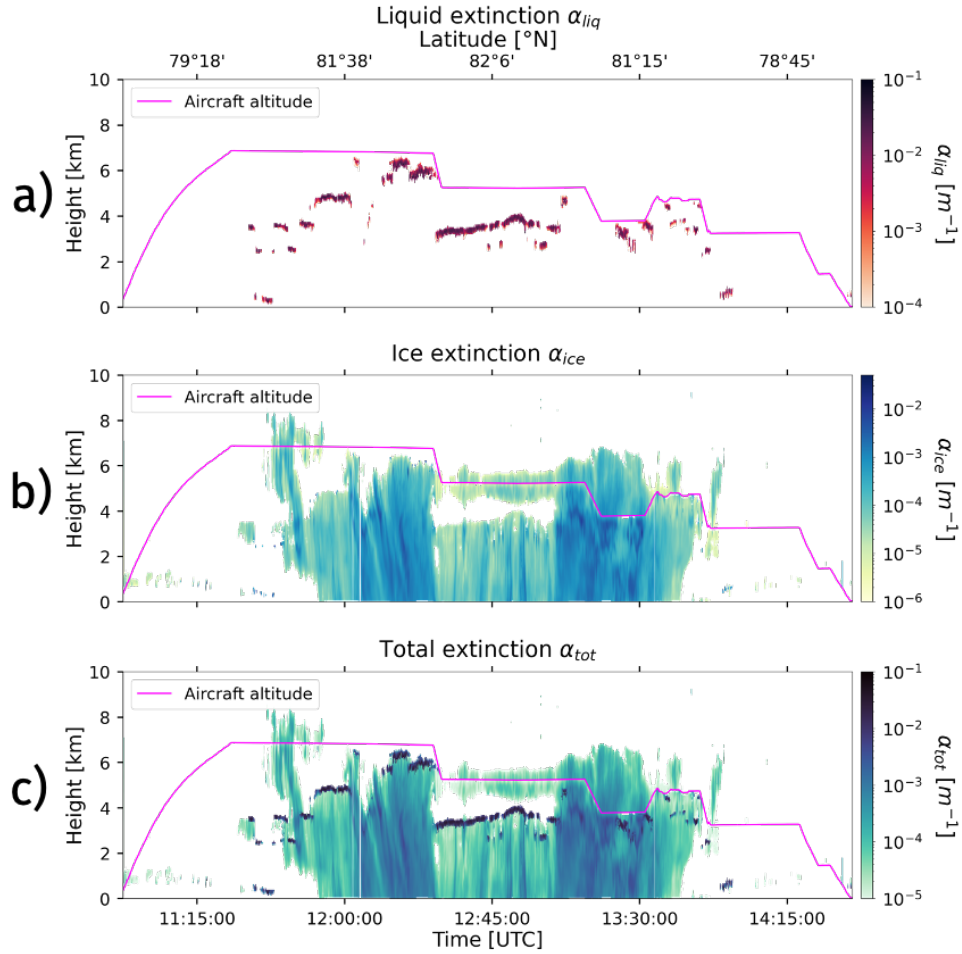


Figure 4.19: Liquid a), ice b) and total c) extinction retrieved by VarPy-mix (RALI-THINICE case, F53). All panels share the same abscissa axes (time difference and latitude). The magenta line indicates the ATR 42 altitude.

- In the mixed-phase layers, supercooled water droplets are on average five times smaller than ice crystals. For ice clouds, two trends can be observed: one cloud area (between 12:30 and 13:00) seems to have ice crystals whose size varies very slightly with altitude and other cloud sections where crystal size increases as altitude decreases.

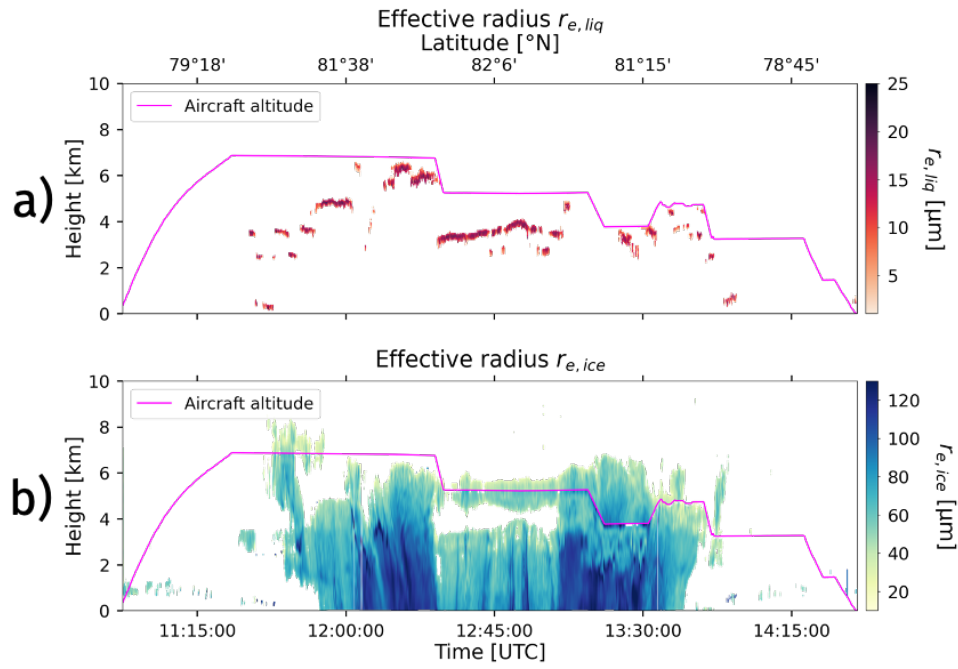


Figure 4.20: Liquid a) and ice b) effective radius retrieved by VarPy-mix (RALI-THINICE case, F53). Both panels share the same abscissa axes (time difference and latitude). The magenta line indicates the ATR 42 altitude.

- LWC in the mixed-phase are on average higher than IWC by a factor 30. The presence of supercooled water droplets increases the TWC of the mixed-phase layers, as shown in panel c) of Figure 4.21.

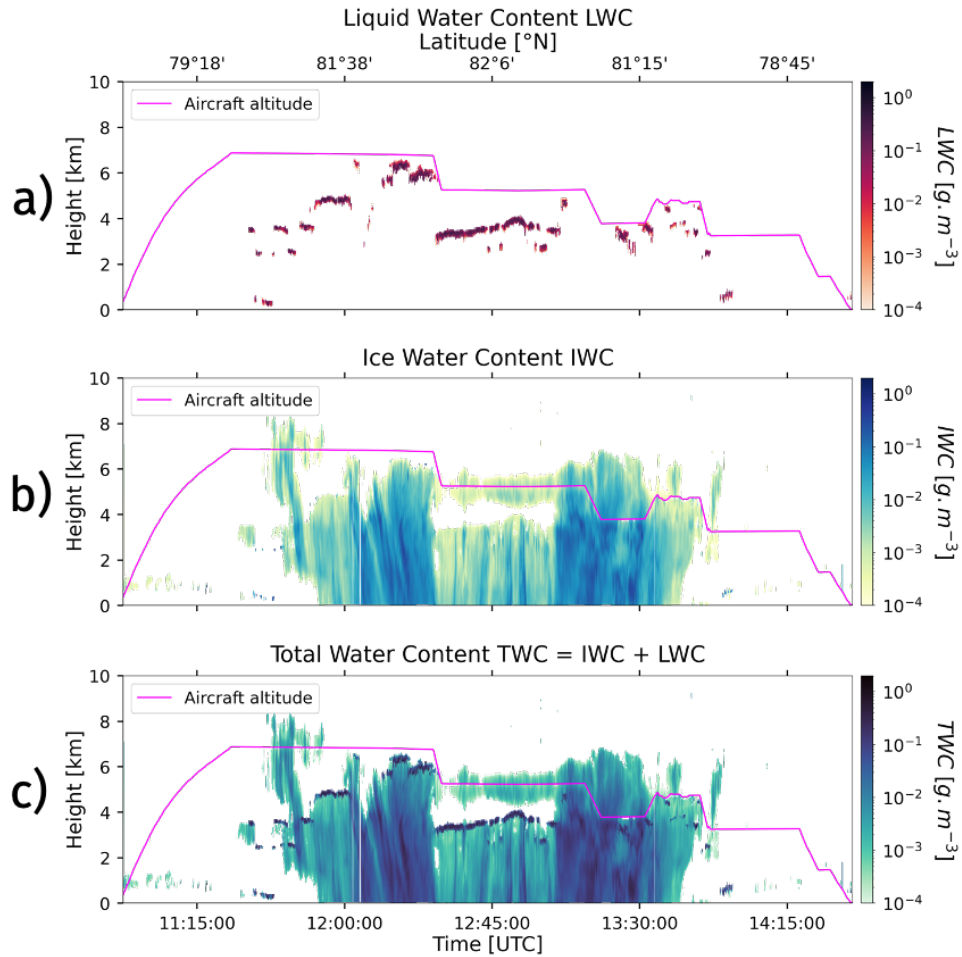


Figure 4.21: Liquid a), ice b) and total c) water content retrieved by VarPy-mix (RALI-THINICE case, F53). All panels share the same abscissa axes (time difference and latitude). The magenta line indicates the ATR 42 altitude.

- The ice crystals are almost 600 less concentrated than supercooled water droplets in all mixed-phase layers. This difference is shown in panel c) of Figure 4.22.

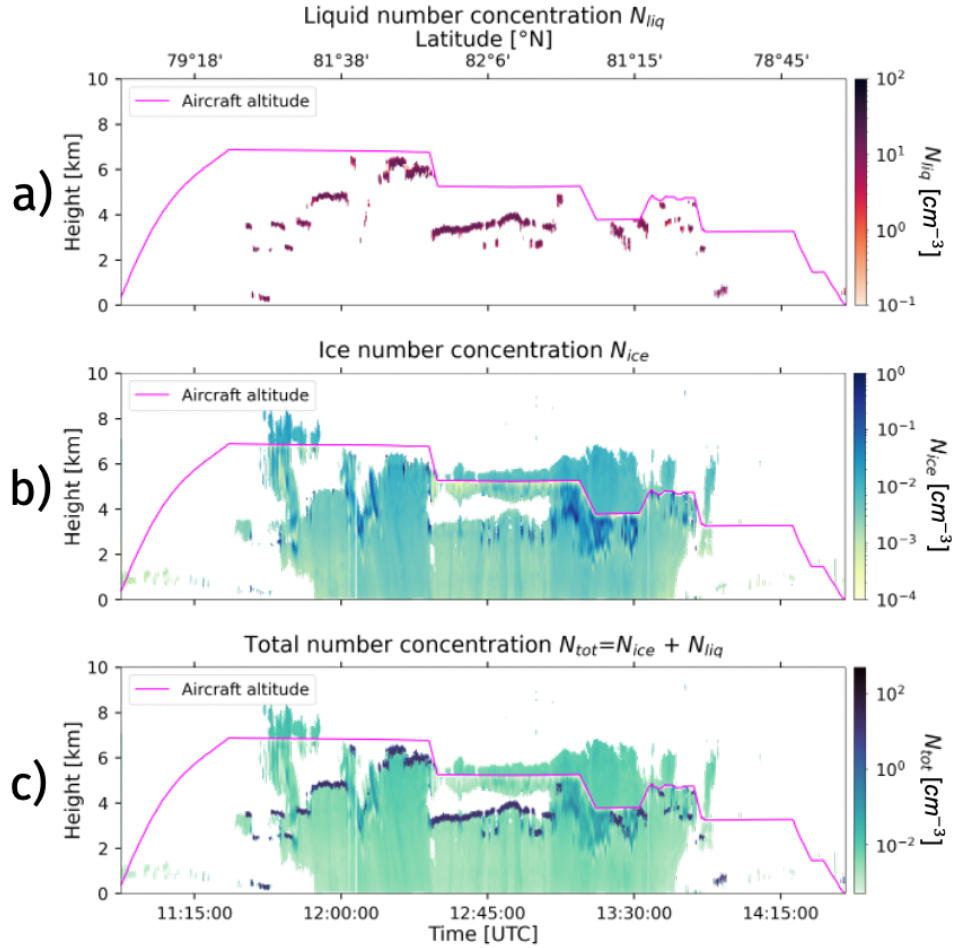


Figure 4.22: Liquid a), ice b) and total c) number concentration retrieved by VarPy-mix (RALI-THINICE case, F53). All panels share the same abscissa axes (time difference and latitude). The magenta line indicates the ATR 42 altitude.

Finally, ice crystals and supercooled water droplets properties can also be retrieved from the RALI airborne platform. As for the ASTAR case, the HALO-(AC)³ and RALI-THINICE cases similarly involve collocations between radar-lidar and *in situ* measurements. However, these campaigns are recent and comparisons have not yet been made. Therefore, we cannot assess the algorithm by comparing these cases with *in situ* measurements from the associated campaign, but this could be the subject for a future study. Consequently,

in the following subsection, I compare the results obtained by VarPy-mix for the ASTAR, HALO-(AC)³ and RALI-THINICE cases with *in situ* data from the scientific literature to assess the retrievals.

4.2.3 . Comparison with *in situ* data from literature

To observe the trend in the microphysical properties retrieved by VarPy-mix, I compare the results obtained for each presented case (ASTAR, HALO-(AC)³ and RALI-THINICE) to each other and to the results derived from *in situ* data and presented by Mioche and Jourdan 2018 (hereafter referred to as MJ18). The ice properties are from the CPI probe and the liquid droplets properties are from the FSSP probe, collected during four measurement campaigns: ASTAR 2004 (Jourdan et al. 2010) and 2007 (Gayet et al. 2009), POLAR-CAT 2008 (Delanoë et al. 2013) and SORPIC 2010 (Bierwirth et al. 2013). These results are presented in Figure 4.23. On the one hand, the top panels are the liquid extinction α_{liq} a), the liquid droplet number concentration N_{liq} b), the liquid water content LWC c) and the liquid droplet effective diameter $D_{e,\text{liq}}$ d). On the other hand, the lower panels are the ice extinction α_{ice} a), the ice crystal number concentration N_{ice} b), the ice water content IWC c) and the ice crystals effective diameter $D_{e,\text{ice}}$ d).

To compare the properties retrieved by VarPy-mix with these *in situ* data, I selected the mixed-phase gates for each variable and represented them as point density distributions with ice properties on the abscissa axis and liquid water droplet properties on the ordinate axis. These results are obtained for each case (ASTAR, HALO-(AC)³ and RALI-THINICE) and are presented in Figures 4.24 and 4.25. In addition, an average value estimated from the *in situ* data is represented by the magenta dot for each variable on these Figures, along with the mean standard deviation.

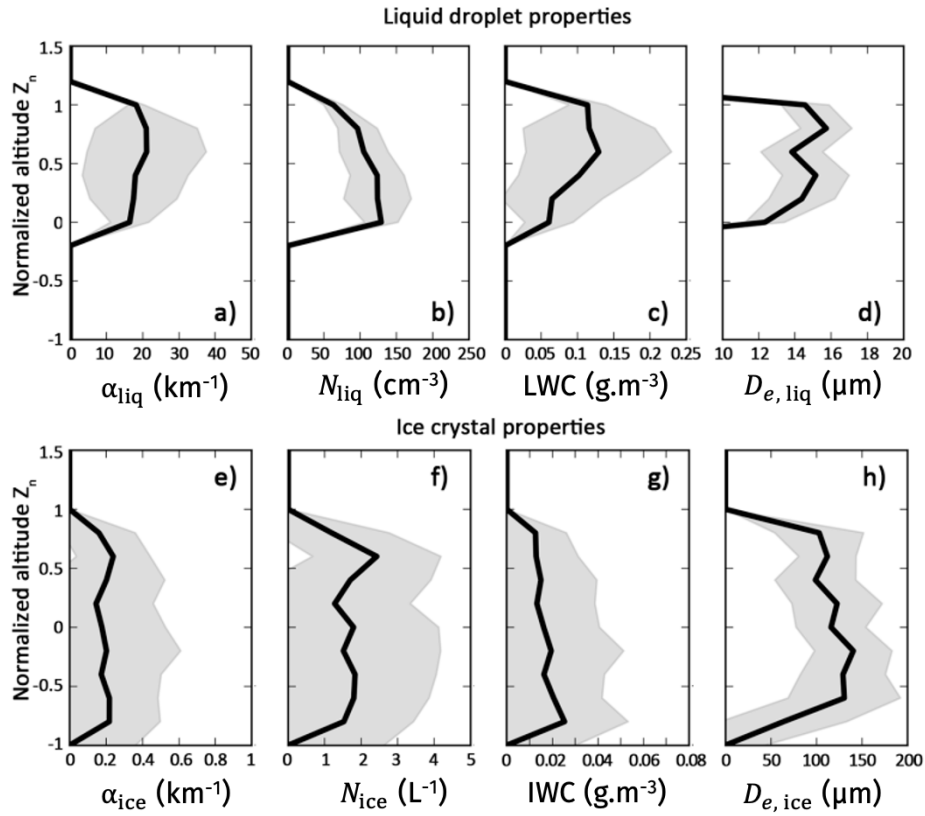


Figure 4.23: Liquid extinction a), droplet number concentration b), liquid water content c) and droplet effective diameter d) from the FSSP and ice extinction e), ice crystal number concentration f), ice water content g) and ice crystal effective diameter h) from the CPI, collected during the four airborne Arctic campaign (ASTAR 2004 and 2007, POLARCAT 2008 and SORPIC 2010). For each panel, the black line represents the average vertical profile over all the campaigns and the grey shaded area indicates the standard deviation. The Figure is from Mioche and Jourdan [2018](#).

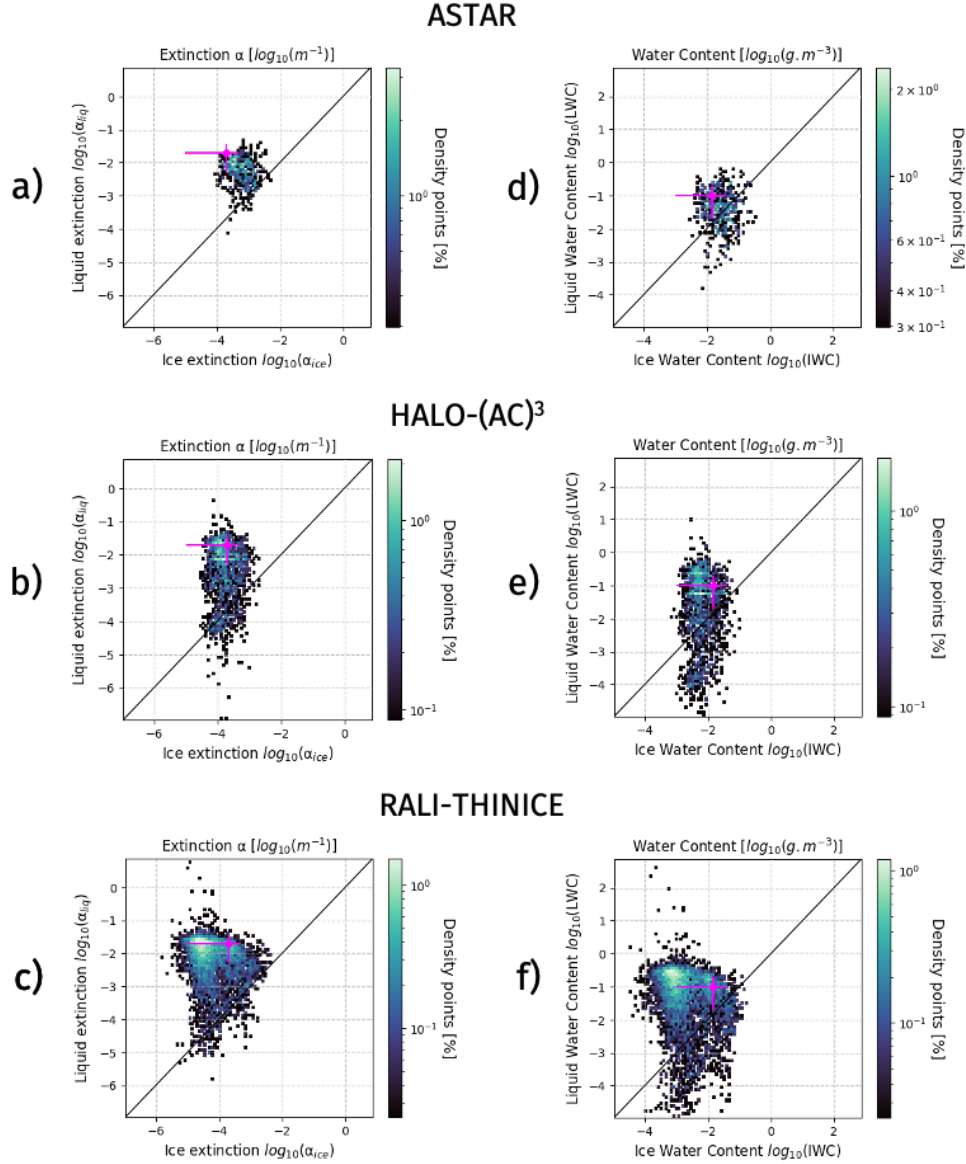


Figure 4.24: Comparison between ice and liquid properties of the mixed-phase retrieved by VarPy-mix and compare to the *in situ* data from Mioche and Jourdan 2018. Left panels: ice and liquid extinction for the ASTAR a), HALO-(AC)³ b) and the RALI-THINICE c) cases. Right panels: ice and liquid water content for the ASTAR d), HALO-(AC)³ e) and the RALI-THINICE f) cases. For all panels, the *in situ* mean values are represented by the magenta dot and the mean standard deviation are represented by magenta lines.

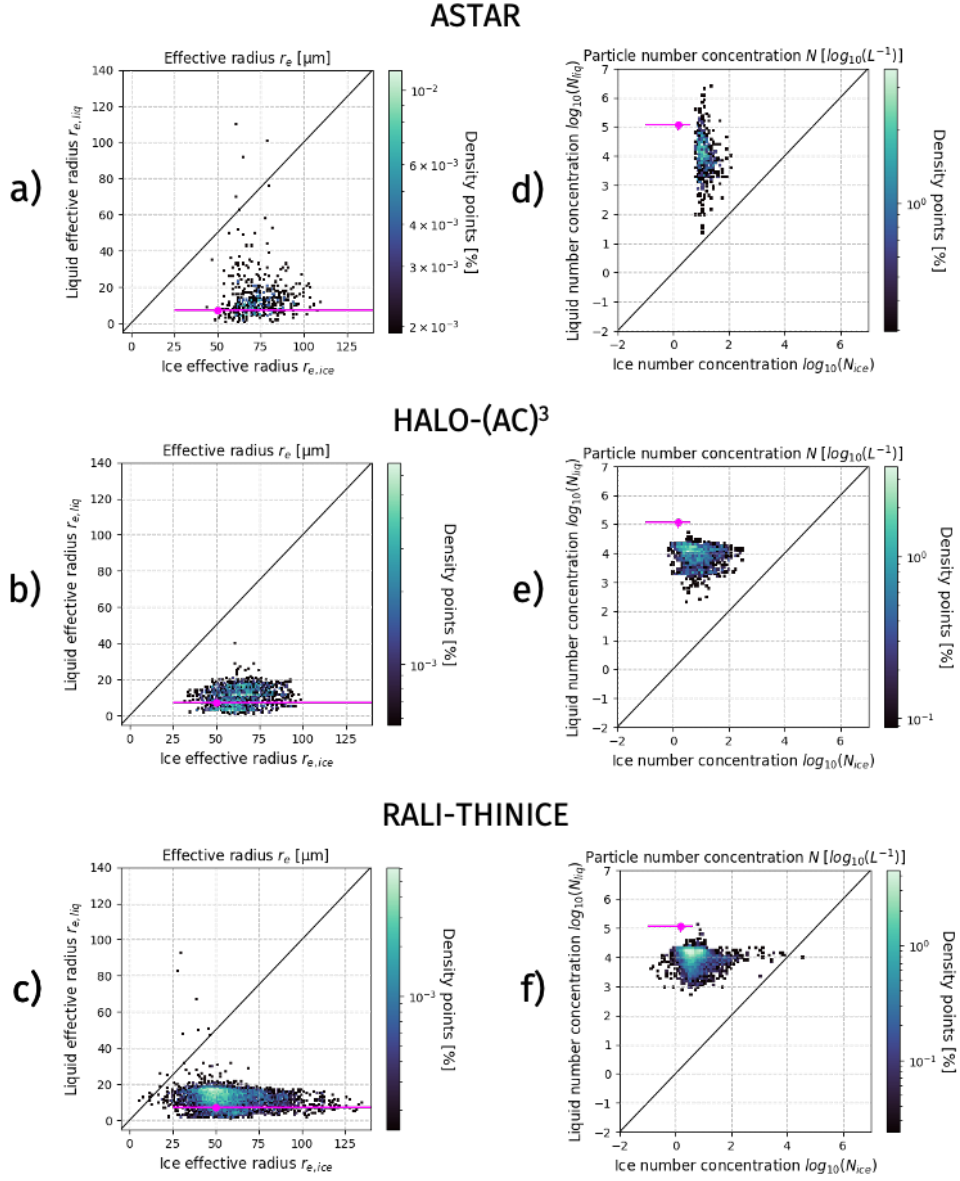


Figure 4.25: Comparison between ice and liquid properties of the mixed-phase retrieved by VarPy-mix and compare to the *in situ* data from Mioche and Jourdan 2018. Left panels: ice crystals and liquid droplets effective radius for the ASTAR a), HALO-(AC)³ b) and the RALI-THINICE c) cases. Right panels: ice crystals and liquid droplets number concentration for the ASTAR d), HALO-(AC)³ e) and the RALI-THINICE f) cases. For all panels, the *in situ* mean values are represented by the magenta dot and the mean standard deviation are represented by magenta lines.

First, for each variable, we can observe similar trends between the three processed cases:

- Panels a) to c) in Figure 4.24: The liquid extinction is globally higher than the ice extinction, with some values close to each other and very few higher for the ice than for liquid. The liquid extinction value range is larger than the ice extinction value range.
- Panels d) to f) in Figure 4.24: The same trend as the extinction is observed between liquid and ice water content, with LWC overall higher than IWC.
- Panels a) to c) in Figure 4.25: The liquid droplet effective radius is between 0.5 and 40 μm , much smaller than the ice crystals effective radius, which range from 20 to 135 μm .
- Panels d) to f) in Figure 4.25: The distribution between HALO-(AC)³ and RALI-THINICE cases is quite similar but differs from the ASTAR case distribution, which has more dispersed liquid droplet number concentration values. Globally, liquid droplets number concentration values are higher than ice crystal values.

In addition, these trends tend to be consistent with MJ18 *in situ* values. For each case, the retrieved extinction values are close to the average ice and liquid extinction value from MJ18. The same applied to the ice and liquid water content and effective radius. However, the ice crystal number concentration of the ASTAR case is higher than the one distribution from MJ18. For HALO-(AC)³ and RALI-THINICE cases, N_{ice} values are close to the values from MJ18, but most values are below the range obtained by MJ18. For N_{liq} , the HALO-(AC)³ and RALI-THINICE cases values are lower than the one from MJ18. Some N_{liq} values retrieved for the ASTAR case are close to the values from MJ18.

To conclude, the trend of the microphysical properties retrieved for the mixed phase by the VarPy-mix algorithm is close to the trends obtained by *in situ* measurements present in the literature for four measurement campaigns. This comparison assesses our algorithm, but also shows that it needs to be compared with other *in situ* measurements to better evaluate and improve it.

4.3 . Comparison between VarPy-ice, 2C-ICE and *in situ*

In this section, I present the summary of a study conducted with Stephen Nicholls and Andrew Heymsfield to compare VarPy-ice and 2C-ICE (Deng et al. 2010, 2013) retrievals on radar-lidar data from the IMPACTS 2020 measurement campaign (McMurdie et al. 2022). These retrievals are compared with *in situ* measurements collected during the campaign as reference. This study has been accepted for publication in the Journal of Atmospheric and Oceanic Technology and is included in Appendix A. For this publication, I worked on adapting the VarPy-ice algorithm to the radar CRS and the lidar CPL data from the ER-2 platform. Both instruments are described in Section 2.3.5. In particular, this has involved creating radar, lidar and radar-lidar classifications corresponding to the needs of the algorithm from several classifications provided for each instrument. Following this, I processed the campaign data with VarPy-ice, for each of the two available LUTs (HC and BF, Section 3.1.2, page 110). In addition, I took part in the writing of the article and its proofreading.

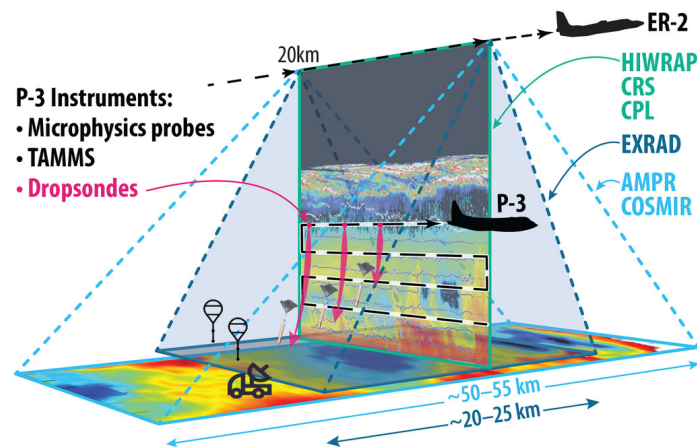


Figure 4.26: Instruments onboard the ER-2 and P-3 aircraft (from McMurdie et al. 2022). The viewing geometry of the different instruments is indicated with dashed colored lines. The surface radars and mobile soundings are represented by the balloons and truck symbols.

The Investigation of Microphysics and Precipitation for Atlantic Coast-Threatening Snowstorms (IMPACTS, McMurdie et al. 2022) field campaign was conducted by the NASA in January and February 2020, 2021 and 2022. During six weeks, the ER-2 and P-3 aircraft flew over the East Coast of United States to chase winter storms with several *in situ* (P-3) and remote sensing (ER-2) instruments, described in McMurdie et al. 2022. Additionally, the P-3 released dropsondes over the ocean. Figure 4.26 lists the instruments onboard each aircraft and shows that ER-2 flew at an altitude of around 20 km, while P-3 flew at a lower altitude inside the clouds. Some flights were colocated between

the two aircraft to compare *in situ* information with remote sensing measurements. All the flights from the 2020 campaign are illustrated in Figure 4.27.

The remote sensing measurements used for the comparison study are the lidar backscatter at 532 nm from CPL and the radar reflectivity at 95 GHz from CRS. The data from these instruments had never been processed by VarPy-ice. Consequently, I introduced the processing of this data to VarPy-ice, notably a method to obtain classifications compatible with the algorithm. Indeed, the provided radar classification does not distinguish between ice clouds and precipitation, but only between clear sky and particle detection. Consequently, I improved the classification by distinguishing precipitation when the temperature is positive. In addition, the provided radar classification was noisy due to numerous isolated gates in clear sky. As a result, these gates have been eroded. For the lidar classification, I merged the two classifications provided. The first distinguishes between clear sky, aerosols and clouds, while the second distinguishes between cloud phase (liquid and ice). Finally, as no radar-lidar classifications were provided, I created one from the previously produced radar and lidar classifications.

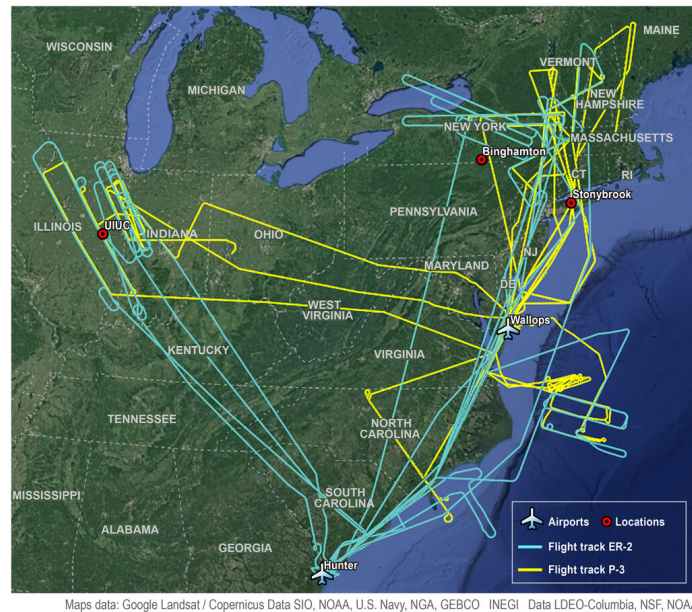


Figure 4.27: Flight tracks of the ER-2 (blue) and P-3 (yellow) aircraft during IMPACTS 2020. Airplane symbols indicate the used airports and red dots indicate home-base locations used for mobile sounding launches.

Four flights were selected and the collocation cases were chosen according to the distance (5 km) and crossing time (10 minutes) between the two aircraft.

In total, 8425 observations between 0 and -25°C are used for the comparison study and are separated into five temperature categories. Further information on data numbers per category is provided in Appendix A.

For this study, the two retrieval algorithms compared are VarPy-ice (described in Section 3.1) and 2C-ICE described in Section 1.2 of Appendix A. In addition, these retrievals are compared with *in situ* data onboard P-3 and the mass-size relationships of Brown and Francis 1995 and Heymsfield et al. 2014. The results are shown in pages 18 to 22 and in the Supplement of Appendix A. Regarding VarPy-ice, the study results show that:

- VarPy-ice using BF LUT (hereafter VarPy-BF), VarPy-ice using HC LUT (hereafter VarPy-HC) and 2C-ICE exhibit similar degrees of spread and divergence from P-3 cloud probes measurements for the extinction values. Nevertheless, 2C-ICE and both VarPy versions retrieval differs with decreasing temperature.
- For IWC, VarPy-HC and VarPy-BF are similar than 2C-ICE retrievals for low IWC, but differ as IWC increases. In addition, the low bias of VarPy-BF IWC is consistent with Cazenave et al. 2019, who found that applying HC LUT instead of BF in VarPy reduced its bias, especially when IWC exceeds 0.1 g.m^{-3} .
- The effective radius retrievals from VarPy-BF is globally lower than the one from VarPy-HC and 2C-ICE. This trend is confirmed by comparing Brown and Francis 1995 mass-size relationship retrievals with *in situ* P-3 measurements.
- For both VarPy-ice and 2C-ICE, IWC and effective radius retrievals tend toward smaller values than the P-3 *in situ* probes, which can be explained by the way the algorithms handle rimed and aggregated ice particles.

In conclusion, this study revealed the strengths and potential biases of each mass-size relationship and the ice properties retrieval algorithms VarPy-ice and 2C-ICE. One suggestion is to improve LUTs by making them temperature-dependent to avoid bias, particularly in regions where temperatures range are close to freezing, from -25 to 0°C . Nevertheless, these results need to be put into perspective, since the data used are from regions where only the radar signal is used to retrieve properties.

4.4 . Conclusion

The application of VarPy-mix on real data reveals its ability to simultaneously retrieve the ice crystal and supercooled water properties. In addition, it is applied to three different platforms, spaceborne and airborne, demonstrating its adaptability to multiple platforms.

The various cases presented have been compared with *in situ* measurements from literature, revealing that VarPy retrievals follow the same trend as these *in situ* measurements. Globally, the extinction and water content of supercooled water droplets are globally higher than those of ice crystals, the water droplets are significantly smaller than ice crystals and the particle number concentrations are much higher for water droplets than for ice crystals. In addition, the ASTAR campaign case provides a more accurate comparison with collocated *in situ* data. This comparison shows that the extinctions and the water contents from VarPy-mix follow similar trends as *in situ* measurements and that the retrieval produces correct results with mean percent error between the retrievals and *in situ* of 39 % for α_{liq} , 398 % for α_{ice} , 49 % for LWC and 75 % for IWC. These first results are promising, and *in situ* data from the HALO-(AC)³ and RALI-THINICE campaigns could be used to further assess the algorithm and improve its parameterization. In addition, the retrieval could be improved with full synergy for each phase of the mixed phase.

Furthermore, VarPy-ice algorithm is compared to another algorithm retrieving ice cloud properties, 2C-ICE. For this study, both HC and BF LUT are used in VarPy-ice to retrieve ice properties. Both VarPy-HC and VarPy-BF can be compared to each other as well as to 2C-ICE and collocated *in situ* measurements. Finally, this study shows that VarPy-HC and VarPy-BF differ for the extinction and IWC values as the IWC increases and that the effective radii retrieved by VarPy-BF are generally smaller than those retrieved by VarPy-HC and 2C-ICE. Additionally, IWC and effective radii retrieved by VarPy-HC, VarPy-BF and 2C-ICE are lower than the values obtained by *in situ* measurements. This can be explained by the way the algorithms handle aggregated and rimed ice particles. These comparisons could be improved, in particular by not limiting them to the gates retrieved solely by radar. The study also suggests improvements to retrieval algorithms, such as making LUTs temperature range-dependent.

Conclusion

With the objective to provide the optimal observations and consequently improve mixed-phase cloud representation in both forecast and climate models, the work conducted during this thesis has led to the development of a new method to retrieve mixed-phase cloud properties. Supercooled water droplets and ice crystals are simultaneously present in mixed-phase clouds. This coexistence and the different microphysical properties of these hydrometeors make their observation challenging. A specific method has therefore been developed to simultaneously retrieve both phase properties. In addition, this method requires assessment, in particular through comparison with *in situ* data. To this end, this manuscript presents in four distinct chapters the path taken during this thesis to achieve this new method, as well as its first assessment.

First, Chapter 1 introduces the fundamentals on our study subject: clouds, and more specifically mixed-phase clouds. Their optical and microphysical properties are described, such as size, shape, extinction, water and ice content and particle concentration. These properties determine how clouds interact with radiation from the Sun and Earth, and influence the radiative impact of clouds on the climate system. This impact can be quantified by the CRE, showing that it is significant and tends to cool considerably the climate system (-19 W.m^{-2}).

Meanwhile, current studies tend to show that climate change related to human activities has an impact on clouds, and that they tend to accentuate global warming with a cloud feedback of $+0.6 \text{ W.m}^{-2}.\text{°C}^{-1}$. This shows that cloud studies, particularly for mixed-phase clouds, are important for a better understanding of their influence on climate. In addition, the radiative impact of mixed-phase clouds is significant and depends on the fraction between liquid droplets and ice crystals, mainly linked to the various processes involved in the formation of these clouds. These processes are complex and our current knowledge does not allow them to be correctly represented in numerical models, implying biases in the forecasts. For these reasons, it is crucial to study mixed-phase clouds.

Second, Chapter 2 presents the various instruments dedicated to cloud observation. There are two main ways to study clouds: 1) by directly collecting a sample and analyzing it using instruments that fly within the clouds, called *in situ* probes, or 2) by measuring the radiation reflected or scattered by the

clouds with instruments located at a distance from the clouds, called remote sensing instruments.

There are several types of *in situ* probe, such as imagers like the CPI or 2D-S, or those that analyze light scattering by particles like the FSSP, PN or CDP. These probes provide microphysical properties of water droplets and/or ice crystals, depending on their sensitivity, for specific areas within the cloud. On the other hand, remote sensing instruments are dedicated to observing a wide cloud area, up to global coverage with instruments onboard satellites. While passive remote sensing instruments measure the energy naturally reflected, scattered or emitted by clouds, active remote sensing instruments emit energy towards the target to be analyzed, and measure the backscattered energy. The active remote sensing instrument approach offers range-resolved information and consequently provides information from inside the cloud, contrary to passive instruments that provide integrated or cloud-top information. Since mixed-phase layers are on top of or inside ice clouds, it is more appropriate to have range-resolved measurements to observe these mixed-phase layers. As a result, we are interested in two active remote-sensing instruments: the radar and the lidar.

On the one hand, cloud radar emits electromagnetic waves at frequencies between 1 and 220 GHz. Radars at 35 and 95 GHz are commonly used for cloud observation. At these frequencies, if cloud particle size is small enough to assume a Rayleigh scattering regime, radar reflectivity is proportional to the sixth moment of the particle size distribution. Consequently, under these conditions the radar is sensitive to particle size, and the reflectivity is higher for large particles such as ice crystals than for small particles such as water droplets. On the other hand, lidar uses a laser as an energy source. For cloud studies, the common wavelengths are 355, 532 and 1064 nm. At these wavelengths, which are smaller than radar wavelengths, the lidar signal can detect very thin particles such as air molecules, aerosols or small cloud particles. For cloud particle detection, the lidar signal follows the Mie scattering regime, implying that the lidar backscatter is sensitive to particle concentration. This means that lidar backscatter is higher for highly concentrated particles, such as water droplets, but is strongly attenuated by these particles and cannot penetrate high optical thicknesses (e.g. greater than 3 for CALIOP).

Finally, the radar-lidar synergy allows us to get the best out of each instrument, and their different sensitivities are an advantage for the study of mixed-phase clouds. Nevertheless, the cloud microphysical properties are not directly accessible from these measurements. For this, it is necessary to rely on retrieval algorithms, which use scattering models to relate radar-lidar measurements to the microphysical properties.

Next, Chapter 3 explains the VarPy-mix method developed during this thesis to retrieve the microphysical properties of supercooled water, ice and mixed-phase clouds with radar-lidar synergy in a unique algorithm. This variational method converts radar and lidar measurements into cloud microphysical properties, by solving an inverse problem with the Bayes theorem and the Gauss-Newton method. VarPy-mix is based on the VarPy-ice algorithm to retrieve ice properties, and has been extended and adapted to include the retrieval of supercooled water, either pure or mixed with ice crystals.

For this, the first step is to identify the hydrometeors to be characterized. For each instrument, a classification identifies the observed particles. Combining these two classifications produces a more detailed radar-lidar classification that distinguishes between clear sky areas, aerosols, precipitation as well as clouds and their phases. During this thesis, I improved and adapted this classification to include supercooled water and mixed-phase in the hydrometeors to be retrieved. In addition, I introduced an intermediate classification required as input to the algorithm, distinguishing between the three cloud types being retrieved: supercooled water clouds, ice clouds and mixed-phase clouds.

Next, numerous adaptations have been introduced to the algorithm, notably to the state vector, which describes ice crystals and water droplets separately. This approach is based on the different sensitivities of radar and lidar to these two types of hydrometeors. As a result, the ice clouds are retrieved with both instruments while the mixed-phase retrieval is split in two parts: the ice crystals are retrieved with the radar signal and the supercooled water with the lidar signal. Besides, pure supercooled water cloud properties are retrieved only with the lidar and rely strongly on *a priori* and error values. The new state vector configuration implies the adaptation of associated matrices such as the Jacobian, calculated by the radar and lidar forward models and used to calculate the cost function that determines profile convergence. The second main change to the algorithm is the introduction of a new LUT dedicated to the water droplet properties retrieval. It is created from a log-normal DSD and links the liquid extinction α_{liq} and the N_0^* parameters to microphysical properties such as water content LWC, effective water droplet radius $r_{e,\text{liq}}$ and liquid droplet number concentration N_{liq} . Additionally, the LUTs designed for VarPy-ice are included in VarPy-mix for retrieving ice crystal properties. In conclusion, VarPy-mix allows us to retrieve microphysical property profiles for both ice crystals and supercooled water droplets.

Finally, Chapter 4 presents the results of VarPy-mix applied to different platforms, and its assessment through comparison with *in situ* data. A first study shows the microphysical properties of an Arctic mixed-phase boundary layer cloud retrieved by VarPy-mix through CloudSat-CALIPSO data and compared

with *in situ* measurements. As a result, this study demonstrates that the properties of supercooled water droplets and ice crystals are retrieved simultaneously for the mixed-phase. Visible extinctions and water contents properties derived from *in situ* measurements and the retrievals showed similar trends and are globally in good agreement. The mean percent error between the retrievals and *in situ* is 39 % for α_{liq} , 398 % for α_{ice} , 49 % for LWC and 75 % for IWC. However, this comparison shows some limitations, such as the difference between sampling volume from *in situ* and CloudSat-CALIPSO.

Next, two studies on mixed-phase clouds observed during two recent airborne Arctic campaigns (HALO-(AC)³ et RALI-THINICE) highlight that VarPy-mix adapts to multiple platforms, spaceborne and airborne. As a result, for mixed-phase, the trends are the same as for the first study:

- the extinction and water contents of supercooled water droplets are globally higher than those of ice crystals.
- water droplets are much smaller than ice crystals.
- particle number concentrations are much higher for water droplets than for ice crystals.

These results are further compared with *in situ* measurements from the literature, revealing that the retrieved properties are close to the *in situ* values and follow the same trend. Nevertheless, it can be interesting and relevant to compare both HALO-(AC)³ and RALI-THINICE cases retrievals to *in situ* data collocated during these campaigns.

Finally, this chapter concludes with the summary of a study comparing the VarPy-ice algorithm to another algorithm retrieving ice clouds properties, 2C-ICE. These algorithms are compared to *in situ* values collocated with airborne measurements from NASA radar-lidar platform. This new platform has been integrated into VarPy-ice (as well as VarPy-mix), in particular by adapting the classifications. For this study, the ice cloud properties were retrieved with the two LUTs available for VarPy-ice, in order to compare these two retrievals, VarPy-HC and VarPy-BF. Finally, this study shows that both versions of VarPy-ice differ for the extinction and IWC values as the IWC increases and that the effective radii retrieved by VarPy-BF are generally smaller than those retrieved by VarPy-HC and 2C-ICE. In addition, the IWC and effective radii retrieved by VarPy-ice and 2C-ICE are lower than the values obtained by *in situ* measurements, which can be explained by the way the retrieval algorithms handle rimed and aggregated ice particles between -25 and 0 °C.

Perspectives

This section presents the most relevant perspectives arising from the work performed during this thesis. There have been a few studies on this topic, even though the need exists. Consequently, the research is still in its early stages, and improvements can still be made.

First, the mixed-phase is currently retrieved with partial synergy. The ideal approach would be to retrieve each phase with radar-lidar synergy, but this is very complex since we do not have access to the exact fraction of each phase with radar reflectivity and lidar backscatter only. To estimate the phase fraction, one or several additional variables that vary according to the hydrometeors type (water droplets and ice particles) are required. The radar Doppler spectrum and the lidar depolarization are two strong possibilities.

Second, the parameterization of *a priori* values and LUTs for liquid properties could be improved. First, the log-normal DSD is parameterized with the standard deviation value from Frisch et al. 1995, Fielding et al. 2014 and Fielding et al. 2015 ($\sigma_{N(r)} = 0.3$) and these studies are not dedicated to mixed-phase clouds. Consequently, it could be a better idea to find the $\sigma_{N(r)}$ that fit the best the DSD in mixed-phase clouds. This could be done from DSD from *in situ* measurements. The second improvement would be to test other DSDs, such as gamma shape. Then, different parameterizations of the log-normal and gamma DSDs could be implemented and the retrievals obtained with these could be compared with collocated *in situ* measurements to determine which DSD is the more appropriate. Recent airborne campaign such as RALI-THINICE and HALO-(AC)³ present several cases of *in situ* measurements collocated with airborne radar-lidar data. Finally, an approach based on deep learning (neural network) from *in situ* measurement data could replace the LUT by predicting the desired variables, for example $\frac{Z}{N_0^*}$ and $\frac{r_a}{N_0^*}$ for the forward models, and $\frac{IWC}{N_0^*}$ and $\frac{LWC}{N_0^*}$ to retrieve IWC and LWC. Additionally, the same approach could be applied to optimize *a priori* settings. Nevertheless, such a method would require gathering and preparation of a large number of *in situ* measurements to create a vast data set to train the neural network.

In addition, the new EarthCARE radar-lidar platform is scheduled for launch in May 2024 and the data could be processed by VarPy-mix. It would then be possible to retrieve the properties of ice, supercooled water and mixed-phase clouds on a new satellite platform, providing valuable data in large numbers.

Another benefit is that it offers new opportunities for improving and extending the VarPy-mix algorithm:

- We could integrate another lidar wavelength (355 nm) in VarPy-mix. In addition to the 532 nm lidar channel currently used for each platform, this opens up the possibility to include a new lidar wavelength and consequently a new sensitivity to cloud particles. This option could be first explored with the lidar LNG, which also operates at 355 nm. Additionally, the integration of this new wavelength would make two wavelengths available for LNG retrievals. This would add additional information and therefore a constraint to the algorithm to potentially improve the retrievals. Moreover, calibration and validation campaigns for EarthCARE with the LNG lidar are planned, and could also enable us to compare the retrievals of VarPy-mix applied to ATLID with those of LNG's 355 nm channel.
- The ATLID High Spectral Resolution and/or the CPR radar Doppler capability can be implemented in VarPy-mix. Consequently, we have additional measurements that can constrain the retrieval and improve it. Another advantage of having an additional measurement is that it can constrain the retrievals when one instrument is attenuated (e.g. the lidar after an optically thick cloud layer) or when it does not have the necessary sensitivity to detect cloud particles (e.g. the radar at the top of a thin ice cloud).
- The retrievals of VarPy-mix applied to EarthCARE could be compared with those of the CAPTIVATE algorithm (Mason et al. 2022) to evaluate both methods. In addition, it would be interesting to compare these results with *in situ* data collocated with EarthCARE.

Furthermore, only few cases have been processed and assessed with *in situ* comparison and they were only in the Arctic. It could be interesting to run VarPy-mix on more CloudSat-CALIPSO (and potentially EarthCARE) data and at different location of the world. This would make it possible to show that the method can be applied to any real situation and if there are some differences according to the latitude and type of mixed-phase clouds.

Another way to assess the importance of this new approach would be to carry out a closure study. This would involve processing the same case with VarPy-ice and VarPy-mix, and providing the resulting optical and microphysical properties to a radiative transfer algorithm like libRadtran (Emde et al. 2016). Such a study could give the radiative impact of the VarPy-mix method,

which includes supercooled water and mixed-phase situations contrary to VarPy-ice.

In addition, CloudSat and CALIPSO provide us over fifteen years of measurements and the VarPy-mix method could result in a version of the DARDAR products that includes supercooled and mixed-phase clouds. Minor corrections and code optimization would potentially be required to reduce runtime and enable processing automatization. With this type of product, it would be possible to produce climatologies. The retrieved optical and microphysical properties could be used in numerical models to calculate the radiative impact of clouds, particularly those composed of supercooled water (pure or mixed). Additionally, these properties could be used as inputs for weather and climate forecasting models to improve them. It would be possible to evaluate this contribution by comparing model predictions with radar-lidar measurements, and seeing whether or not the models match the observations.

Publications associated with this thesis

During this thesis, I was involved in two collaborations that led to publications that were both accepted:

1. The study presented in Section 4.1 has been accepted to the Atmospheric Measurement Techniques journal (Aubry et al. [2024](#)).
2. The study presented in Section 4.3 has been accepted to the Journal of Atmospheric and Oceanic Technology (Appendix A).

In addition, I took part in four field campaigns that resulted in a publication for each of them:

1. The results shown in Section 4.2.1 are part of the HALO-(AC)³ Overview Paper being submitted to the Atmospheric Chemistry and Physics journal (Wendisch et al. [2024](#)). I processed the radar-lidar data with VarPy-mix and created a graph to synthetically represent the ice and liquid effective radii of the selected case.
2. The ICE-GENESIS campaign publication to the Bulletin of the American Meteorological Society (BAMS) (Billault-Roux et al. [2023](#))
3. The CADDIWA campaign publication to BAMS (Flamant et al. [2024](#)). I processed the radar-lidar data with VarPy-ice.
4. The RALI-THINICE campaign publication to BAMS (Rivière et al. [2024](#)). I processed the radar-lidar data with VarPy-ice.

A Appendix

Evaluation of Lidar-Radar Based Hydrometeorological Retrievals During the 2020 IMPACTS Field Campaign

Stephen D. Nicholls^{1,2}, Andrew Heymsfield³, Gerald M. Heymsfield², John E. Yorks², Aaron Bansemer³, Clémantyne Aubry^{4,5}, Min Deng⁶, and Julien Delanoë⁴

¹ *Science Systems and Applications, Inc. Greenbelt, MD*

² *NASA Goddard Space Flight Center, Greenbelt, MD*

³ *National Center for Atmospheric Research, Boulder, CO*

⁴ *LATMOS/IPSL, UVSQ Université Paris-Saclay, Sorbonne Université, CNRS, Guyancourt, France*

⁵ *Deutsches Zentrum für Luft- und Raumfahrt (DLR), Institut für Physik der Atmosphäre, Oberpfaffenhofen, Germany*

⁶ *Brookhaven National Laboratory, Upton, NY*

Manuscript submitted to Journal of Meteorological and Oceanic Technology on 21 Aug 2023

Corresponding author: Stephen Nicholls, stephen.d.nicholls@nasa.gov

Abstract

The NASA Investigation of Microphysics and Precipitation for Atlantic Coast Threatening Snowstorms (IMPACTS) field campaign provides high quality, co-located high-altitude lidar (532 nm), radar (W-band) and in-cloud microphysical aircraft data during a wide range of intense winter storm events impacting the United States. This study evaluates the capability of well-used mass-dimensional relationships (Brown and Francis (1995, BF95); Heymsfield (2014, H14) and two lidar-radar microphysical retrieval algorithms (Cloudsat and CALIPSO Ice Cloud Property Product (2C-ICE); VarPy (a variational method derived from the satellite lidar-radar data community)) to estimate nearly 4,000 data points of aircraft-retrieved ice water content (IWC), effective radius (r_e), and the volume extinction coefficient (σ) during the first IMPACTS deployment in 2020. Both BF95 and H14 have a close 1:1 correlation with in-situ observations of σ . However, only BF95 displays a linear, consistent, and almost temperature-independent low bias for IWC and r_e . This difference probably arises from the environmental conditions used to determine each. Unlike BF95 and H14, which used observed microphysical data, VarPy and 2C-ICE used only high-altitude lidar and radar data to derive their estimates of IWC, r_e , and σ . For all three microphysical parameters, VarPy and 2C-ICE retrievals errors became notably more pronounced around the dendritic growth zone (-15°C to -10°C) and near freezing ($\geq -5^{\circ}\text{C}$), which suggests that both algorithms experience difficulty addressing riming and aggregation processes and with larger particles (dendrites and plates) due in part to their simplified ice particle assumptions. However, the mean-melt diameter ice-particle assumption did yield more accurate IWC estimates, which led to slightly better overall results for VarPy.

1. Introduction

Spaceborne lidar and cloud radar offer an opportunity to quantitatively evaluate representations of clouds in global climate models (GCMs) and provide global surveys of vertical profiles of cloud microphysical properties (Stephens et al., 2002). The NASA Cloud-Aerosol Lidar and Infrared Pathfinder Satellite Observations (CALIPSO; Winker et al. 2009) and CloudSat (Stephens et al. 2002) satellites have been collecting nearly coincident data since their launch in 2006 and have been used in numerous cloud-related studies (i.e., Delanoë and Hogan, 2010; Liu, 2018; Battaglia et al., 2020; Turk et al. 2021). While spaceborne lidar and radar provide unique yet complementary cloud and microphysical data, field campaign

operations often simulate these data from airborne lidar and radar systems, such as Cloud Physics Lidar (CPL; McGill et al. 2002) and Cloud Resolving System W-band radar (CRS, McLinden et al., 2021), due to the long return periods inherent to spaceborne data. As Figure 1 shows, CPL (left panel) is adept at detecting optically thin clouds and cloud particles below the minimum detection threshold of CRS (-28 dBZ), whereas CRS (right panel) can detect moderate-to-thick cloud layers and precipitating structures within cloud systems below where CPL attenuates (\sim cumulative optical depth of ~ 3.0). Notably, CPL and CRS exhibit considerable overlap near the CRS-detected cloud top (8-9 km, 20:01 - 20:03 UTC), especially in the absence of supercooled cloud water.

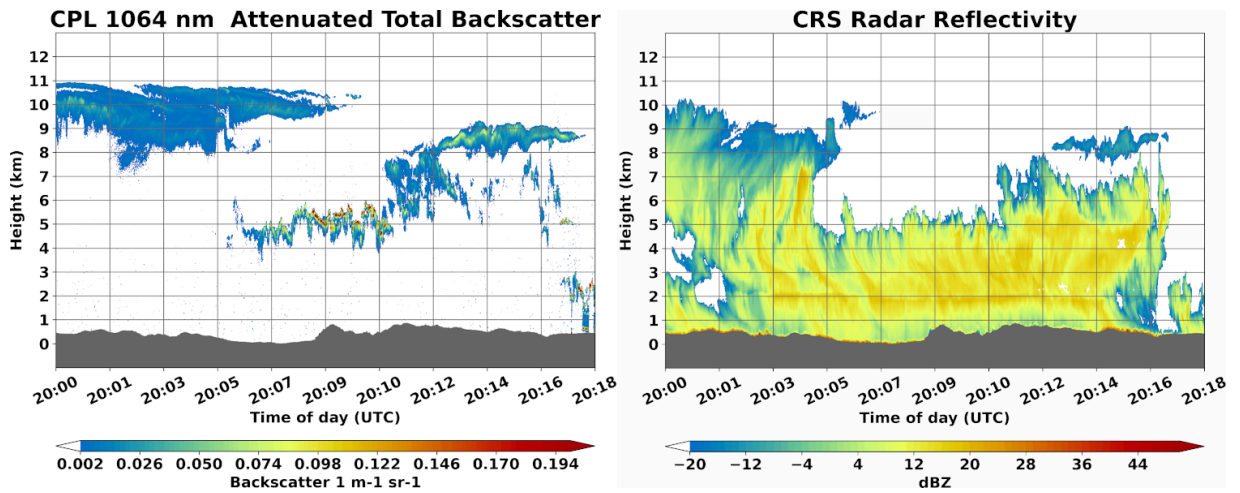


Fig. 1. Airborne 1064-nm lidar (left) and W-band radar (right) taken during a wintertime cyclone sampled by the IMPACTS field campaign on 25 Jan. 2020.

Previous studies (i.e., Intrieri et al., 1993; Hogan et al., 2006; Deng et al., 2010) combined coincident lidar and radar measurements synergistically to provide retrievals of ice water content (IWC), a GCM-prognostic variable, which improves upon either measurement alone. Because lidar can detect radiatively significant thin cirrus not detected by radar (McGill et al., 2004), algorithms deriving IWC and other GCM variables from lidar measurements alone are highly desirable.

Particle size distributions (PSD), together with characteristic size-dependent (D) ice particle mass dimensional relationships ($m(D)$) and particle shape information, can yield IWC, particle cross-sectional area (A_{cr}), and the effective radius (r_e). IWC is roughly related to the diameter squared and directly proportional to A_{cr} . Effective radius is used to prescribe cloud radiative

properties and is given by $c(IWC/A_{cr})$, where c is 1.64 for ice particles of any shape, according to Foot (1988).

Boudala et al. (2002) used PSDs from airborne particle probes from four higher latitude field projects to derive IWC and volume extinction coefficient (σ) and used direct IWC measurements to evaluate the ice crystal densities they assumed. They expressed these results in terms of the effective particle diameter and mean effective size (D_{ge}) and developed temperature-dependent relationships for D_{ge} and IWC; together, these can be used to derive IWC from σ and temperature (T). They developed separate relationships with and without including small particle size data to mitigate the possible effects of ice crystal shattering and incomplete knowledge of the small particle properties:

$$D_{ge} = 57.133 IWC \sigma^{-0.0313} e^{0.011T} \quad (1)$$

Heymsfield et al. (2005) examined the relationships between direct measurements of the IWC and σ from the PSD for ice- and mixed-phase clouds, using data from several field programs (CRYSTAL-FACE, CEPEX, and FIRE-2). From these data, they developed the relationship,

$$IWC = 119 \sigma^{1.22}, \quad (2)$$

where IWC is in units of g/m^3 and σ is in units of m^{-1} . More recently, Heymsfield et al. (2014, hereafter H14) build upon this previous work by using data from eight field campaigns spanning from the tropics to the Arctic, covering a wide temperature range ($-80^\circ C$ to $0^\circ C$), to derive new temperature-dependent IWC- relationships in $10^\circ C$ increments. Based on these relationships, they derived a broader relationship,

$$IWC = 186 \sigma^{1.15}, \quad (3)$$

to cover the entire temperature range. More recently, Thornberry et al. (2017) used data collected in the tropical tropopause layer at temperatures from -66 to $-88^\circ C$ to derive relationships between IWC and very low-temperature ice clouds ($T < 192K$). Bulk IWC was measured and calculated from the PSD. Their study yielded a single IWC- relationship covering the temperature range sampled ($185K < T < 207K$):

$$IWC = 12.3 \sigma^{1.01}, \quad (4)$$

More recently, Dolinar et al. (2022) proposed a novel satellite-based approach, using global CloudSat and CALIPSO data, to parameterize ice cloud effective diameter, IWC, and lidar-derived extinction for application in numerical weather prediction models and cirrus cloud radiative forcing studies. The parameterizations developed attempt to address the time- and region-limited nature of field campaign-based parameterization schemes but are subject to numerous caveats, including a dependence upon lidar-radar microphysical models, a thin cirrus and ice-phase clouds only focus, and an under representation of larger ice crystals at warmer temperatures.

This investigation builds upon these previous studies by evaluating the capability of well-used mass-dimensional relationships and spaceborne lidar-radar microphysical algorithms to retrieve key microphysical properties (IWC, r_e , and σ) using co-located high-altitude airborne lidar and W-band radar data in concert with in-situ microphysical measurements from the 2020 NASA IMPACTS field campaign deployment. For this study, both microphysical algorithms were modified to assimilate CPL 532 nm lidar and CRS W-band radar retrievals. Section 2 describes the two lidar-radar algorithms evaluated in this study. The IMPACTS field campaign and the relevant lidar, radar, and microphysical instruments are detailed in Section 3. Sections 4, 5, 6, and 7 show our study methodology, results, discussion, and conclusions.

2. Lidar-Radar Algorithms

As our understanding of IWC- σ relationships has advanced through field campaigns, so have the lidar-radar algorithms that attempt to simulate these and other microphysical properties. Delanoë and Hogan (2008) developed a variational method based on optimal estimation theory that uses the combination of ground-based or spaceborne-radar reflectivity, lidar backscatter, and infrared radiometer radiances for retrieving profiles of σ and IWC, from which r_e is derived. Unlike previous lidar-radar algorithms (i.e., Mitrescu et al. 2005, Tinel et al. 2005), their method was not limited solely to the radar-lidar overlap region, and it could be readily adapted to use other measurement sources, such as passive radiances. By carefully selecting both the state variables and the associated priori estimates, their method can be applied not only to the radar-lidar overlap regions but to the lidar- and radar-only regions and could be adapted to other measurement types, such as passive radiances.

More recently, studies such as Deng et al. (2013), Sourdeval et al. (2016), and Cazenave et al. (2018), have continued to evaluate and improve upon existing lidar-radar combined algorithms (raDAR/liDAR [DARDAR] and Cloudsat and CALIPSO Ice Cloud Property Product [2C-ICE, Deng et al. 2010]) and their capabilities to retrieve key cloud and microphysical properties for large satellite datasets. Deng et al. (2013) noted the tendency of the DARDAR (Delanoë and Hogan, 2010) algorithm to overestimate IWC in CloudSat lidar-only regions. Sourdeval et al. (2016) noted that the DARDAR retrieved ice water path biased high for values below 10 g/m². Following these studies, Cazenave et al. (2018) attempted to refine the DARDAR retrieved estimates of IWC and other cloud microphysical properties via adjustments to the assumed mass-size distribution, the normalized PSD, and the assumed a priori values were adjusted to better fit additional measurements. Their updates to DARDAR yielded an average reduction of retrieved IWC and ice water path by 16% and 24%, respectively, and closer to observations.

We will evaluate two leading airborne remote-sensing-based microphysical algorithms, 2C-ICE and VarPy (e.g., a variational method derived from DARDAR used in the satellite community), (Delanoë, J., and Hogan, R. J., 2010), and two well-used, aircraft-based mass dimensional relationships (H14, BF95), using in-situ cloud microphysical and airborne radar and lidar data from the recent Investigation of Microphysics Precipitation for Atlantic Coast-Threatening Snowstorms (IMPACTS, McMurdie et al. 2022) field campaign. More details about 2C-ICE (2.1), VarPy (2.2), and IMPACTS (Section 3) are found below.

2.1. 2C-ICE

The 2C-ICE is the primary algorithm used by the CALIPSO and CloudSat algorithm teams to retrieve IWC, r_e , and σ for identified ice clouds measured using the spaceborne W-band Cloud Profiling Radar (CPR) on CloudSat and 532 nm Cloud-Aerosol Lidar with Orthogonal Polarization (CALIOP) on CALIPSO (Deng et al. 2010, Deng et al. 2013). This algorithm applies the dimensional power law relation parameters of idealized crystal habits calculated by Yang et al. (2000), assuming a mixture of hollow and solid columns (Hong et al. (2007), and calculates the extinction properties of non-spherical ice crystals at 532 nm via accurate light scattering calculations and parameterizations from Yang et al. (2000). 532 nm lidar backscattering properties and W-band radar are calculated using extinction coefficients assuming a constant lidar ratio and those reported by Hong et al. (2007), respectively. To increase

computation efficiency, 2C-ICE incorporates look-up tables for corresponding ice crystal habits in the retrieval framework and a modified gamma PSD (Deng et al. 2010).

The 2C-ICE algorithm detects clouds by examining the cloud mask (2B-GEOPROF-LIDAR), cloud type, and phase (2BCLDCLASS-Lidar); modeled temperature profiles are then used to identify ice-phase clouds. Below -5°C CRS signals are assumed to be scattered from ice clouds, and then CPL is used to classify supercooled liquid and ice clouds. Ice crystal habits in 2C-ICE are assumed to be columnar to increase computational efficiency, regardless of the temperature or degree of ice supersaturation, which can introduce potential biases into retrieved 2C-ICE microphysical properties. Additional algorithm descriptions and retrieval validation can be found in Deng et al. 2010 and 2013.

2.2. VarPy

VarPy is a variational method derived from DARDAR that uses attenuated lidar backscatter and radar reflectivity to retrieve the microphysical properties of ice clouds. It was first developed in 2008 (Delanoë and Hogan 2008 and 2010) and has seen further parameterization enhancements (Ceccaldi et al. 2013, Cazenave et al. 2019). It can operate on satellite, airborne, or ground-based data with minor modifications. For this study, VarPy ingested CPL 532 nm lidar backscatter, CRS W-band radar reflectivity, their associated target mask (indicating the nature of the signal for each instrument), and the cloud phase classification.

The VarPy state vector is composed of three variables: the visible extinction coefficient (α [m^{-1}]), the lidar extinction-to-backscatter ratio ($S=\alpha/\beta$ [sr]), and the number concentration parameter (N'), which is linked to the normalized number concentration parameter (N_0^* [m^{-4}]) and extinction ($N'=N_0^*/\alpha^v$). The first guess and the *a priori* values of the state vector are shown in greater detail in Table A1. The final values of the state vector (α and N') are used to retrieve ice microphysical properties such as IWC and r_e using either the Brown and Francis (Brown and Francis, 1995; Mitchell, 1996; hereafter known as BF95) and Heymsfield (Heymsfield et al. 2010; hereafter H10) mass-size relationship look-up tables (LUTs) (Delanoë et al. 2014, Cazenave et al. 2019). The *a priori* and first guess values of N' vary according to the LUT used (See Table A1). Both LUTs are set for a range of mean volume-weighted melted-equivalent diameter and do not assume a prescribed ice crystal habit as in 2C-ICE. Should the CRS- and CPL-identified cloud phase disagree, the cloud phase is set to “mixed phase”. Further details on

the forward processing model and VarPy, in general, can be found in Delanoë and Hogan (2010) and Cazenave et al. (2019).

3. IMPACTS Field Campaign

IMPACTS is a multi-year NASA field campaign to study the formation, organization, and evolution of snowbands during three 6-week deployments (January and February of 2020, 2022, and 2023) for the first comprehensive study of East Coast snowstorms in 30 years (McMurdie et al., 2022). This campaign leveraged a suite of ground (radar, rawinsondes), satellite simulating (lidar, radar, radiometer), and in-situ instrumentation (cloud probes, dropsondes) to address its science objectives. Combining these various data provides a detailed 3-D structure of clouds and precipitation and the vertical and horizontal air motions associated with the snowbands. Research results and data obtained from IMPACTS are being used to improve remote sensing and modeling of snowfall (see Finlon et al., 2022; Heymsfield et al., 2023).

When this investigation was conducted, only the IMPACTS 2020 microphysical data were available, limiting the scope of this investigation to the 2020 data only. Despite a warmer-than-average winter, IMPACTS conducted ten research missions, which included several coordinated flights between the high-altitude NASA ER-2 and in-cloud NASA P-3 aircraft during winter storms of various stages (McMurdie et al. 2022). This investigation will focus on four coordinated flights from the IMPACTS 2020 campaign (See section 4, Table 1) because direct measurements of the IWC had relatively few errors, the lidar and radar data are of high quality, and there were many ER-2/P-3 aircraft co-locations. Additional details about CPL, CRS, and the P-3 cloud probes are described below.

3.1. CPL Airborne Lidar

The CPL is a multi-wavelength (355, 532, 1064 nm) elastic backscatter lidar built originally for use on the NASA ER-2 aircraft (McGill et al. 2002; 2003). It was first deployed in 2000 and has since participated in over two dozen field campaigns, collecting hundreds of hours of data aboard the NASA ER-2, C-130, WB-57, and Global Hawk aircraft. CPL fundamentally measures the total (aerosol plus Rayleigh) attenuated backscatter at each wavelength as a function of

altitude. Additional cloud and aerosol properties derived from the CPL attenuated backscatter include the volume depolarization ratio, cloud phase, particulate extinction coefficient, optical depth, and backscatter color ratio.

CPL measurements enable a wide range of cloud applications, including: (1) cloud top heights (McGill et al. 2004; Sinclair et al. 2017; Janiszski et al. 2023), (2) microphysical properties near cloud top (Yorks et al. 2011a; Diedenhoven et al. 2016; Midzak et al. 2020), (3) radiative properties of thin high clouds (Davis et al. 2010; Dolinar et al. 2020), and (4) validation of satellite retrievals (McGill et al. 2007; Yorks et al. 2011b; Hlavka et al. 2012; Pauly et al. 2019). For IMPACTS, the CPL provides sensitivity to the optically thin (smaller particles) cloud tops, specifically where the cloud optical depths are between 0.01 and 3.00. The CPL lidar beam is fully attenuated at an optical depth of about 3.00. This part of the cloud is typically below the detection limits of the airborne radar sensors, making CPL a perfect complement to the radars. The CPL data products used in this paper are provided at 1-second averages, corresponding to ~200 m horizontal resolution (given the typical ground speed of the ER-2), with 30 m vertical resolution.

3.2. CRS Airborne Radar

The IMPACTS ER-2 payload includes three nadir-pointing Doppler radars: the W-band (94 GHz) CRS, the Ku- and Ka-band (13.5 GHz, 35 GHz) High-altitude Imaging Wind and Rain Airborne Profiler (HIWRAP), and the 9.6 GHz ER-2 X-band Doppler Radar (EXRAD) (McMurdie et al. 2022). These radars flew in many field campaigns for scientific data collection and calibration, and validation of spaceborne instruments. CRS is extremely sensitive to ice clouds but suffers strong attenuation when larger particles in precipitating clouds are present. CRS has an 0.46° antenna beamwidth that provides a 160 m footprint at the surface and a sensitivity of -28 dBZ at 10 km altitude, assuming a 20 km nominal ER-2 altitude. The vertical gate spacing for CRS is 26 m. In IMPACTS, the multiple frequencies provided by these radars are used to gain insights into the characteristics of the precipitation (snow and rain) particles. The differential reflectivities provide information on the Mie and Rayleigh scattering and attenuation present in the profiles. The Doppler information provides information on the vertical motions in the snow and rain regions. Both 2C-ICE and VarPy are designed as single-radar frequency

algorithms (Ka- or W-band); we chose W-band for this study due to its higher sensitivity and improved capability to detect optically thin clouds.

3.3. In-situ Microphysical Cloud Probes

Throughout IMPACTS, the ER-2 aircraft and its suite of lidar, radar, and radiometer measurements were underflown by the P-3 aircraft taking in-situ microphysical and meteorological measurements along coordinated flight legs (McMurdie et al. 2022). Instruments on board the P-3 measured various microphysical properties and their associated PSDs for particle sizes ranging from 2 μm to 2 cm or larger and particle shapes at or above 25 μm (McMurdie et al., 2022). To capture the entire particle size spectrum, IMPACTS used three different cloud probes: Droplet Measurement Technologies Cloud Droplet Probe (CDP) with a SPEC Fast-CDP, SPEC 2D-S, and SPEC HVPS-3 for particle ranges of 2–50 μm , 50–2000 μm , 1.0–19.2 mm, respectively. Hereafter, we refer to the combined microphysical probe data derived from CDP, 2DS, and HVPS-3 as the “P-3 probe data”. The P-3 probe data were then combined to generate composite PSDs. Qualitative estimates of particle habit were retrieved from a SPEC Cloud Particle Imager (CPI), 2D-S, and HVPS-3 images, which afford a pixel resolution of 2.3 μm , 10 μm , and 150 μm , respectively. Raw particle images from the P-3 cloud probes were analyzed and processed using co-author Bansemer’s Software for OAP Data Analysis (SODA2). Finally, total condensed water content was measured by the Water Isotope System for Precipitation and Entrainment Research (WISPER; D. Henze et al. 2020, unpublished manuscript). The accuracy of WISPER is approximately $\pm 15\%$. This investigation targets 2C-ICE and VarPy retrieved parameters (IWC, σ , and R_e) obtained from the P-3 cloud probes and, to a less extent, WISPER. Science questions related to ice crystal habit are beyond the scope of this paper and may potentially be the subject of future studies.

4. Study Methodology

This investigation focuses on four 2020 IMPACTS missions with “good coordination and co-location” between the ER-2 and P-3 aircraft (25 Jan. and 1, 5, and 7 February; see Table 1) using their native 1-second time resolution. We define a “good” co-location as any instance where both aircraft were in level flight and separated horizontally by 1-km or less, which is a

compromise between the accuracy of the co-located observations with the dataset sample size. Additionally, because VarPy and 2C-ICE were geared toward ice-phase clouds and precipitation retrievals, all data (P-3, ER-2, and algorithm) this investigation includes only data where the P-3/ER-2 horizontal separation was 1-km or less, P-3-measured air temperature was less than 0°C, P-3-measured LWC was less than 0.1 g/m³, P-3-measured IWC less than 1.5 g/m³ and CRS radar reflectivity was less than 15 dBZ. Applying these restrictions yields a dataset with 3,903 co-located observations with a temperature range between -25°C and 0°C (See Table 1 for more details).

IMPACTS Mission Date	-25C ≤ T < 20C	-20C ≤ T < 15C	-15C ≤ T < 10C	-10C ≤ T < 5C	-5C ≤ T < 0C	-25C ≤ T < 0C (No LWC)	-25C ≤ T < 0C (With LWC)	Case Description
25 Jan 2020	417	82	861	18	10	1388	180	Warm occluded front with generating cells over New York State and New England
01 Feb 2020	0	0	54	17	229	300	28	Warm developing Atlantic frontal system east of North Carolina and over Gulf Stream
05 Feb 2020	0	0	835	358	1007	2200	0	Shallow frontal zone over Midwest US with snowbands
07 Feb 2020	0	0	15	0	0	15	0	Rapidly deepening cyclone with heavy snow and multiple snowbands over New York State
Total All Cases	417	82	1765	393	1246	3903	208	

Table 1. Summary of IMPACTS events used in this study and the total number of co-located observations (i.e., level flight of both aircraft with 1-km or less horizontal separation) used as a function of flight-level temperature. The last column of data shows the number of observations where the LWC exceeds 0.1 g/m³ threshold but met all other imposed constraints (Section 4).

Previous cloud-observation-focused studies, such as Thornberry et al. (2017) and H14, highlight the strong linkages between temperature and IWC (via Clausius- Clapeyron) and a less-defined linkage between temperature to other cloud microphysical properties, such as σ (Figure 2). Heymsfield et al. (2023) recently demonstrated that the often applied BF95 relationship tends to underpredict IWC compared to IMPACTS field campaign observations. Similarly, Cazenave et al. (2019) noted a similar tendency in the DARDAR retrievals when BF95 was applied to CloudSat and CALIOP data.

This investigation aims to use IMPACTS data to evaluate the capability of 2C-ICE, VarPy, and the H14 and BF95 mass-dimensional relationships to retrieve key microphysical properties (IWC, r_e , and σ). Both 2C-ICE and VarPy ingested identical datasets containing level 1B CRS and CPL data, MERRA-2 model temperature and relative humidity data, CPL and CRS level 2 cloud mask, and CPL level 2 cloud phase data. Following previous studies (i.e., H14, Cazenave et al. 2019; Heymsfield et al. 2023), the results presented in this investigation focus on IWC, r_e , and σ across key temperature regimes tied to notable ice crystal habit regimes (i.e., columns, dendrites, etc.). The results section, presented below, will address the entire -25°C to 0°C temperature range of our IMPACTS 2020 dataset. However, for brevity, the figures presented in the results section will focus on the region within (-15°C to -10°C) and just warmer (-10°C to -5°C) than the dendritic growth zone where the variability between the analyzed temperature ranges tended to be most prominent. For brevity, we will mention supplementary figures showing corresponding results from other temperature ranges in Section 5, but these figures are not crucial to the conclusions of this investigation, therefore we opted to include these strictly as supplementary material. Notably, during the IMPACTS 2020 deployment, the P-3 flew below the CPL lidar attenuation depth for nearly all co-located observations, which limits the scope of this study to the radar-only regions.

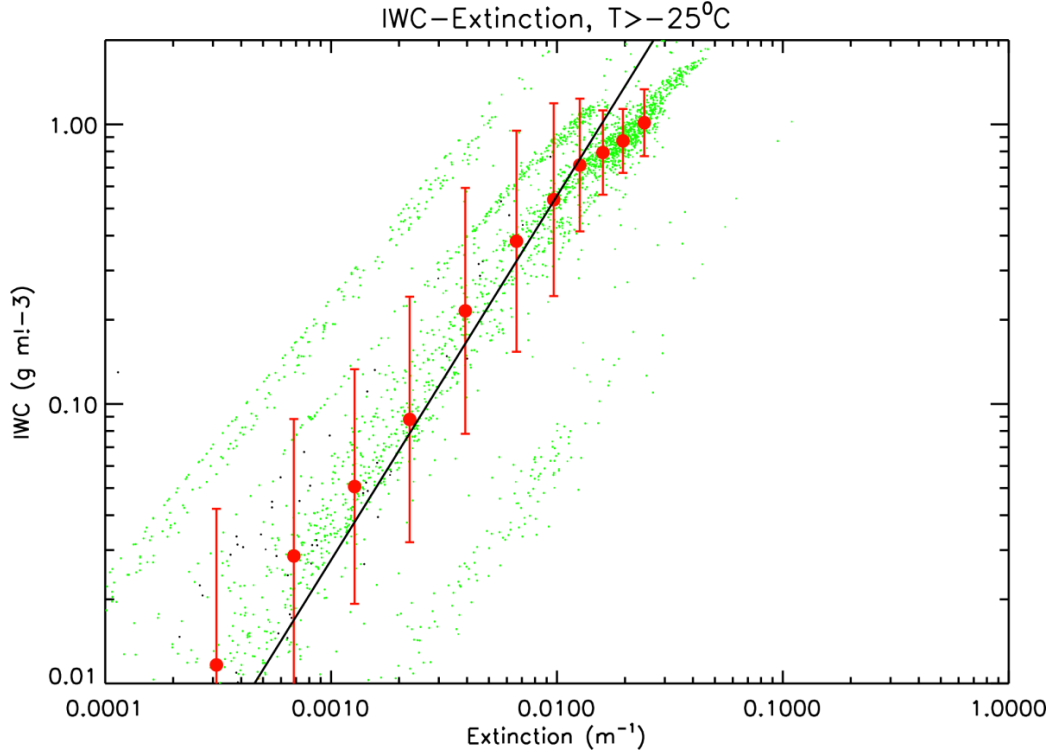


Fig. 2. Relationship between ice water content (IWC) and extinction (σ) derived from airborne field campaign data for temperatures of -25°C and 0°C . The red dots and lines denote the median and the interquartile range for each IWC bin, respectively.

5. Results

Comparisons between both retrieved and estimated σ from the P-3 cloud probes, mass-dimensional relationships, and microphysical algorithms for the -15°C to -10°C and -10°C to -5°C temperature ranges are shown in Figures 3 and 4, respectively (See Figures A1-A4 for other temperature ranges). The H14 IWC- σ relationship (Eq. 3 above) yields σ values with a near 1:1 correspondence to the P-3 cloud probes ($R^2 = 0.97$). Therefore, although IMPACTS has more modern sensors than those used to derive the H14 mass-dimensional relationship, it remains an excellent predictor of σ for a given IWC measurement across the temperature range sampled by IMPACTS. Similarly, BF95 σ values (not shown) also shares a near 1:1 correspondence with the P-3 cloud probes. In contrast to the empirical formulas, VarPy H10 (i.e., VarPy using the H10 LUT), VarPy BF95 (i.e., VarPy using the BF95 LUT), and 2C-ICE retrieved σ values exhibit similar degrees of spread and divergence from P-3 cloud probe measurements ($R^2 = 0.43, 0.34$), yet all yield qualitatively similar σ values when compared to each other. However, as temperatures decrease, 2C-ICE and VarPy tend to bias lower relative to P-3 cloud probe

measurements, where 2C-ICE produces even smaller σ values than the VarPy. Hence despite their internal algorithm differences, 2C-ICE and VarPy have similar degrees of predictive skill, yet factors such as their treatment of ice particle shape (2C-ICE: hexagonal columns; VarPy: mean volume-weighted melted-equivalent diameter) and the resulting PSDs likely have a notable role in explaining more fine-scale differences amongst them. Comparing VarPy H10 to both H14 and VarPy BF95 suggests that σ variability between VarPy and the P-3 cloud probes are likely more associated with the algorithm's underlying assumptions (i.e., application of mean melt diameter and also its lidar and radar forward model errors) more so than the applied LUTs.

VarPy and 2C-ICE tend bias towards higher extinction values as cloud top height lower. Mass and size distribution tend to bias larger with lower, warmer cloud tops.

Figures 5 and 6 compare P-3 cloud probe IWC retrievals to those from VarPy, 2C-ICE, BF95, and WISPER for the same temperature ranges as for σ (See Figures A5-A8 for other temperature ranges). Like H14, BF95 requires P-3 cloud probe data to derive IWC. Despite using the P-3 data, BF95 IWC retrievals exhibit a linear but robust low bias that grows with increasing IWC. This result suggests that this bias is systematic and is likely related to the coefficients applied in the BF95 IWC- σ relationship. H14-based IWC values (not shown) show a near 1:1 correspondence to the P-3 cloud probes, an expected result because H14 requires IWC to calculate σ . As compared to σ , VarPy and 2C-ICE IWC retrievals qualitatively diverge similarly and “fan out” more notably from the P-3 cloud probe data, especially within the dendritic growth zone (Figure 5) and at near-freezing temperatures (Figure A8), as IWC increases. Therefore despite their different LUTs and forward scattering models, both VarPy- and 2C-ICE-based IWC values are similarly biased and tend toward smaller values and smaller particle sizes than the P-3 cloud probes, which may be in part due to issues in how the algorithms treat rimed and aggregated ice particles. However, unlike for σ , considerable and increasing variability exists amongst VarPy H10, VarPy BF95, and 2C-ICE as IWC increases, particularly above 0.2 g/m³. The “fan-like spread” and the tendency of VarPy BF95 to bias low relative to VarPy H10, is likely a byproduct of the BF95 LUT being biased toward smaller particle sizes and differences in its initial state vector. As for 2C-ICE, it tended toward smaller IWC values than VarPy, likely due to its treatment of ice particles as hexagonal columns. Surprisingly, despite being on board the

P-3, WISPER IWC retrievals exhibit considerable spread from the P-3 cloud probes above 0.25 g/m^3 , which may be in part due to issues with measuring rimed and aggregated particles, but also a known issue where air inflow into WISPER can change or even become blocked by ice accretion on the probe inlet. WISPER inlet blockage issues motivate our decision to use only the P-3 cloud probe data for evaluation.

Retrieved and estimated r_e from the P-3 cloud probes, BF95, VarPy, and 2C-ICE are shown in Figures 7 and 8 (Figs. A9-A12 for other temperature ranges). Simialr to IWC, BF95 r_e retrievals demonstrate a consistent linear low bias relative to the P-3 cloud probes. The presence of a similar BF95 low bias in r_e can likely be attributed to the relationship between IWC, r_e , and σ , which is given by:

$$r_e = 3/2 * IWC / (0.91 * \sigma) \quad (5)$$

Hence, even if BF95 σ is consistent with the P-3 cloud probes, the low-bias in r_e is seemingly driven by the low-bias tendency of BF95 IWC. The BF95 bias is also reflected in VarPy BF95 r_e retrievals, which are consistently smaller than those from VarPy H10. Qualitatively, both 2C-ICE and VarPy H10 r_e retrievals demonstrate considerably reduced spread relative to the P-3 cloud probes than for IWC. Smaller errors in σ retrievals likely helped mitigate r_e errors because it was approximated to first order as IWC/σ . Notably, r_e spread from VarPy H10 and 2C-ICE increases at warmer temperatures where riming, accretion, and aggregation processes become more prevalent. However, upon closer inspection, VarPy H10 is biased towards even smaller r_e values than 2C-ICE, and VarPy BF95 produced even smaller r_e values than its H10 counterpart. Hence, although 2C-ICE assumes only hexagonal column ice crystal habits, the mean melted diameter treatment of ice crystals by VarPy leads to even smaller particle sizes. Once temperatures approach freezing (Figure A12), VarPy and 2C-ICE lose almost all their r_e predictive skill due to the increased frequency of riming and aggregation processes.

Figures 9 and 10 depict the log relationship between IWC and σ from VarPy H10, 2C-ICE, BF95, and H14 and compare each to the P-3 cloud probes (black dots) retrieved values within and just above the dendritic growth zone, respectively (Other temperature ranges, Figs. A13-A16). VarPy H10 demonstrates similar overall data spread to the P-3 cloud probes, yet the slope between IWC and σ exhibits a notable temperature dependence (it becomes less steep with increasing temperature) because as temperatures warm, lower σ values become associated with higher IWC values. The change in slope and higher IWC values for a given σ suggests that the

mean mass melted diameter assumption may lead to simulated properties indicative of larger aggregates but with lower number concentration. In comparison to VarPy H10, the IWC- σ relationship for 2C-ICE has reduced data spread but a steeper slope that largely remains fixed with increasing temperature. The lack of a temperature dependence stems from its fixed hexagonal particle shape assumption, which causes 2C-ICE to over-constrain the particle types observed by the P-3 cloud probes. Because both BF95 and H14 are derived from previous field campaign data, both can capture the size and shape variability of ice crystals sampled by the P-3 cloud probes. However, due to the sampled environments used as the basis to derive these mass-dimensional relationships (H14: heavy and thick ice clouds, BF95: cirrus and thin clouds), differences from the P-3 cloud probes data do exist. Specifically, BF95 is biased towards lower σ values, but its slope remains steady. In contrast, H14 captures the general local and data spread, yet its IWC- σ slope is steeper than observations, especially at colder temperatures.

Figures 11 and 12 depict the relationship between IWC and the CRS power-to- σ ratio using P-3 cloud probes, BF95, H14, VarPy H14, and 2C-ICE data and the division of the median CRS power-to- σ ratio (product / P-3 cloud probes) binned along the IWC axis (bottom right panel). These two figures show data within and just above the dendritic growth zone region (Other temperature ranges, Figures A17-A20). Using the power-to- σ ratio permits the examination of predictive skill because each data product is normalized by CRS power. Qualitatively, both BF95- and H14-based data compare well to the P-3 cloud probes, which likely reflects their usage of P-3 cloud probe IWC and σ data to derive the other parameter. However, upon closer inspection, the BF95 IWC low bias causes its data to increasingly bias lower, relative to the P-3 probes, as IWC and σ increase. In contrast, H14 compares much more favorably P-3 measurements than BF95 due to its comparatively smaller IWC and σ errors. Despite this tendency, the BF95 and H14 median power-to- σ ratios are well-correlated to each other up through an IWC of 0.8 g/m^3 where the low bias in BF95-based σ shifts their medians apart.

In contrast, the VarPy H10 and 2C-ICE algorithms underrepresent overall data spread and favor lower IWC values than as analyzed by the P-3 cloud probes, particularly at lower IWC values. Despite these problems, VarPy H10 can correctly characterize the region where the bulk of observations occur and adjust the slope of its data accordingly (i.e., become steeper with increasing temperature). Commensurate with Figures 8 and 9, the slope of the 2C-ICE data remains fixed and is far more constrained than both VarPy H10 and the P-3 cloud probes. When

analyzed across all temperature ranges, the VarPy H10 and 2C-ICE power-to- σ ratios are seen to be biased low (as low as 20% of cloud probes) for IWC values below 0.2 g/m^3 , be within 10% of the P-3 observations between $0.2\text{-}0.4 \text{ g/m}^3$, and then above 0.4 g/m^3 VarPy H10 median tends to be biased high, but it remains within 10% of the P-3 cloud probes, whereas the 2C-ICE median ratio continues to increase to as high as 1.9 times the P-3 cloud probes (Fig. 10) as IWC values exceed 0.7 g/m^3 . Therefore, VarPy yields more accurate results because its PSD favors larger particle sizes than those from 2C-ICE, consistent with the P-3 cloud probe retrievals.

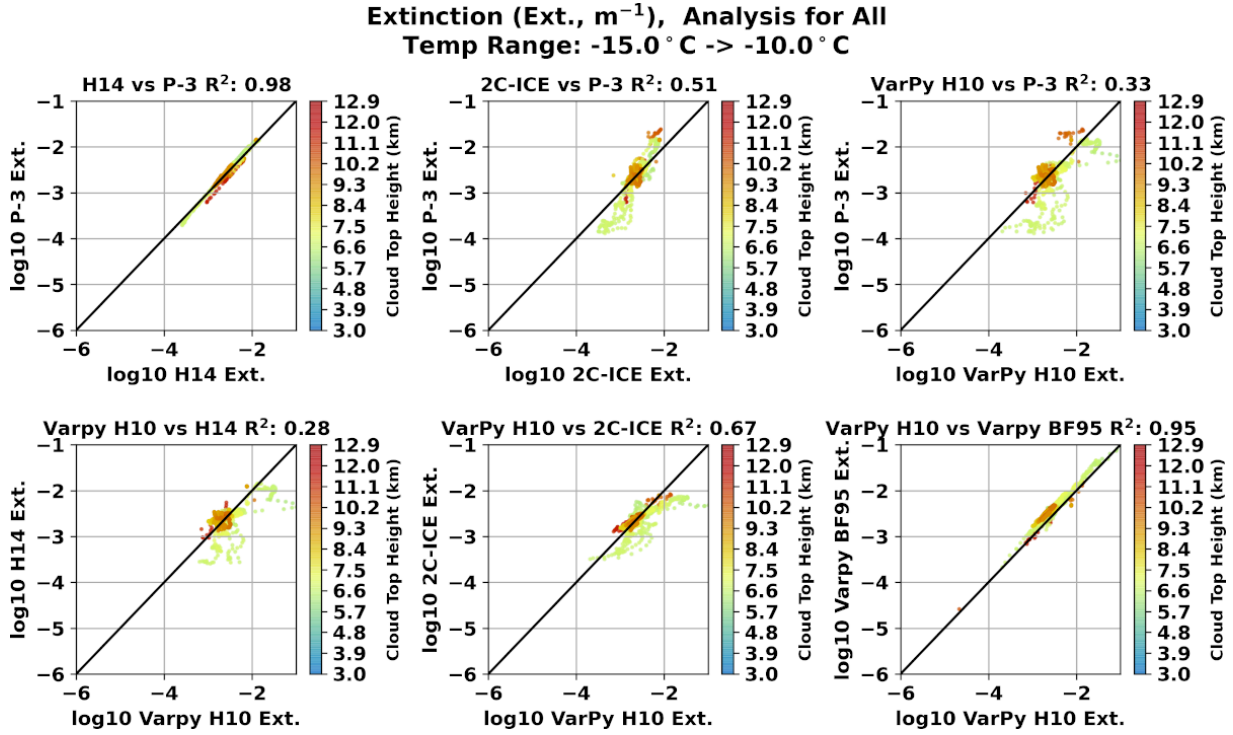


Fig. 3. Cross comparison amongst H14-, VarPy-, 2C-ICE- and P-3-retrieved extinction values for all co-located aircraft observations between -15°C and -10°C and color shaded by cloud-top height (km).

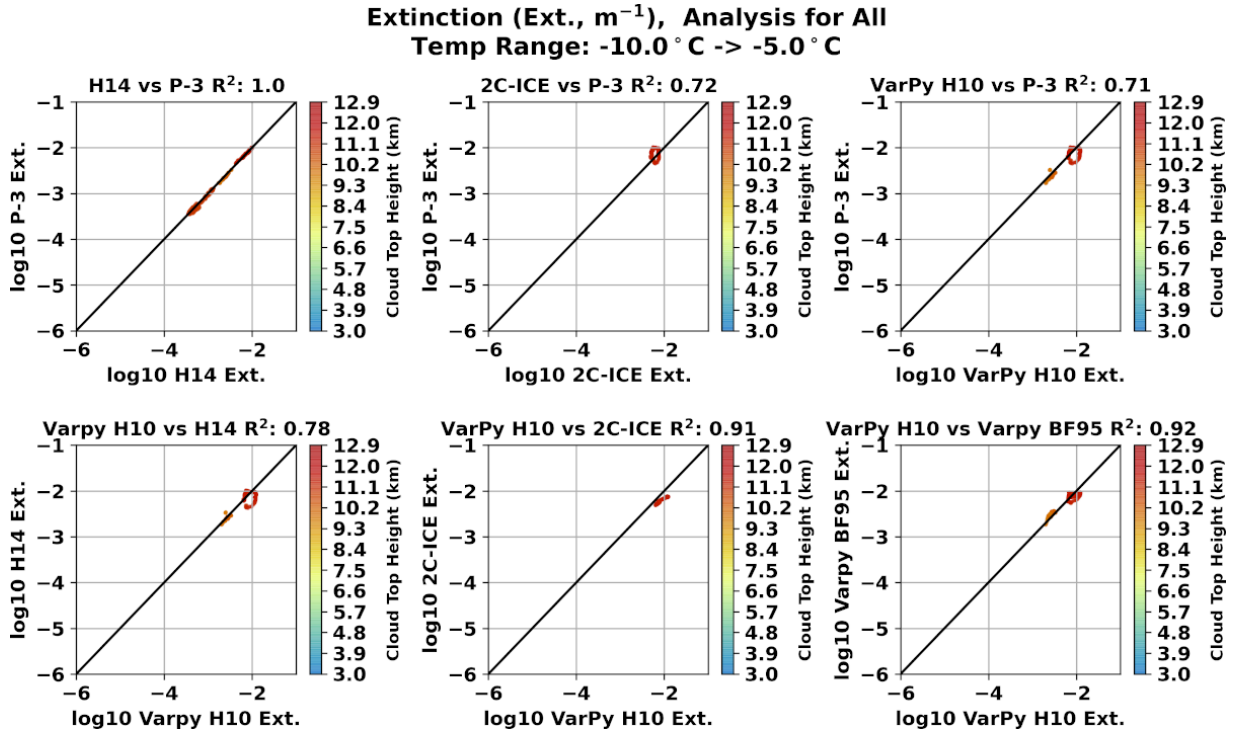


Fig 4. Same as Fig. 3, except for temperatures between -10°C and -5°C .

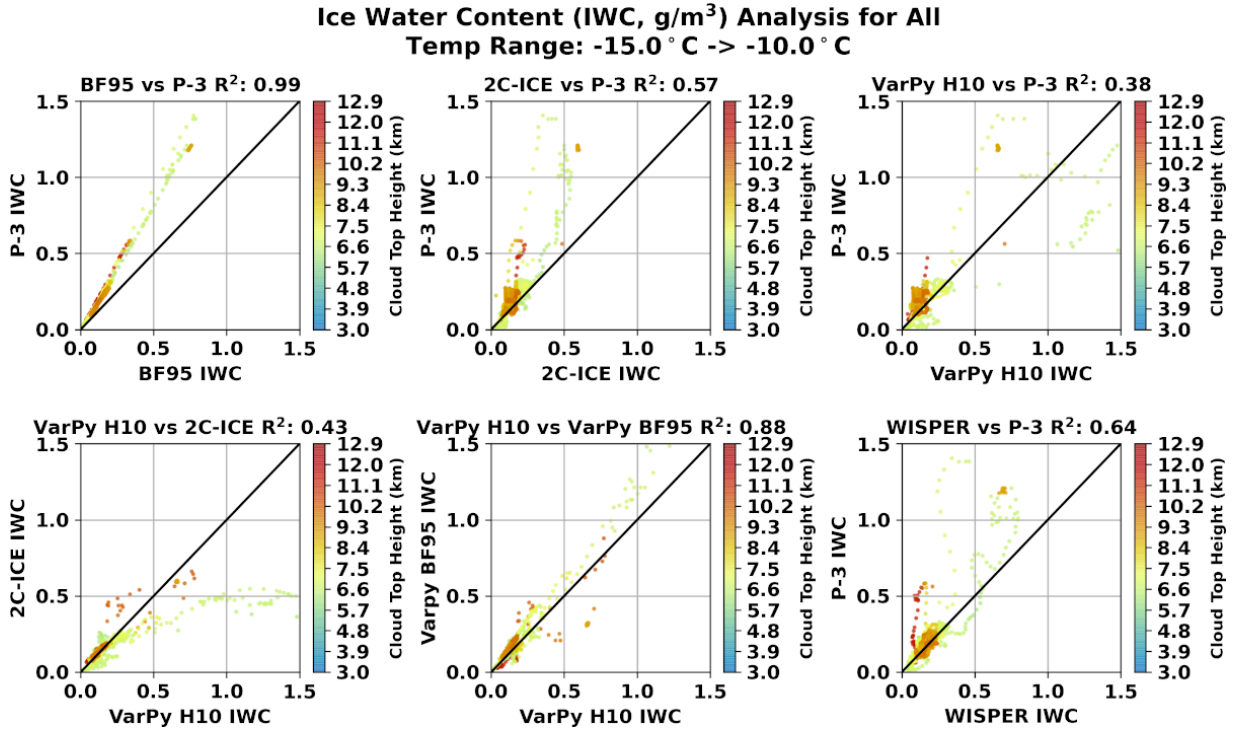


Fig. 5. Cross comparison amongst BF95-, VarPy-, 2C-ICE-, WISPER-, and P-3-retrieved IWC values for all co-located aircraft observations between -15°C and -10°C and color shaded by cloud-top height (km).

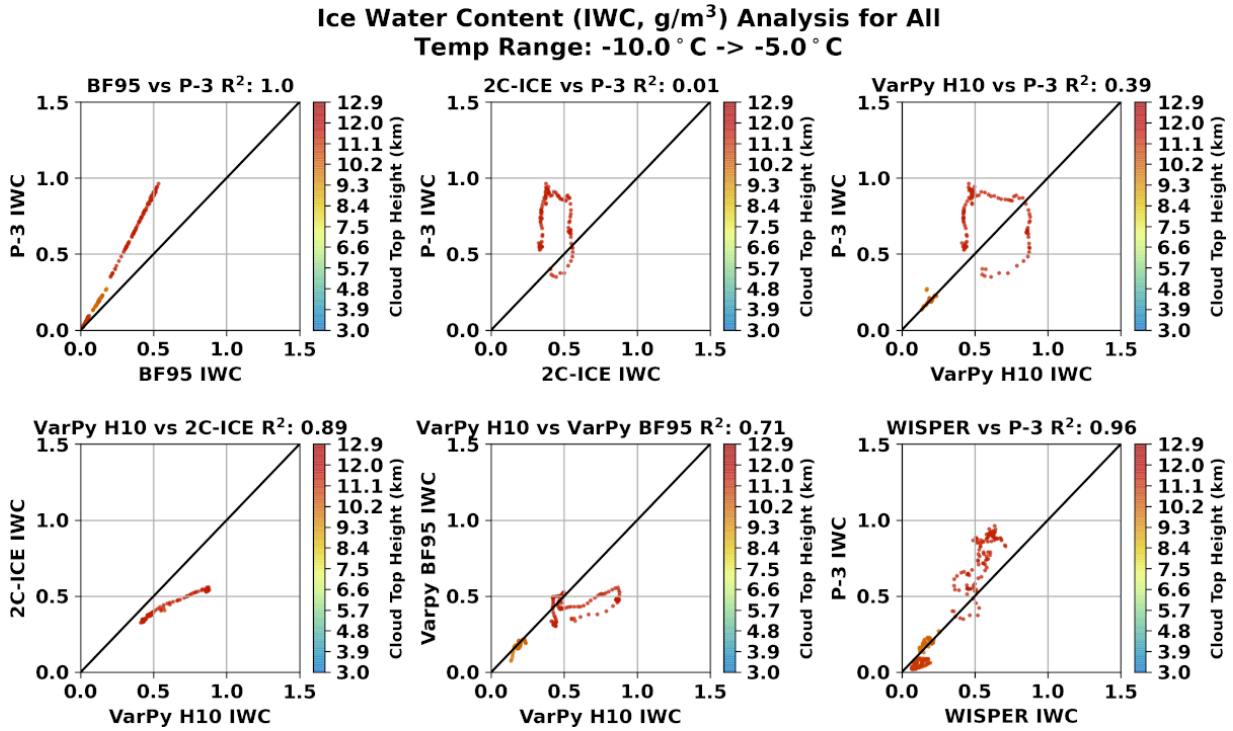


Fig. 6. Same as Fig. 5, except temperatures between -10°C and -5°C.

**Effective Radius (Eff. Rad., microns) Analysis for All
Temp Range: -15.0 °C -> -10.0 °C**

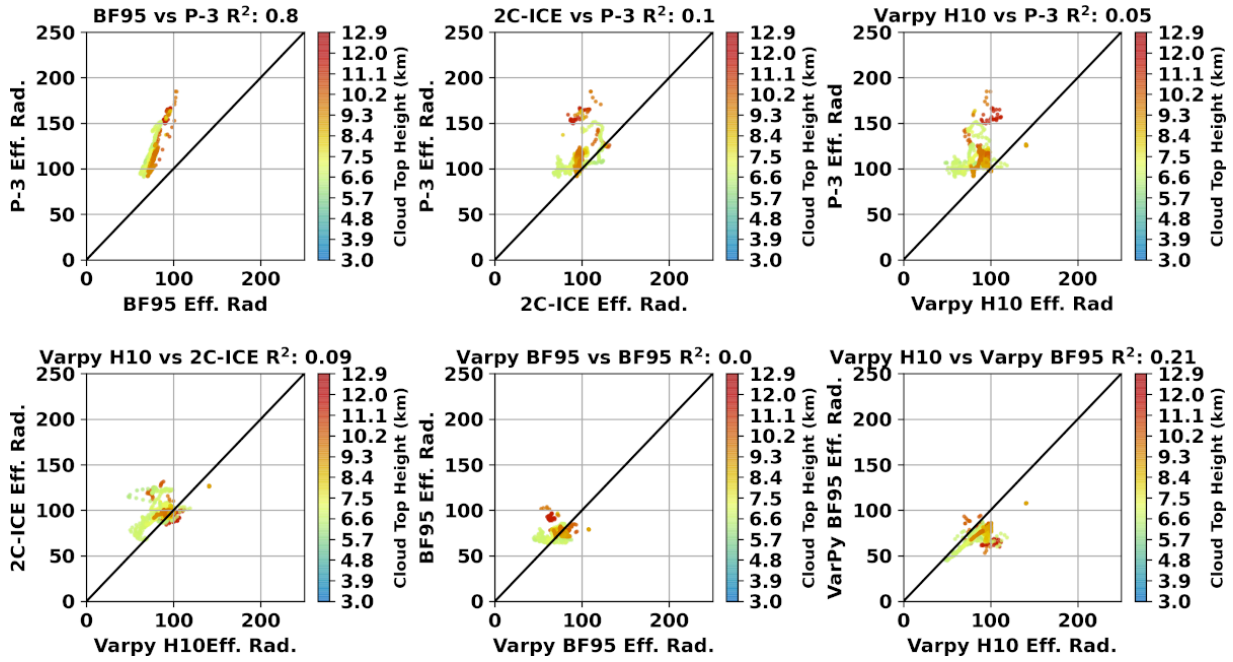


Fig. 7. Cross comparison amongst BF95-, VarPy-, 2C-ICE-, and P-3-retrieved effective radius values for all co-located aircraft observations at temperatures between -15°C and -10°C and color shaded by cloud-top height (km).

**Effective Radius (Eff. Rad., microns) Analysis for All
Temp Range: -10.0 °C -> -5.0 °C**

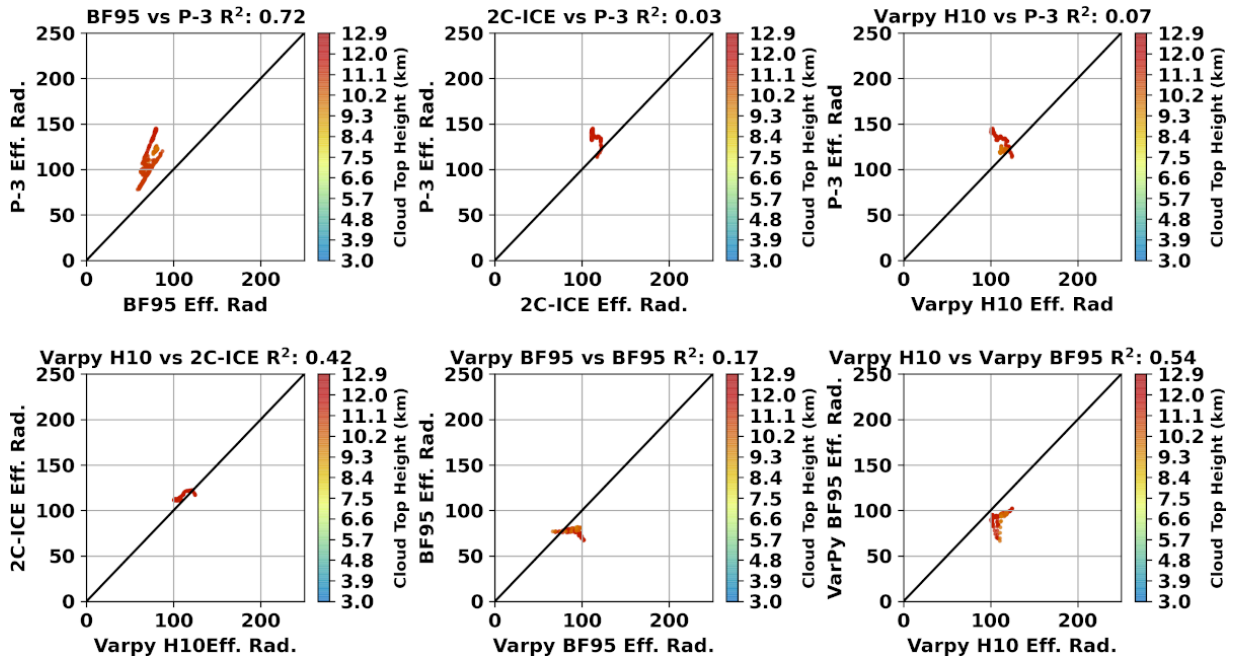


Fig. 8. Same as Fig. 7, except for temperatures between -10°C and -5°C.

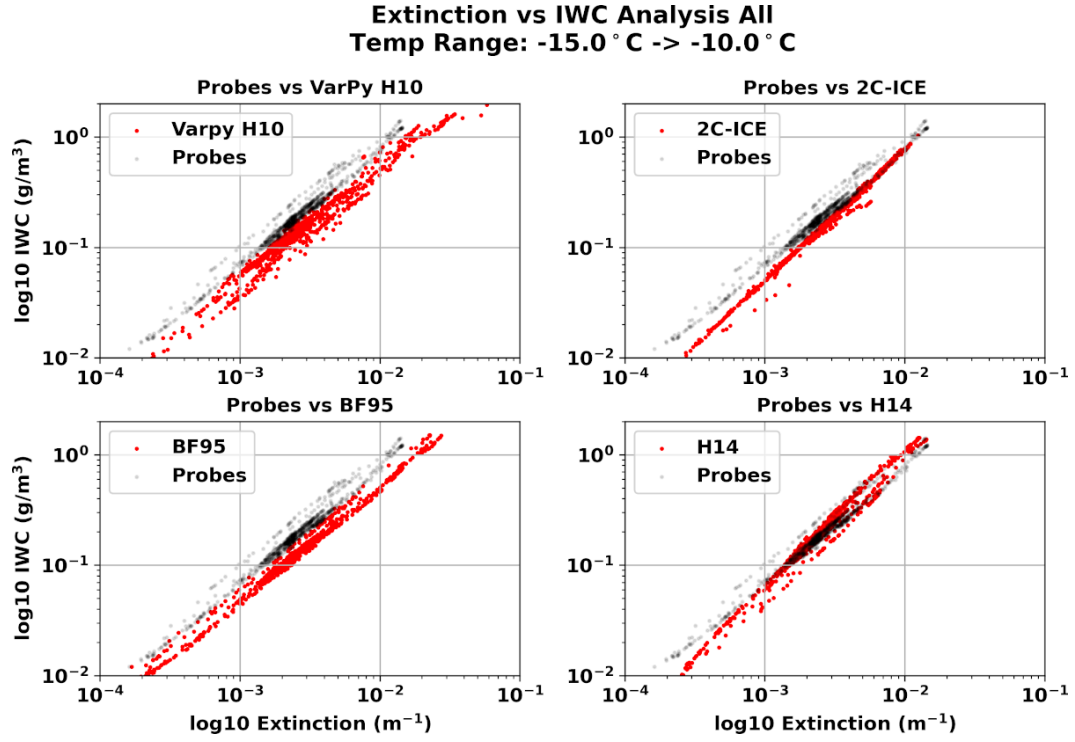


Fig. 9. The IWC-extinction relationship as derived from VarPy H10-, 2C-ICE-, BF95-, and H14-based retrievals (red dots), and the P-3 cloud probe retrievals (black dots) for all co-locations at temperatures between -15°C and -10°C.

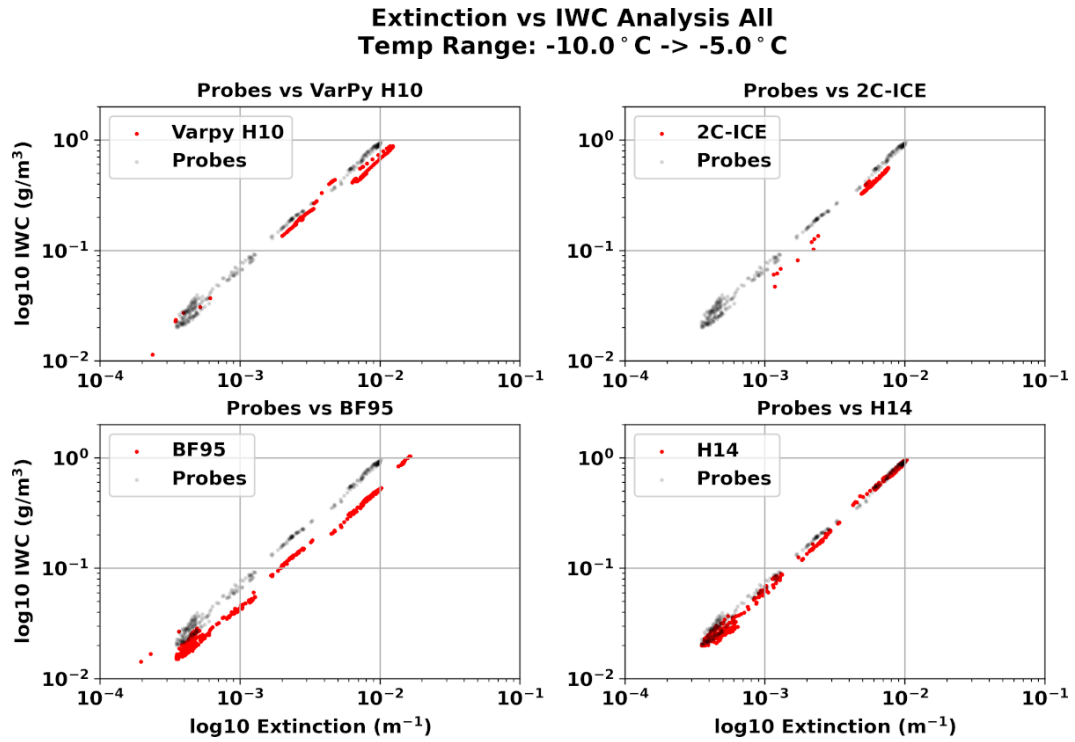


Fig. 10. Same as Fig. 8, except for temperatures between -10°C and -5°C.

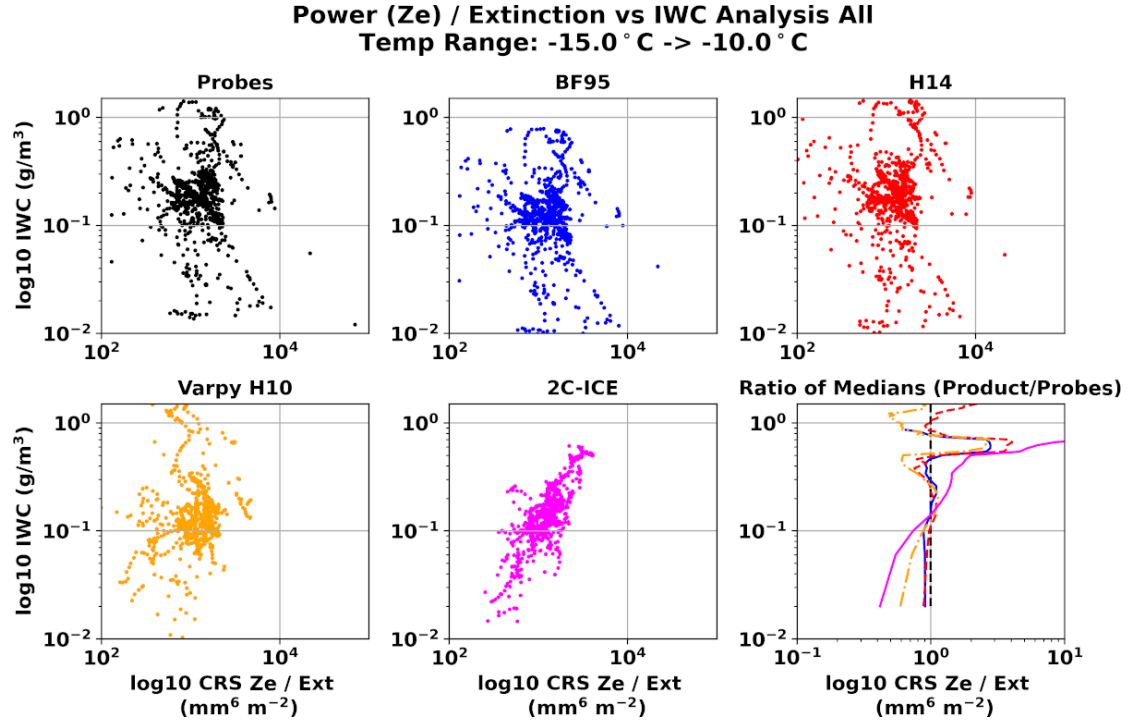


Fig. 11: The relationship between IWC and the CRS reflectivity to extinction ratio derived from the P-3 cloud probes (Probes), BF95, H14, VarPy H10, and 2C-ICE. The bottom right panel shows the absolute difference in ratio median between each product and the P-3 cloud probes using a 0.04 g/m³ IWC bin size; the colors match the corresponding data sources shown in the other five panels. The data shown is valid for temperatures between -15°C and -10°C.

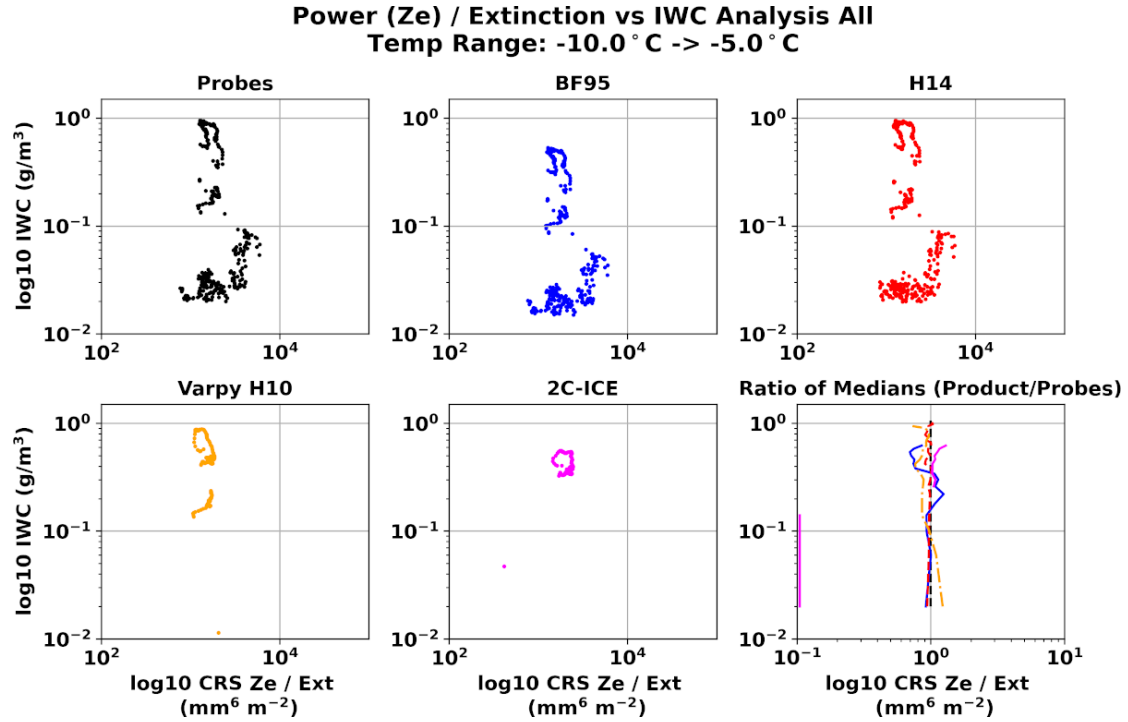


Fig. 12. Same as Fig. 10, except for temperatures between -10°C and -5°C .

6. Discussion

The results of this investigation underscore the importance of temperature, treatment of ice particles, PSDs, and LUTs to the accuracy of empirically- and algorithm-derived microphysical properties. Figure 13 shows the observed ice particle property temperature dependence during the 25 Jan. 2020 IMPACTS mission via in-situ 2D-S probe imagery. These in-cloud images were taken primarily around ER-2/P-3 co-location periods. In each panel, the separation between the horizontal lines corresponds to a diameter of about 1.25 mm. At all temperature levels, aggregates as large as 1.25 mm were observed. The larger particles display some indication of riming. Indeed, liquid water contents above 0.1 g/m^3 were sampled at times during each penetration, and P-3-measured vertical wind motions exceeded 1 m/s many times during the flight. Some indications of columns and capped columns were noted at the coldest level. Dendrites as part of aggregates were observed near the -15°C level. Well-defined needle-like crystals, evidence of secondary ice production, were sampled at temperatures of -10°C and warmer. One might expect that the particle mass at a given diameter would be larger than those of unrimed bullets, columns, and side planes used to develop BF95. The observed variability in ice particle characteristics (sizes, habit, riming, and aggregation) highlights the challenge microphysical and cloud scientists face when attempting to represent these particles and their radiative impacts in numerical prediction models.

To address these challenges, algorithms apply LUTs, particle assumptions (e.g., hexagonal columns versus mean melt diameter), and forward models to retrieve microphysical properties and keep computational costs feasible. All of these assumptions and components have unique sources of errors stemming from parameterizations, assumed PSDs, temperature-dependent particle shapes, and environment sampled to create the LUTs. Previous VarPy and 2C-ICE investigations differed from this IMPACTS-focused study because they focused on low-temperature (-60°C to -20°C) ice cloud environments (Deng et al. 2010, Delanoë et al. 2014, Cazenave et al. 2019). In contrast, IMPACTS sampled mid-latitude winter storms where temperatures often approached the freezing level, convection could be present, and where particle habit variability, riming, and aggregation processes are more prevalent (See Figure 13). Testing these algorithms in mid-altitude wintertime cyclones provides value by evaluating these often-used mass-dimensional relationships and lidar-radar retrieval algorithms in less commonly

studied complex and dynamic environment. Therefore, this study has shown that each relationship and algorithm has its strengths, weaknesses, and potential biases, which can aid with their future refinement and also help train future algorithms, especially pertaining to cloud systems where the temperatures are closer to freezing ($> -25^{\circ}\text{C}$). However, the inclusion of IMPACTS 2022 and 2023 data (not available at the time of this manuscript) would almost certainly provide additional added value.

Figure 14 adds to the results presented in Section 5 (i.e., Figures 11 and 12) by showing the median IWC and microphysical property ratios (product/P-3) as a function of temperature in 1°C increments for VarPy H10, VarPy BF95, and 2C-ICE. Median IWC, r_e , and σ ratios exhibit considerable temperature dependence, not an unexpected result given the previous field campaign measurement-based studies of H10, H14, and Thornberry et al. 2017. IWC results (Figure 14, top two panels) reveal that the VarPy and 2C-ICE algorithms generally have a low bias relative to the P-3 cloud probes, which is commensurate with the results shown in Figures 5 and 6. This low bias in algorithm-derived IWC is fairly robust, but it is seemingly more pronounced in regions away from the dendritic growth (-18°C to -12°C), likely due to aggregation processes being under-estimated at temperatures closer to freezing and then again at colder temperatures where particle size or number concentration may be similarly biased lower. As temperatures approach freezing, the overall median bias decreases, which is potentially associated with how each algorithm treats the CRS bright band, where higher reflectivity values may map to larger particle sizes. Like IWC, the median σ and r_e ratios (bottom two panels of Figure 13) demonstrate general median low bias in these ratios across most temperature bins. The similarity in median ratio biases tendencies can be partially explained by the relationship between IWC, r_e , and σ defined in Equation 5.

However, even given this empirical linkage between all three microphysical properties, there does exist some disagreement within the dendritic growth zone -15°C to -10°C , where σ ratios tend to bias higher than the P-3 cloud probes, which highlights the importance of particle habits to σ given its direct relationship to both cross-sectional area and number concentration. Hence, the algorithms may produce too many ice particles in their PSDs; the derived cross-section areas or some combinations thereof are too small. Therefore, VarPy, DARDAR, and 2C-ICE could potentially be improved if they could address particle shapes as a function of temperature or possibly implement a fractal model relationship (i.e., Schmitt and Heymsfield 2010).

Additionally, the low bias in VarPy BF95 IWC is commensurate with Cazenave et al. (2019), who found that applying the H10 LUT instead of BF95 in VarPy reduced its bias, particularly when IWC exceeds 0.1 g/m^3 , which is consistent with this investigation (See Figs. 5 and 6)

Finally, Figure 15 contains box and whisker plots of both H14- and BF95-retrieved IWCs normalized by the P-3 cloud probe IWCs during all ER-2/P-3 co-locations used in this study. P-3 cloud probe IWC values are retrieved using SODA2, whereas H10 and BF95 IWC retrievals are derived from P-3 cloud probe σ values. Commensurate with our earlier results for IWC and σ (Figures 3-6) and Cazenave et al. (2019), BF95 retrieved IWC show a consistent and systematic low bias in median IWC values, which does not tend to increase or decrease with increasing IWC. Similarly, H10 does not show any trends in IWC bias with increasing IWC, yet its median values have a near 1:1 relationship with the P-3 cloud probes. As both BF95 and H10 are derived from field campaign IWC and σ values, this further supports our earlier claim that the BF95 mass-dimensional coefficients are likely too small because BF95's sampling only included cirrus and thin ice clouds, whereas H10 sampled heavy and thick ice clouds, which are more similar to those sampled in IMPACTS. Despite their difference, BF95 and H10 exhibit qualitatively similar wave-like patterns in their IWC ratios as IWC increases. The similarity of this pattern for both BF95 and H10 hints at a potential systematic source, whether from ice crystal shattering or differences in cloud probe retrieval errors amongst the various field campaigns. Additionally, Figure 15 maps these data to a second Y-axis, the particle area ratio, which is defined as the ratio of the particle area to a circumscribed circle around the maximum dimension of each particle. When all particles are considered in a given time period (here, 10 seconds), a power-law curve fit is derived between the area ratio and diameter. Figure 15, right ordinate, shows the power in the area ratio-diameter relationship. According to Schmitt and Heymsfield (2010), the two- and three-dimensional fractal dimension values-the latter is the power in the mass dimensional relationship, were found to be related by the following:

$$b = (2-p)*1.275, \quad (6)$$

where b is the power in the mass dimensional relationship, and p is the power in the area diameter relationship. The results plotted in Figure 14 suggest that the value of b is approximately 2.3, as suggested by Heymsfield et al. (2023). The inclusion of fractal dimension relationships in future LUTs may offer one potential route to improve their accuracy.

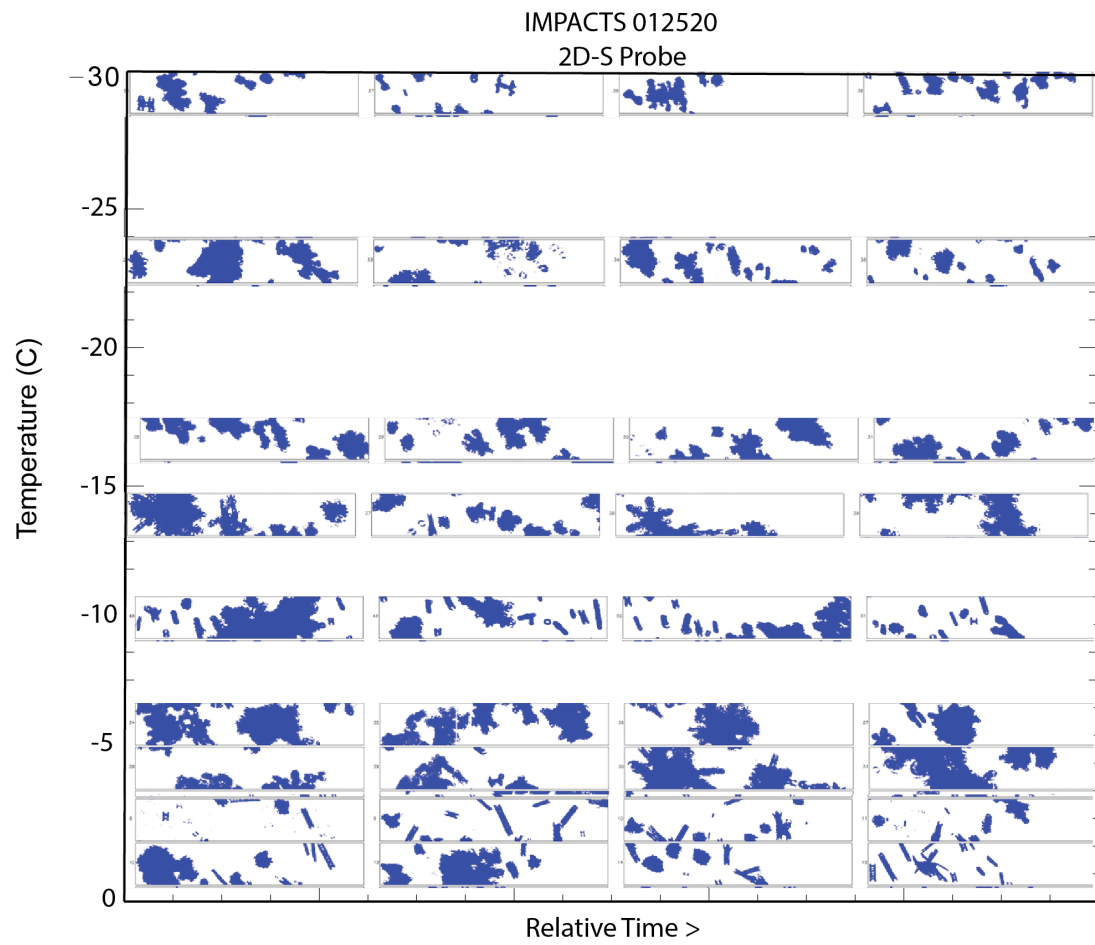


Fig. 13. Images of particles from the 2D-S probe on 25 Jan. 2020. The horizontal lines in each panel are separated by 1.25 mm. The sampling temperature for each sample is shown.

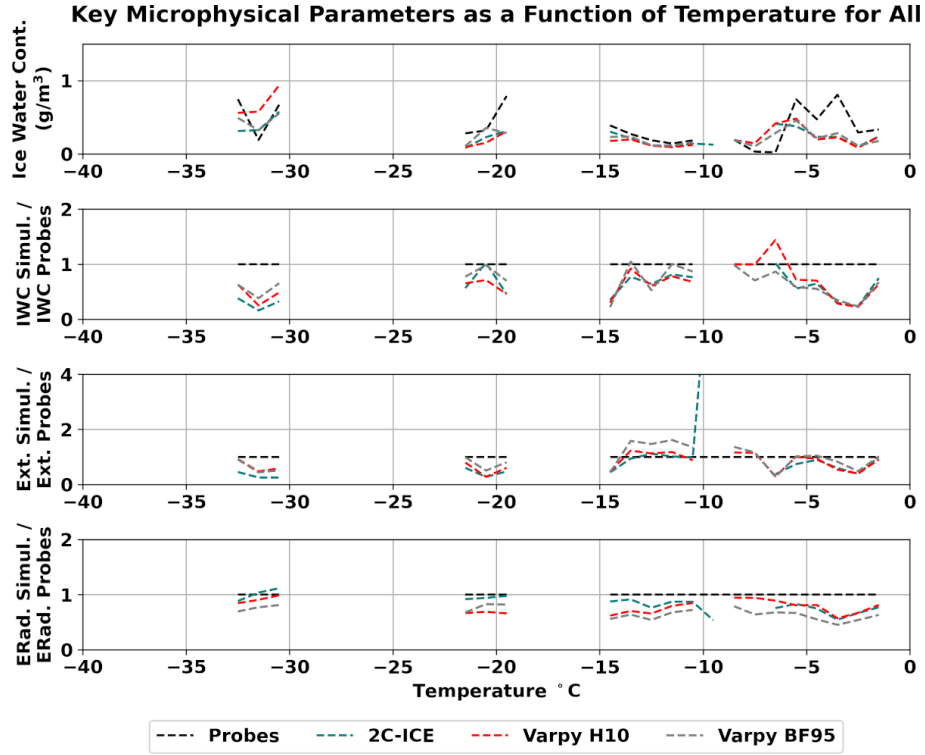


Fig. 14. (top) Median values of ice water content (g/m^3) from the P-3 cloud probes and the 2C-ICE and VarPy simulation and (bottom three panels) the ratios of ice water content, extinction, and effective radius relative to the P-3 cloud probes in 1°C increments. The black line denotes a 1:1 match with P-3 cloud probes.

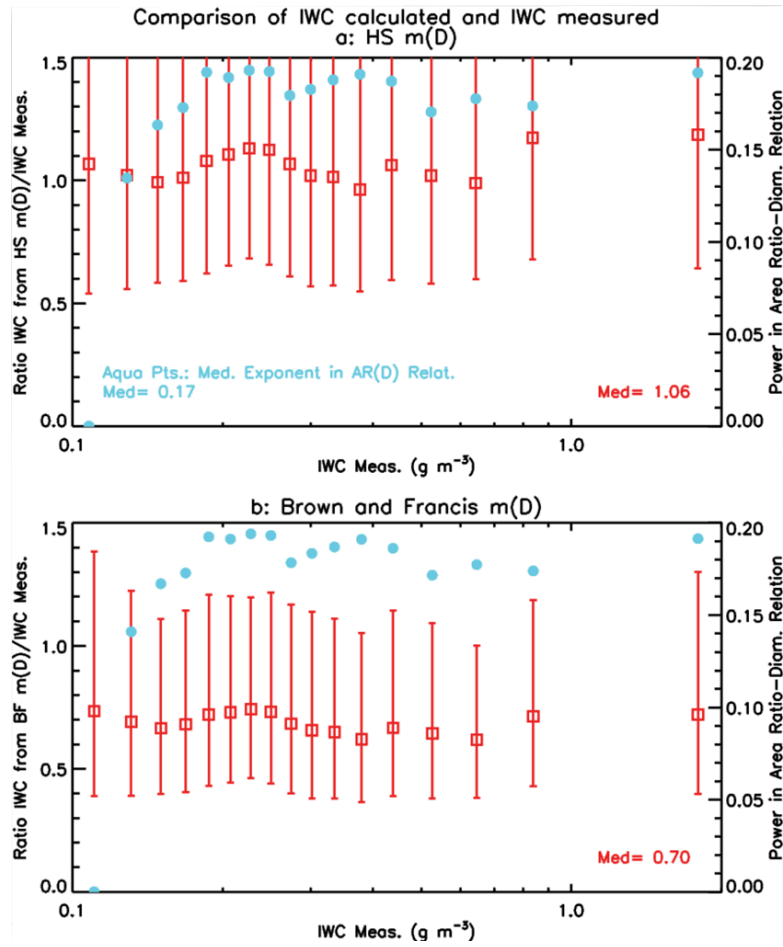


Fig. 15. Left ordinate compares the ratio of the IWC calculated based on the H10 study, $a=0.0061$ (cgs) and $b=2.05$, and BF95, $a=0.00294$ (cgs) and $b=1.9$. Noted in the figure are the median values of the ratios, where it is noted that the Heymsfield et al. (2010) relationship agrees more closely with the measured values than the Brown and Francis (1995) relationship.

7. Conclusions

The IMPACTS field campaign provides a unique, rich, and high-quality co-located dataset containing in-situ microphysical cloud probe measurements (2D-S, CDP, HVPS-3) and overflying ER-2 radar (CRS), lidar (CPL), and radiometer data geared towards characterizing ice and snow microphysics during high-impact mid-latitude winter storms. Using IMPACTS data affords the unique opportunity to evaluate the capability and accuracy of both empirical- (H14, BF95) and algorithm (2C-ICE, VarPy) -based microphysical retrievals methods during the four IMPACTS 2020 field campaign flights (25 Jan., 1 Feb., 5 Feb., and 7 Feb.), where the data are known to be of high accuracy and have been well vetted (McMurdie et al., 2022). Despite both VarPy and 2C-ICE being actively used by the CloudSat and CALIPSO communities for satellite-based ice phase retrievals, studies investigating evaluating both algorithms against a common high-quality microphysical dataset is unprecedented in the literature. Commensurate with previous studies, our investigation found that the retrieved microphysical properties (IWC, r_e , and σ) have a notable temperature dependence, which was used to frame and characterize our results in various key temperature regimes (i.e., dendritic growth zone near freezing, etc.) where key microphysical particle properties and processes (i.e., aggregation, riming, particle size, and habit) are known to vary considerably. The ER-2/P-3 IMPACTS 2020 dataset, with over 3,900 samples, is limited to radar-only regions since the P-3 almost always flew below the CPL attenuation depth (cloud optical depth of 3.00), which limits this investigation to radar-only regions. Additionally, the P-3 probe data used to evaluate the various retrievals methods required the use of SODA2 to merge the IMPACTS P-3 microphysical probe data (2D-S, and HVPS-3) into a continuous dataset across all particle sizes.

Our investigation evaluated the retrieval methods using three key microphysical properties (IWC, r_e , and σ) retrieved by the P-3 aircraft, which were used in previous microphysical field campaigns (H10, H14, Thornberry et al. 2017), VarPy- (Delanoë and Hogan, 2010, Cazenave et al. 2019) and 2C-ICE- (Deng et al. 2010, Deng et al. 2013) -based studies. Between the two empirical relationships, BF95 and H14, BF95 are shown to have a linear, systematic, and nearly temperature-independent low bias for IWC and r_e , whereas H14 has a near 1:1 relationship to these same P-3 cloud probe data. For σ , BF95 and H14 share a close 1:1 relationship with the P-3 cloud probes. Given that H14 and BF95 apply similar methods to derive their mass-dimensional relationship and the three-way relationship between IWC, r_e , and σ given in equation 5, the

difference in performance between these two empirical methods is likely associated with the environment sampled in H14 (heavy and thick ice clouds) sharing greater similarities to those sampled by IMPACTS than BF95 (cirrus and thin clouds). This difference seemingly leads to BF95 IWC values being biased low for IMPACTS-like storm environments, which leads the derived BF95 mass-dimensional coefficients to be too low. Should BF95 IWC values and the associated coefficients be reevaluated using IMPACTS data, the accuracy of its retrieved data may be greatly improved.

The algorithm component of this investigation included three retrievals (VarPy BF95, VarPy H10, and 2C-ICE), where the two VarPy retrievals are identical except for their application of the BF95 and H10 LUTs respectively, and 2C-ICE used the Yang et al. (2000) LUT. VarPy H10 and VarPy BF95 produced results that paralleled H14 and BF95, where VarPy BF95 retrievals show a near 1:1 σ correspondence with VarPy H10, yet IWC and r_e are biased systematically lower than VarPy H10. For σ , both VarPy H10 and 2C-ICE exhibit qualitatively similar degrees of error relative to the P-3 cloud probes, yet both have a near 1:1 correspondence, and their errors vary similarly with temperature. Notably, algorithm-retrieved σ errors near the dendritic growth zone (-15°C to -10°C) increase sharply, which suggests that the increase is not due to the LUT, but instead to how each algorithm forward model treats the CRS radar data similarly and potentially Rayleigh scattering given the particle sizes tend to be larger in this zone. Unlike σ , the variability between VarPy H10- and 2C-ICE-based IWC is considerably more pronounced, particularly above 0.2 g/m³, within the dendritic growth zone, and near freezing.

Compared to the P-3 cloud probes, both VarPy H10 and 2C-ICE, the spread in retrieved IWC error increasingly fans out with increasing IWC, but on average, both algorithms tend to bias lower than P-3 retrieved IWC. Because ice particle size tends to increase with increasing IWC, this bias could result from several factors, including the treatment of ice particle shape (2C-ICE: hexagon columns, VarPy: mean melt diameter) and modeling of Rayleigh scattering effects. For r_e , VarPy BF95 biases toward smaller particle sizes than VarPy H10 due to the BF95 LUT being biased toward smaller IWC values than the H10 LUT. To first order, both VarPy H10- and 2C-ICE-based r_e values show similar levels of error relative to the P-3 cloud probe retrieved r_e values. However, close inspection revealed that VarPy H10 is biased towards even smaller r_e values than 2C-ICE, and VarPy BF95 retrieved even smaller r_e values than its H10 counterpart. Hence, even though 2C-ICE assumes only hexagonal column ice crystal habits, the mean melted

diameter treatment of ice crystals by VarPy leads to even smaller particle sizes. Once temperatures approach freezing, both VarPy H10 and 2C-ICE lose almost all their r_e predictive skill due to the increased frequency of riming and aggregation processes.

The result of this investigation are subject to four key limitations: 1) Our results are limited to the radar-only regions of VarPy and 2C-ICE, 2) the IMPACTS 2020 dataset includes only four co-located flights, 3) our results did not address IMPACTS P-3 cloud probe measurement uncertainties or discuss ice particle habits, which both go beyond the intended scope of this paper, 4) our decision to assimilate W-band radar into 2C-ICE and VarPy, which subject to Rayleigh scatter effects as particle sizes increase. Despite these limitations, our investigation revealed that the 2C-ICE and VarPy forward models show similar degrees of error for σ , but more notable differences in IWC and r_e retrievals due to ice particle assumptions made by each (hexagonal crystals versus mean melt diameter) and their assumed LUTs. We believe that this study has shown these algorithms could be potentially improved by replacing existing LUT with temperature-dependent LUTs, introducing a fractal dimension relationship, and further refinement of their respective forward models. New LUTs could be built from existing field campaign data and implemented following the first-guess solution, as is done presently and potentially offer more refined and accurate estimates of IWC and other key parameters due reduced table averaging effects. A fractal dimension relationship could also be built from field campaign particle imagery and implemented within forward model of an algorithm and would afford the potential of better estimates of particle mass and the relationship of particle mass to particle area. All together these changes offer better enabling microphysical models to more capably address cloud-radiative forcing, which remains a grand challenge and notable source of error in numerical prediction models.

We plan to address many of the limitations of this study in future work, which will further this investigation by including co-located IMPACTS flights from the 2022 and 2023 deployments. These deployments include 19 additional co-located flights between the ER-2 and P-3 aircrafts, including several flights where the P-3 aircraft was at or near cloud top where the CPL did attenuate before reaching the altitude of the P-3. This study revealed that microphysical properties retrieved from the H14 and BF95 empirical relationships were subject to varying degrees of error compared to the P-3 microphysical cloud probe data. We believe that the high-quality data gathered by the IMPACTS field campaign can create updated

mass-dimensional relationships or train a machine-learning model that would potentially be subject to less error than both H14 and BF95. Finally, the influence of Rayleigh scattering on the results of this study could be addressed by reprocessing the IMPACTS dataset using the Ka-band HIWRAP radar dataset instead, which is less subject to this scattering. However, such a study would have far less radar-lidar overlap due to the reduced sensitivity of Ku-band radars, which ultimately led us to use W-band radar for this investigation.

Acknowledgments.

We thank the support of the NASA Earth Science Division (ESD) and Earth Venture Suborbital Program under the NASA Airborne Science Program for funding, making the IMPACTS field campaign possible, and funding this research.

Data Availability Statement.

All data used for this study part of the IMPACTS Collection, which contains all IMPACTS field-campaign-related datasets, which are stored, managed, and openly available via the NASA Global Hydrometeorology Resource Center (https://ghrc.nsstc.nasa.gov/uso/ds_details/collections/impactsC.html). Datasets specific to this study include:

- 1) CPL: <http://dx.doi.org/10.5067/IMPACTS/CPL/DATA101>
- 2) CRS: <http://dx.doi.org/10.5067/IMPACTS/CRS/DATA101>
- 3) NCAR Particle Probes: <http://dx.doi.org/10.5067/IMPACTS/PROBES/DATA101>
- 4) UND Cloud Microphysics: <http://dx.doi.org/10.5067/IMPACTS/MULTIPLE/DATA101>
- 5) WISPER: <https://dx.doi.org/10.5067/IMPACTS/WISPER/DATA101>
- 6) P-3 Meteorological and Navigational Data:
<http://dx.doi.org/10.5067/IMPACTS/P3/DATA101>
- 7) ER-2 Navigational Data: <http://dx.doi.org/10.5067/IMPACTS/ER2/DATA101>

SODA2, used to generate the multi-sensor microphysical data from the P-3 2D-S, and HVPS-3 cloud probes, can be downloaded from <https://github.com/abansemer/soda2>.

REFERENCES

- Battaglia, A., Kollias, P., Dhillon, R., Roy, R., Tanelli, S., Lamer, K., et al., 2020: Spaceborne cloud and precipitation radars: Status, challenges, and ways forward. *Reviews of Geophysics*, **58**, e2019RG000686. <https://doi.org/10.1029/2019RG000686>
- Brown, P. R. A. and Francis, P. N.: Improved measurements of the ice water content in cirrus using a total–water probe, *J. Atmos. Ocean. Tech.*, **12**, 410–414, 1995
- Boudala, F. S., G. A. Isaac, Q. Fu, and S. G. Cober, 2002: Parameterization of effective ice particle size for high-latitude clouds. *Int. J. Climatol.*, **22**, 1267–1284.
- Cazenave, Q., Ceccaldi, M., Delanoë, J., Pelon, J., Groß, S., and Heymsfield, A.: Evolution of DARDAR-CLOUD ice cloud retrievals, 2019: new parameters and impacts on the retrieved microphysical properties, *Atmos. Meas. Tech.*, **12**, 2819–2835, <https://doi.org/10.5194/amt-12-2819-2019>.
- Ceccaldi, M., Delanoë, J., Hogan, R. J., Pounder, N., Protat, A., and Pelon, J.: From CloudSat-CALIPSO to EarthCare: Evolution of the DARDAR cloud classification and its comparison to airborne radar-lidar observations, *J. Geophys. Res.-Atmos.*, **118**, 7962–7981, <https://doi.org/10.1002/jgrd.50579>, 2013.
- Davis, S., Hlavka, D., Jensen, E., Rosenlof, K., Yang, Q., Schmidt, S., Borrmann, S., Frey, W., Lawson, P., Voemel, H. and Bui, T.P., 2010: In situ and lidar observations of tropopause subvisible cirrus clouds during TC4, *J. Geophysical Research*, **115**, doi:doi:10.1029/2009JD013093.
- Delanoë, J., and R. J. Hogan, 2008: A variational scheme for retrieving ice cloud properties from combined radar, lidar, and infrared radiometer. *J. Geophys. Res.*, **113**, D07204, doi:10.1029/2007JD009000.
- Delanoë, J., and Hogan, R. J., 2010: Combined CloudSat-CALIPSO-MODIS retrievals of the properties of ice clouds, *J. Geophys. Res.*, **115**, D00H29, doi:10.1029/2009JD012346.
- Delanoë, J. M. E., Heymsfield, A. J., Protat, A., Bansemer, A., and Hogan, R. J., 2014: Normalised Particle Size Distribution for remote sensing application, *J. Geophys. Res.-Atmos.*, **119**, 4204–4227, <https://doi.org/10.1002/2013JD020700>.
- Deng, M., G. G. Mace, Z. Wang, and H. Okamoto, 2010: Tropical Composition, Cloud and Climate Coupling Experiment validation for cirrus cloud profiling retrieval using CloudSat radar and CALIPSO lidar. *J. Geophys. Res.*, **115**, D00J15, doi:10.1029/2009JD013104

- Deng, M., G. G. Mace, Z. Wang, and R. P. Lawson, 2013: Evaluation of Several A-Train Ice Cloud Retrieval Products with In Situ Measurements Collected during the SPARTICUS Campaign. *J. Appl. Meteor. Climatol.*, **52**, 1014–1030, <https://doi.org/10.1175/JAMC-D-12-054.1>.
- Diedenhoven, B., A. M. Fridlind, B. Cairns, A. S. Ackerman, and J. E. Yorks (2016), Vertical variation of ice particle size in convective cloud tops, *Geophys. Res. Lett.*, **43**, doi:10.1002/2016GL068548.
- Dolinar, E. K., Campbell, J. R., Lolli, S., Ozog, S. C., Yorks, J. E., Camacho, C., et al., 2020: Sensitivities in satellite lidar-derived estimates of daytime top-of-the-atmosphere optically thin cirrus cloud radiative forcing: A case study. *Geophys. Res. Lett.*, **47**, e2020GL088871. <https://doi.org/10.1029/2020GL088871>.
- Dolinar, E. K., J. R. Campbell, J. W. Marquis, A. E. Garnier, and B. M. Karpowicz, 2022: Novel Parameterization of Ice Cloud Effective Diameter from Collocated CALIOP-IIR and CloudSat Retrievals. *J. Appl. Meteor. Climatol.*, **61**, 891–907, <https://doi.org/10.1175/JAMC-D-21-0163.1>.
- Finlon, J. A., L. A. McMurdie, and R. J. Chase, 2022: Investigation of Microphysical Properties within Regions of Enhanced Dual-Frequency Ratio during the IMPACTS Field Campaign. *J. Atmos. Sci.*, **79**, 2773–2795.
- Foot, J. S., 1988: Some observations of the optical properties of clouds. Part II: Cirrus. *Quart. J. Roy. Meteor. Soc.*, **114**, 145–164.
- Heymsfield, A. J., D. Winker, D., and G.-J. van Zadelhoff, 2005: Extinction-ice water content-effective radius algorithms for CALIPSO, *Geophysical Research Letters*, **32**, <https://doi.org/10.1029/2005GL022742>
- Heymsfield, A. J., C. Schmitt, A. Bansemer, and C. H. Twohy, 2010: Improved representation of ice particle masses based on observations in natural clouds. *J. Atmos. Sci.*, **67**, 3303–3318.
- Heymsfield, A., D. Winker, M. Avery, M. Vaughan, G. Diskin, M. Deng, V. Mitev, and R. Matthey, 2014: Relationships between Ice Water Content and Volume Extinction Coefficient from In Situ Observations for Temperatures from 0° to –86°C: Implications for Spaceborne Lidar Retrievals, *J. Appl. Meteor. Climatol.*, **53**, 479–505, <https://doi.org/10.1175/JAMC-D-13-087.1>

- Heymsfield, A., A. Bansemer, G. Heymsfield, D. Noone, M. Grecu, and D. Toohey, 2023: Relationship of Multi-wavelength Radar Measurements to Ice Microphysics from the IMPACTS Field Program. *J. Appl. Meteor. Climatol.*, **62**, 289–315
- Hlavka, D. L., J. E. Yorks, S. A. Young, M. A. Vaughan, R. E. Kuehn, M. J. McGill, and S. D. Rodier (2012), Airborne validation of cirrus cloud properties derived from CALIPSO lidar measurements: Optical properties, *J. Geophys. Res.*, **117**, D09207, doi:10.1029/2011JD017053.
- Hogan, R. J., D. P. Donovan, C. Tinel, M. A. Brooks, A. J. Illingworth, and J. P. V. Poyares Baptista, 2006: Independent evaluation of the ability of spaceborne radar and lidar to retrieve the microphysical and radiative properties of ice clouds, *J. Atmos. Oceanic Technol.*, **23**, 211–227.
- Hong, G., 2007: Radar backscattering properties of non-spherical ice crystals at 94 GHz. *J. Geophys. Res.*, **112**, D22203, doi:10.1029/2007JD008839.
- Intrieri, J. M., G. L. Stephens, W. L. Eberhard, and T. Uttal, 1993: A Method for Determining Cirrus Cloud Particle Sizes Using Lidar and Radar Backscatter Technique. *J. Appl. Meteor. Climatol.*, **32**, 1074–1082, [https://doi.org/10.1175/1520-0450\(1993\)032<1074:AMFDCC>2.0.CO;2](https://doi.org/10.1175/1520-0450(1993)032<1074:AMFDCC>2.0.CO;2).
- Janiszewski, A., R. M. Rauber, B. F. Jewett, G. M. McFarquhar, T. Zaremba, and J.E. Yorks, 2023: Kinematic Modeling Study of the Re-Organization of Snowfall beneath Cloud-top Generating Cells in Midlatitude Winter Storms. Part I: Idealized Study Using a 3-Dimensional Deformation Wind Field, *J. Atmos. Sci.*, in review.
- Li, L., G. M. Heymsfield, P. E. Racette, L. Tian, and E. Zenker, 2004: A 94-GHz cloud radar system on a NASA high-altitude ER-2 aircraft. *J. Atmos. Oceanic Technol.*, **21**, 1378–1388, [https://doi.org/10.1175/1520-0426\(2004\)021,1378:AGCRSO.2.0.CO;2](https://doi.org/10.1175/1520-0426(2004)021,1378:AGCRSO.2.0.CO;2).
- , ———, L. Tian, and P. E. Racette, 2005: Measurements of ocean surface backscattering using an airborne 94-GHz cloud radar-implication for calibration of airborne and spaceborne W-band radars. *J. Atmos. Oceanic Technol.*, **22**, 1033–1045, <https://doi.org/10.1175/JTECH1722.1>.
- , and Co-authors, 2016: The NASA High-Altitude Imaging Wind and Rain Airborne Profiler (HIWRAP). *IEEE Trans. Geosci. Remote Sens.*, **54**, 298–310, <https://doi.org/10.1109/TGRS.2015.2456501>.

- Liu, 2018: Toward Improving Ice Water Content and Snow-Rate Retrievals from Radars. Part II: Results from Three Wavelength Radar-Collocated In Situ Measurements and CloudSat–GPM–TRMM Radar Data. *J. Appl. Meteor. Climatol.*, **57**, 365–389.
- McGill, M.J., D.L. Hlavka, W.D. Hart, J.D. Spinhirne, V.S. Scott, and B. Schmid, 2002: The Cloud Physics Lidar: Instrument description and initial measurement results, *Applied Optics*, **41**, 3725–3734.
- McGill, M.J., L. Li, W.D. Hart, G.M. Heymsfield, D.L. Hlavka, P.E. Racette, L. Tian, M.A. Vaughan, and D.M. Winker, 2004: Combined lidar-radar remote sensing: Initial results from CRYSTAL-FACE, *J. Geophys. Res.*, **109**, doi: 10.1029/2003JD004030.
- McGill, M. J., M. A. Vaughan, C. R. Trepte, W. D. Hart, D. L. Hlavka, D. M. Winker, and R. Kuehn, 2007: Airborne validation of spatial properties measured by the CALIPSO lidar, *J. Geophys. Res.*, **112**, D20201, doi:10.1029/2007JD008768.
- McLinden M.L.W., L. Li, G. M. Heymsfield, et al. The NASA GSFC 94-GHz Airborne Solid-State Cloud Radar System (CRS), 2021: *J. Atmos. Ocean. Tech.*, **38**, 1001–1017.
- McMurdie, L.A., G.M. Heymsfield, J.E. Yorks, S.A. Braun, G. Skofronick-Jackson, R. Rauber, S. Yuter, B. Colle, G. McFarquar, M. Poellet, D. Novak, T. Lang, R. Kroodsma, M. McLinden, J. Finlon, V. McDonald, S. Nicholls, M. Oue, P. Kollias, S. Brodzik, 2022:, Chasing Snowstorms: The Investigation of Microphysics and Precipitation for Atlantic Coast-Threatening Snowstorms (IMPACTS) Campaign, *Bull. Amer. Meteor. Soc.*, **103**, E1243–E1269, <https://doi.org/10.1175/BAMS-D-20-0246.1>.
- McLinden, M. L., L. Li, G. M. Heymsfield, M. Coon, and A. Emory, 2021: The NASA GSFC 94-GHz Airborne Solid-State Cloud Radar System (CRS). *J. Atmos. Oceanic Technol.*, **38**, 1001–1017, <https://doi.org/10.1175/JTECH-D-20-0127.1>.
- Midzak, N., J. E. Yorks, J. Zhang, B. van Dierenhoven, S. Woods, and M. McGill, 2020: A Classification of Ice Crystal Habits Using Combined Lidar and Scanning Polarimeter Observations during the SEAC4RS Campaign. *J. Atmos. Oceanic Technol.*, **37**, 2185–2196, <https://doi.org/10.1175/JTECH-D-20-0037.1>.
- Mitrescu, C., Haynes, J. M., Stephens, G. L., Miller, S. D., Heymsfield, G. M., and McGill, M. J., 2005: Cirrus cloud optical, microphysical, and radiative properties observed during the CRYSTAL-FACE experiment: A lidar-radar retrieval system, *J. Geophys. Res.*, **110**, D09208, doi:10.1029/2004JD005605.

- Pauly, R., J.E. Yorks, D.L. Hlavka, M.J. McGill, V. Amiridis, S.P. Palm, S.D. Rodier, M.A. Vaughan, P. Selmer, A.W. Kupchok, H. Baars, and A. Gialitaki, 2019: CATS 1064 nm Calibration and Validation, *Atmos. Meas. Tech.*, **12**, 6241–6258, <https://doi.org/10.5194/amt-12-6241-2019>.
- Rodgers, C. D., 2000: Inverse methods for atmospheric sounding: theory and practice. Vol. 2. World Scientific Publishing, ISBN 981-0202740-X. 235 pp.
- Schmitt, C. G., and A. J. Heymsfield, 2010: The Dimensional Characteristics of Ice Crystal Aggregates from Fractal Geometry. *J. Atmos. Sci.*, **67**, 1605–1616, <https://doi.org/10.1175/2009JAS3187.1>.
- Sinclair, K., van Diedenhoven, B., Cairns, B., Yorks, J., Wasilewski, A., and McGill, M., 2017: Remote Sensing of Multiple Cloud Layer Heights using Multi-Angular Measurements, *Atmos. Meas. Tech.*, **10**, 2361–2375, <https://doi.org/10.5194/amt-10-2361-2017>.
- Sourdeval, O., C.-Labonnote, L., Baran, A. J., Mülmenstädt, J., and Brogniez, G., 2016: A methodology for simultaneous retrieval of ice and liquid water cloud properties. Part 2: Near-global retrievals and evaluation against A-Train products, *Q. J. Roy. Meteor. Soc.*, **142**, 3063–3081, <https://doi.org/10.1002/qj.2889>.
- Stephens, G. L., and Co-authors, 2002: THE CLOUDSAT MISSION AND THE A-TRAIN. *Bull. Amer. Meteor. Soc.*, **83**, 1771–1790, <https://doi.org/10.1175/BAMS-83-12-1771>.
- Thornberry, T. D., A. W. Rollins, M. A. Avery, S. Woods, R. P. Lawson, T. V. Bui, and R.-S. Gao, 2017: Ice water content-extinction relationships and effective diameter for TTL cirrus derived from in situ measurements during ATTREX 2014, *J. Geophys. Res. Atmos.*, **122**, 4494–4507.
- Tinel, C., J. Testud, J. Pelon, R. J. Hogan, A. Protat, J. Delanoë, and D. Bouniol, 2005: The Retrieval of Ice-Cloud Properties from Cloud Radar and Lidar Synergy. *J. Appl. Meteor. Climatol.*, **44**, 860–875, <https://doi.org/10.1175/JAM2229.1>.
- Turk F. J., S. E Ringerud, A. Camplani, D. Casella, R. J. Chase R.J., A. Ebtehaj, J. Gong, M. Kulie, G. Liu, L. Milani, G. Panegrossi, R. Padullés, J.-F.Rysman, P Sanò P., S. Vahedizade, and N. B. Wood, 2021: Applications of a CloudSat-TRMM and CloudSat-GPM Satellite Coincidence Dataset. *Remote Sensing*, **13**, doi:10.3390/rs13122264.
- Winker, D. M., W. H. Hunt, and M. J. McGill, 2007: Initial performance assessment of CALIOP. *Geophys. Res. Lett.*, **34**, L19803, doi:10.1029/2007GL030135.

- Winker, D. M., M. A. Vaughan, A. Omar, Y. Hu, K. A. Powell, Z. Liu, W. H. Hunt, and S. A. Young, 2009: Overview of the CALIPSO Mission and CALIOP Data Processing Algorithms. *J. Atmos. Oceanic Technol.*, **26**, 2310–2323, <https://doi.org/10.1175/2009JTECHA1281.1>.
- Yang, P., K. Liou, K. Wyser, and D. Mitchell, 2000: Parameterization of the scattering and absorption properties of individual ice crystals. *J. Geophys. Res.*, **105**, 4699–4718.
- Yorks, J. E., M. McGill, D. Hlavka and W. Hart (2011a), Statistics of Cloud Optical Properties from Airborne Lidar Measurements, *J. Atmos. Oceanic Technol.*, **28**, 869–883, doi:10.1175/2011JTECHA1507.1.
- Yorks, J. E., D. L. Hlavka, M. A. Vaughan, M. J. McGill, W. D. Hart, S. Rodier, and R. Kuehn (2011b), Airborne validation of cirrus cloud properties derived from CALIPSO lidar measurements: Spatial properties, *J. Geophys. Res.*, **116**, D19207, doi:10.1029/2011JD015942.
- Young, S. A., and M. A. Vaughan, 2009: The retrieval of profiles of particulate extinction from Cloud-Aerosol Lidar Infrared Pathfinder Satellite Observations (CALIPSO) data: Algorithm description. *J. Atmos. Oceanic Technol.*, **26**, 1105–1119.

SUPPLEMENT

Supplemental Tables and Figures

	VarPy
State vector	$X = \begin{pmatrix} \ln N'_0 \\ \vdots \\ \ln N'_m \\ a_{\ln S} \\ b_{\ln S} \\ \ln \alpha_0 \\ \vdots \\ \ln \alpha_n \end{pmatrix}$
State vector explanations	$\ln S = a_{\ln S} + b_{\ln S} \times T$ n : total number of gates processed in the profile $m = \frac{n}{4}$: number of $\ln N'$ gates (a cubic-spline basis function is used to interpolate the profile for $\ln N'$ values)
State vector <i>a priori</i>	$\ln N'_a = A_{N'} + B_{N'} \times T$ with $A_{N'} = 21.94$, $B_{N'} = -0.095$ et $\gamma = 0.67$ for “Heymsfield Composite” look-up table or $A_{N'} = 22.234435$, $B_{N'} = -0.090736$ et $\gamma = 0.61$ for “BF95 Modified” look-up table $\ln S_a = a_{\ln S, a} + b_{\ln S, a} \times T$ with $a_{\ln S, a} = 3.18$ and $b_{\ln S, a} = -8.6 \times 10^{-3}$ $\ln \alpha_a = -7$
State vector first guess	$\ln N'_i = \ln N'_a$ $\ln S_i = \ln S_a$ $\ln \alpha_i = -9$
Look up tables	<ul style="list-style-type: none"> • « Heymsfield 2010 composite » • « Brown and Francis 1995 modified »
Retrieval method	Variational method
Multiple scattering	Numerical C code developed by Robin Hogan (http://www.met.reading.ac.uk/clouds/multiscatter/)
Measurements	Radar reflectivity Z at 95 or 35 GHz Lidar attenuated backscatter β at 532 nm

Table A1: Table describing the structure and details of VarPy.

**Extinction ($\text{Ext.}, \text{m}^{-1}$), Analysis for All
Temp Range: $-999^\circ \text{C} \rightarrow 999^\circ \text{C}$**

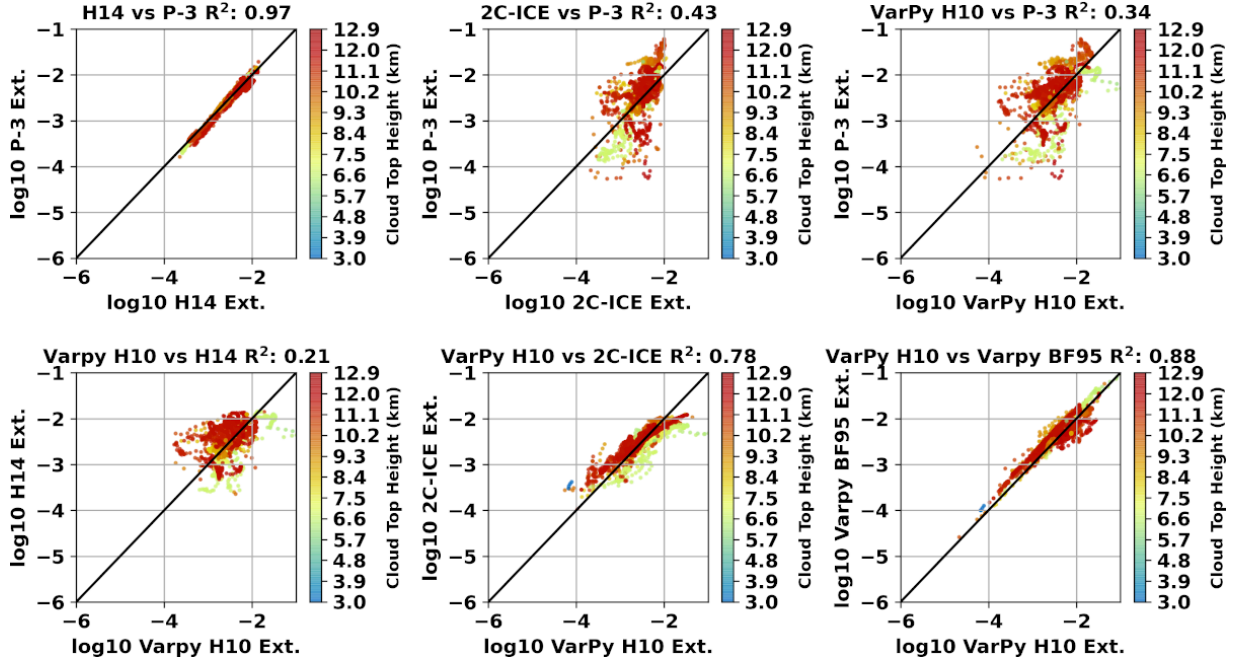


Fig. A1. Cross comparison amongst H14-, VarPy-, 2C-ICE- and P-3-retrieved extinction values for all co-located aircraft observations at all observed temperatures below 0°C and color shaded by cloud-top height (km).

**Extinction ($\text{Ext.}, \text{m}^{-1}$), Analysis for All
Temp Range: $-999^\circ \text{C} \rightarrow -25.0^\circ \text{C}$**

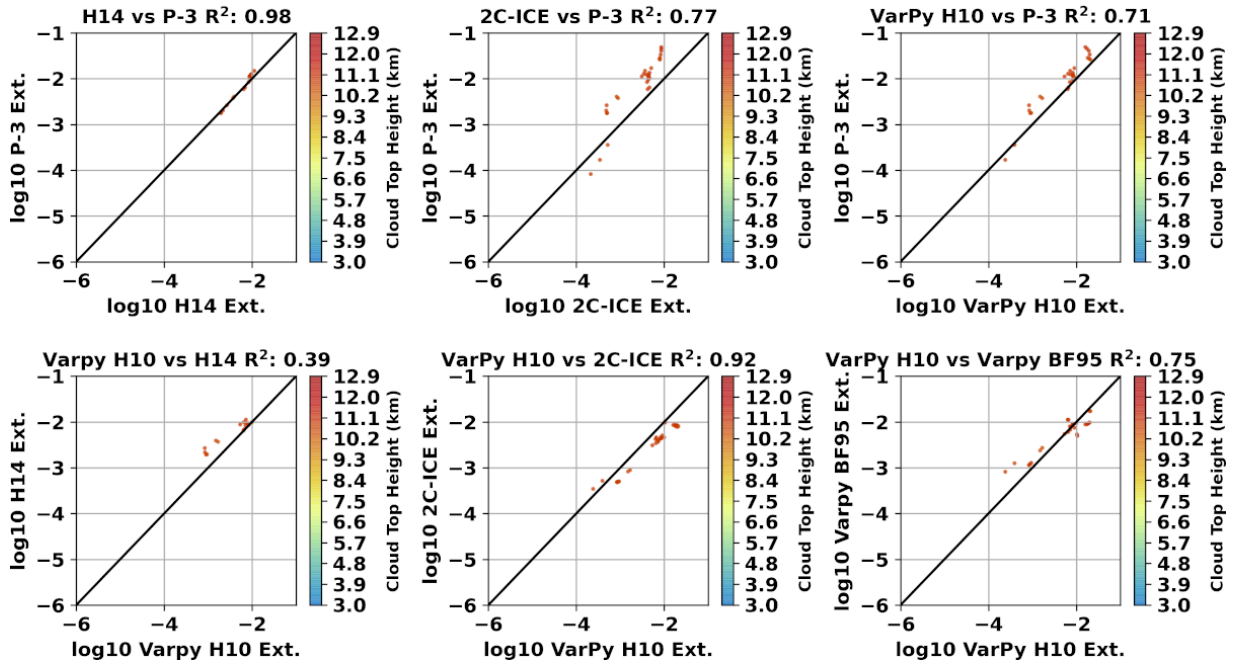


Fig. A2. Same as Fig. A1, except for temperatures less than -25°C.

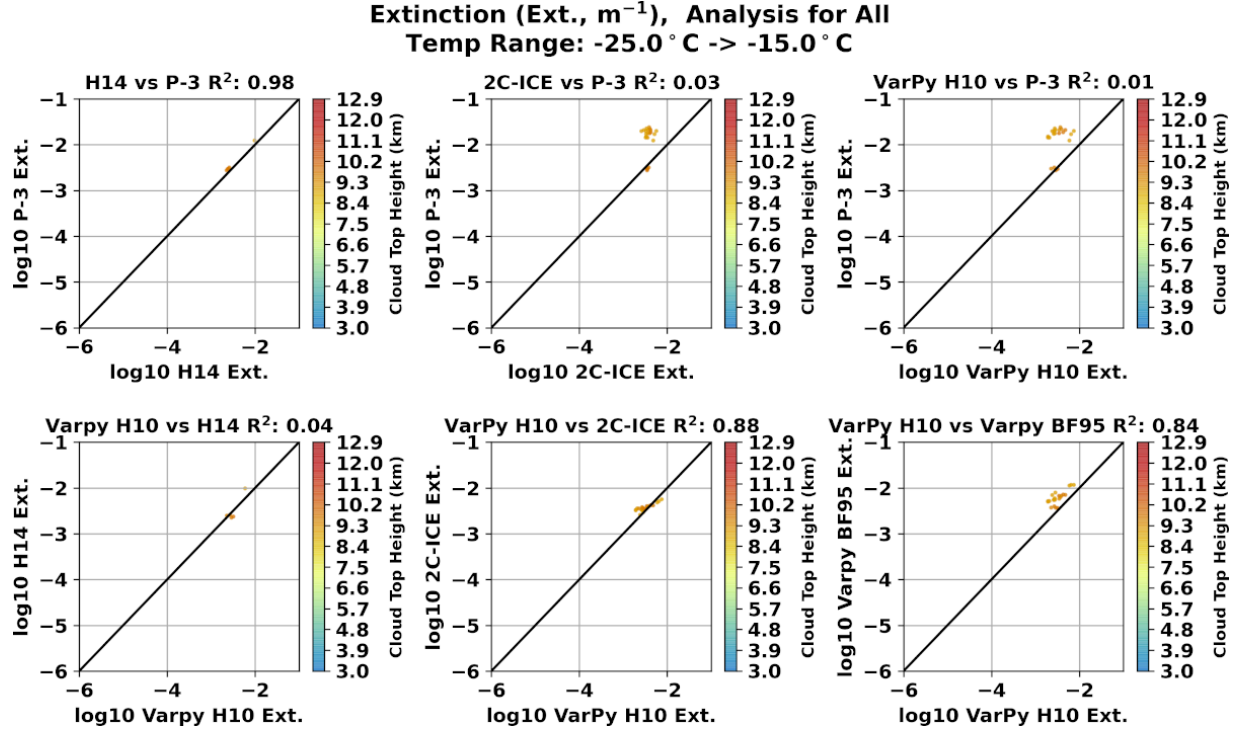


Fig. A3. Same as Fig. A1, except for temperatures between -25°C and -15°C.

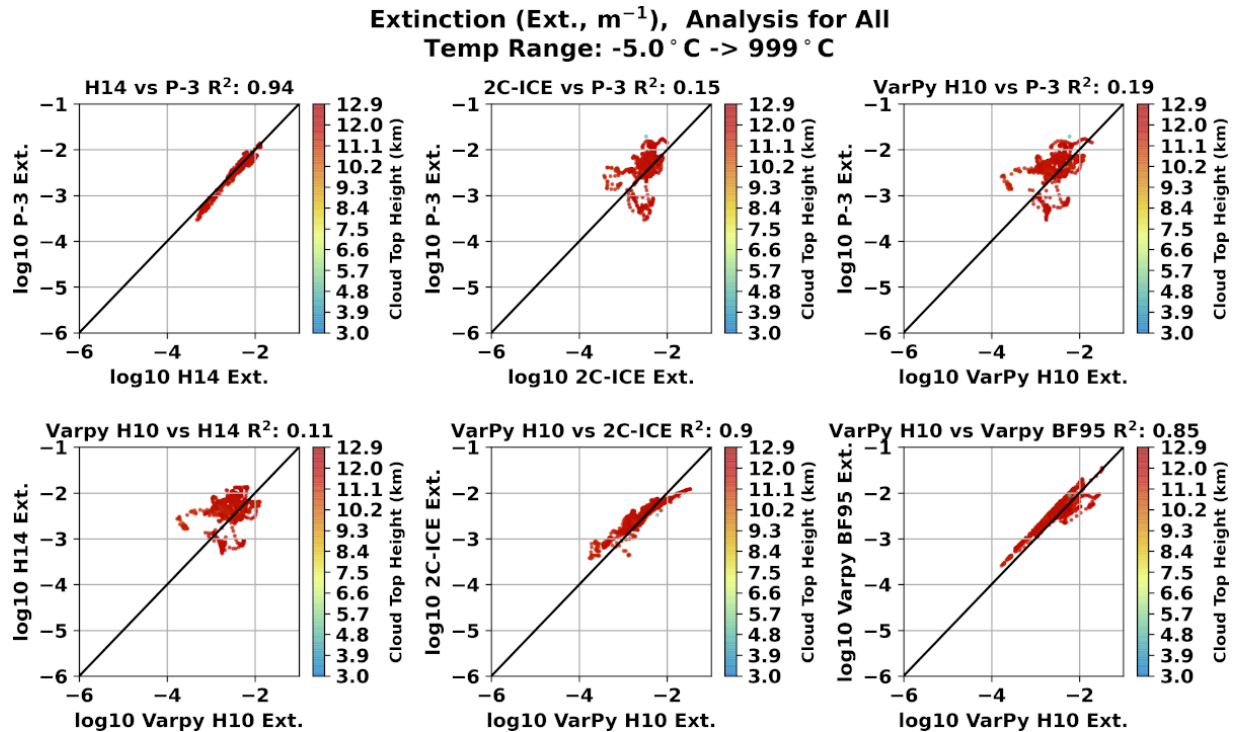


Fig. A4. Same as Fig. A1, except for temperatures between -5°C and 0°C.

**Ice Water Content (IWC, g/m³) Analysis for All
Temp Range: -999 °C -> 999 °C**

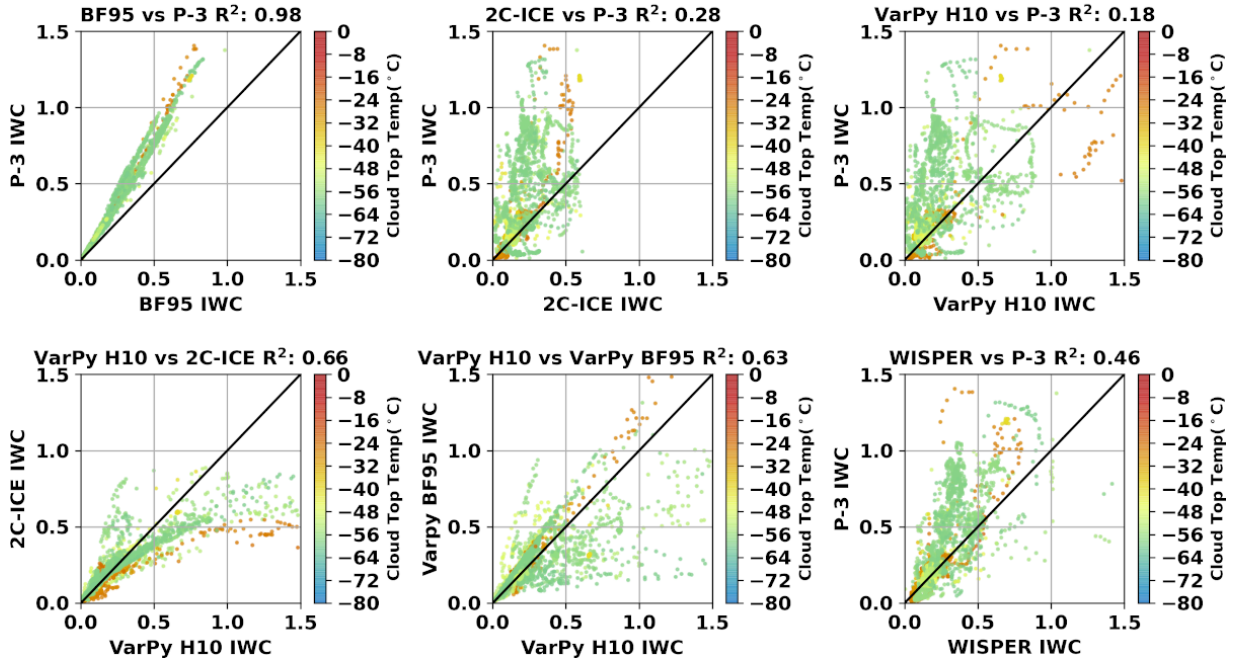


Fig. A5. Cross comparison amongst BF95-, VarPy-, 2C-ICE-, WISPER-, and P-3-retrieved IWC values for all co-located aircraft observations at all observed temperatures below 0°C and color shaded by cloud-top height (km).

**Ice Water Content (IWC, g/m³) Analysis for All
Temp Range: -999 °C -> -25.0 °C**

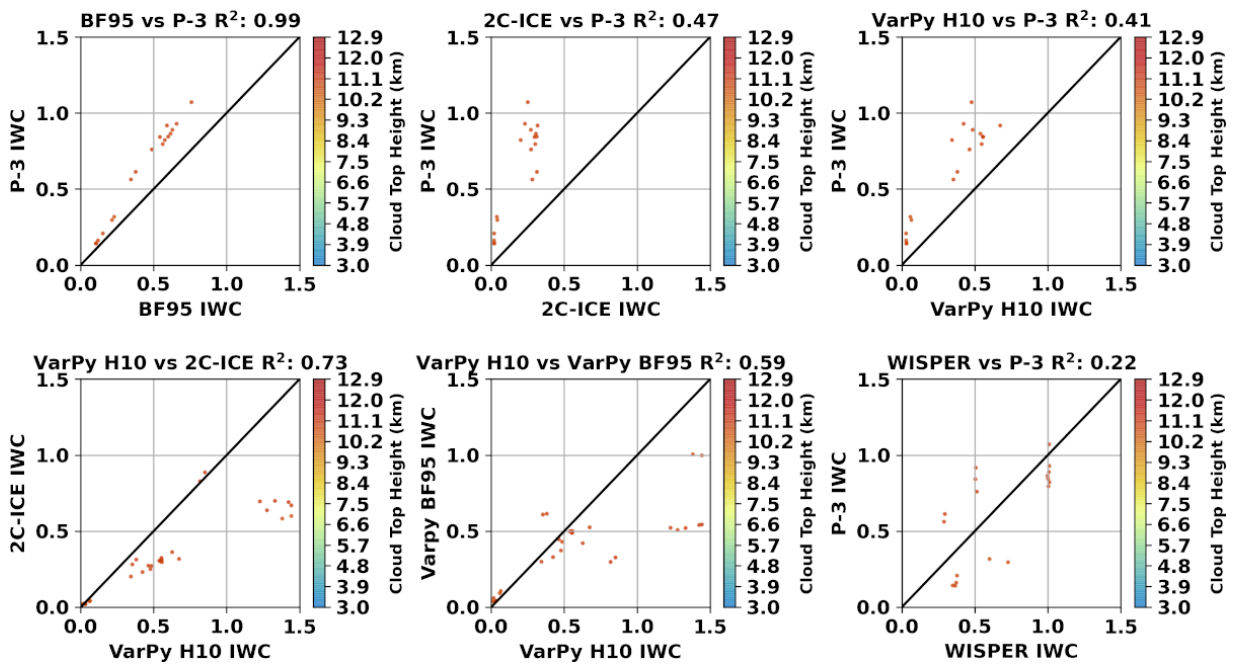


Fig A6. Same as Fig. A5, except for temperatures less than -25°C .

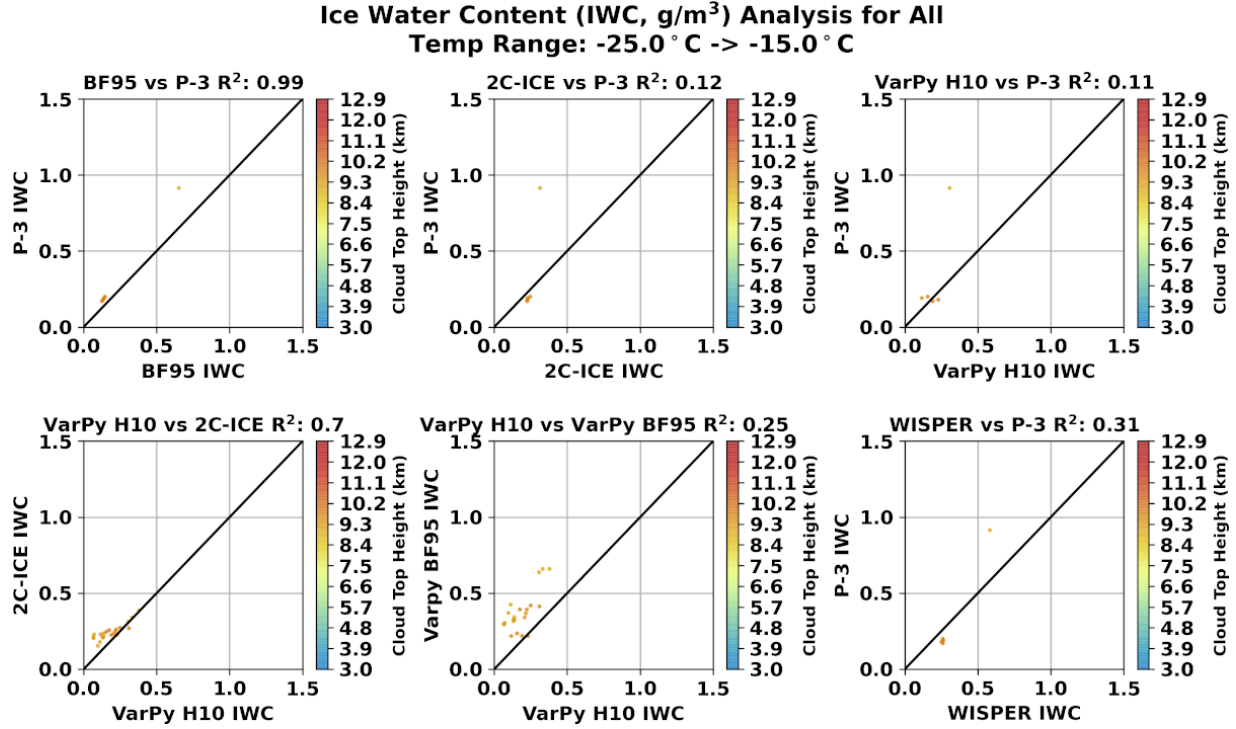


Fig. A7. Same as Fig. A5, except for temperatures between -25°C and -15°C .

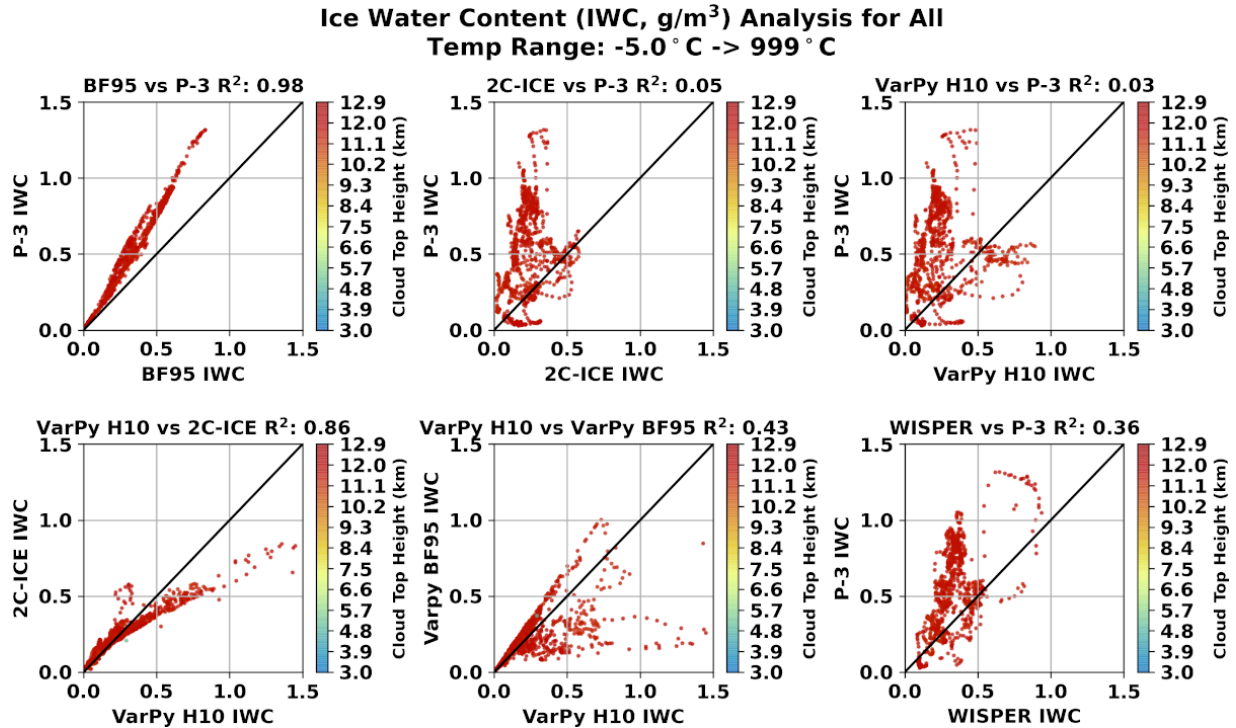


Fig. A8. Same as Fig. A5, except for temperatures between -5°C and 0°C .

**Effective Radius (Eff. Rad., microns) Analysis for All
Temp Range: -999 °C -> 999 °C**

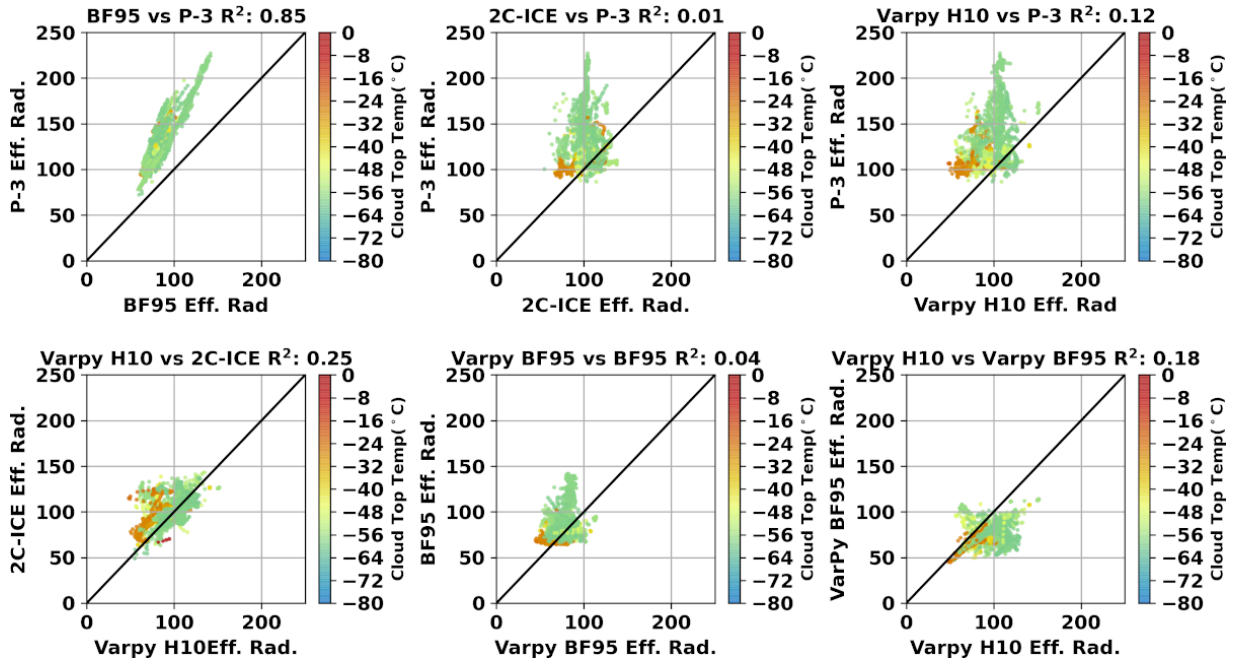


Fig. A9. Cross comparison amongst BF95-, VarPy-, 2C-ICE-, and P-3-retrieved effective radius values for all co-located aircraft observations for all P-3 aircraft observed temperatures below 0°C and color shaded by cloud-top height (km).

**Effective Radius (Eff. Rad., microns) Analysis for All
Temp Range: -999 °C -> -25.0 °C**

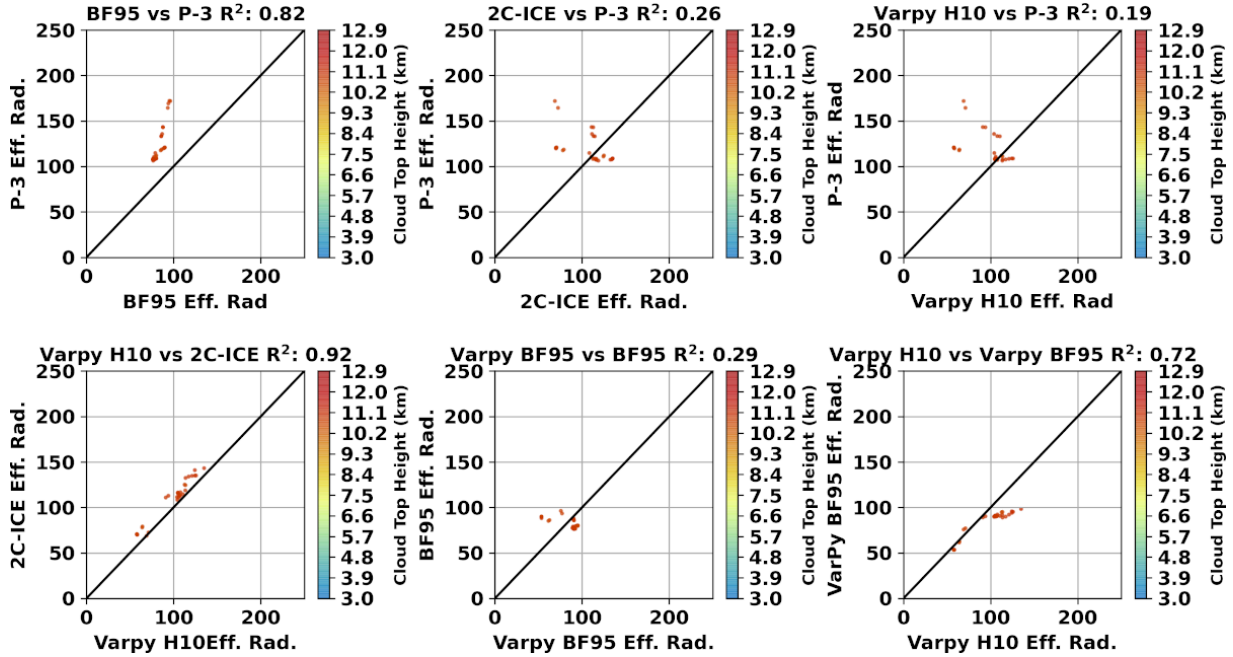


Fig. A10. Same as Fig. A9, except for temperatures less than -25°C.

**Effective Radius (Eff. Rad., microns) Analysis for All
Temp Range: -25.0 °C -> -15.0 °C**

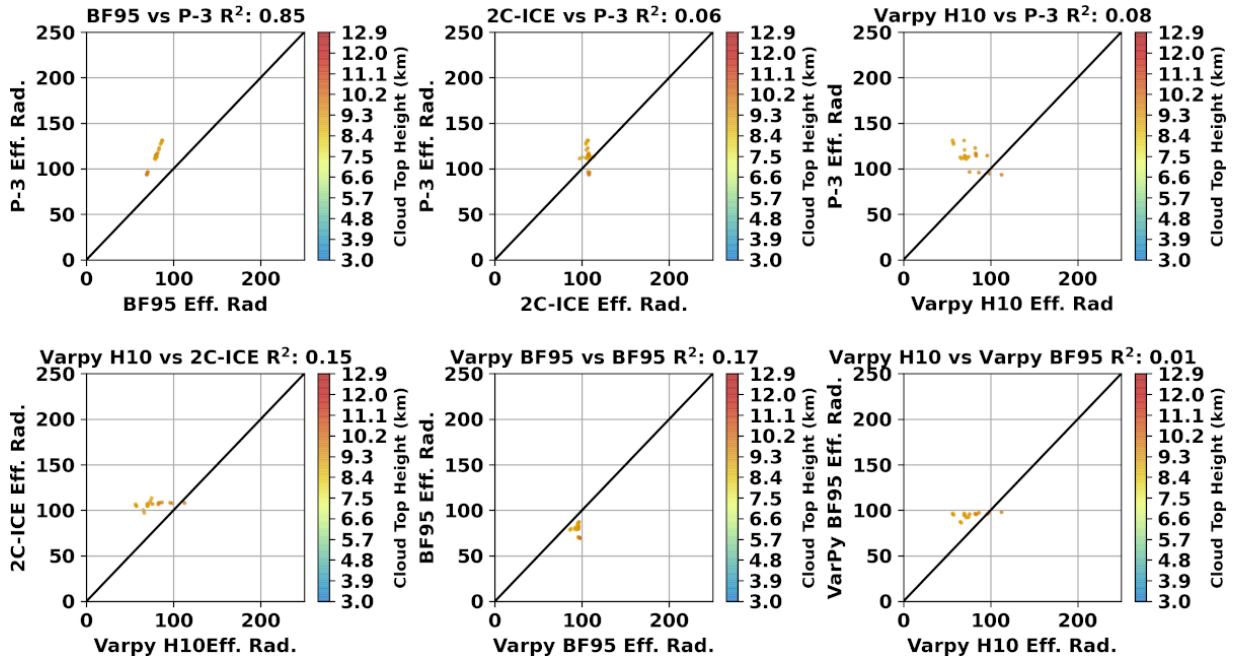


Fig. A11. Same as Fig. A9, except for temperatures between -25°C and -15°C.

**Effective Radius (Eff. Rad., microns) Analysis for All
Temp Range: -5.0 °C -> 999 °C**

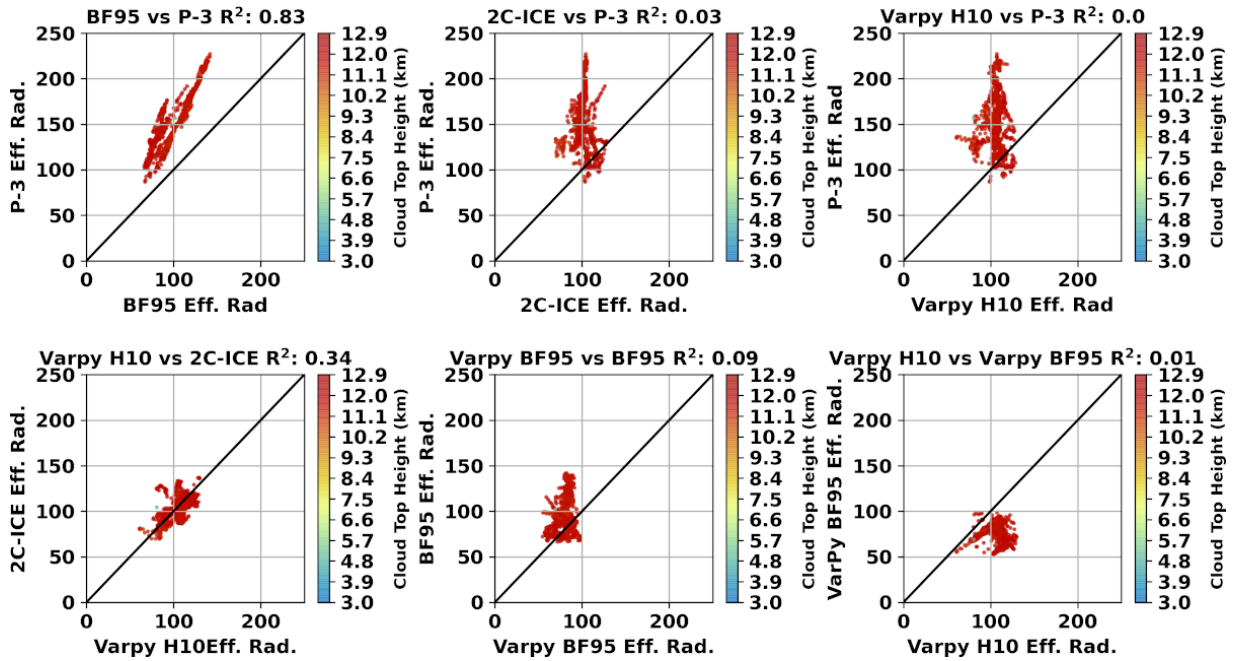


Fig. A12. Same as Fig. A9, except for temperatures between -5°C and 0°C.

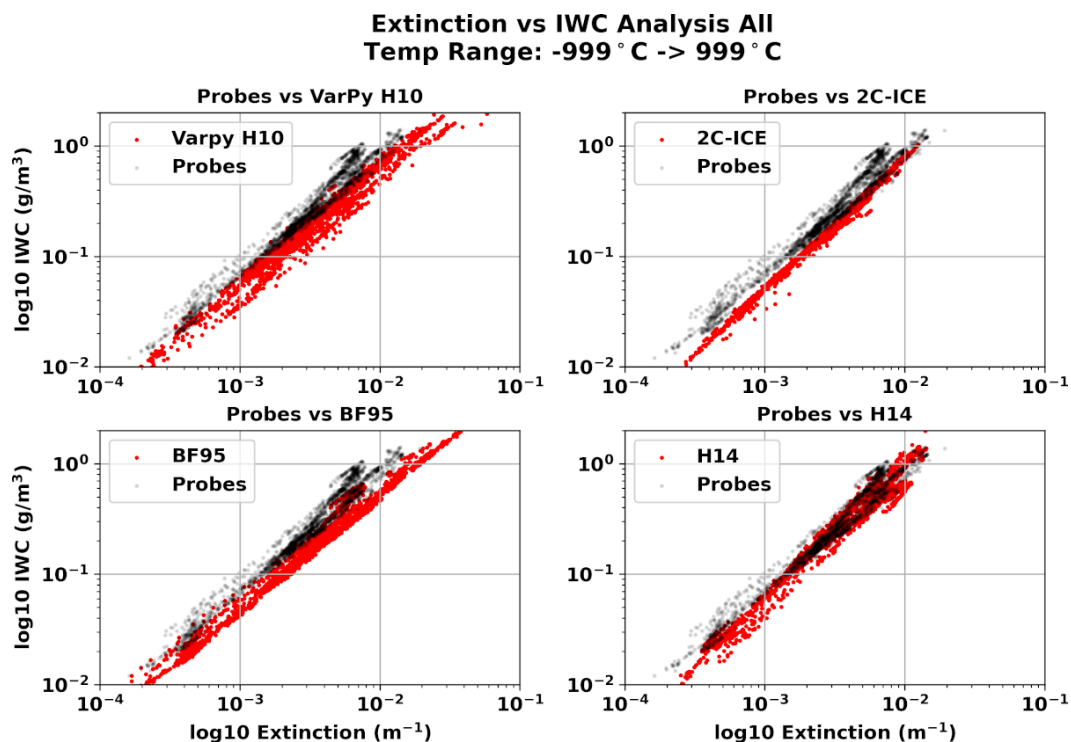


Fig. A13. The IWC-extinction relationship as derived from VarPy-, 2C-ICE-, BF95-, and H14-based retrievals (red dots), and the P-3 cloud probe retrievals (black dots) for all co-locations for all observed temperatures below 0°C.

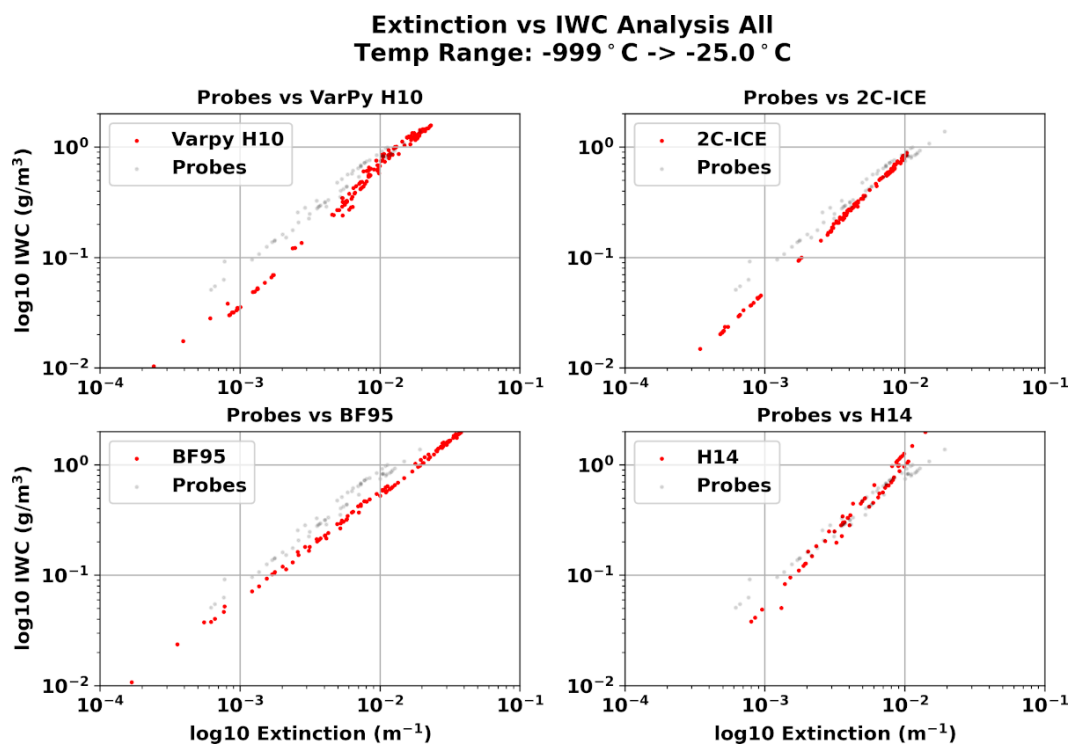


Fig. A14. Same as Fig. A13, except for temperatures less than -25°C.

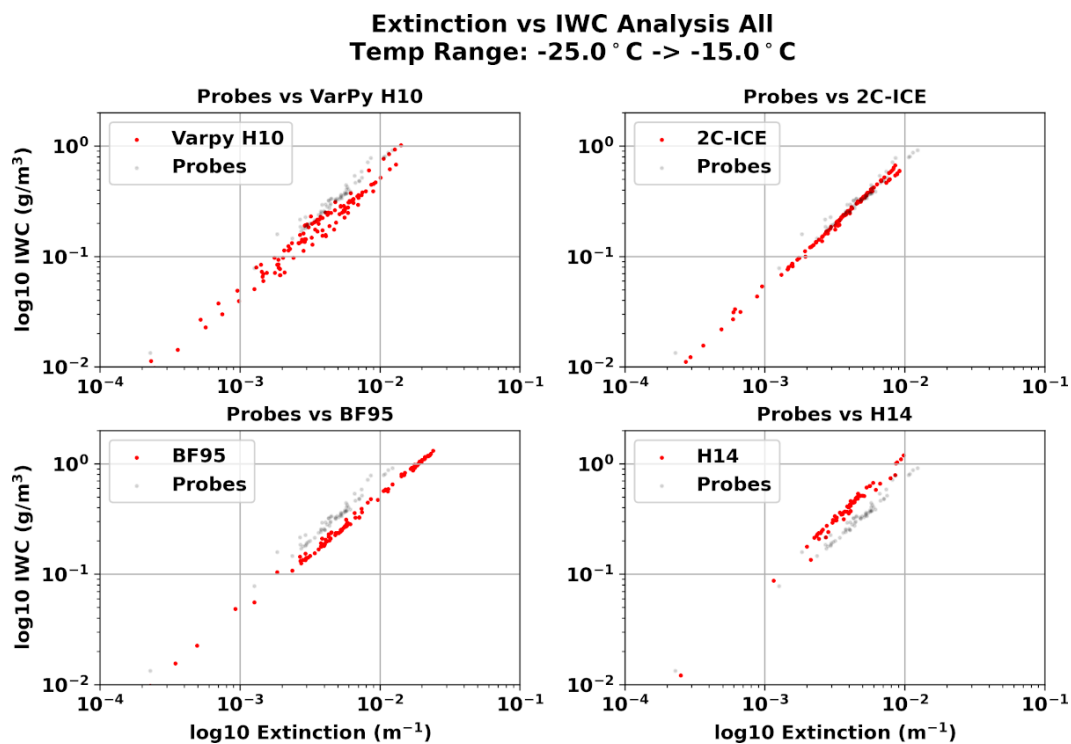


Fig. A15. Same as Fig. A13, except for temperatures between -25°C and -15°C.

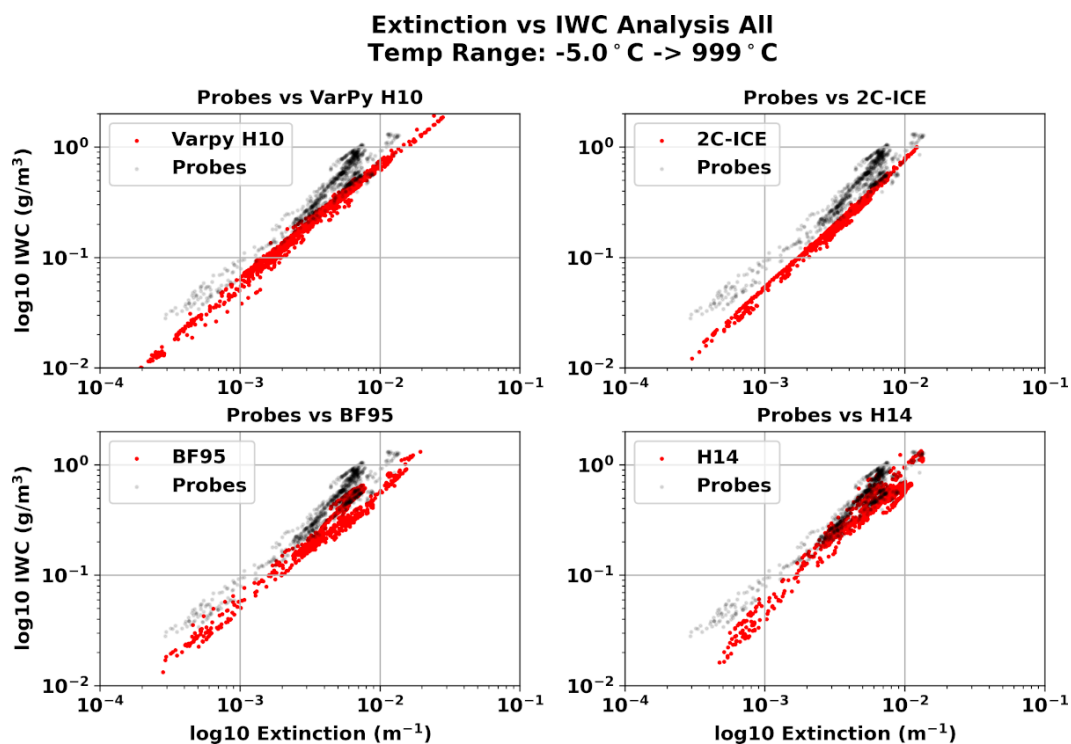


Fig. A16. Same as Fig. A13, except for temperatures between -5°C and 0°C.

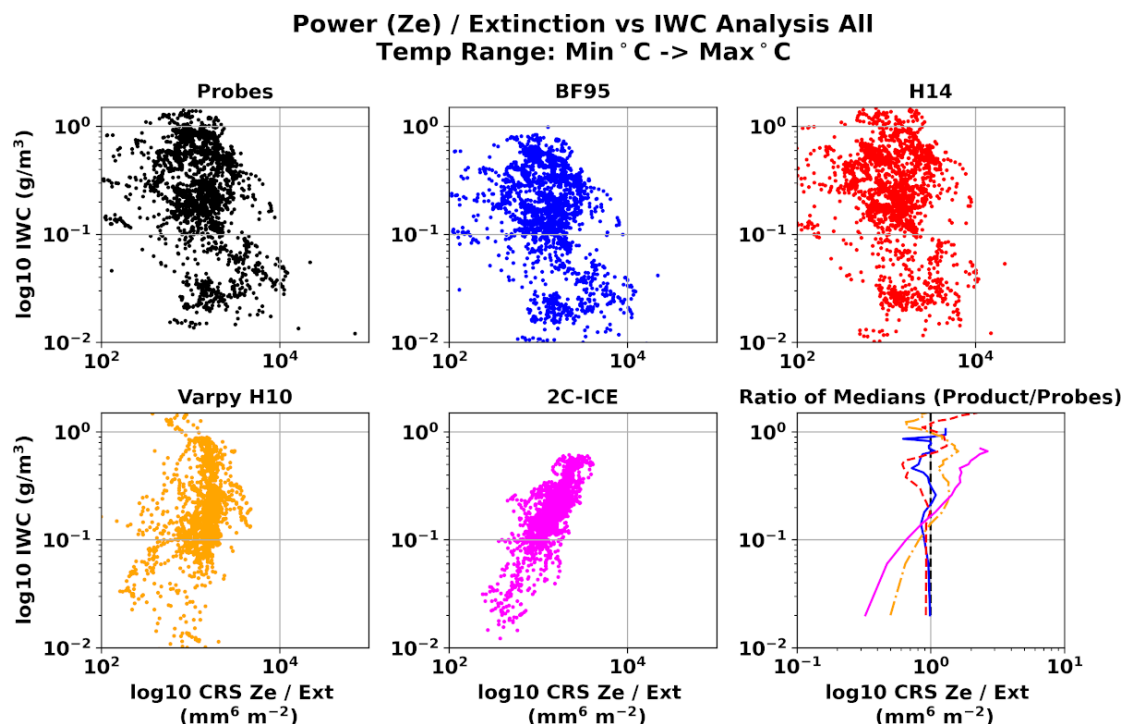


Fig. A17. The relationship between IWC and the CRS reflectivity to extinction ratio derived from the P-3 cloud probes (Probes), BF95, H14, VarPy H10, and 2C-ICE. The bottom right panel shows the absolute difference in ratio median between each product and the P-3 cloud probes using a 0.04 g/m^3 IWC bin size; the colors match the corresponding data sources shown in the other five panels. The data shown is valid for all observed temperatures below 0°C .

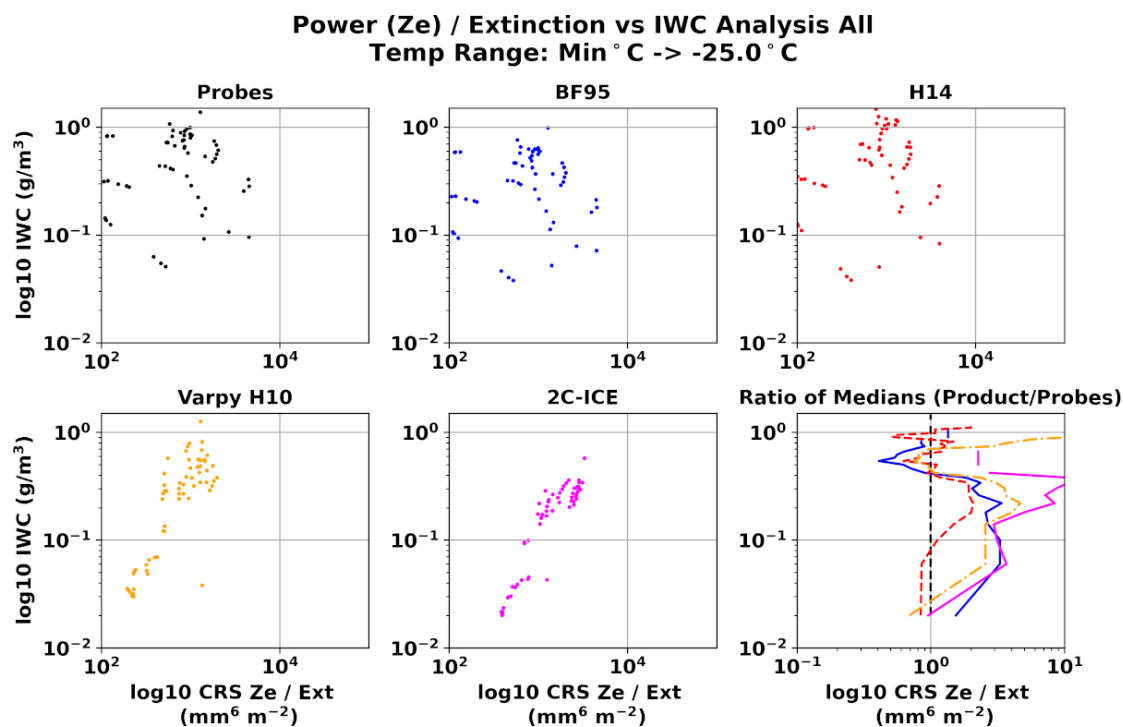


Fig. A18. Same as Figure A17, except for temperatures less than -25°C .

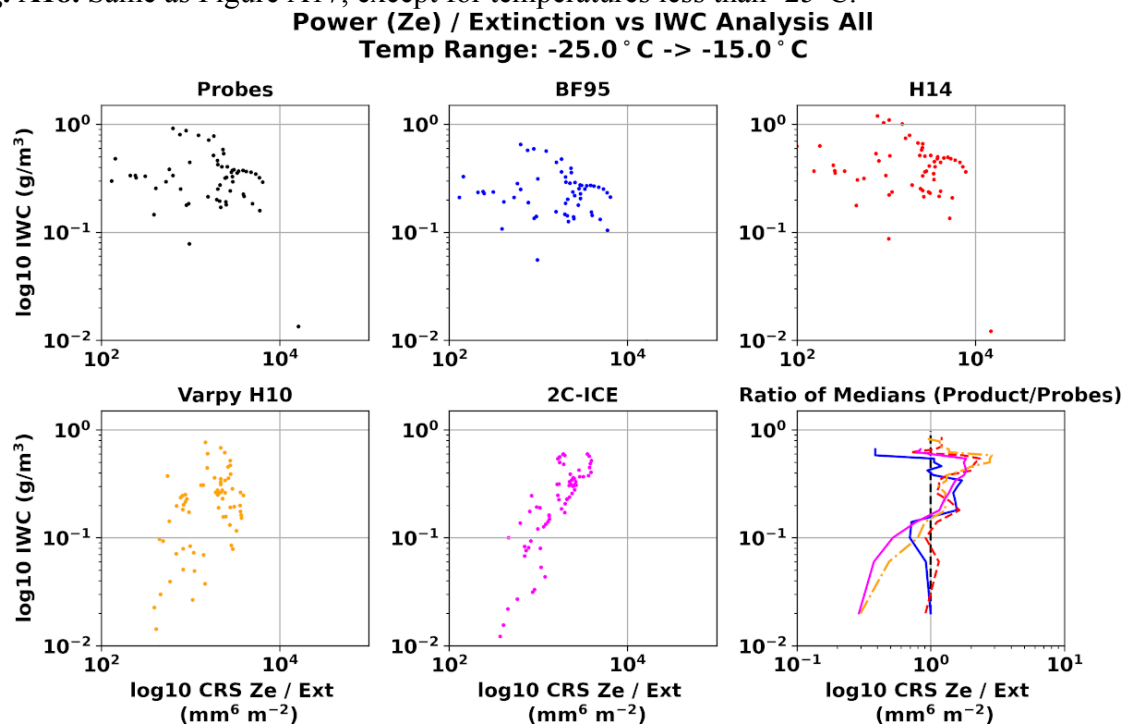


Fig. A19. Same as Fig. A17, except for temperatures between -25°C and -15°C .

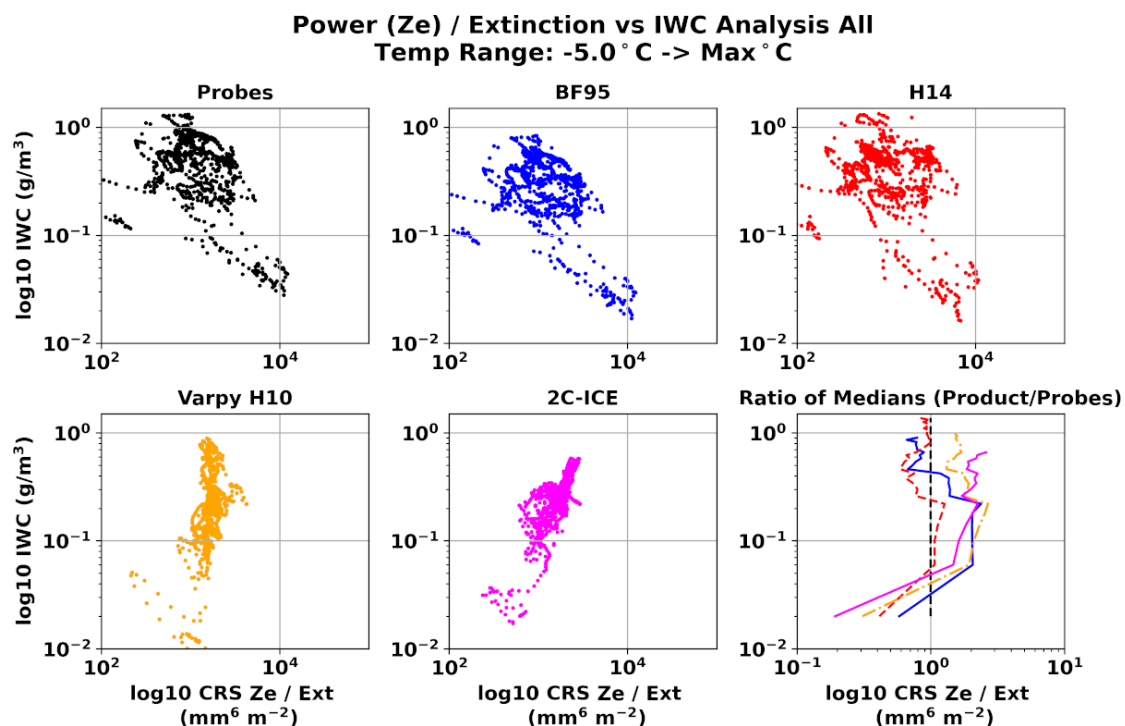


Fig. A20 Same as Fig. A17, except for temperatures between -5°C and 0°C .

List of Figures

1	Earth's climate system components	11
2	Net Cloud Radiative Effect from CERES.	13
3	CALIOP lidar attenuated backscatter and CPR radar reflectivity	15
1.1	Diagram of ice nucleation processes	22
1.2	Illustration of the 10 <i>genera</i>	24
1.3	Illustration of mixed-phase formation in different cloud types .	26
1.4	Photography of different ice crystals	27
1.5	Diagram of various crystal shapes depending on water vapor supersaturation relative to ice and temperature	28
1.6	Schema of the electromagnetic spectrum.	32
1.7	Graph of the solar radiation spectrum	33
1.8	Model of the Earth's thermal radiance	34
1.9	Energy diagram for absorption and emission phenomena. . . .	35
1.10	Spectral radiance distribution according to Planck's law	36
1.11	Graph of the different scattering regimes depending on the particle size, the radiation wavelength and the size parameter. . .	38
1.12	Graph of the scattering efficiency according to Mie calculations.	40
1.13	Illustration of the scattering direction and intensity for Rayleigh and Mie regime, for small and large particle.	40
1.14	Illustration of the Earth water cycle	41
1.15	Illustration of the Earth's energy budget	42
1.16	Illustration of the SW, LW and net CRE at the Earth's TOA, atmosphere and surface	45
2.1	The CPI on the Polar 2 aircraft flying over the Svalbard archipelago.	49
2.2	CPI probe detection principle	49
2.3	The ten classes of particle shapes recognized by the CPI image processing algorithm	51
2.4	The Forward Scattering Spectrometer Probe introduced in 1976	52
2.5	The FSSP detection principle	53
2.6	The Polar Nephelometer on the ATR 42 scientific aircraft during the RALI-THINICE campaign.	54
2.7	The PN measurement principle	55
2.8	Photography of the 2D-S probe.	56
2.9	OAP principle detection	57
2.10	Example of particle images from the 2D-S and CPI	58
2.11	The Cloud Droplet Probe	59
2.12	The CDP optical scheme	59

2.13	Passive and active remote sensing.	61
2.14	The specMACS VNIR and SWIR cameras	63
2.15	Example of specMACS measurements of cloud sides during the HOPE-Melpitz campaign.	64
2.16	Viewing geometry of MSI and BBR onboard EarthCARE.	65
2.17	Divergence of the emitted beam Θ and range resolution Δd for active remote sensing instrument.	67
2.18	The BASTA radar.	70
2.19	Geometry of the laser beam and the receiver FOV.	73
2.20	Spectral backscattered energy distribution from air molecules and cloud particles	75
2.21	Mach-Zehnder interferometer principle.	76
2.22	The electric field and the magnetic field of an electromagnetic wave	77
2.23	Example of CALIOP lidar attenuated backscatter, CPR radar re- flectivity and instrument synergy.	79
2.24	The CloudSat satellite and its components.	82
2.25	The CALIPSO satellite and its components.	84
2.26	The Afternoon Constellation (A-Train and C-Train) in 2018. . . .	85
2.27	Artistic view of the EarthCARE satellite	86
2.28	Viewing geometry of CPR, ATLID, MSI and BBR onboard Earth- CARE.	86
2.29	Configuration of RALI onboard the ATR 42 (since 2022).	89
2.30	LNG and RASTA instrument onboard the ATR 42 aircraft.	92
2.31	WALES and MIRA positioning and pointing onboard HALO.	92
2.32	The SAFIRE ATR 42 and HALO aircraft.	93
2.33	MIRA and WALES onboard HALO.	95
2.34	CRS and CPL positioning and pointing on ER-2 aircraft.	96
3.1	VarPy-ice retrieval method scheme.	106
3.2	Correction implemented in the interface with the Multiscatter code.	112
3.3	Example of CALIOP and CPR measurements and DARDAR-MASK classifications (rain / aerosols).	119
3.4	Example of CALIOP and CPR measurements and DARDAR-MASK classifications (supercooled water / mixed-phase).	120
3.5	DARDAR-MASK decision tree to classify layers with a strong lidar backscatter signal	124
3.6	Example of classification corrections.	125
3.7	VarPy-mix retrieval method scheme.	126

4.1	Selected profiles of CloudSat and CALIPSO measurements, intermediate classification and instrument synergy on 7 th April 2007.	142
4.2	CPI, FSSP and PN range sensitivities.	143
4.3	Liquid, ice and total extinction from VarPy-mix retrievals and <i>in situ</i> data regarding height and latitude.	145
4.4	Liquid, ice and total water content from VarPy-mix retrievals and <i>in situ</i> data regarding height and latitude.	146
4.5	Liquid and ice number concentration and liquid and ice effective radius retrieved by VarPy-mix.	147
4.6	Liquid, ice and total extinction from VarPy-mix retrievals and <i>in situ</i> data regarding the latitude.	149
4.7	Liquid, ice and total water content from VarPy-mix retrievals and <i>in situ</i> data regarding the latitude.	151
4.8	Flight tracks during HALO-(AC) ³	154
4.9	WALES and MIRA measurements and classifications for the HALO-(AC) ³ case.	155
4.10	Corrected intermediate classification and instrument synergy for the HALO-(AC) ³ case	157
4.11	Liquid, ice and total extinctions retrieved by VarPy-mix for the HALO-(AC) ³ case.	159
4.12	Liquid and ice effective radius retrieved by VarPy-mix for the HALO-(AC) ³ case.	160
4.13	Liquid, ice and total water content retrieved by VarPy-mix for the HALO-(AC) ³ case.	161
4.14	Liquid, ice and total number concentration retrieved by VarPy-mix for the HALO-(AC) ³ case.	162
4.15	Flight tracks during RALI-THINICE.	164
4.16	LNG backscatter at 532 nm and RASTA reflectivity at 95 GHz measurements for the RALI-THINICE case.	164
4.17	Lidar, radar and radar-lidar classifications for the RALI-THINICE case.	165
4.18	Intermediate classification and instrument synergy for the RALI-THINICE case	166
4.19	Liquid, ice and total extinctions retrieved by VarPy-mix for the RALI-THINICE case.	168
4.20	Liquid and ice effective radius retrieved by VarPy-mix for the RALI-THINICE case.	169
4.21	Liquid, ice and total water content retrieved by VarPy-mix for the RALI-THINICE case.	170
4.22	Liquid, ice and total number concentration retrieved by VarPy-mix for the RALI-THINICE case.	171

4.23 Ice and liquid microphysical properties of the mixed-phase . .	173
4.24 Comparison between ice and liquid extinction and water content of the mixed-phase retrieved by VarPy-mix for each campaign.	174
4.25 Comparison between ice and liquid effective radius and number concentration of the mixed-phase retrieved by VarPy-mix for each campaign.	175
4.26 Instruments onboard the ER-2 and P-3 aircraft and their viewing geometry.	177
4.27 Flight tracks of the ER-2 and P-3 aircraft during IMPACTS 2020 .	178

List of Tables

1	Radar-lidar airborne and satellite platforms specifications. . . .	17
2.1	CPI specifications.	50
2.2	FFSP specifications.	53
2.3	PN specifications.	55
2.4	Microphysical properties determined using 2D-S images.	58
2.5	CDP specifications.	60
2.6	Radar frequency bands	69
2.7	Lidar ratio S for liquid droplet depending on cloud type, particle size and lidar wavelength.	74
2.8	Advantages and drawbacks of spaceborne, airborne and ground-based radar-lidar platform.	81
2.9	CPR (CloudSat) specifications.	82
2.10	CALIOP (CALIPSO) specifications.	83
2.11	CPR (EarthCARE) specifications.	87
2.12	ATLID specifications.	88
2.13	Number of values per profile depending on RASTA range resolution and distance.	90
2.14	Specifications of RASTA.	90
2.15	Specifications of LNG transmitter and receiver.	91
2.16	MIRA specifications	93
2.17	WALEs specifications	94
2.18	CRS specifications.	97
2.19	CPL specifications.	97
3.1	<i>A priori</i> and first guess values for each variable of the state vector in VarPy-ice.	111
3.2	<i>A priori</i> error variances used in VarPy-ice for the <i>a priori</i> error covariance matrix B	114
3.3	DARDAR-MASK v2.23 classes.	122
3.4	Cloud phases processed by VarPy-ice and VarPy-mix.	123
3.5	<i>A priori</i> and first guess values for each variable of the state vector in VarPy-mix.	133
3.6	<i>A priori</i> error variances used in VarPy-mix for the <i>a priori</i> error covariance matrix B_{mix}	135
4.1	Uncertainties of extinction and water contents from CPI, FFSP and PN probes	143
4.2	Mean values of retrieved properties.	148

4.3	Mean absolute error and mean percent error for each property regarding <i>in situ</i>	150
4.4	Mean, minimum and maximum values for each variables in the mixed-phase (HALO-(AC) ³ case study).	158
4.5	Mean, minimum and maximum values for each variables in the mixed-phase (RALI-THINICE case study).	167

Nomenclature

α	Extinction coefficient	m^{-1}
α_{ice}	Ice crystal visible extinction	m^{-1}
α_{liq}	Water droplet visible extinction	m^{-1}
α_{tot}	Total visible extinction	m^{-1}
α_m	Molecular extinction coefficient	m^{-1}
α_p	Particular extinction coefficient	m^{-1}
$\alpha_{\lambda}^{\text{abs}}$	Absorption coefficient	m^{-1}
$\alpha_{\lambda}^{\text{ext}}$	Extinction coefficient	m^{-1}
$\alpha_{\lambda}^{\text{sca}}$	Scattering coefficient	m^{-1}
β	Backscatter coefficient	$\text{m}^{-1}.\text{sr}^{-1}$
β_{fwd}	Lidar forward model backscatter	$\text{m}^{-1}.\text{sr}^{-1}$
β_{obs}	Measured lidar backscatter	$\text{m}^{-1}.\text{sr}^{-1}$
β_a	Attenuated lidar backscatter	$\text{m}^{-1}.\text{sr}^{-1}$
β_m	Molecular backscatter coefficient	$\text{m}^{-1}.\text{sr}^{-1}$
β_p	Particular backscatter coefficient	$\text{m}^{-1}.\text{sr}^{-1}$
χ_i^2	Chi-square value at iteration i	
dI	Electromagnetic wave intensity attenuation	$\text{W}.\text{sr}^{-1}$
dx	Electromagnetic wave length propagation	m
$\Delta\nu$	Frequency difference between the emitted and received signals	s^{-1}
ΔE	Difference between two energy levels	J
Δt	Time delay	s
δ	Optical depth	
ϵ_{λ}	Emissivity of a body at the wavelength λ	

η	Total radar reflectivity	m^{-1}
Γ	Solar irradiance	W.m^{-2}
γ	Coefficient normalizing N'	
\hat{X}	State vector best estimate	
κ	Smoothness degree coefficient for T	
Λ	Slope parameter of $N(D)$ gamma function	
λ	Wavelength	m
λ_{max}	Wien's law maximum wavelength	m
$\langle r^k \rangle$	k^{th} moment of the log-normal DSD	
\mathbb{I}	Possible iteration set	
\mathcal{B}	Chirp bandwidth	s^{-1}
$\mathcal{C}_{\text{instr}}$	Instrumental constant	
$\mathcal{C}_{\text{lidar}}$	Lidar instrumental constant	
$\mathcal{C}_{\text{radar}}$	Radar instrumental constant	
\mathcal{D}	Depolarization ratio	
$\mathcal{O}(d)$	Overlap function	
\mathcal{P}_{\parallel}	Parallel polarization	
\mathcal{P}_{\perp}	Perpendicular polarization	
$\mathcal{T}(d, \lambda)$	Atmospheric transmission at wavelength λ and distance d	
μ	Shape parameter of $N(D)$ gamma function	
ν	Frequency	s^{-1}
ω_{cloudy}	Cloud albedo	
Φ_{clear}	Clear sky atmosphere radiative energy	W.m^{-2}
Φ_{cloudy}	Cloudy atmosphere radiative energy	W.m^{-2}
$\psi(\theta)$	Angular scattering coefficient	$\mu\text{m}^{-1} \text{sr}^{-1}$
ρ_i	Density of ice	kg.m^{-3}

ρ_w	Density of water	kg.m ⁻³
σ_β	Lidar backscatter error variance	
σ_{lidar}	Lidar instrumental error	
σ_{radar}	Radar instrumental error	
σ_X	<i>A priori</i> state vector error variance	
σ_Y	Observation vector error variance	
σ_Z	Radar reflectivity error variance	
$\sigma_{\beta_{\text{fwd}}}$	Lidar forward model error	
$\sigma_{\ln(\alpha)}$	α error variance	
$\sigma_{\ln(\alpha_{\text{ice}})}$	α_{ice} error variance	
$\sigma_{\ln(\alpha_{\text{liq}})}$	α_{liq} error variance	
$\sigma_{\ln(N')}$	N' error variance	
$\sigma_{\ln(N_{0,\text{ice}}^*)}$	$N_{0,\text{ice}}^*$ error variance	
$\sigma_{\ln(N_{0,\text{liq}}^*)}$	$N_{0,\text{liq}}^*$ error variance	
σ_{abs}	Absorption cross section	m ²
σ_{ext}	Extinction cross section	m ²
σ_{sca}	Scattering cross section	m ²
$\sigma_{a_{\ln(S)}}$	$a_{\ln(S)}$ error variance	
$\sigma_{b_{\ln(S)}}$	$b_{\ln(S)}$ error variance	
$\sigma_{N(r)}$	Geometric standard deviation of the log-normal DSD	
$\sigma_{Z_{\text{fwd}}}$	Radar forward model error	
τ	Transmittance	
Θ	Beam divergence	rad
θ	Scattering angle	rad
$Y_{(i,j)}$	Values derived from the cubic-spline basis function	
ε	Error vector	

φ	Multiple scattering coefficient	
\vec{B}	Magnetic field	T
\vec{E}	Electric field	V m ⁻¹
ζ	Mass-size relationship exponent (power law)	
ζ	Mass-size relationship coefficient (power law)	
A	Attenuation effect coefficient	
a_k	Mie first coefficient	
$a_{\ln(N')}$	N' parameter slope coefficient	
$a_{\ln(S)}$	Lidar ratio slope coefficient	
B	Error covariance matrix of the <i>a priori</i> state vector	
B	<i>A priori</i> error covariance matrix	
$B_\lambda(T)$	Emitted spectral radiance of a black body at λ	W.m ⁻³ .sr ⁻¹
b_k	Mie second coefficient	
$b_{\ln(N')}$	N' parameter intercept coefficient	
$b_{\ln(S)}$	Lidar ratio intercept coefficient	
C	Conversion matrix	
C_{mix}	VarPy-mix conversion matrix	
D	Maximum dimension or particle diameter	m
d	Distance	m
D_m	Mean volume-weighted diameter	m
$D_{e,\text{ice}}$	Ice crystal effective diameter	m
$D_{e,\text{liq}}$	Liquid droplet effective diameter	m
D_{eq}	Mass-equivalent diameter	m
E_i	Atom energy level i	J
f	Forward function	
F_{cloudy}	LW radiative flux emitted to space in cloud condition	W.m ⁻²

g	Assymetry parameter	
H	Hessian matrix	
I	Electromagnetic wave intensity	W.sr^{-1}
J	Cost function	
J_X	cost function for the state vector X	
J_{X_i}	Cost function for the state vector at iteration i	
K	Jacobian matrix (or Kernel)	
k	Lidar ratio dimension in X	
K_β	Lidar backscatter Jacobian matrix	
K_K	Radar reflectivity Jacobian matrix	
$K_{\text{mix, ice}}$	Ice part of the Jacobian matrix (for VarPy-mix)	
$K_{\text{mix, liq}}$	Liquid part of the Jacobian matrix (for VarPy-mix)	
K_{mix}	Jacobian matrix for VarPy-mix	
$L_\lambda(T)$	Emitted spectral radiance of a body at the wavelength λ	$\text{W.m}^{-3}.\text{sr}^{-1}$
$M(D)$	Mass-size relationship	
M	Particle masse	kg
m	Concentration parameter gate number per profile according to the spacing factor	
m_i	Ice concentration parameter gate number per profile according to the spacing factor	
N'	Number concentration parameter	$\text{m}^{\gamma-4}$
$N(D)$	Particle Size Distribution, Droplet Size Distribution	m^{-3}
$N(r)$	Droplet Size Distribution at a given cloud droplet radius r	m^{-3}
N	Particle number concentration	
n	Total gate number per profile	
N_0	Intercept parameter of $N(D)$ gamma function	
N_0^*	Normalized number concentration	m^{-4}

N_{ice}	Ice particle number concentration	m^{-3}
N_{liq}	Liquid particle number concentration	m^{-3}
N_{tot}	Total particle number concentration	m^{-3}
n_i	Ice gate number per profile	
n_l	Liquid gate number per profile	
$N_{0,\text{ice}}^*$	Normalized number concentration for ice crystals	m^{-4}
$N_{0,\text{liq}}^*$	Normalized number concentration for water droplets	m^{-4}
$P(X)$	Probability density function of X	
$P(Y)$	Probability density function of Y	
$P(X Y)$	Conditional probability of X given Y	
$P(Y X)$	Conditional probability of Y given X	
p	Lidar measurement dimension in Y	
$P_r(d, \lambda)$	Received power at wavelength λ and distance d	W
$P_r^{\text{lidar}}(d, \lambda)$	Lidar received power at wavelength λ and distance d	W
$P_r^{\text{radar}}(d, \lambda)$	Radar received power at wavelength λ and distance d	W
$P_r e(\lambda)$	Emitted power at wavelength λ	W
q	Radar measurement dimension in Y	
$Q_{\text{sca}}^{\text{Mie}}$	Mie scattering efficiency	
$Q_{\text{sca}}^{\text{Rayleigh}}$	Rayleigh scattering efficiency	
Q_{abs}	Absorption efficiency	
Q_{ext}	Extinction efficiency	
Q_{sca}	Scattering efficiency	
R	Measurement error covariance matrix	
r	Particle radius	m
r_0	Modal radius	m
r_a	Equivalent area radius	m

r_e	Effective radius	m
$r_{e,ice}$	Ice particle effective radius	m
$r_{e,liq}$	Liquid particle effective radius	m
S	Extinction-to-backscatter lidar ratio	sr
s_i	Ice gate number detected by the lidar (VarPy-mix)	
$S_{\hat{X}}$	State vector best estimate covariance matrix	
T	« Twomey-Tikhonov » matrix	
T_α	« Twomey-Tikhonov » matrix corresponding to α	
T_{mix}	« Twomey-Tikhonov » matrix for VarPy-mix	
t_{sweep}	Chirp period (sweep time)	s
u	State vector dimension	
v	Observation vector dimension	
V_a	Ambiguous velocity	m.s ⁻¹
X	State vector	
x	Size parameter (scattering)	
X_0	Initial state vector (first guess)	
X_{mix}	VarPy-mix state vector	
X_a	<i>A priori</i> state vector	
X_f	Final state vector	
X_i	State vector at iteration i	
Y	Observation vector	
Z	Radar reflectivity factor	mm ⁶ .m ⁻³
z_0	Decorrelation distance	m
Z_{fwd}	Radar forward model reflectivity	mm ⁶ .m ⁻³
Z_{obs}	Measured radar reflectivity	mm ⁶ .m ⁻³
z_i	Height corresponding to i index	m

BR	Backscatter ratio	
CRE	Cloud Radiative Effect	W.m^{-2}
CRE _{LW}	Longwave Cloud Radiative Effect	W.m^{-2}
CRE _{Net}	Net Cloud Radiative Effect	W.m^{-2}
CRE _{SW}	Shortwave Cloud Radiative Effect	W.m^{-2}
IWC	Ice Water Content	kg.m^{-3}
K	Dielectric factor	
LWC	Liquid Water Content	kg.m^{-3}
n	Refractive index of the medium	
T	Temperature	K
TWC	Total Water Content	kg.m^{-3}

Physics constants

σ_B	Stefan-Boltzmann constant	$5.670374419 \times 10^{-8} \text{ W m}^{-2} \text{ K}^{-4}$
b	Wien wavelength displacement law constant	$2.898 \times 10^{-3} \text{ m K}$
c	Speed of light in vacuum	$299\,792\,458 \text{ m s}^{-1}$
h	Planck constant	$6.62607015 \times 10^{-34} \text{ J Hz}^{-1}$
k_B	Boltzmann constant	$1.380649 \times 10^{-23} \text{ J K}^{-1}$

Acronyms

(AC)³ ArctiC Amplification: Climate relevant Atmospheric and surfaCe processes and feedback mechanisms

2D-S Two-Dimensional Stereo Probe

ADM-Aeolus Atmospheric Dynamics Mission Aeolus

ALADIN Atmospheric LAsEr Doppler INstrument

AMSR-2 Advanced Microwave Scanning Radiometer 2

ASTAR Arctic Study of Tropospheric Aerosol, Cloud and Radiation

ATLID ATmospheric LIDar

ATR Avions de Transport Régional

AVHRR Advanced Very High Resolution Radiometer

AWI Alfred Wegener Institute for polar and marine research

BASTA Bistatic rAdar SysTem for Atmospheric studies

BBR Broad-Band Radiometer

CALIOP Cloud-Aerosol Lidar with Orthogonal Polarization

CALIPSO Cloud Aerosol Lidar and Infrared Pathfinder Satellite Observations

CAPTIVATE Cloud, Aerosol, and Precipitation from mulTiple Instruments using a VAriational TEchnique

CCD Charge-Coupled Device

CCN Cloud Condensation Nuclei

CDP Cloud Droplet Probe

CERES Clouds and the Earth's Radiant Energy Systems

CERES-EBAF Clouds and the Earth's Radiant Energy Systems Energy Balanced and Filled

CloudSat Cloud Satellite

CNES Centre National d'Études Spatiales

CNN Convolutional Neural Network

CPI Cloud Particle Imager

CPL Cloud Physics Lidar

CPR Cloud Profiling Radar

CRE Cloud Radiative Effect

CRS Cloud Radar System

DARDAR raDAR/liDAR

DIAL Differential Absorption Lidar

DLR Deutsches Zentrum für Luft- und Raumfahrt

DMT Droplet Measurement Technologies

DSD Droplet Size Distribution

DT-INSU Division Technique de l'Institut National des Sciences de l'Univers

EarthCARE Earth Clouds, Aerosols and Radiation Explorer

ECMWF European Centre for Medium-Range Weather Forecasts

EOS Earth Observing System

ER-2 Earth Resources 2

ESA European Space Agency

EXRAD ER-2 X-band Doppler Radar

FMCW Frequency-Modulated Continuous Wave

FOV Field-of-view

FSSP Forward Scattering Spectrometer Probe

GCOM Global Change Observation Mission

HALO High Altitude and Long Range Research Aircraft

HAMP HALO Microwave Package

HIWRAP High-altitude Imaging Wind and Rain Airborne Profiler

HSR High Spectral Resolution

HSRL High Spectral Resolution Lidar

IEEE Institute of Electrical and Electronics Engineers

IIR Infrared Imager Radiometer

IMPACTS Investigation of Microphysics and Precipitation for Atlantic Coast-Threatening Snowstorms

INP Ice Nucleating Particle

IR Infrared

IWC Ice Water Content

JAXA Japan Aerospace eXploration Agency

LaMP Laboratoire de Météorologie Physique

LASER or laser Light Amplification by Stimulated Emission of Radiation

LATMOS Laboratoire Atmosphères et Observations spatiales

LiDAR Light Detection And Ranging

LNG LÉANDRE New Generation

LUT Look Up Table

LW Longwave

LWC Liquid Water Content

LÉANDRE Lidars aéroportés pour l'Étude des Aérosols, des Nuages, de la Dynamique, du Rayonnement et du cycle de l'Eau

METEK Meteorologische Messtechnik

MODIS Moderate Resolution Imaging Spectroradiometer

MSI Multi-Spectral Imager

NASA National Aeronautics and Space Administration

OAP Optical Array Probe

OCO-2 Orbiting Carbon Observatory-2

OPC Optical Particle Counter

PARASOL Polarization and Anisotropy of Reflectances for Atmospheric Sciences coupled with Observations from a Lidar

PDF Probability Density Function

PDS Particle Detection System

PMS Particle Measuring Systems

PN Polar Nephelometer

POLDER POLarization and Directionality of the Earth's Reflectances

PSD Particle Size Distribution

RADAR RAdio Detection And Ranging

RALI RAdar-LIdar

RASTA RAdar SysTem Airborne

SAFIRE Service des Avions Français Instrumentés pour la Recherche en Environnement

SEVIRI Spinning Enhanced Visible Infrared Imager

SMART Spectral Modular Airborne Radiation measurement sysTem

SPEC Stratton Park Engineering Company

specMACS spectrometer of the Munich Aerosol Cloud Scanner

SSFR Solar Spectral Flux Radiometer

SW Shortwave

TOA Top of the atmosphere

TWC Total Water Content

UV Ultraviolet

WALES WAter vapor Lidar Experiment in Space

WBF Wegener-Bergeron-Findeisen

WFC Wide Field of View Camera

References

- Anagnostou, Emmanouil N., Carlos A. Morales, and Tufa Dinku (Apr. 2001). "The Use of TRMM Precipitation Radar Observations in Determining Ground Radar Calibration Biases." en. In: *Journal of Atmospheric and Oceanic Technology* 18.4, pp. 616–628. issn: 0739-0572, 1520-0426. doi: [10.1175/1520-0426\(2001\)018<0616:TUOTPR>2.0.CO;2](https://doi.org/10.1175/1520-0426(2001)018<0616:TUOTPR>2.0.CO;2). url: https://journals.ametsoc.org/view/journals/atot/18/4/1520-0426_2001_018_0616_tuotpr_2_0_co_2.xml (cit. on p. 71).
- Atlas, David (Aug. 1954). "THE ESTIMATION OF CLOUD PARAMETERS BY RADAR." en. In: *Journal of the Atmospheric Sciences* 11.4, pp. 309–317. issn: 1520-0469. doi: [10.1175/1520-0469\(1954\)011<0309:TEOCPB>2.0.CO;2](https://doi.org/10.1175/1520-0469(1954)011<0309:TEOCPB>2.0.CO;2). url: https://journals.ametsoc.org/view/journals/atasc/11/4/1520-0469_1954_011_0309_teocpb_2_0_co_2.xml (cit. on p. 100).
- Aubry, Clémantyne, Julien Delanoë, Silke Groß, Florian Ewald, Frédéric Tridon, Olivier Jourdan, and Guillaume Mioche (Jan. 2024). "Lidar-radar synergistic method to retrieve ice, supercooled and mixed-phase clouds properties." en. In: *Atmospheric Measurement Techniques Discussions*, pp. 1–28. doi: [10.5194/amt-2023-252](https://doi.org/10.5194/amt-2023-252). url: <https://amt.copernicus.org/preprints/amt-2023-252/> (cit. on pp. 140, 187).
- Baker, Brad A. and R. Paul Lawson (Dec. 2006). "In Situ Observations of the Microphysical Properties of Wave, Cirrus, and Anvil Clouds. Part I: Wave Clouds." en. In: *Journal of the Atmospheric Sciences* 63.12, pp. 3160–3185. issn: 0022-4928, 1520-0469. doi: [10.1175/JAS3802.1](https://doi.org/10.1175/JAS3802.1). url: <https://journals.ametsoc.org/view/journals/atasc/63/12/jas3802.1.xml> (cit. on p. 25).
- Battaglia, Alessandro and Giulia Panegrossi (Jan. 2020). "What Can We Learn from the CloudSat Radiometric Mode Observations of Snowfall over the Ice-Free Ocean?" en. In: *Remote Sensing* 12.20, p. 3285. issn: 2072-4292. doi: [10.3390/rs12203285](https://doi.org/10.3390/rs12203285). url: <https://www.mdpi.com/2072-4292/12/20/3285> (cit. on p. 72).
- Baumgardner, D, H Jonsson, W Dawson, D O'Connor, and R Newton (Oct. 2001). "The cloud, aerosol and precipitation spectrometer: a new instrument for cloud investigations." en. In: *Atmospheric Research* 59-60, pp. 251–264. issn: 01698095. doi: [10.1016/S0169-8095\(01\)00119-3](https://doi.org/10.1016/S0169-8095(01)00119-3). url: <https://linkinghub.elsevier.com/retrieve/pii/S0169809501001193> (cit. on p. 57).

- Baumgardner, D., S. J. Abel, D. Axisa, R. Cotton, J. Crosier, P. Field, C. Gurganus, A. Heymsfield, A. Korolev, M. Krämer, P. Lawson, G. McFarquhar, Z. Ulanowski, and J. Um (Jan. 2017). "Cloud Ice Properties: In Situ Measurement Challenges." en. In: *Meteorological Monographs* 58.1, pp. 9.1–9.23. doi: [10.1175/AMSMONOGRAPH5-D-16-0011.1](https://doi.org/10.1175/AMSMONOGRAPH5-D-16-0011.1). url: <https://journals.ametsoc.org/view/journals/amsm/58/1/amsmonographs-d-16-0011.1.xml> (cit. on p. 48).
- Baumgardner, Darrel and Michael Spowart (Oct. 1990). "Evaluation of the Forward Scattering Spectrometer Probe. Part III: Time Response and Laser Inhomogeneity Limitations." en. In: *Journal of Atmospheric and Oceanic Technology* 7.5, pp. 666–672. issn: 0739-0572, 1520-0426. doi: [10.1175/1520-0426\(1990\)007<0666:EOTFSS>2.0.CO;2](https://doi.org/10.1175/1520-0426(1990)007<0666:EOTFSS>2.0.CO;2). url: https://journals.ametsoc.org/view/journals/atot/7/5/1520-0426_1990_007_0666_eotfss_2_0_co_2.xml (cit. on p. 52).
- Bergeron, T. (1935). "On the physics of clouds and precipitation." In: *Proces Verbaux de l'Association de Meteorologie, Paris. Int. Union of Geodesy and Geophys.*, pp. 156–178 (cit. on pp. 14, 24, 25).
- Beswick, K., Darrel Baumgardner, Martin Gallagher, A. Volz-Thomas, P. Nedelec, K. Wang, and Sara Lance (May 2014). "The backscatter cloud probe - a compact low-profile autonomous optical spectrometer." In: *Atmospheric Measurement Techniques* 7, pp. 1443–1457. doi: [10.5194/amt-7-1443-2014](https://doi.org/10.5194/amt-7-1443-2014) (cit. on p. 52).
- Beyerle, G., M. R. Gross, D. A. Haner, N. T. Kjome, I. S. McDermid, T. J. McGee, J. M. Rosen, H.-J. Schäfer, and O. Schrems (May 2001). "A Lidar and Backscatter Sonde Measurement Campaign at Table Mountain during February–March 1997: Observations of Cirrus Clouds." en. In: *Journal of the Atmospheric Sciences* 58.10, pp. 1275–1287. issn: 0022-4928, 1520-0469. doi: [10.1175/1520-0469\(2001\)058<1275:ALABSM>2.0.CO;2](https://doi.org/10.1175/1520-0469(2001)058<1275:ALABSM>2.0.CO;2). url: https://journals.ametsoc.org/view/journals/atsc/58/10/1520-0469_2001_058_1275_alabsm_2_0_co_2.xml (cit. on p. 78).
- Bierwirth, E., A. Ehrlich, M. Wendisch, J.-F. Gayet, C. Gourbeyre, R. Dupuy, A. Herber, R. Neuber, and A. Lampert (May 2013). "Optical thickness and effective radius of Arctic boundary-layer clouds retrieved from airborne nadir and imaging spectrometry." en. In: *Atmospheric Measurement Techniques* 6.5, pp. 1189–1200. issn: 1867-1381. doi: [10.5194/amt-6-1189-2013](https://doi.org/10.5194/amt-6-1189-2013). url: <https://amt.copernicus.org/articles/6/1189/2013/> (cit. on p. 172).
- Billault-Roux, Anne-Claire et al. (Feb. 2023). "ICE GENESIS: Synergetic Aircraft and Ground-Based Remote Sensing and In Situ Measurements of Snowfall Microphysical Properties." en. In: *Bulletin of the American Meteorological Society* 104.2, E367–E388. issn: 0003-0007,

- 1520-0477. doi: 10.1175/BAMS-D-21-0184.1. url: <https://journals.ametsoc.org/view/journals/bams/104/2/BAMS-D-21-0184.1.xml> (cit. on p. 187).
- Bodhaine, Barry A., Norman B. Wood, Ellsworth G. Dutton, and James R. Slusser (Nov. 1999). "On Rayleigh Optical Depth Calculations." en. In: *Journal of Atmospheric and Oceanic Technology* 16.11, pp. 1854–1861. issn: 0739-0572, 1520-0426. doi: 10.1175/1520-0426(1999)016<1854:ORODC>2.0.CO;2. url: https://journals.ametsoc.org/view/journals/atot/16/11/1520-0426_1999_016_1854_orodc_2_0_co_2.xml (cit. on p. 78).
- Bony, Sandrine and Jean-Louis Dufresne (2005). "Marine boundary layer clouds at the heart of tropical cloud feedback uncertainties in climate models." en. In: *Geophysical Research Letters* 32.20. issn: 1944-8007. doi: 10.1029/2005GL023851. url: <https://onlinelibrary.wiley.com/doi/abs/10.1029/2005GL023851> (cit. on p. 46).
- Boucher, O., C. Bretherton, G. Feingold, P. Forster, V.-M. Kerminen, Y. Kondo, H. Liao, U. Lohmann, P. Rasch, S.K. Satheesh, S. Sherwood, B. Stevens, and X.Y. Zhan (2013). "Clouds and Aerosols." In: *Climate Change 2013: The Physical Science Basis. Contribution of Working Group I to the Fifth Assessment Report of the Intergovernmental Panel on Climate Change [Stocker, T.F., D. Qin, G.-K. Plattner, M. Tignor, S.K. Allen, J. Boschung, A. Nauels, Y. Xia, V. Bex and P.M. Midgley (eds.)]* url: https://www.ipcc.ch/site/assets/uploads/2018/02/WG1AR5_Chapter07_FINAL-1.pdf (cit. on pp. 12, 46).
- Bringi, V. N. and V. Chandrasekar (2001). *Polarimetric Doppler Weather Radar: Principles and Applications*. Cambridge: Cambridge University Press. isbn: 978-0-521-62384-1. doi: 10.1017/CB09780511541094. url: <https://www.cambridge.org/core/books/polarimetric-doppler-weather-radar/C93A3269D222708EADB81C1E4504BB4F> (cit. on p. 89).
- Brown, Philip R. A. and Peter N. Francis (Apr. 1995). "Improved Measurements of the Ice Water Content in Cirrus Using a Total-Water Probe." en. In: *Journal of Atmospheric and Oceanic Technology* 12.2, pp. 410–414. issn: 0739-0572, 1520-0426. doi: 10.1175/1520-0426(1995)012<0410:IMOTIW>2.0.CO;2. url: https://journals.ametsoc.org/view/journals/atot/12/2/1520-0426_1995_012_0410_imotiw_2_0_co_2.xml (cit. on pp. 31, 110, 179).
- Brown, Rodger A and Vincent T Wood (2007). *A Guide for Interpreting Doppler Velocity Patterns: Northern Hemisphere Edition*. en. U.S. Department of Commerce, National Weather Service (cit. on p. 90).

- Bruneau, D., J. Pelon, F. Blouzon, J. Spatazza, P. Genau, G. Buchholtz, N. Amarouche, A. Abchiche, and O. Aouji (Oct. 2015). "355-nm high spectral resolution airborne lidar LNG: system description and first results." en. In: *Applied Optics* 54.29, p. 8776. issn: 0003-6935, 1539-4522. doi: [10.1364/AO.54.008776](https://doi.org/10.1364/AO.54.008776). url: <https://opg.optica.org/abstract.cfm?URI=ao-54-29-8776> (cit. on pp. 75, 78, 88).
- Bucholtz, Anthony (May 1995). "Rayleigh-scattering calculations for the terrestrial atmosphere." en. In: *Applied Optics* 34.15, pp. 2765–2773. issn: 2155-3165. doi: [10.1364/AO.34.002765](https://doi.org/10.1364/AO.34.002765). url: <https://opg.optica.org/ao/abstract.cfm?uri=ao-34-15-2765> (cit. on p. 78).
- Bugliaro, L., T. Zinner, C. Keil, B. Mayer, R. Hollmann, M. Reuter, and W. Thomas (June 2011). "Validation of cloud property retrievals with simulated satellite radiances: a case study for SEVIRI." en. In: *Atmospheric Chemistry and Physics* 11.12, pp. 5603–5624. issn: 1680-7324. doi: [10.5194/acp-11-5603-2011](https://doi.org/10.5194/acp-11-5603-2011). url: <https://acp.copernicus.org/articles/11/5603/2011/> (cit. on p. 62).
- Burton, S. P., C. A. Hostetler, A. L. Cook, J. W. Hair, S. T. Seaman, S. Scola, D. B. Harper, J. A. Smith, M. A. Fenn, R. A. Ferrare, P. E. Saide, E. V. Chemyakin, and D. Müller (July 2018). "Calibration of a high spectral resolution lidar using a Michelson interferometer, with data examples from ORACLES." en. In: *Applied Optics* 57.21, p. 6061. issn: 1559-128X, 2155-3165. doi: [10.1364/AO.57.006061](https://doi.org/10.1364/AO.57.006061). url: <https://opg.optica.org/abstract.cfm?URI=ao-57-21-6061> (cit. on p. 75).
- Cazenave, Quitterie (2019). "Development and evaluation of multi-sensor methods for EarthCare mission based on A-Train and airborne measurements." en. PhD Thesis. Université Paris-Saclay (cit. on pp. 78, 110, 115).
- Cazenave, Quitterie, Marie Ceccaldi, Julien Delanoë, Jacques Pelon, Silke Groß, and Andrew Heymsfield (May 2019). "Evolution of DARDAR-CLOUD ice cloud retrievals: new parameters and impacts on the retrieved microphysical properties." en. In: *Atmospheric Measurement Techniques* 12.5, pp. 2819–2835. issn: 1867-1381. doi: [10.5194/amt-12-2819-2019](https://doi.org/10.5194/amt-12-2819-2019). url: <https://amt.copernicus.org/articles/12/2819/2019/> (cit. on pp. 14, 17, 105, 108, 117, 179).
- Ceccaldi, M., J. Delanoë, R. J. Hogan, N. L. Pounder, A. Protat, and J. Pelon (2013). "From CloudSat-CALIPSO to EarthCare: Evolution of the DARDAR cloud classification and its comparison to airborne radar-lidar observations." en. In: *Journal of Geophysical Research: Atmospheres* 118.14, pp. 7962–7981. issn: 2169-8996. doi: <https://doi.org/10.1002/jgrd.50579>. url: <https://agupubs.onlinelibrary.wiley.com/doi/abs/10.1002/jgrd.50579> (cit. on pp. 116–118, 123, 124).

- Ceccaldi, Marie (2014). "Combinaison de mesures actives et passives pour l'étude des nuages dans le cadre de la préparation à la mission EarthCARE." fr. PhD thesis. Université de Versailles Saint Quentin en Yvelines (cit. on pp. 17, 105).
- Choi, Yong-Sang, Richard S. Lindzen, Chang-Hoi Ho, and Jinwon Kim (June 2010). "Space observations of cold-cloud phase change." In: *Proceedings of the National Academy of Sciences* 107.25, pp. 11211–11216. doi: [10.1073/pnas.1006241107](https://doi.org/10.1073/pnas.1006241107). url: <https://www.pnas.org/doi/full/10.1073/pnas.1006241107> (cit. on pp. 13, 25).
- Clarke, Ben, Friederike Otto, Rupert Stuart-Smith, and Luke Harrington (June 2022). "Extreme weather impacts of climate change: an attribution perspective." en. In: *Environmental Research: Climate* 1.1, p. 012001. issn: 2752-5295. doi: [10.1088/2752-5295/ac6e7d](https://doi.org/10.1088/2752-5295/ac6e7d). url: <https://dx.doi.org/10.1088/2752-5295/ac6e7d> (cit. on p. 13).
- Dekoutsidis, Georgios, Silke Groß, Martin Wirth, Martina Krämer, and Christian Rolf (Mar. 2023). "Characteristics of supersaturation in midlatitude cirrus clouds and their adjacent cloud-free air." en. In: *Atmospheric Chemistry and Physics* 23.5, pp. 3103–3117. issn: 1680-7324. doi: [10.5194/acp-23-3103-2023](https://doi.org/10.5194/acp-23-3103-2023). url: <https://acp.copernicus.org/articles/23/3103/2023/> (cit. on p. 94).
- Del Guasta, Massimo (2001). "Simulation of LIDAR returns from pristine and deformed hexagonal ice prisms in cold cirrus by means of "face tracing"." en. In: *Journal of Geophysical Research: Atmospheres* 106.D12, pp. 12589–12602. issn: 2156-2202. doi: [10.1029/2000JD900724](https://doi.org/10.1029/2000JD900724). url: <https://onlinelibrary.wiley.com/doi/abs/10.1029/2000JD900724> (cit. on p. 74).
- Delanoë, J. M. E., A. J. Heymsfield, A. Protat, A. Bansemer, and R. J. Hogan (Apr. 2014). "Normalized particle size distribution for remote sensing application." en. In: *Journal of Geophysical Research: Atmospheres* 119.7, pp. 4204–4227. issn: 2169897X. doi: [10.1002/2013JD020700](https://doi.org/10.1002/2013JD020700). url: <http://doi.wiley.com/10.1002/2013JD020700> (cit. on pp. 108, 110, 117).
- Delanoë, Julien (2023a). *DARDAR CLOUD - Brown and Francis mass-size relationship*. AERIS. doi: <https://doi.org/10.25326/450> (cit. on pp. 110, 117).
- (2023b). *DARDAR CLOUD - Heymsfield's composite mass-size relationship*. AERIS. doi: <https://doi.org/10.25326/449> (cit. on pp. 110, 117).
- Delanoë, Julien and Robin J. Hogan (Apr. 2008). "A variational scheme for retrieving ice cloud properties from combined radar, lidar, and infrared radiometer." en. In: *Journal of Geophysical Research* 113.D7, p. D07204. issn: 0148-0227. doi: [10.1029/2007JD009000](https://doi.org/10.1029/2007JD009000). url: <http://doi.org/10.1029/2007JD009000>

- [//doi.wiley.com/10.1029/2007JD009000](https://doi.wiley.com/10.1029/2007JD009000) (cit. on pp. 16, 80, 100, 101, 105, 108, 111–113).
- Delanoë, Julien and Robin J. Hogan (2010). "Combined CloudSat-CALIPSO-MODIS retrievals of the properties of ice clouds." en. In: *Journal of Geophysical Research: Atmospheres* 115.D4. issn: 2156-2202. doi: <https://doi.org/10.1029/2009JD012346>. url: <https://agupubs.onlinelibrary.wiley.com/doi/abs/10.1029/2009JD012346> (cit. on pp. 80, 108, 116, 117, 123).
- Delanoë, Julien, Alain Protat, Olivier Jourdan, Jacques Pelon, Mathieu Papazzoni, Régis Dupuy, Jean-François Gayet, and Caroline Jouan (2013). "Comparison of airborne in-situ, airborne radar-lidar, and spaceborne radar-lidar retrievals of polar ice cloud properties sampled during the POLARCAT campaign." In: *Journal of Atmospheric and Oceanic Technology* 30.1, pp. 57–73. doi: [10.1175/JTECH-D-11-00200.1](https://doi.org/10.1175/JTECH-D-11-00200.1). url: <https://hal.archives-ouvertes.fr/hal-00730535> (cit. on pp. 14, 88, 152, 172).
- Delanoë, Julien, Alain Protat, Jacques Testud, Dominique Bouniol, A. J. Heymsfield, A. Bansemer, P. R. A. Brown, and R. M. Forbes (2005). "Statistical properties of the normalized ice particle size distribution." en. In: *Journal of Geophysical Research: Atmospheres* 110.D10. issn: 2156-2202. doi: <https://doi.org/10.1029/2004JD005405>. url: <https://agupubs.onlinelibrary.wiley.com/doi/abs/10.1029/2004JD005405> (cit. on pp. 30, 31).
- Delanoë, Julien, Alain Protat, Jean-Paul Vinson, Williams Brett, Christophe Caudoux, Fabrice Bertrand, Jacques Parent du Chatelet, Ruben Hallali, Laurent Barthes, Martial Haeffelin, and Jean-Charles Dupont (May 2016). "BASTA: A 95-GHz FMCW Doppler Radar for Cloud and Fog Studies." en. In: *Journal of Atmospheric and Oceanic Technology* 33.5, pp. 1023–1038. issn: 0739-0572, 1520-0426. doi: [10.1175/JTECH-D-15-0104.1](https://doi.org/10.1175/JTECH-D-15-0104.1). url: https://journals.ametsoc.org/view/journals/atot/33/5/jtech-d-15-0104_1.xml (cit. on pp. 69, 89).
- Deng, Min, Gerald G. Mace, Zhien Wang, and R. Paul Lawson (2013). "Evaluation of Several A-Train Ice Cloud Retrieval Products with In Situ Measurements Collected during the SPARTICUS Campaign." In: *Journal of Applied Meteorology and Climatology* 52.4, pp. 1014–1030. issn: 1558-8424. url: <https://www.jstor.org/stable/26175811> (cit. on p. 177).
- Deng, Min, Gerald G. Mace, Zhien Wang, and Hajime Okamoto (2010). "Tropical Composition, Cloud and Climate Coupling Experiment validation for cirrus cloud profiling retrieval using CloudSat radar and CALIPSO lidar." en. In: *Journal of Geophysical Research: Atmospheres*

- 115.D10. issn: 2156-2202. doi: [10.1029/2009JD013104](https://onlinelibrary.wiley.com/doi/abs/10.1029/2009JD013104). url: <https://onlinelibrary.wiley.com/doi/abs/10.1029/2009JD013104> (cit. on pp. 16, 80, 177).
- Donovan, D. P. and A. C. a. P. van Lammeren (2001). "Cloud effective particle size and water content profile retrievals using combined lidar and radar observations: 1. Theory and examples." en. In: *Journal of Geophysical Research: Atmospheres* 106.D21, pp. 27425–27448. issn: 2156-2202. doi: [10.1029/2001JD900243](https://onlinelibrary.wiley.com/doi/abs/10.1029/2001JD900243). url: <https://onlinelibrary.wiley.com/doi/abs/10.1029/2001JD900243> (cit. on pp. 16, 80).
- Dye, James E. and Darrel Baumgardner (Dec. 1984). "Evaluation of the Forward Scattering Spectrometer Probe. Part I: Electronic and Optical Studies." en. In: *Journal of Atmospheric and Oceanic Technology* 1.4, pp. 329–344. issn: 0739-0572, 1520-0426. doi: [10.1175/1520-0426\(1984\)001<0329:EOTFSS>2.0.CO;2](https://journals.ametsoc.org/view/journals/atot/1/4/1520-0426_1984_001_0329_eotfss_2_0_co_2.xml). url: https://journals.ametsoc.org/view/journals/atot/1/4/1520-0426_1984_001_0329_eotfss_2_0_co_2.xml (cit. on p. 53).
- Ehrlich, A., E. Bierwirth, M. Wendisch, J.-F. Gayet, G. Mioche, A. Lampert, and J. Heintzenberg (Dec. 2008). "Cloud phase identification of Arctic boundary-layer clouds from airborne spectral reflection measurements: test of three approaches." en. In: *Atmospheric Chemistry and Physics* 8.24, pp. 7493–7505. issn: 1680-7324. doi: [10.5194/acp-8-7493-2008](https://acp.copernicus.org/articles/8/7493/2008/). url: <https://acp.copernicus.org/articles/8/7493/2008/> (cit. on p. 62).
- Ehrlich, A., M. Wendisch, E. Bierwirth, J.-F. Gayet, G. Mioche, A. Lampert, and B. Mayer (Dec. 2009). "Evidence of ice crystals at cloud top of Arctic boundary-layer mixed-phase clouds derived from airborne remote sensing." en. In: *Atmospheric Chemistry and Physics* 9.24, pp. 9401–9416. issn: 1680-7316. doi: [10.5194/acp-9-9401-2009](https://acp.copernicus.org/articles/9/9401/2009/). url: <https://acp.copernicus.org/articles/9/9401/2009/> (cit. on pp. 62, 140).
- Eidenshink, J. C. and J. L. Faundeen (Nov. 1994). "The 1 km AVHRR global land data set: first stages in implementation." en. In: *International Journal of Remote Sensing* 15.17, pp. 3443–3462. issn: 0143-1161, 1366-5901. doi: [10.1080/01431169408954339](https://www.tandfonline.com/doi/full/10.1080/01431169408954339). url: <https://www.tandfonline.com/doi/full/10.1080/01431169408954339> (cit. on p. 62).
- Emde, Claudia, Robert Buras-Schnell, Arve Kylling, Bernhard Mayer, Josef Gasteiger, Ulrich Hamann, Jonas Kylling, Bettina Richter, Christian Pause, Timothy Dowling, and Luca Bugliaro (May 2016). "The libRadtran software package for radiative transfer calculations (version 2.0.1)." en. In: *Geoscientific Model Development* 9.5, pp. 1647–

1672. issn: 1991-959X. doi: 10.5194/gmd-9-1647-2016. url: <https://gmd.copernicus.org/articles/9/1647/2016/> (cit. on p. 186).
- Erfani, Ehsan and David L. Mitchell (Apr. 2016). "Developing and bounding ice particle mass- and area-dimension expressions for use in atmospheric models and remote sensing." en. In: *Atmospheric Chemistry and Physics* 16.7, pp. 4379–4400. issn: 1680-7316. doi: 10.5194/acp-16-4379-2016. url: <https://acp.copernicus.org/articles/16/4379/2016/> (cit. on p. 31).
- Esselborn, Michael, Martin Wirth, Andreas Fix, Matthias Tesche, and Gerhard Ehret (Jan. 2008). "Airborne high spectral resolution lidar for measuring aerosol extinction and backscatter coefficients." en. In: *Applied Optics* 47.3, p. 346. issn: 0003-6935, 1539-4522. doi: 10.1364/AO.47.000346. url: <https://opg.optica.org/abstract.cfm?URI=ao-47-3-346> (cit. on pp. 75, 94).
- Evans, K. Franklin, James R. Wang, Paul E. Racette, Gerald Heymsfield, and Lihua Li (June 2005). "Ice Cloud Retrievals and Analysis with the Compact Scanning Submillimeter Imaging Radiometer and the Cloud Radar System during CRYSTAL FACE." en. In: *Journal of Applied Meteorology and Climatology* 44.6, pp. 839–859. issn: 1520-0450, 0894-8763. doi: 10.1175/JAM2250.1. url: <https://journals.ametsoc.org/view/journals/apme/44/6/jam2250.1.xml> (cit. on p. 78).
- Ewald, Florian (2016). "Retrieval of Vertical Profiles of Cloud Droplet Effective Radius using solar reflectance from cloud sides." en. PhD thesis. Faculty of Physics Ludwig-Maximilians-University Munich (cit. on p. 63).
- Ewald, Florian, Silke Groß, Martin Hagen, Lutz Hirsch, Julien Delanoë, and Matthias Bauer-Pfundstein (Mar. 2019). "Calibration of a 35 GHz airborne cloud radar: lessons learned and intercomparisons with 94 GHz cloud radars." en. In: *Atmospheric Measurement Techniques* 12.3, pp. 1815–1839. issn: 1867-1381. doi: 10.5194/amt-12-1815-2019. url: <https://amt.copernicus.org/articles/12/1815/2019/> (cit. on p. 71).
- Ewald, Florian, Tobias Kölling, Andreas Baumgartner, Tobias Zinner, and Bernhard Mayer (May 2016). "Design and characterization of specMACS, a multipurpose hyperspectral cloud and sky imager." en. In: *Atmospheric Measurement Techniques* 9.5, pp. 2015–2042. issn: 1867-1381. doi: 10.5194/amt-9-2015-2016. url: <https://amt.copernicus.org/articles/9/2015/2016/amt-9-2015-2016.html> (cit. on pp. 62–64).
- Feofilov, Artem G., Hélène Chepfer, Vincent Noël, and Frederic Szczap (July 2023). "Incorporating EarthCARE observations into a multi-

- lidar cloud climate record: the ATLID (Atmospheric Lidar) cloud climate product." en. In: *Atmospheric Measurement Techniques* 16.13, pp. 3363–3390. issn: 1867-1381. doi: [10.5194/amt-16-3363-2023](https://doi.org/10.5194/amt-16-3363-2023). url: <https://amt.copernicus.org/articles/16/3363/2023/> (cit. on pp. 83, 87).
- Field, P. R., A. J. Heymsfield, B. J. Shipway, P. J. DeMott, K. A. Pratt, D. C. Rogers, J. Stith, and K. A. Prather (Mar. 2012). "Ice in Clouds Experiment–Layer Clouds. Part II: Testing Characteristics of Heterogeneous Ice Formation in Lee Wave Clouds." en. In: *Journal of the Atmospheric Sciences* 69.3, pp. 1066–1079. issn: 0022-4928, 1520-0469. doi: [10.1175/JAS-D-11-026.1](https://doi.org/10.1175/JAS-D-11-026.1). url: <https://journals.ametsoc.org/view/journals/atsc/69/3/jas-d-11-026.1.xml> (cit. on pp. 25, 41).
- Field, P. R., A. A. Hill, K. Furtado, and A. Korolev (Apr. 2014). "Mixed-phase clouds in a turbulent environment. Part 2: Analytic treatment: Mixed-phase clouds in a turbulent environment. Part 2." en. In: *Quarterly Journal of the Royal Meteorological Society* 140.680, pp. 870–880. issn: 00359009. doi: [10.1002/qj.2175](https://doi.org/10.1002/qj.2175). url: <https://onlinelibrary.wiley.com/doi/10.1002/qj.2175> (cit. on p. 25).
- Field, P. R., R. J. Hogan, P. R. A. Brown, A. J. Illingworth, T. W. Choulaton, and R. J. Cotton (2005). "Parametrization of ice-particle size distributions for mid-latitude stratiform cloud." en. In: *Quarterly Journal of the Royal Meteorological Society* 131.609, pp. 1997–2017. issn: 1477-870X. doi: [10.1256/qj.04.134](https://doi.org/10.1256/qj.04.134). url: <https://onlinelibrary.wiley.com/doi/abs/10.1256/qj.04.134> (cit. on p. 30).
- Field, P. R. et al. (Jan. 2017). "Secondary Ice Production: Current State of the Science and Recommendations for the Future." en. In: *Meteorological Monographs* 58.1, pp. 7.1–7.20. doi: [10.1175/AMSMONOGRAPHS-D-16-0014.1](https://doi.org/10.1175/AMSMONOGRAPHS-D-16-0014.1). url: <https://journals.ametsoc.org/view/journals/amsm/58/1/amsmonographs-d-16-0014.1.xml> (cit. on pp. 13, 25).
- Fielding, M. D., J. C. Chiu, R. J. Hogan, G. Feingold, E. Eloranta, E. J. O'Connor, and M. P. Cadetdu (July 2015). "Joint retrievals of cloud and drizzle in marine boundary layer clouds using ground-based radar, lidar and zenith radiances." en. In: *Atmospheric Measurement Techniques* 8.7, pp. 2663–2683. issn: 1867-8548. doi: [10.5194/amt-8-2663-2015](https://doi.org/10.5194/amt-8-2663-2015). url: <https://amt.copernicus.org/articles/8/2663/2015/> (cit. on pp. 131, 185).
- Fielding, Mark D., J. Christine Chiu, Robin J. Hogan, and Graham Feingold (2014). "A novel ensemble method for retrieving properties of warm cloud in 3-D using ground-based scanning radar and zenith radiances." en. In: *Journal of Geophysical Research: Atmo-*

- spheres 119.18, pp. 10, 912–10, 930. issn: 2169-8996. doi: [10.1002/2014JD021742](https://doi.org/10.1002/2014JD021742). url: <https://onlinelibrary.wiley.com/doi/abs/10.1002/2014JD021742> (cit. on pp. 131, 185).
- Findeisen, W. (1938). "Kolloid-meteorologische Vorgänge bei Niederschlags-bildung." In: *Meteorologische Zeitschrift* 55, pp. 121–133 (cit. on pp. 14, 24, 25).
- Flamant, Cyrille et al. (Jan. 2024). "Cyclogenesis in the tropical Atlantic: First scientific highlights from the Clouds-Atmospheric Dynamics-Dust Interactions in West Africa (CADDIWA) field campaign." en. In: *Bulletin of the American Meteorological Society* -1.aop. issn: 0003-0007, 1520-0477. doi: [10.1175/BAMS-D-23-0230.1](https://doi.org/10.1175/BAMS-D-23-0230.1). url: <https://journals.ametsoc.org/view/journals/bams/aop/BAMS-D-23-0230.1/BAMS-D-23-0230.1.xml> (cit. on p. 187).
- Fleishauer, Robert P., Vincent E. Larson, and Thomas H. Vonder Haar (June 2002). "Observed Microphysical Structure of Midlevel, Mixed-Phase Clouds." en. In: *Journal of the Atmospheric Sciences* 59.11, pp. 1779–1804. issn: 0022-4928, 1520-0469. doi: [10.1175/1520-0469\(2002\)059<1779:OMSOMM>2.0.CO;2](https://doi.org/10.1175/1520-0469(2002)059<1779:OMSOMM>2.0.CO;2). url: https://journals.ametsoc.org/view/journals/atsc/59/11/1520-0469_2002_059_1779_omsomm_2.0.co_2.xml (cit. on p. 27).
- Foot, J. S. (1988). "Some observations of the optical properties of clouds. II: Cirrus." en. In: *Quarterly Journal of the Royal Meteorological Society* 114.479, pp. 145–164. issn: 1477-870X. doi: [10.1002/qj.49711447908](https://doi.org/10.1002/qj.49711447908). url: <https://onlinelibrary.wiley.com/doi/abs/10.1002/qj.49711447908> (cit. on p. 30).
- Fox, Neil I. and Anthony J. Illingworth (May 1997). "The Retrieval of Stratocumulus Cloud Properties by Ground-Based Cloud Radar." en. In: *Journal of Applied Meteorology and Climatology* 36.5, pp. 485–492. issn: 1520-0450, 0894-8763. doi: [10.1175/1520-0450\(1997\)036<0485:TROSCP>2.0.CO;2](https://doi.org/10.1175/1520-0450(1997)036<0485:TROSCP>2.0.CO;2). url: https://journals.ametsoc.org/view/journals/apme/36/5/1520-0450_1997_036_0485_troscp_2.0.co_2.xml (cit. on p. 71).
- Frisch, A. S., C. W. Fairall, and J. B. Snider (Aug. 1995). "Measurement of Stratus Cloud and Drizzle Parameters in ASTEX with a Ka-Band Doppler Radar and a Microwave Radiometer." en. In: *Journal of the Atmospheric Sciences* 52.16, pp. 2788–2799. issn: 0022-4928, 1520-0469. doi: [10.1175/1520-0469\(1995\)052<2788:MOSCAD>2.0.CO;2](https://doi.org/10.1175/1520-0469(1995)052<2788:MOSCAD>2.0.CO;2). url: https://journals.ametsoc.org/view/journals/atsc/52/16/1520-0469_1995_052_2788_moscad_2_0_co_2.xml (cit. on pp. 131, 185).
- Garnier, Anne, Jacques Pelon, Philippe Dubuisson, Michaël Faivre, Olivier Chomette, Nicolas Pascal, and David P. Kratz (July 2012).

- "Retrieval of Cloud Properties Using CALIPSO Imaging Infrared Radiometer. Part I: Effective Emissivity and Optical Depth." en. In: *Journal of Applied Meteorology and Climatology* 51.7, pp. 1407–1425. issn: 1558-8424, 1558-8432. doi: [10.1175/JAMC-D-11-0220.1](https://doi.org/10.1175/JAMC-D-11-0220.1). url: <https://journals.ametsoc.org/view/journals/apme/51/7/jamc-d-11-0220.1.xml> (cit. on p. 78).
- Garnier, Anne, Jacques Pelon, Philippe Dubuisson, Ping Yang, Michaël Faivre, Olivier Chomette, Nicolas Pascal, Pat Lucker, and Tim Murray (Nov. 2013). "Retrieval of Cloud Properties Using CALIPSO Imaging Infrared Radiometer. Part II: Effective Diameter and Ice Water Path." en. In: *Journal of Applied Meteorology and Climatology* 52.11, pp. 2582–2599. issn: 1558-8424, 1558-8432. doi: [10.1175/JAMC-D-12-0328.1](https://doi.org/10.1175/JAMC-D-12-0328.1). url: <https://journals.ametsoc.org/view/journals/apme/52/11/jamc-d-12-0328.1.xml> (cit. on p. 78).
- Gayet, J. F., O. Crépel, J. F. Fournol, and S. Oshchepkov (Apr. 1997). "A new airborne polar Nephelometer for the measurements of optical and microphysical cloud properties. Part I: Theoretical design." en. In: *Annales Geophysicae* 15.4, pp. 451–459. issn: 0992-7689. doi: [10.1007/s00585-997-0451-1](https://doi.org/10.1007/s00585-997-0451-1). url: <https://angeo.copernicus.org/articles/15/451/1997/> (cit. on pp. 54, 55).
- Gayet, J.-F., G. Mioche, A. Dörnbrack, A. Ehrlich, A. Lampert, and M. Wendisch (Sept. 2009). "Microphysical and optical properties of Arctic mixed-phase clouds. The 9 April 2007 case study." en. In: *Atmospheric Chemistry and Physics* 9.17, pp. 6581–6595. issn: 1680-7316. doi: [10.5194/acp-9-6581-2009](https://doi.org/10.5194/acp-9-6581-2009). url: <https://acp.copernicus.org/articles/9/6581/2009/> (cit. on pp. 15, 140, 172).
- Gayet, Jean-François, Frédérique Auriol, Andreas Minikin, Johan Ström, Marco Seifert, Radovan Krejci, Andreas Petzold, Guy Febvre, and Ulrich Schumann (2002). "Quantitative measurement of the microphysical and optical properties of cirrus clouds with four different in situ probes: Evidence of small ice crystals." en. In: *Geophysical Research Letters* 29.24, pp. XXX–XXX. issn: 1944-8007. doi: [10.1029/2001GL014342](https://doi.org/10.1029/2001GL014342). url: <https://onlinelibrary.wiley.com/doi/abs/10.1029/2001GL014342> (cit. on pp. 55, 56).
- Gerber, H., Y. Takano, Timothy J. Garrett, and Peter V. Hobbs (Sept. 2000). "Nephelometer Measurements of the Asymmetry Parameter, Volume Extinction Coefficient, and Backscatter Ratio in Arctic Clouds." en. In: *Journal of the Atmospheric Sciences* 57.18, pp. 3021–3034. issn: 0022-4928, 1520-0469. doi: [10.1175/1520-0469\(2000\)057<3021:NMOTAP>2.0.CO;2](https://doi.org/10.1175/1520-0469(2000)057<3021:NMOTAP>2.0.CO;2). url: https://journals.ametsoc.org/view/journals/atsc/57/18/1520-0469_2000_057_3021_nmotap_2.0.co_2.xml (cit. on p. 55).

- Glenar, D., Timothy Stubbs, Edward Schwieterman, Tyler Robinson, and Timothy Livengood (Mar. 2019). "Earthshine as an Illumination Source at the Moon." In: *Icarus* 321, pp. 841–856. doi: [10.1016/j.icarus.2018.12.025](https://doi.org/10.1016/j.icarus.2018.12.025) (cit. on p. 34).
- Grund, Christian J., Robert M. Banta, Joanne L. George, James N. Howell, Madison J. Post, Ronald A. Richter, and Ann M. Weickmann (Mar. 2001). "High-Resolution Doppler Lidar for Boundary Layer and Cloud Research." en. In: *Journal of Atmospheric and Oceanic Technology* 18.3, pp. 376–393. issn: 0739-0572, 1520-0426. doi: [10.1175/1520-0426\(2001\)018<0376:HRDLFB>2.0.CO;2](https://doi.org/10.1175/1520-0426(2001)018<0376:HRDLFB>2.0.CO;2). url: https://journals.ametsoc.org/view/journals/atot/18/3/1520-0426_2001_018_0376_hrdlfb_2_0_co_2.xml (cit. on p. 78).
- Hair, Johnathan W., Chris A. Hostetler, Anthony L. Cook, David B. Harper, Richard A. Ferrare, Terry L. Mack, Wayne Welch, Luis Ramos Izquierdo, and Floyd E. Hovis (Dec. 2008). "Airborne High Spectral Resolution Lidar for profiling aerosol optical properties." en. In: *Applied Optics* 47.36, p. 6734. issn: 0003-6935, 1539-4522. doi: [10.1364/AO.47.006734](https://doi.org/10.1364/AO.47.006734). url: <https://opg.optica.org/abstract.cfm?URI=ao-47-36-6734> (cit. on p. 75).
- Hallett, J. and S. C. Mossop (May 1974). "Production of secondary ice particles during the riming process." en. In: *Nature* 249.5452, pp. 26–28. issn: 1476-4687. doi: [10.1038/249026a0](https://doi.org/10.1038/249026a0). url: <https://www.nature.com/articles/249026a0> (cit. on pp. 14, 25).
- Heymsfield, Andrew, Dave Winker, Melody Avery, Mark Vaughan, Glenn Diskin, Min Deng, Valentin Mitev, and Renaud Matthey (Feb. 2014). "Relationships between Ice Water Content and Volume Extinction Coefficient from In Situ Observations for Temperatures from 0° to –86°C: Implications for Spaceborne Lidar Retrievals." en. In: *Journal of Applied Meteorology and Climatology* 53.2, pp. 479–505. issn: 1558-8424, 1558-8432. doi: [10.1175/JAMC-D-13-087.1](https://doi.org/10.1175/JAMC-D-13-087.1). url: <https://journals.ametsoc.org/view/journals/apme/53/2/jamc-d-13-087.1.xml> (cit. on p. 179).
- Heymsfield, Andrew J., Carl Schmitt, Aaron Bansemer, and Cynthia H. Twohy (Oct. 2010). "Improved Representation of Ice Particle Masses Based on Observations in Natural Clouds." en. In: *Journal of the Atmospheric Sciences* 67.10, pp. 3303–3318. issn: 0022-4928, 1520-0469. doi: [10.1175/2010JAS3507.1](https://doi.org/10.1175/2010JAS3507.1). url: <https://journals.ametsoc.org/view/journals/atms/67/10/2010jas3507.1.xml> (cit. on pp. 31, 110).
- Hobbs, Peter V., Shirley Chang, and John D. Locatelli (May 1974). "The dimensions and aggregation of ice crystals in natural clouds." en. In: *Journal of Geophysical Research* 79.15, pp. 2199–2206. issn:

01480227. doi: [10.1029/JC079i015p02199](https://doi.org/10.1029/JC079i015p02199). url: <http://doi.wiley.com/10.1029/JC079i015p02199> (cit. on pp. 14, 25).
- Hogan, R. J., A. J. Illingworth, E. J. O'Connor, and J. P. V. Poiares-Baptista (July 2003a). "Characteristics of mixed-phase clouds. II: A climatology from ground-based lidar." en. In: *Quarterly Journal of the Royal Meteorological Society* 129.592, pp. 2117–2134. issn: 1477870X, 00359009. doi: [10.1256/qj.01.209](https://doi.org/10.1256/qj.01.209). url: <http://doi.wiley.com/10.1256/qj.01.209> (cit. on p. 74).
- Hogan, Robin J. (Aug. 2006). "Fast approximate calculation of multiply scattered lidar returns." en. In: *Applied Optics* 45.23, p. 5984. issn: 0003-6935, 1539-4522. doi: [10.1364/AO.45.005984](https://doi.org/10.1364/AO.45.005984). url: <https://opg.optica.org/abstract.cfm?URI=ao-45-23-5984> (cit. on pp. 110, 133).
- (Oct. 2007). "A Variational Scheme for Retrieving Rainfall Rate and Hail Reflectivity Fraction from Polarization Radar." en. In: *Journal of Applied Meteorology and Climatology* 46.10, pp. 1544–1564. issn: 1558-8424, 1558-8432. doi: [10.1175/JAM2550.1](https://doi.org/10.1175/JAM2550.1). url: <https://journals.ametsoc.org/view/journals/apme/46/10/jam2550.1.xml> (cit. on pp. 108, 113).
- Hogan, Robin J., Dominique Bouniol, Darcy N. Ladd, Ewan J. O'Connor, and Anthony J. Illingworth (Apr. 2003b). "Absolute Calibration of 94/95-GHz Radars Using Rain." en. In: *Journal of Atmospheric and Oceanic Technology* 20.4, pp. 572–580. issn: 0739-0572, 1520-0426. doi: [10.1175/1520-0426\(2003\)20<572:ACOGRU>2.0.CO;2](https://doi.org/10.1175/1520-0426(2003)20<572:ACOGRU>2.0.CO;2). url: https://journals.ametsoc.org/view/journals/atot/20/4/1520-0426_2003_20_572_acogru_2_0_co_2.xml (cit. on p. 71).
- Hogan, Robin J., Malcolm E. Brooks, Anthony J. Illingworth, David P. Donovan, Claire Tinel, Dominique Bouniol, and J. Pedro V. Poiares Baptista (Feb. 2006a). "Independent Evaluation of the Ability of Spaceborne Radar and Lidar to Retrieve the Microphysical and Radiative Properties of Ice Clouds." en. In: *Journal of Atmospheric and Oceanic Technology* 23.2, pp. 211–227. issn: 0739-0572, 1520-0426. doi: [10.1175/JTECH1837.1](https://doi.org/10.1175/JTECH1837.1). url: https://journals.ametsoc.org/view/journals/atot/23/2/jtech1837_1.xml (cit. on p. 114).
- Hogan, Robin J., Marion P. Mittermaier, and Anthony J. Illingworth (Feb. 2006b). "The Retrieval of Ice Water Content from Radar Reflectivity Factor and Temperature and Its Use in Evaluating a Mesoscale Model." en. In: *Journal of Applied Meteorology and Climatology* 45.2, pp. 301–317. issn: 1558-8424, 1558-8432. doi: [10.1175/JAM2340.1](https://doi.org/10.1175/JAM2340.1). url: <https://journals.ametsoc.org/view/journals/apme/45/2/jam2340.1.xml> (cit. on p. 101).

- Howard, Luke (1803). *Essay on the Modifications of Clouds*. en (cit. on p. 23).
- IEEE Standard Letter Designations for Radar-Frequency Bands (Feb. 2020). en. Tech. rep. IEEE Std 521-2019 (Revision of IEEE Std 521-2002), pp. 1–15. doi: [10.1109/IEEESTD.2020.8999849](https://doi.org/10.1109/IEEESTD.2020.8999849). url: <https://ieeexplore.ieee.org/document/8999849/> (cit. on pp. 68, 69).
- Illingworth, A. J. et al. (Aug. 2015). “The EarthCARE Satellite: The Next Step Forward in Global Measurements of Clouds, Aerosols, Precipitation, and Radiation.” en. In: *Bulletin of the American Meteorological Society* 96.8, pp. 1311–1332. issn: 0003-0007, 1520-0477. doi: [10.1175/BAMS-D-12-00227.1](https://doi.org/10.1175/BAMS-D-12-00227.1). url: <https://journals.ametsoc.org/view/journals/bams/96/8/bams-d-12-00227.1.xml> (cit. on pp. 16, 85, 87).
- Intrieri, Janet M., Graeme L. Stephens, Wynn L. Eberhard, and Taneil Uttal (June 1993). “A Method for Determining Cirrus Cloud Particle Sizes Using Lidar and Radar Backscatter Technique.” en. In: *Journal of Applied Meteorology and Climatology* 32.6, pp. 1074–1082. issn: 1520-0450, 0894-8763. doi: [10.1175/1520-0450\(1993\)032<1074:AMFDCC>2.0.CO;2](https://doi.org/10.1175/1520-0450(1993)032<1074:AMFDCC>2.0.CO;2). url: https://journals.ametsoc.org/view/journals/apme/32/6/1520-0450_1993_032_1074_amfdcc_2_0_co_2.xml (cit. on pp. 16, 80).
- IPCC (2022). “Climate Change 2022: Impacts, Adaptation and Vulnerability. Contribution of Working Group II to the Sixth Assessment Report of the Intergovernmental Panel on Climate Change [H.-O. Pörtner, D.C. Roberts, M. Tignor, E.S. Poloczanska, K. Mintenbeck, A. Alegría, M. Craig, S. Langsdorf, S. Löschke, V. Möller, A. Okem, B. Rama (eds.)]” en. In: p. 3056. doi: [10.1017/9781009325844](https://doi.org/10.1017/9781009325844) (cit. on p. 13).
- Irbah, Abdanour, Julien Delanoë, Gerd-Jan van Zadelhoff, David P. Donovan, Pavlos Kollias, Bernat Puigdomènech Treserras, Shannon Mason, Robin J. Hogan, and Aleksandra Tatarevic (June 2023). “The classification of atmospheric hydrometeors and aerosols from the EarthCARE radar and lidar: the A-TC, C-TC and AC-TC products.” en. In: *Atmospheric Measurement Techniques* 16.11, pp. 2795–2820. issn: 1867-1381. doi: [10.5194/amt-16-2795-2023](https://doi.org/10.5194/amt-16-2795-2023). url: <https://amt.copernicus.org/articles/16/2795/2023/> (cit. on pp. 80, 87).
- Jaffeux, Louis, Alfons Schwarzenböck, Pierre Coutris, and Christophe Duroure (Sept. 2022). “Ice crystal images from optical array probes: classification with convolutional neural networks.” en. In: *Atmospheric Measurement Techniques* 15.17, pp. 5141–5157. issn: 1867-8548. doi: [10.5194/amt-15-5141-2022](https://doi.org/10.5194/amt-15-5141-2022). url: <https://amt.copernicus.org/articles/15/5141/2022/> (cit. on p. 57).

- Jäkel, E., J. Walter, and M. Wendisch (Mar. 2013). "Thermodynamic phase retrieval of convective clouds: impact of sensor viewing geometry and vertical distribution of cloud properties." en. In: *Atmospheric Measurement Techniques* 6.3, pp. 539–547. issn: 1867-1381. doi: [10.5194/amt-6-539-2013](https://doi.org/10.5194/amt-6-539-2013). url: <https://amt.copernicus.org/articles/6/539/2013/> (cit. on p. 62).
- Jorquera, Susana, Felipe Toledo Bittner, Julien Delanoë, Alexis Berne, Anne-Claire Billault-Roux, Alfons Schwarzenboeck, Fabien Dezitter, Nicolas Viltard, and Audrey Martini (July 2023). "Calibration Transfer Methodology for Cloud Radars Based on Ice Cloud Observations." en. In: *Journal of Atmospheric and Oceanic Technology* 40.7, pp. 773–788. issn: 0739-0572, 1520-0426. doi: [10.1175/JTECH-D-22-0087.1](https://doi.org/10.1175/JTECH-D-22-0087.1). url: <https://journals.ametsoc.org/view/journals/atot/40/7/JTECH-D-22-0087.1.xml> (cit. on p. 71).
- Jourdan, Olivier, Guillaume Mioche, Timothy J. Garrett, Alfons Schwarzenböck, Jérôme Vidot, Yu Xie, Valery Shcherbakov, Ping Yang, and Jean-François Gayet (2010). "Coupling of the microphysical and optical properties of an Arctic nimbostratus cloud during the ASTAR 2004 experiment: Implications for light-scattering modeling." en. In: *Journal of Geophysical Research: Atmospheres* 115.D23. issn: 2156-2202. doi: [10.1029/2010JD014016](https://doi.org/10.1029/2010JD014016). url: <https://onlinelibrary.wiley.com/doi/abs/10.1029/2010JD014016> (cit. on pp. 56, 141, 172).
- Jourdan, Olivier, Sergey Oshchepkov, Jean-François Gayet, Valery Shcherbakov, and Harumi Isaka (2003a). "Statistical analysis of cloud light scattering and microphysical properties obtained from airborne measurements." en. In: *Journal of Geophysical Research: Atmospheres* 108.D5. issn: 2156-2202. doi: [10.1029/2002JD002723](https://doi.org/10.1029/2002JD002723). url: <https://onlinelibrary.wiley.com/doi/abs/10.1029/2002JD002723> (cit. on p. 56).
- Jourdan, Olivier, Sergey Oshchepkov, Valery Shcherbakov, Jean-François Gayet, and Harumi Isaka (Sept. 2003b). "Assessment of cloud optical parameters in the solar region: Retrievals from airborne measurements of scattering phase functions." en. In: *Journal of Geophysical Research: Atmospheres* 108.D18, 2003JD003493. issn: 0148-0227. doi: [10.1029/2003JD003493](https://doi.org/10.1029/2003JD003493). url: <https://agupubs.onlinelibrary.wiley.com/doi/10.1029/2003JD003493> (cit. on p. 56).
- Kahnert, F. Michael (June 2003). "Numerical methods in electromagnetic scattering theory." In: *Journal of Quantitative Spectroscopy and Radiative Transfer*. Electromagnetic and Light Scattering by Non-Spherical Particles 79-80, pp. 775–824. issn: 0022-4073. doi: [10.1016/S0022-4073\(03\)00079-8](https://doi.org/10.1016/S0022-4073(03)00079-8).

- 1016/S0022-4073(02)00321-7. url: <https://www.sciencedirect.com/science/article/pii/S0022407302003217> (cit. on p. 39).
- Kanji, Zamin A., Luis A. Ladino, Heike Wex, Yvonne Boose, Monika Burkert-Kohn, Daniel J. Cziczo, and Martina Krämer (Jan. 2017). "Overview of Ice Nucleating Particles." en. In: *Meteorological Monographs* 58.1, pp. 1.1–1.33. doi: 10.1175/AMSMONOGRAPHSD-16-0006.1. url: <https://journals.ametsoc.org/view/journals/amsm/58/1/amsmonographs-d-16-0006.1.xml> (cit. on pp. 13, 22, 25).
- Kikuchi, Nobuhiro, Teruyuki Nakajima, Hiroshi Kumagai, Hiroshi Kuroiwa, Akihide Kamei, Ryosuke Nakamura, and Takashi Y. Nakajima (2006). "Cloud optical thickness and effective particle radius derived from transmitted solar radiation measurements: Comparison with cloud radar observations." en. In: *Journal of Geophysical Research: Atmospheres* 111.D7. issn: 2156-2202. doi: 10.1029/2005JD006363. url: <https://onlinelibrary.wiley.com/doi/abs/10.1029/2005JD006363> (cit. on p. 62).
- King, Michael D., Steven Platnick, W. Paul Menzel, Steven A. Ackerman, and Paul A. Hubanks (July 2013). "Spatial and Temporal Distribution of Clouds Observed by MODIS Onboard the Terra and Aqua Satellites." In: *IEEE Transactions on Geoscience and Remote Sensing* 51.7, pp. 3826–3852. issn: 1558-0644. doi: 10.1109/TGRS.2012.2227333 (cit. on p. 12).
- King, Michael D., Steven Platnick, Ping Yang, G. Thomas Arnold, Mark A. Gray, Jérôme C. Riedi, Steven A. Ackerman, and Kuo-Nan Liou (June 2004). "Remote Sensing of Liquid Water and Ice Cloud Optical Thickness and Effective Radius in the Arctic: Application of Airborne Multispectral MAS Data." en. In: *Journal of Atmospheric and Oceanic Technology* 21.6, pp. 857–875. issn: 0739-0572. doi: 10.1175/1520-0426(2004)021<0857:RSOLWA>2.0.CO;2. url: <https://journals.ametsoc.org/jtech/article/21/6/857/2515/Remote-Sensing-of-Liquid-Water-and-Ice-Cloud> (cit. on p. 62).
- Knollenberg, R.G. (1976). *Three New Instruments for Cloud Physics Measurements: The 2-D Spectrometer, the Forward Scattering Spectrometer Probe, and the Active Scattering Aerosol Spectrometer*. American Meteorological Society. url: <https://books.google.fr/books?id=ahVKtwAACAAJ> (cit. on p. 52).
- Kokhanovsky, A. (Feb. 2004). "Optical properties of terrestrial clouds." en. In: *Earth-Science Reviews* 64.3-4, pp. 189–241. issn: 00128252. doi: 10.1016/S0012-8252(03)00042-4. url: <https://linkinghub.elsevier.com/retrieve/pii/S0012825203000424> (cit. on p. 38).

- Kopp, Greg and Judith L. Lean (2011). "A new, lower value of total solar irradiance: Evidence and climate significance." en. In: *Geophysical Research Letters* 38.1. issn: 1944-8007. doi: [10.1029/2010GL045777](https://doi.org/10.1029/2010GL045777). url: <https://onlinelibrary.wiley.com/doi/abs/10.1029/2010GL045777> (cit. on p. 42).
- Korolev, A., Greg Mcfarquhar, Paul Field, Charmaine Franklin, Paul Lawson, Z. Wang, E. Williams, S. Abel, Duncan Axisa, S. Borrmann, J. Crosier, Jacob Fugal, M. Krämer, Ulrike Lohmann, Oliver Schlenker, and Manfred Wendisch (June 2017). "Mixed-Phase Clouds: Progress and Challenges." In: *Meteorological Monographs* 58, pp. 5.1–5.50. doi: [10.1175/AMSMONOGRAPHS-D-17-0001.1](https://doi.org/10.1175/AMSMONOGRAPHS-D-17-0001.1) (cit. on pp. 25, 26).
- Lamorte, Caroline, Agnès Borbon, Alfons Schwarzenboeck, and Jean-Christophe Canonici (2016). "Safire : des avions au service de la recherche en environnement." fr. In: *La Météorologie* 8.93, p. 30. issn: 0026-1181. doi: [10.4267/2042/59939](https://doi.org/10.4267/2042/59939). url: https://lameteorologie.fr/issues/2016/93/meteo_2016_93_30 (cit. on p. 54).
- Lance, S., C. A. Brock, D. Rogers, and J. A. Gordon (Dec. 2010). "Water droplet calibration of the Cloud Droplet Probe (CDP) and in-flight performance in liquid, ice and mixed-phase clouds during ARCPAC." en. In: *Atmospheric Measurement Techniques* 3.6, pp. 1683–1706. issn: 1867-8548. doi: [10.5194/amt-3-1683-2010](https://doi.org/10.5194/amt-3-1683-2010). url: <https://amt.copernicus.org/articles/3/1683/2010/> (cit. on pp. 58, 59).
- Lau, K. M., H. T. Wu, Y. C. Sud, and G. K. Walker (Nov. 2005). "Effects of Cloud Microphysics on Tropical Atmospheric Hydrologic Processes and Intraseasonal Variability." en. In: *Journal of Climate* 18.22, pp. 4731–4751. issn: 0894-8755, 1520-0442. doi: [10.1175/JCLI3561.1](https://doi.org/10.1175/JCLI3561.1). url: <https://journals.ametsoc.org/view/journals/clim/18/22/jcli3561.1.xml> (cit. on p. 41).
- Lawson, R. Paul, Brad A. Baker, Carl G. Schmitt, and T. L. Jensen (2001). "An overview of microphysical properties of Arctic clouds observed in May and July 1998 during FIRE ACE." en. In: *Journal of Geophysical Research: Atmospheres* 106.D14, pp. 14989–15014. issn: 2156-2202. doi: [10.1029/2000JD900789](https://doi.org/10.1029/2000JD900789). url: <https://onlinelibrary.wiley.com/doi/abs/10.1029/2000JD900789> (cit. on pp. 27, 48).
- Lawson, R. Paul, Darren O'Connor, Patrick Zmarzly, Kim Weaver, Brad Baker, Qixu Mo, and Haflidi Jonsson (Nov. 2006). "The 2D-S (Stereo) Probe: Design and Preliminary Tests of a New Airborne, High-Speed, High-Resolution Particle Imaging Probe." en. In: *Journal of Atmospheric and Oceanic Technology* 23.11, pp. 1462–1477. issn:

- 1520-0426, 0739-0572. doi: [10.1175/JTECH1927.1](https://doi.org/10.1175/JTECH1927.1). url: <http://journals.ametsoc.org/doi/10.1175/JTECH1927.1> (cit. on p. 56).
- Lefèvre, R. (2007). "Physique de la mesure de la sonde CPI pour la mesure des propriétés des cristaux de glace. Application aux observations réalisées durant la campagne ASTAR 2004." fr. PhD thesis. Université Blaise Pascal (cit. on pp. 50, 51).
- Li, Lihua, Gerald M. Heymsfield, Paul E. Racette, Lin Tian, and Ed Zenker (Sept. 2004). "A 94-GHz Cloud Radar System on a NASA High-Altitude ER-2 Aircraft." en. In: *Journal of Atmospheric and Oceanic Technology* 21.9, pp. 1378–1388. issn: 0739-0572, 1520-0426. doi: [10.1175/1520-0426\(2004\)021<1378:AGCRSO>2.0.CO;2](https://doi.org/10.1175/1520-0426(2004)021<1378:AGCRSO>2.0.CO;2). url: https://journals.ametsoc.org/view/journals/atot/21/9/1520-0426_2004_021_1378_agcrso_2_0_co_2.xml (cit. on p. 96).
- Li, Lihua, Gerald M. Heymsfield, Lin Tian, and Paul E. Racette (July 2005). "Measurements of Ocean Surface Backscattering Using an Airborne 94-GHz Cloud Radar—Implication for Calibration of Airborne and Spaceborne W-Band Radars." en. In: *Journal of Atmospheric and Oceanic Technology* 22.7, pp. 1033–1045. issn: 1520-0426, 0739-0572. doi: [10.1175/JTECH1722.1](https://doi.org/10.1175/JTECH1722.1). url: <http://journals.ametsoc.org/doi/10.1175/JTECH1722.1> (cit. on p. 71).
- Libbrecht, Kenneth (Apr. 2005). "The physics of snow crystals." In: *Rep. Prog. Phys.* 68. doi: [10.1088/0034-4885/68/4/R03](https://doi.org/10.1088/0034-4885/68/4/R03) (cit. on pp. 27, 28).
- Loeb, Norman G., David R. Doelling, Hailan Wang, Wenying Su, Cathy Nguyen, Joseph G. Corbett, Lusheng Liang, Cristian Mitrescu, Fred G. Rose, and Seiji Kato (Jan. 2018). "Clouds and the Earth's Radiant Energy System (CERES) Energy Balanced and Filled (EBAF) Top-of-Atmosphere (TOA) Edition-4.0 Data Product." en. In: *Journal of Climate* 31.2, pp. 895–918. issn: 0894-8755, 1520-0442. doi: [10.1175/JCLI-D-17-0208.1](https://doi.org/10.1175/JCLI-D-17-0208.1). url: <https://journals.ametsoc.org/view/journals/clim/31/2/jcli-d-17-0208.1.xml> (cit. on pp. 12, 44).
- Magono, Choji and Chung Woo Lee (1966). "Meteorological Classification of Natural Snow Crystals." en. In: *Journal Faculty of Science, Hokkaido University* (cit. on p. 50).
- Majewski, Adam, Jeffrey R. French, and Samuel Haimov (Nov. 2023). "Airborne Radar Doppler Spectrum Width as a Scale-Dependent Turbulence Metric." en. In: *Journal of Atmospheric and Oceanic Technology* 40.12, pp. 1541–1555. issn: 0739-0572, 1520-0426. doi: [10.1175/JTECH-D-23-0056.1](https://doi.org/10.1175/JTECH-D-23-0056.1). url: <https://journals.ametsoc.org/view/journals/atot/40/12/JTECH-D-23-0056.1.xml> (cit. on p. 72).

- Mason, Shannon L., Robin J. Hogan, Alessio Bozzo, and Nicola L. Pounder (Nov. 2022). *A unified synergistic retrieval of clouds, aerosols and precipitation from EarthCARE: the ACM-CAP product*. en. preprint. Clouds/Remote Sensing/Data Processing and Information Retrieval. doi: [10.5194/egusphere-2022-1195](https://doi.org/10.5194/egusphere-2022-1195). url: <https://egusphere.copernicus.org/preprints/2022/egusphere-2022-1195/> (cit. on pp. 16, 80, 88, 186).
- Matus, Alexander V. and Tristan S. L'Ecuyer (2017). "The role of cloud phase in Earth's radiation budget." en. In: *Journal of Geophysical Research: Atmospheres* 122.5, pp. 2559–2578. issn: 2169-8996. doi: [10.1002/2016JD025951](https://doi.org/10.1002/2016JD025951). url: <https://onlinelibrary.wiley.com/doi/abs/10.1002/2016JD025951> (cit. on pp. 13, 14, 25, 46).
- McBride, P. J., K. S. Schmidt, P. Pilewskie, A. S. Kittelman, and D. E. Wolfe (July 2011). "A spectral method for retrieving cloud optical thickness and effective radius from surface-based transmittance measurements." en. In: *Atmospheric Chemistry and Physics* 11.14, pp. 7235–7252. issn: 1680-7316. doi: [10.5194/acp-11-7235-2011](https://doi.org/10.5194/acp-11-7235-2011). url: <https://acp.copernicus.org/articles/11/7235/2011/> (cit. on p. 62).
- McGill, M. J., L. Li, W. D. Hart, G. M. Heymsfield, D. L. Hlavka, P. E. Racette, L. Tian, M. A. Vaughan, and D. M. Winker (2004). "Combined lidar-radar remote sensing: Initial results from CRYSTAL-FACE." en. In: *Journal of Geophysical Research: Atmospheres* 109.D7. issn: 2156-2202. doi: [10.1029/2003JD004030](https://doi.org/10.1029/2003JD004030). url: <https://onlinelibrary.wiley.com/doi/abs/10.1029/2003JD004030> (cit. on p. 96).
- McMurdie, Lynn A. et al. (May 2022). "Chasing Snowstorms: The Investigation of Microphysics and Precipitation for Atlantic Coast-Threatening Snowstorms (IMPACTS) Campaign." en. In: *Bulletin of the American Meteorological Society* 103.5, E1243–E1269. issn: 0003-0007, 1520-0477. doi: [10.1175/BAMS-D-20-0246.1](https://doi.org/10.1175/BAMS-D-20-0246.1). url: <https://journals.ametsoc.org/view/journals/bams/103/5/BAMS-D-20-0246.1.xml> (cit. on p. 177).
- Mech, M., E. Orlandi, S. Crewell, F. Ament, L. Hirsch, M. Hagen, G. Peters, and B. Stevens (Dec. 2014). "HAMP – the microwave package on the High Altitude and Long range research aircraft (HALO)." en. In: *Atmospheric Measurement Techniques* 7.12, pp. 4539–4553. issn: 1867-8548. doi: [10.5194/amt-7-4539-2014](https://doi.org/10.5194/amt-7-4539-2014). url: <https://amt.copernicus.org/articles/7/4539/2014/> (cit. on pp. 92, 93).
- Melchionna, Sabrina, Matthias Bauer, and Gerhard Peters (Oct. 2008). "A new algorithm for the extraction of cloud parameters using multiple peak analysis of cloud radar data First application and preliminary results." en. In: *Meteorologische Zeitschrift*, pp. 613–620. issn: , doi: [10.1127/0941-2948/2008/0322](https://doi.org/10.1127/0941-2948/2008/0322). url: <https://www.>

- schweizerbart.de/papers/metz/detail/17/56776/A_new_algorithm_for_the_extraction_of_cloud_parameters_using_multipeak_analysis_of_cloud_radar_data_First_application_and_preliminary_results (cit. on p. 92).
- Meyers, Michael P., Paul J. DeMott, and William R. Cotton (July 1992). "New Primary Ice-Nucleation Parameterizations in an Explicit Cloud Model." en. In: *Journal of Applied Meteorology and Climatology* 31.7, pp. 708–721. issn: 1520-0450, 0894-8763. doi: [10.1175/1520-0450\(1992\)031<0708:NPINPI>2.0.CO;2](https://doi.org/10.1175/1520-0450(1992)031<0708:NPINPI>2.0.CO;2); 2. url: https://journals.ametsoc.org/view/journals/apme/31/7/1520-0450_1992_031_0708_npinpi_2_0_co_2.xml (cit. on pp. 13, 14, 25).
- Mie, Gustav (1908). "Beiträge zur Optik trüber Medien, speziell kolloidaler Metallösungen." en. In: *Annalen der Physik* 330.3, pp. 377–445. issn: 1521-3889. doi: [10.1002/andp.19083300302](https://doi.org/10.1002/andp.19083300302). url: <https://onlinelibrary.wiley.com/doi/abs/10.1002/andp.19083300302> (cit. on pp. 37, 39, 40).
- Miles, Natasha L., Johannes Verlinde, and Eugene E. Clothiaux (Jan. 2000). "Cloud Droplet Size Distributions in Low-Level Stratiform Clouds." en. In: *Journal of the Atmospheric Sciences* 57.2, pp. 295–311. issn: 0022-4928, 1520-0469. doi: [10.1175/1520-0469\(2000\)057<0295:CDSDIL>2.0.CO;2](https://doi.org/10.1175/1520-0469(2000)057<0295:CDSDIL>2.0.CO;2); 2. url: https://journals.ametsoc.org/view/journals/atsc/57/2/1520-0469_2000_057_0295_cdsdil_2.0.co_2.xml (cit. on p. 131).
- Mioche, Guillaume (2012). "Validation des produits d'inversion des observations satellitaires CALIPSO/CloudSat pour la caractérisation des propriétés optiques et microphysiques des nuages de glace et en phase mixte." fr. PhD thesis (cit. on pp. 49, 51).
- Mioche, Guillaume and Olivier Jourdan (2018). "Spaceborne Remote Sensing and Airborne In Situ Observations of Arctic Mixed-Phase Clouds." en. In: *Mixed-Phase Clouds*. Elsevier, pp. 121–150. isbn: 978-0-12-810549-8. doi: [10.1016/B978-0-12-810549-8.00006-4](https://doi.org/10.1016/B978-0-12-810549-8.00006-4). url: <https://linkinghub.elsevier.com/retrieve/pii/B9780128105498000064> (cit. on pp. 141, 172–175).
- Mioche, Guillaume, Olivier Jourdan, Julien Delanoë, Christophe Gournbeyre, Guy Febvre, Régis Dupuy, Marie Monier, Frédéric Szczap, Alfons Schwarzenboeck, and Jean-François Gayet (Oct. 2017). "Vertical distribution of microphysical properties of Arctic springtime low-level mixed-phase clouds over the Greenland and Norwegian seas." en. In: *Atmospheric Chemistry and Physics* 17.20, pp. 12845–12869. issn: 1680-7324. doi: [10.5194/acp-17-12845-2017](https://doi.org/10.5194/acp-17-12845-2017). url: <https://acp.copernicus.org/articles/17/12845/2017/> (cit. on pp. 15, 143).

- Mitchell, David L. (June 1996). "Use of Mass- and Area-Dimensional Power Laws for Determining Precipitation Particle Terminal Velocities." en. In: *Journal of the Atmospheric Sciences* 53.12, pp. 1710–1723. issn: 0022-4928, 1520-0469. doi: 10.1175/1520-0469(1996)053<1710:UOMAAD>2.0.CO;2. url: https://journals.ametsoc.org/view/journals/atsc/53/12/1520-0469_1996_053_1710_uomaad_2_0_co_2.xml (cit. on pp. 31, 41, 110).
- Mitrescu, C., J. M. Haynes, G. L. Stephens, S. D. Miller, G. M. Heymsfield, and M. J. McGill (2005). "Cirrus cloud optical, microphysical, and radiative properties observed during the CRYSTAL-FACE experiment: A lidar-radar retrieval system." en. In: *Journal of Geophysical Research: Atmospheres* 110.D9. issn: 2156-2202. doi: 10.1029/2004JD005605. url: <https://onlinelibrary.wiley.com/doi/abs/10.1029/2004JD005605> (cit. on pp. 16, 80).
- Morrison, Hugh, Gijs de Boer, Graham Feingold, Jerry Harrington, Matthew D. Shupe, and Kara Sulia (Jan. 2012). "Resilience of persistent Arctic mixed-phase clouds." en. In: *Nature Geoscience* 5.1, pp. 11–17. issn: 1752-0908. doi: 10.1038/ngeo1332. url: <https://www.nature.com/articles/ngeo1332> (cit. on pp. 14, 25).
- Morrison, Hugh, James O. Pinto, Judith A. Curry, and Greg M. McFarquhar (2008). "Sensitivity of modeled arctic mixed-phase stratocumulus to cloud condensation and ice nuclei over regionally varying surface conditions." en. In: *Journal of Geophysical Research: Atmospheres* 113.D5. issn: 2156-2202. doi: 10.1029/2007JD008729. url: <https://onlinelibrary.wiley.com/doi/abs/10.1029/2007JD008729> (cit. on p. 14).
- Nakajima, Teruyuki and Michael D. King (Aug. 1990). "Determination of the Optical Thickness and Effective Particle Radius of Clouds from Reflected Solar Radiation Measurements. Part I: Theory." en. In: *Journal of the Atmospheric Sciences* 47.15, pp. 1878–1893. issn: 0022-4928, 1520-0469. doi: 10.1175/1520-0469(1990)047<1878:DOTOTA>2.0.CO;2. url: https://journals.ametsoc.org/view/journals/atsc/47/15/1520-0469_1990_047_1878_dotota_2_0_co_2.xml (cit. on p. 62).
- O'Connor, Ewan J., Anthony J. Illingworth, and Robin J. Hogan (May 2004). "A Technique for Autocalibration of Cloud Lidar." en. In: *Journal of Atmospheric and Oceanic Technology* 21.5, pp. 777–786. issn: 0739-0572, 1520-0426. doi: 10.1175/1520-0426(2004)021<0777:ATFAOC>2.0.CO;2. url: https://journals.ametsoc.org/view/journals/atot/21/5/1520-0426_2004_021_0777_atfaoc_2_0_co_2.xml (cit. on p. 74).

- Pacific Northwest National Laboratory (PNNL), Brookhaven National Laboratory (BNL), Argonne National Laboratory (ANL), Oak Ridge National Laboratory (ORNL), Susanne Glienke, and Fan Mei (Nov. 2019). *Two-Dimensional Stereo (2D-S) Probe Instrument Handbook*. en. Tech. rep. DOE/SC-ARM-TR-233, 1597436, DOE/SC-ARM-TR-233, 1597436. doi: [10 . 2172 / 1597436](https://doi.org/10.2172/1597436). url: [https : // www . osti . gov / servlets/purl/1597436/](https://www.osti.gov/servlets/purl/1597436/) (cit. on p. 56).
- Pilewskie, P., J. Pommier, R. Bergstrom, W. Gore, S. Howard, M. Rabbette, B. Schmid, P. V. Hobbs, and S. C. Tsay (2003). "Solar spectral radiative forcing during the Southern African Regional Science Initiative." en. In: *Journal of Geophysical Research: Atmospheres* 108.D13. issn: 2156-2202. doi: [10 . 1029 / 2002JD002411](https://doi.org/10.1029/2002JD002411). url: [https : // onlinelibrary . wiley . com/doi/abs/10 . 1029/2002JD002411](https://onlinelibrary.wiley.com/doi/abs/10.1029/2002JD002411) (cit. on p. 62).
- Pinnick, R. G., S. G. Jennings, Petr Chýlek, Chris Ham, and W. T. Grandy (1983). "Backscatter and extinction in water clouds." en. In: *Journal of Geophysical Research* 88.C11, p. 6787. issn: 0148-0227. doi: [10 . 1029 / JC088iC11p06787](https://doi.org/10.1029/JC088iC11p06787). url: [http : // doi . wiley . com/10 . 1029 / JC088iC11p06787](http://doi.wiley.com/10.1029/JC088iC11p06787) (cit. on pp. 74, 128).
- Pithan, Felix, Brian Medeiros, and Thorsten Mauritsen (July 2014). "Mixed-phase clouds cause climate model biases in Arctic wintertime temperature inversions." en. In: *Climate Dynamics* 43.1-2, pp. 289-303. issn: 0930-7575, 1432-0894. doi: [10 . 1007 / s00382 - 013-1964-9](https://doi.org/10.1007/s00382-013-1964-9). url: [http : // link . springer . com/10 . 1007/s00382-013-1964-9](http://link.springer.com/10.1007/s00382-013-1964-9) (cit. on p. 14).
- Platnick, S., M.D. King, S.A. Ackerman, W.P. Menzel, B.A. Baum, J.C. Riedi, and R.A. Frey (Feb. 2003). "The MODIS cloud products: algorithms and examples from Terra." In: *IEEE Transactions on Geoscience and Remote Sensing* 41.2, pp. 459-473. issn: 1558-0644. doi: [10 . 1109 / TGRS . 2002 . 808301](https://doi.org/10.1109/TGRS.2002.808301). url: [https : // ieeexplore . ieee . org / document/1196061](https://ieeexplore.ieee.org/document/1196061) (cit. on p. 62).
- Platt, C. M. R., S. A. Young, R. T. Austin, G. R. Patterson, D. L. Mitchell, and S. D. Miller (Nov. 2002). "LIRAD Observations of Tropical Cirrus Clouds in MCTEX. Part I: Optical Properties and Detection of Small Particles in Cold Cirrus*." en. In: *Journal of the Atmospheric Sciences* 59.22, pp. 3145-3162. issn: 0022-4928, 1520-0469. doi: [10 . 1175 / 1520 - 0469 \(2002\) 059<3145 : L00TCC>2 . 0 . CO ; 2](https://doi.org/10.1175/1520-0469(2002)059<3145:L00TCC>2.0.CO;2). url: [http : // journals . ametsoc . org/doi/10 . 1175/1520-0469\(2002\)059%3C3145:L00TCC%3E2.0.CO;2](http://journals.ametsoc.org/doi/10.1175/1520-0469(2002)059%3C3145:L00TCC%3E2.0.CO;2) (cit. on p. 108).
- Powell, Kathleen A., Chris A. Hostetler, Mark A. Vaughan, Kam-Pui Lee, Charles R. Trepte, Raymond R. Rogers, David M. Winker, Zhaoyan Liu, Ralph E. Kuehn, William H. Hunt, and Stuart A. Young (Oct.

- 2009). "CALIPSO Lidar Calibration Algorithms. Part I: Nighttime 532-nm Parallel Channel and 532-nm Perpendicular Channel." en. In: *Journal of Atmospheric and Oceanic Technology* 26.10, pp. 2015–2033. issn: 0739-0572, 1520-0426. doi: [10.1175/2009JTECHA1242.1](https://doi.org/10.1175/2009JTECHA1242.1). url: https://journals.ametsoc.org/view/journals/atot/26/10/2009jtecha1242_1.xml (cit. on p. 78).
- Praz, C., S. Ding, G. M. McFarquhar, and A. Berne (2018). "A Versatile Method for Ice Particle Habit Classification Using Airborne Imaging Probe Data." en. In: *Journal of Geophysical Research: Atmospheres* 123.23, pp. 13, 472–13, 495. issn: 2169-8996. doi: [10.1029/2018JD029163](https://doi.org/10.1029/2018JD029163). url: <https://onlinelibrary.wiley.com/doi/abs/10.1029/2018JD029163> (cit. on pp. 57, 58).
- Protat, A., D. Bouniol, J. Delanoë, E. O'Connor, P. T. May, A. Plana-Fattori, A. Hasson, U. Górsdorf, and A. J. Heymsfield (Sept. 2009). "Assessment of Cloudsat Reflectivity Measurements and Ice Cloud Properties Using Ground-Based and Airborne Cloud Radar Observations." en. In: *Journal of Atmospheric and Oceanic Technology* 26.9, pp. 1717–1741. issn: 0739-0572, 1520-0426. doi: [10.1175/2009JTECHA1246.1](https://doi.org/10.1175/2009JTECHA1246.1). url: https://journals.ametsoc.org/view/journals/atot/26/9/2009jtecha1246_1.xml (cit. on p. 71).
- Pruppacher, Hans R. (1997). *Microphysics of clouds and precipitation*. eng. 2nd rev. and enl. ed. Atmospheric and oceanographic sciences library ; v. 18. Dordrecht ; Kluwer Academic Publishers. isbn: 978-1-282-92634-9. doi: [10.1007/978-0-306-48100-0](https://doi.org/10.1007/978-0-306-48100-0) (cit. on p. 26).
- Przybylo, Vanessa M., Kara J. Sulia, Carl G. Schmitt, and Zachary J. Lebo (Apr. 2022). "Classification of Cloud Particle Imagery from Aircraft Platforms Using Convolutional Neural Networks." en. In: *Journal of Atmospheric and Oceanic Technology* 39.4, pp. 405–424. issn: 0739-0572, 1520-0426. doi: [10.1175/JTECH-D-21-0094.1](https://doi.org/10.1175/JTECH-D-21-0094.1). url: <https://journals.ametsoc.org/view/journals/atot/39/4/JTECH-D-21-0094.1.xml> (cit. on p. 50).
- Ramanathan, V., R. D. Cess, E. F. Harrison, P. Minnis, B. R. Barkstrom, E. Ahmad, and D. Hartmann (Jan. 1989). "Cloud-Radiative Forcing and Climate: Results from the Earth Radiation Budget Experiment." en. In: *Science* 243.4887, pp. 57–63. issn: 0036-8075, 1095-9203. doi: [10.1126/science.243.4887.57](https://doi.org/10.1126/science.243.4887.57). url: <https://www.science.org/doi/10.1126/science.243.4887.57> (cit. on pp. 12, 43, 44).
- Rayleigh, Lord (Apr. 1899). "On the transmission of light through an atmosphere containing small particles in suspension, and on the origin of the blue of the sky." In: *The London, Edinburgh, and Dublin Philosophical Magazine and Journal of Science* 47.287, pp. 375–384. issn: 1941-5982. doi: [10.1080/14786449908621276](https://doi.org/10.1080/14786449908621276). url: [https://](https://doi.org/10.1080/14786449908621276)

- www.tandfonline.com/doi/abs/10.1080/14786449908621276 (cit. on p. 37).
- Reichle, David E. (2023). "The global carbon cycle and the biosphere." en. In: *The Global Carbon Cycle and Climate Change*. Elsevier, pp. 235–283. isbn: 978-0-443-18775-9. doi: [10.1016/B978-0-443-18775-9.00014-0](https://doi.org/10.1016/B978-0-443-18775-9.00014-0). url: <https://linkinghub.elsevier.com/retrieve/pii/B9780443187759000140> (cit. on p. 22).
- Reitebuch, Oliver, Christian Lemmerz, Engelbert Nagel, Ulrike Paf-frath, Yannig Durand, Martin Endemann, Frederic Fabre, and Marc Chaloupy (Dec. 2009). "The Airborne Demonstrator for the Direct-Detection Doppler Wind Lidar ALADIN on ADM-Aeolus. Part I: In-strument Design and Comparison to Satellite Instrument." en. In: *Journal of Atmospheric and Oceanic Technology* 26.12, pp. 2501–2515. issn: 0739-0572, 1520-0426. doi: [10.1175/2009JTECHA1309.1](https://doi.org/10.1175/2009JTECHA1309.1). url: https://journals.ametsoc.org/view/journals/atot/26/12/2009jtecha1309_1.xml (cit. on pp. 75, 78).
- Ricaud, Philippe, Massimo Del Guasta, Eric Bazile, Niramson Azouz, Angelo Lupi, Pierre Durand, Jean-Luc Attié, Dana Veron, Vincent Guidard, and Paolo Grigioni (Apr. 2020). "Supercooled liquid water cloud observed, analysed, and modelled at the top of the plane-tary boundary layer above Dome C, Antarctica." en. In: *Atmospheric Chemistry and Physics* 20.7, pp. 4167–4191. issn: 1680-7316. doi: [10.5194/acp-20-4167-2020](https://doi.org/10.5194/acp-20-4167-2020). url: <https://acp.copernicus.org/articles/20/4167/2020/> (cit. on p. 26).
- Rivière, Gwendal et al. (2024). "The THINICE field campaign: Interac-tions between Arctic cyclones, tropopause polar vortices, clouds and sea ice." en. In: *Bulletin of the American Meteorological Society*. doi: [Submitted](https://doi.org/10.1175/BAMS-D-23-0111.1) (cit. on pp. 163, 187).
- Rodgers, Clive D (July 2000). *Inverse Methods for Atmospheric Sound-ing: Theory and Practice*. en. Vol. 2. Series on Atmospheric, Oceanic and Planetary Physics. WORLD SCIENTIFIC. isbn: 978-981-02-2740-1 978-981-281-371-8. doi: [10.1142/3171](https://doi.org/10.1142/3171). url: <https://www.worldscientific.com/worldscibooks/10.1142/3171> (cit. on pp. 101, 103, 105).
- Roebeling, R. A., A. J. Feijt, and P. Stammes (2006). "Cloud prop-erty retrievals for climate monitoring: Implications of differences between Spinning Enhanced Visible and Infrared Imager (SEVIRI) on METEOSAT-8 and Advanced Very High Resolution Radiometer (AVHRR) on NOAA-17." en. In: *Journal of Geophysical Research: At-mospheres* 111.D20. issn: 2156-2202. doi: [10.1029/2005JD006990](https://doi.org/10.1029/2005JD006990). url: <https://onlinelibrary.wiley.com/doi/abs/10.1029/2005JD006990> (cit. on p. 62).

- Sauvage, Laurent, Pierre H. Flamant, Hélène Chepfer, Gérard Brogniez, Vincent Trouillet, Jacques Pelon, and Franck Albers (Apr. 1999). "Remote Sensing of Cirrus Radiative Parameters during EUCREX'94. Case Study of 17 April 1994. Part I: Observations." en. In: *Monthly Weather Review* 127.4, pp. 486–503. issn: 1520-0493, 0027-0644. doi: 10.1175/1520-0493(1999)127<0486:RSOCR>2.0.CO;2. url: https://journals.ametsoc.org/view/journals/mwre/127/4/1520-0493_1999_127_0486_rsocrp_2.0.co_2.xml (cit. on pp. 38, 39, 78).
- Sauvageot, Henri (1992). *Radar Meteorology*. en. Artech House. isbn: 978-0-89006-318-7 (cit. on pp. 69–71).
- Schmetz, Johannes, Paolo Pili, Stephen Tjemkes, Dieter Just, Jochen Kerkmann, Sergio Rota, and Alain Ratier (July 2002). "Supplement to An Introduction to Meteosat Second Generation (MSG): SEVIRI CALIBRATION." en. In: *Bulletin of the American Meteorological Society* 83.7, pp. 992–992. issn: 0003-0007, 1520-0477. doi: 10.1175/BAMS-83-7-Schmetz-2. url: <https://journals.ametsoc.org/doi/10.1175/BAMS-83-7-Schmetz-2> (cit. on p. 62).
- She, Chiao-Yao (Sept. 2001). "Spectral structure of laser light scattering revisited: bandwidths of nonresonant scattering lidars." en. In: *Applied Optics* 40.27, pp. 4875–4884. issn: 2155-3165. doi: 10.1364/AO.40.004875. url: <https://opg.optica.org/ao/abstract.cfm?uri=ao-40-27-4875> (cit. on p. 78).
- Shupe, Matthew D. (Mar. 2011). "Clouds at Arctic Atmospheric Observatories. Part II: Thermodynamic Phase Characteristics." en. In: *Journal of Applied Meteorology and Climatology* 50.3, pp. 645–661. issn: 1558-8424, 1558-8432. doi: 10.1175/2010JAMC2468.1. url: <https://journals.ametsoc.org/view/journals/apme/50/3/2010jamc2468.1.xml> (cit. on pp. 13, 25).
- Skolnik, Merrill I. (2008). *Radar Handbook, Third Edition*. en. McGraw-Hill Education. isbn: 978-0-07-148547-0 (cit. on p. 67).
- Song, Naihui and Dennis Lamb (Jan. 1994). "Experimental Investigations of Ice in Supercooled Clouds. Part 1: System Description and Growth of Ice by Vapor Deposition." en. In: *Journal of the Atmospheric Sciences* 51.1, pp. 91–103. issn: 0022-4928, 1520-0469. doi: 10.1175/1520-0469(1994)051<0091:EIOIIS>2.0.CO;2. url: https://journals.ametsoc.org/view/journals/atsc/51/1/1520-0469_1994_051_0091_eioiis_2_0_co_2.xml (cit. on pp. 14, 25).
- Sourdeval, Odran (Oct. 2012). "Étude des propriétés optiques et radiatives des nuages de type cirrus déduites de la synergie des mesures de rayonnement passif et actif : application dans le contexte de l'A-

- Train et des futures missions spatiales." These de doctorat. Lille 1. url: <https://www.theses.fr/2012LIL10137> (cit. on p. 78).
- Sourdeval, Odran, Edward Gryspeerd, Martina Krämer, Tom Goren, Julien Delanoë, Armin Afchine, Friederike Hemmer, and Johannes Quaas (Oct. 2018). "Ice crystal number concentration estimates from lidar-radar satellite remote sensing – Part 1: Method and evaluation." en. In: *Atmospheric Chemistry and Physics* 18.19, pp. 14327–14350. issn: 1680-7316. doi: [10.5194/acp-18-14327-2018](https://doi.org/10.5194/acp-18-14327-2018). url: <https://acp.copernicus.org/articles/18/14327/2018/> (cit. on p. 117).
- Stephens, Graeme L. (Jan. 2005). "Cloud Feedbacks in the Climate System: A Critical Review." en. In: *Journal of Climate* 18.2, pp. 237–273. issn: 0894-8755, 1520-0442. doi: [10.1175/JCLI-3243.1](https://doi.org/10.1175/JCLI-3243.1). url: <https://journals.ametsoc.org/view/journals/clim/18/2/jcli-3243.1.xml> (cit. on p. 12).
- Stephens, Graeme L., Deborah G. Vane, Ronald J. Boain, Gerald G. Mace, Kenneth Sassen, Zhien Wang, Anthony J. Illingworth, Ewan J. O'connor, William B. Rossow, Stephen L. Durden, Steven D. Miller, Richard T. Austin, Angela Benedetti, and Cristian Mitrescu (Dec. 2002). "THE CLOUDSAT MISSION AND THE A-TRAIN: A New Dimension of Space-Based Observations of Clouds and Precipitation." en. In: *Bulletin of the American Meteorological Society* 83.12, pp. 1771–1790. issn: 0003-0007, 1520-0477. doi: [10.1175/BAMS-83-12-1771](https://doi.org/10.1175/BAMS-83-12-1771). url: <https://journals.ametsoc.org/view/journals/bams/83/12/bams-83-12-1771.xml> (cit. on p. 15).
- Strandgren, Johan, Luca Bugliaro, Frank Sehnke, and Leon Schröder (Sept. 2017). "Cirrus cloud retrieval with MSG/SEVIRI using artificial neural networks." en. In: *Atmospheric Measurement Techniques* 10.9, pp. 3547–3573. issn: 1867-8548. doi: [10.5194/amt-10-3547-2017](https://doi.org/10.5194/amt-10-3547-2017). url: <https://amt.copernicus.org/articles/10/3547/2017/> (cit. on p. 62).
- Suleymanov, Suleyman (2016). "Design and Implementation of an FMCW Radar Signal Processing Module for Automotive Applications." en. Master's thesis. University of Twente (cit. on p. 67).
- Testud, Jacques (2001). "The Concept of "Normalized" Distribution to Describe Raindrop Spectra: A Tool for Cloud Physics and Cloud Remote Sensing." en. In: *JOURNAL OF APPLIED METEOROLOGY* 40, p. 24 (cit. on p. 30).
- Tinel, Claire, Jacques Testud, Jacques Pelon, Robin J. Hogan, Alain Protat, Julien Delanoë, and Dominique Bouniol (June 2005). "The Retrieval of Ice-Cloud Properties from Cloud Radar and Lidar Synergy." en. In: *Journal of Applied Meteorology and Climatology* 44.6, pp. 860–

875. issn: 1520-0450, 0894-8763. doi: [10.1175/JAM2229.1](https://doi.org/10.1175/JAM2229.1). url: <https://journals.ametsoc.org/view/journals/apme/44/6/jam2229.1.xml> (cit. on pp. 16, 80).
- Toledo, Felipe, Julien Delanoë, Martial Haeffelin, Jean-Charles Dupont, Susana Jorquera, and Christophe Le Gac (Dec. 2020). "Absolute calibration method for frequency-modulated continuous wave (FMCW) cloud radars based on corner reflectors." en. In: *Atmospheric Measurement Techniques* 13.12, pp. 6853–6875. issn: 1867-1381. doi: [10.5194/amt-13-6853-2020](https://doi.org/10.5194/amt-13-6853-2020). url: <https://amt.copernicus.org/articles/13/6853/2020/> (cit. on p. 71).
- Vali, G., P. J. DeMott, O. Möhler, and T. F. Whale (Sept. 2015). "Technical Note: A proposal for ice nucleation terminology." en. In: *Atmospheric Chemistry and Physics* 15.18, pp. 10263–10270. issn: 1680-7316. doi: [10.5194/acp-15-10263-2015](https://doi.org/10.5194/acp-15-10263-2015). url: <https://acp.copernicus.org/articles/15/10263/2015/> (cit. on p. 22).
- Vishwakarma, Pragya, Julien Delanoë, Susana Jorquera, Pauline Martinet, Frederic Burnet, Alistair Bell, and Jean-Charles Dupont (Jan. 2022). "Climatology of estimated LWC and scaling factor for warm clouds using radar & microwave radiometer synergy." en. In: *Atmospheric Measurement Techniques Discussions*, pp. 1–42. issn: 1867-1381. doi: [10.5194/amt-2022-3](https://doi.org/10.5194/amt-2022-3). url: <https://amt.copernicus.org/preprints/amt-2022-3/> (cit. on p. 78).
- Wang, Quan, Chen Zhou, Xiaoyong Zhuge, Chao Liu, Fuzhong Weng, and Minghuai Wang (Sept. 2022). "Retrieval of cloud properties from thermal infrared radiometry using convolutional neural network." In: *Remote Sensing of Environment* 278, p. 113079. issn: 0034-4257. doi: [10.1016/j.rse.2022.113079](https://doi.org/10.1016/j.rse.2022.113079). url: <https://www.sciencedirect.com/science/article/pii/S0034425722001936> (cit. on p. 101).
- Wegener, A. (1911). "Thermodynamik der Atmosphäre." In: *Barth, Leipzig, Poland: J. A.* (cit. on pp. 14, 24, 25).
- Wehr, Tobias, Takuji Kubota, Georgios Tzeremes, Kotska Wallace, Hiro-taka Nakatsuka, Yuichi Ohno, Rob Koopman, Stephanie Rusli, Maki Kikuchi, Michael Eisinger, Toshiyuki Tanaka, Masatoshi Taga, Patrick Deghaye, Eichi Tomita, and Dirk Bernaerts (Aug. 2023). "The Earth-CARE mission – science and system overview." en. In: *Atmospheric Measurement Techniques* 16.15, pp. 3581–3608. issn: 1867-1381. doi: [10.5194/amt-16-3581-2023](https://doi.org/10.5194/amt-16-3581-2023). url: <https://amt.copernicus.org/articles/16/3581/2023/> (cit. on pp. 64, 75, 86, 87).
- Weitekamp, Claus, ed. (2005). *Lidar: Range-Resolved Optical Remote Sensing of the Atmosphere*. en. Vol. 102. Springer Series in Optical Sciences. New York: Springer-Verlag. isbn: 978-0-387-40075-4. doi: [10.](https://doi.org/10.1007/978-0-387-40075-4)

- 1007/b106786. url: <http://link.springer.com/10.1007/b106786> (cit. on pp. 73, 74).
- Wendisch, Manfred, Dörthe Müller, Dieter Schell, and Jost Heintzenberg (Nov. 2001). "An Airborne Spectral Albedometer with Active Horizontal Stabilization." en. In: *Journal of Atmospheric and Oceanic Technology* 18.11, pp. 1856–1866. issn: 0739-0572, 1520-0426. doi: 10.1175/1520-0426(2001)018<1856:AASAWA>2.0.CO;2. url: https://journals.ametsoc.org/view/journals/atot/18/11/1520-0426_2001_018_1856_aasawa_2_0_co_2.xml (cit. on p. 62).
- Wendisch, Manfred et al. (Mar. 2024). "Overview: Quasi-Lagrangian observations of Arctic air mass transformations & Introduction and initial results of the HALO–(AC)³ aircraft campaign." en. In: *EGUsphere*, pp. 1–46. doi: 10.5194/egusphere-2024-783. url: <https://egusphere.copernicus.org/preprints/2024/egusphere-2024-783/> (cit. on p. 187).
- Westbrook, C. D., A. J. Illingworth, E. J. O'Connor, and R. J. Hogan (Jan. 2010). "Doppler lidar measurements of oriented planar ice crystals falling from supercooled and glaciated layer clouds." en. In: *Quarterly Journal of the Royal Meteorological Society* 136.646, pp. 260–276. issn: 0035-9009, 1477-870X. doi: 10.1002/qj.528. url: <https://rmets.onlinelibrary.wiley.com/doi/10.1002/qj.528> (cit. on p. 78).
- Whiteman, D. N., B. Demoz, and Z. Wang (2004). "Subtropical cirrus cloud extinction to backscatter ratios measured by Raman Lidar during CAMEX-3." en. In: *Geophysical Research Letters* 31.12. issn: 1944-8007. doi: 10.1029/2004GL020003. url: <https://onlinelibrary.wiley.com/doi/abs/10.1029/2004GL020003> (cit. on p. 74).
- Wild, Martin, Maria Z. Hakuba, Doris Folini, Patricia Dörig-Ott, Christoph Schär, Seiji Kato, and Charles N. Long (Apr. 2019). "The cloud-free global energy balance and inferred cloud radiative effects: an assessment based on direct observations and climate models." en. In: *Climate Dynamics* 52.7, pp. 4787–4812. issn: 1432-0894. doi: 10.1007/s00382-018-4413-y. url: <https://doi.org/10.1007/s00382-018-4413-y> (cit. on pp. 44, 45).
- Williams, Christopher R. (Nov. 2011). "Inexpensive FM-CW Radar for Boundary-Layer Precipitation Studies." en. In: *IEEE Geoscience and Remote Sensing Letters* 8.6, pp. 1031–1035. issn: 1545-598X, 1558-0571. doi: 10.1109/LGRS.2011.2150733. url: <http://ieeexplore.ieee.org/document/5873120/> (cit. on p. 67).
- Winker, David, Mark Vaughan, Ali Omar, Yongxiang Hu, Kathleen Powell, Zhaoyan Liu, William Hunt, and Stuart Young (Nov. 2009).

- "Overview of the CALIPSO mission and CALIOP data processing algorithms." In: *Journal of Atmospheric and Oceanic Technology* 26, pp. 2310–2323. doi: [10.1175/2009JTECHA1281.1](https://doi.org/10.1175/2009JTECHA1281.1) (cit. on p. 83).
- Winker, David M., Jacques R. Pelon, and M. Patrick McCormick (Mar. 2003). "The CALIPSO mission: spaceborne lidar for observation of aerosols and clouds." en. In: ed. by Upendra N. Singh, Toshikasu Itabe, and Zhishen Liu. Hangzhou, China, p. 1. doi: [10.1117/12.466539](https://doi.org/10.1117/12.466539). url: <http://proceedings.spiedigitallibrary.org/proceeding.aspx?doi=10.1117/12.466539> (cit. on p. 15).
- Wirth, M., A. Fix, P. Mahnke, H. Schwarzer, F. Schrandt, and G. Ehret (July 2009). "The airborne multi-wavelength water vapor differential absorption lidar WALES: system design and performance." en. In: *Applied Physics B* 96.1, pp. 201–213. issn: 1432-0649. doi: [10.1007/s00340-009-3365-7](https://doi.org/10.1007/s00340-009-3365-7). url: <https://doi.org/10.1007/s00340-009-3365-7> (cit. on pp. 92, 94).
- Xiao, Haixia, Feng Zhang, Qianshan He, Pu Liu, Fei Yan, Lijuan Miao, and Zhipeng Yang (2019). "Classification of Ice Crystal Habits Observed From Airborne Cloud Particle Imager by Deep Transfer Learning." en. In: *Earth and Space Science* 6.10, pp. 1877–1886. issn: 2333-5084. doi: [10.1029/2019EA000636](https://doi.org/10.1029/2019EA000636). url: <https://onlinelibrary.wiley.com/doi/abs/10.1029/2019EA000636> (cit. on p. 50).
- Yorks, J., Dennis Hlavka, William Hart, and Matthew McGill (July 2011). "Statistics of Cloud Optical Properties from Airborne Lidar Measurements." In: *Journal of Atmospheric and Oceanic Technology* 28, pp. 869–883. doi: [10.1175/2011JTECHA1507.1](https://doi.org/10.1175/2011JTECHA1507.1) (cit. on p. 74).
- Zelinka, Mark D., Stephen A. Klein, and Dennis L. Hartmann (June 2012a). "Computing and Partitioning Cloud Feedbacks Using Cloud Property Histograms. Part I: Cloud Radiative Kernels." en. In: *Journal of Climate* 25.11, pp. 3715–3735. issn: 0894-8755, 1520-0442. doi: [10.1175/JCLI-D-11-00248.1](https://doi.org/10.1175/JCLI-D-11-00248.1). url: <https://journals.ametsoc.org/view/journals/clim/25/11/jcli-d-11-00248.1.xml> (cit. on p. 45).
- (June 2012b). "Computing and Partitioning Cloud Feedbacks Using Cloud Property Histograms. Part II: Attribution to Changes in Cloud Amount, Altitude, and Optical Depth." en. In: *Journal of Climate* 25.11, pp. 3736–3754. issn: 0894-8755, 1520-0442. doi: [10.1175/JCLI-D-11-00249.1](https://doi.org/10.1175/JCLI-D-11-00249.1). url: <https://journals.ametsoc.org/doi/10.1175/JCLI-D-11-00249.1> (cit. on p. 45).
- Zelinka, Mark D., Timothy A. Myers, Daniel T. McCoy, Stephen Po-Chedley, Peter M. Caldwell, Paulo Ceppi, Stephen A. Klein, and Karl E. Taylor (2020). "Causes of Higher Climate Sensitivity in CMIP6 Models." en. In: *Geophysical Research Letters* 47.1, e2019GL085782.

issn: 1944-8007. doi: 10 . 1029 / 2019GL085782. url: [https : / /
onlinelibrary.wiley.com/doi/abs/10.1029/2019GL085782](https://onlinelibrary.wiley.com/doi/abs/10.1029/2019GL085782) (cit.
on p. 46).

Zhu, Z-L. and L. Yang (July 1996). "Characteristics of the 1 km AVHRR
data set for North America." en. In: *International Journal of Remote
Sensing* 17.10, pp. 1915–1924. issn: 0143-1161, 1366-5901. doi: 10.
1080/01431169608948747. url: [https : / / www . tandfonline . com /
doi/full/10.1080/01431169608948747](https://www.tandfonline.com/doi/full/10.1080/01431169608948747) (cit. on p. 62).

Résumé de la thèse

Les nuages jouent un rôle important dans le cycle de l'eau et le bilan radiatif de la Terre, et tendent à significativement refroidir le climat. Cependant, des études montrent que de nombreuses incertitudes demeurent concernant leurs rétroactions et leur évolution dans le contexte du réchauffement climatique. En effet, les études tendent à montrer que les nuages amplifient le réchauffement climatique. Il devient donc crucial de mieux connaître l'effet radiatif des nuages, notamment ceux de phase mixte, qui représentent une part importante de l'effet radiatif des nuages (environ 20 %). Ces nuages sont constitués d'un mélange de cristaux de glace, de gouttelettes d'eau surfondues et de vapeur d'eau. Cette coexistence implique des processus complexes et la fraction de liquide et de glace affecte de manière significative leurs propriétés radiatives. Par ailleurs, cette complexité les rend difficiles à représenter dans les modèles numériques, introduisant des biais significatifs. Il est donc essentiel de mieux comprendre les processus microphysiques de ces nuages afin de réduire les incertitudes des prévisions climatiques et météorologiques.

Plusieurs types d'instruments permettent d'observer les nuages, tels que les sondes *in situ*, qui collectent directement un échantillon du nuage pour l'analyser, et les instruments de télédétection, qui observent à distance. Dans cette seconde catégorie, se trouvent les radars et les lidars, qui sont des instruments de télédétection dite active puisqu'ils émettent leur propre énergie et mesurent l'énergie rétrodiffusée par les nuages. Cette technique possède l'avantage d'offrir des informations résolues en distance. Ces instruments peuvent être embarqués à bord d'avions ou de satellites, offrant ainsi des couvertures régionale et globale, mais également être installés au sol pour observer une même zone de façon fréquente voire permanente. D'une part, les radars nuages fonctionnent à des fréquences (35 et 95 GHz) pour lesquelles la réflectivité est sensible à la taille des particules. Par conséquent, la réflectivité est plus élevée pour les grosses particules nuageuses (les cristaux de glace) que pour les petites particules (les gouttelettes d'eau). D'autre part, les lidars fonctionnent, généralement, à des longueurs d'onde comprises entre 355 et 1064 nm et sont donc plus sensibles à la concentration des particules (régime de diffusion de Mie). Ainsi, la rétrodiffusion lidar s'avère plus élevée pour les particules très concentrées, telles que les gouttelettes d'eau. En outre, la combinaison de ces deux instruments offre une synergie radar-lidar permettant de tirer parti des forces et des faiblesses de chaque instrument pour restituer les propriétés des nuages.

Cependant, les mesures radar-lidar ne permettent pas d'accéder directement aux propriétés optiques et microphysiques des nuages. Il s'avère donc nécessaire d'utiliser des algorithmes de restitution pour lier les mesures aux propriétés nuageuses. Cette situation peut être assimilée à un problème inverse $Y = f(X) + \epsilon$ où Y est composé de la réflectivité radar observée Z_{obs} et de la rétrodiffusion lidar observée β_{obs} . X est le vecteur d'état composé de variables permettant de décrire l'état des nuages. La fonction f représente les *forward models* radar et lidar permettant d'estimer une réflectivité radar Z_{fwd} et une rétrodiffusion lidar β_{fwd} à partir du vecteur d'état. Le principe de cette méthode est d'obtenir la meilleure estimation de X permettant de minimiser la différence entre les valeurs modélisées Z_{fwd} et β_{fwd} avec les valeurs des observations Z_{obs} et β_{obs} .

Ces travaux de thèse proposent une nouvelle méthode synergique radar-lidar basée sur ce principe, appelée VarPy-mix et dédiée à la restitution des propriétés des nuages d'eau surfondue, de glace et de phase mixte. Sur la base d'une méthode existante dédiée uniquement aux nuages de glace, cette nouvelle approche inclut à la fois l'eau surfondue et les situations de phase mixte. Pour cela, la première étape a été d'adapter et d'améliorer la classification servant à identifier la nature des particules observées. En complément des classes de cristaux de glace, les classes d'eau surfondue et de phase mixte ont été incorporées pour pouvoir être traitées par l'algorithme. L'amélioration de cette classification consistait à corriger certaines erreurs de classification, comme par exemple de la glace faussement classifiée en phase mixte ou encore à éroder des valeurs isolées. Ensuite, de nombreuses adaptations ont été apportées à l'algorithme afin de restituer séparément les propriétés des cristaux de glace et de l'eau surfondue, en tenant compte des propriétés différentes de chaque hydrométéore. Cette approche est basée sur les sensibilités spécifiques du radar et du lidar vis-à-vis des deux types d'hydrométéores : les cristaux de glace dominant le signal radar, tandis que l'eau surfondue domine le signal lidar. Chaque hydrométéore est donc restitué par le signal qu'il domine. Par conséquent, la composition du vecteur d'état X a été revue et divisée en deux parties : une partie pour les propriétés des cristaux de glace et l'autre pour les propriétés de l'eau surfondue. En outre, les matrices liées au vecteur d'état ont été modifiées en conséquence. Par ailleurs, les *forward models* sont constitués de *look-up tables* (LUT) créées à partir de distribution de la taille des particules. D'une part, pour les cristaux de glace, deux LUTs existantes sont utilisées. D'autre part, pour l'eau surfondue, une LUT a été créée à partir d'une distribution log-normale de la taille des particules. Finalement, avec VarPy-mix, il est désormais possible de restituer, à la fois pour les cristaux de glace et l'eau surfondue, l'extinction (α_{ice} et α_{liq}), le rayon effectif ($r_{e,\text{ice}}$ et $r_{e,\text{liq}}$), la concentration en nombre de particules (N_{ice} et

N_{liq}) et le contenu en eau (IWC et LWC) à partir de mesures radar-lidar.

Afin d'évaluer cette nouvelle méthode, les restitutions de VarPy-mix sont comparées à des mesures *in situ*, provenant d'observations colocalisées et de la littérature. Une première étude compare les restitutions obtenues à partir des données satellites CloudSat-CALIPSO avec des mesures *in situ* aéroportées colocalisées lors de la campagne ASTAR 2007 près du Svalbard. Cette étude montre que les restitutions à partir des mesures radar-lidar suivent les mêmes tendances que les mesures *in situ* et fournissent des résultats prometteurs avec un pourcentage d'erreur moyen de 49 % pour le contenu en eau liquide et 75 % pour le contenu en glace et ce malgré des échelles de mesures différentes et une colocalisation imparfaite. En plus des données satellites de CloudSat et CALIPSO, la méthode VarPy-mix a également été appliquée aux plateformes radar-lidar aéroportées française, RALI, et allemande, HALO. Les premiers résultats obtenus à partir des données de ces plateformes sont présentés dans cette thèse. Pour chaque plateforme, les résultats concernant la phase mixte sont comparés à des données *in situ* issues de la littérature. Les résultats de cette comparaison montrent que les restitutions ont une tendance proche de celles observées par l'*in situ*: (a) l'extinction des gouttes d'eau surfondues et le contenu en eau liquide sont globalement plus élevés que l'extinction des cristaux de glace et que le contenu en glace, (b) les gouttes d'eau surfondues s'avèrent bien plus petites que les cristaux de glace, (c) la concentration des gouttes d'eau surfondues est bien plus importante que celle des cristaux de glace. Cette méthode étant nouvelle, des améliorations peuvent être apportées, notamment par un meilleur paramétrage apporté par des comparaisons avec des données *in situ* colocalisées obtenues, par exemple, lors de campagnes récentes avec les plateformes RALI et HALO.